SWIR EMITTING RARE EARTH ALBUMIN NANOCOMPOSITES FOR TARGETED IMAGING, MOLECULAR PHENOTYPING, AND IMPROVED DRUG DELIVERY TO TUMORS

By

MARGOT ALEXANDRA NASH ZEVON

A dissertation submitted to the

Graduate School-New Brunswick

And

The Graduate School of Biomedical Sciences

Rutgers, The State University of New Jersey

In partial fulfillment of the requirements

For the degree of

Doctor of Philosophy

Graduate program in in Biomedical Engineering

Written under the direction of

Prabhas V. Moghe, Charles M. Roth

And approved by

_____
_____
_____
_____
_____

New Brunswick, New Jersey

October 2016

ABSTRACT OF THE DISSERTATION

Short Wave Infrared Radiation Emitting Rare Earth Albumin Nanocomposites for Targeted Imaging, Molecular Phenotyping, and Improved Drug Delivery to Tumors

By MARGOT ALEXANDRA NASH ZEVON

Dissertation Director:

Prabhas V. Moghe, Ph.D. and Charles M. Roth, Ph.D.

Early detection and effective drug delivery remain unresolved challenges that limit the effectiveness of therapeutic regimens against a variety of cancers. Particularly acute are the challenges associated with penetration into the dense matrix of solid tumors and the targeting of metastatic lesions before they become unmanageable. Current clinical imaging techniques employed to detect these lesions are only able to provide anatomical macroscopic information on a tumor state. Additionally, many of these modalities lack the resolution to detect microlesions at a stage ideal for therapeutic intervention, and are unable to resolve lesions in specific tissues such as bone. The early detection and sensitive tracking of disease states is critical to successful management and treatment. While imaging modalities such as MRI and ultrasound provide only anatomical details, optical imaging techniques can provide high content, high resolution images detailing the location and molecular phenotype of a tumor. This is critical in the management of many malignancies including breast cancer, as cell receptor expression dictates therapeutic regimen and is often not conserved through disease

progression. Despite the potential for optical imaging to fill this critical role in breast cancer management, there are still numerous challenges that limit its clinical translation.

Rare earth nanoprobes (ReNPs) are bright, stable, optically efficient contrast agents that provide many unique advantages over traditional optical imaging fluorophores. When excited with near infrared (NIR, 700-1000 nm) photons, ReNPs emit fluorescence in both the visible (400-700 nm) and short wave infrared (SWIR, 1000-3000 nm) ranges. While the "upconverted" visible photons are quickly absorbed or scattered by biological tissue, SWIR photons can more easily penetrate tissue and be detected via specialized cameras and sensors. In order to impart solubility and cytocompatability, we have encapsulated ReNPs in human serum albumin to generate rare earth albumin nanocomposites (ReANCs). The tunable albumin coating of ReANCs allows for a wide range of ligands, therapeutic payloads, and permeation enhancers to be conjugated to the surface of the particle's shell. These characteristics yield multifunctional nanoprobes that can be adapted for many purposes including targeted imaging.

This dissertation is focused on engineering biocompatible ReANCs as a multifunctional contrast agent capable of improved payload delivery, *in vivo* SWIR based optical imaging, and targeted imaging and molecular mapping of solid tumors. This study describes the development of drug loaded, tumor penetrating albumin nanoshells designed to overcome physiological barriers to solid tumor drug delivery. These nanoparticles are then further engineered to encapsulate SWIR emitting contrast agents, which form the basis of a novel optical imaging platform capable of the sensitive and specific detection of metastatic breast cancer. The resulting ReANCs were targeted to markers of breast cancer metastasis to enable early detection of small–scale lesions in the animal's lungs. Strikingly, these targeted particles were capable of identifying receptor positive lesions, allowing for a non-invasive 'optical biopsy' that

could be used to determine therapeutic intervention. These nanoparticles were then used to detect distant site metastasis in animal's long bones and adrenal glands. Notably, ReANCs were capable of accumulating in and identifying metastatic lesions in animal's bones prior to their detection with MRI. The cumulative findings of this work describe a multifunctional probe capable of surveillance of metastatic disease and of its therapeutic responsiveness.

ACKNOWLEDGEMENTS

I would first like to acknowledge and express my gratitude to my thesis advisors, Dr. Prabhas Moghe and Dr. Charles Roth, for the mentorship and support provided over the course of my PhD. Their guidance has shaped me as a scientist and as a person and has shown me the true joy of scientific discovery. I am grateful for the opportunity to complete this journey with them. Thank you for all the lessons you have taught me.

Next, I would like to thank my committee members, Dr. Mark Pierce, Dr. Rick Riman, and Dr. Shridar Ganesan. I have benefitted greatly from your expertise, guidance, and knowledge and this work is better for your involvement. I would also like to acknowledge Dr. Suzie Chen and Dr. Rob Sherrell for their support at the beginning of my time at Rutgers. Suzie and Rob have both been instrumental in the animal studies described in chapter 3, adopting me into their groups and providing both technical and moral support.

During my time at Rutgers I have had the great fortune of working with some talented and inspiring individuals. Their mentorship has been invaluable and I am grateful for all they have given me. Dr. Dominik Naczynski, thank you for your guidance and your friendship. From you I have learned what it means to be a scientist and to persevere through the many hardships of graduate school. Dr. MC Tan, thank you for your encouragement, advice, and support. You have taught me not only about materials science, but how to stand up for myself and navigate difficult processes. Dr. Brian Wall, thank you for the time you took away from your own work to assist with animal studies. I appreciate your training as much as I appreciate your enthusiasm.

I am fortunate to leave the future of this work in very capable hands. Dr. Vidya Ganapathy, thank you for everything you have done. You consistently amaze me with your insight and love of science, and I (and my thesis) am better for having you in my life. I thank

Laura Higgins for the time she spent assisting me with the optical aspects of this project. Laura's support has enabled me to explore new directions, and I am grateful for both her expertise and her friendship. I would also like to thank Harini Kantamneni for her assistance in this work. I am happy she is the student to continue this project and guide it in new directions, and I have the utmost faith in her abilities and success.

Finally, none of this would have been possible without my friends and family to support me along the way. To my friends both at Rutgers and elsewhere, thank you for your enduring friendship. To the Strelnikov and Polyakov families, thank you for welcoming me into your homes during my time in New Jersey. To my parents Linda Nash and Michael Zevon and my stepfather Frank Alabiso, thank you for your belief in me. I would also like to acknowledge my sister Emily Zevon for her support with editing much of this work.

For those who I have not mentioned, know that you have made a great impact on my life. I love and thank you all.

DEDICATION

This dissertation is dedicated to my parents Linda Nash and Michael Zevon and my stepfather Frank Alabiso whose constant love and unwavering belief in my abilities have helped me complete graduate school. My sister Emily has likewise been a source of support and homemade chocolates.

This work is also dedicated to the friends who have been a source of strength and patience along this sometimes tedious path. Thank you for giving me the confidence I need to see this through, and for your patience when I am stuck in lab late.

PRIOR PUBLICATIONS

Sections of this dissertation have been previously published or are being prepared for publication, as listed below:

-Chapter 2 has been published in its entirety:

Cui, M., Naczynski, D.J., Zevon, M.A., Griffith, K., Sheihet, L., Poventud-Fuentes, I., Chen, S., Roth, C.M., Moghe, P.V. Multifunctional Albumin Nanoparticles As Combination Drug Carriers for Intra-Tumoral Chemotherapy. *Advanced Healthcare Materials*, 2013. 2(9), p. 1236-1245**. Co-first author**

-Chapter 3 has been published in its entirety. The work and writing described in this chapter was done in close collaboration with the first two authors Dr. Dominik Naczynski and Dr. MC Tan. This author's primary contributions were collaboration on qualitative *in vivo* imaging studies and quantification of particle distribution, clearance, and pharmacokinetic profile.

D.J. Naczynski, M.C. Tan, M. Zevon, B. Wall, J. Kohl, A. Kulesa, S. Chen, C.M. Roth, R.E. Riman, P.V. Moghe. Rare-earth-doped biological composites as in vivo shortwave infrared reporters. *Nature Communications*, 2013. 4(2199).

-Chapter 4 has been published in its entirety:

Margot Zevon, Vidya Ganapathy, Harini Kantamneni, Marco Mingozzi, Paul Kim, Derek Adler, Yang Sheng, Mei Chee Tan, Mark Pierce, Richard E. Riman, Charles M. Roth, Prabhas V. Moghe. Cxcr-4 Targeted Swir Emitting Nanoprobes for Enhanced Deep Tissue Imaging and Micrometastatic Lesion Detection. *Small* 11: 6347–6357 (2015)

-Sections of Chapter 5 have been submitted for publication with the following citation: **Zevon, M., Katamneni, Ganapathy, V., H., Higgins, L., Mingozzi, M., Adler, D., Tan, M.C., Pierce, M., Riman, R., Roth, C.M., Moghe, P.V.** Early detection and longitudinal imaging of cancer micrometastases using biofunctionalized rare-earth albumin nanocomposites. *Proc. SPIE Laser Sensors and Systems; and Next-Generation Sensors and Systems Includes volumes*, 2016. Accepted for Publication

-Sections of Chapter 5 are being prepared for publication elsewhere entitled: "Early detection and longitudinal imaging of cancer micrometastases using biofunctionalized rare-earth albumin nanocomposites" **Zevon, M., Katamneni, Ganapathy, V., H., Tan, M.C., Pierce, M., Riman, R., Roth, C.M., Moghe, P.V.**

TABLE OF CONTENTS

Contents

ABSTRACT OF THE DISSERTATION ii

ACKNOWLEDGEMENTS v

DEDICATION vii

PRIOR PUBLICATIONS viii

TABLE OF CONTENTS x

LIST OF FIGURES xv

CHAPTER 1 BACKGROUND AND SIGNIFICANCE 1

1.1 Breast cancer 2

1.1.2 Epidemiology 2

1.1.3 Surgical options for breast cancer treatment 3

1.1.4 Chemotherapy for breast cancer treatment 5

1.1.5 Targeted therapies 6

1.1.6 Breast Cancer Metastasis 7

1.2 Cancer Imaging 9

1.3 Optical imaging of disease states 12

1.3.1 Contrast agents for biomedical optical imaging 13

1.3.2 Wavelengths for biomedical optical imaging 14

1.3.3 Benefits of SWIR wavelengths for optical imaging 17

1.4 Rare earth nanoparticles as optical imaging contrast agents 19

1.4.1 Synthesis of RE nanoparticles 21

1.5 Nanoparticles for cancer drug delivery and imaging 21

1.5.1 Nanoparticle based delivery systems 21

1.5.2 Nanoparticle design considerations 24

1.5.3 Nanoparticle materials 28

1.6 Albumin as a nanoparticle agent 30

1.6.1 Benefits of albumin nanocarriers 30

1.6.2 FDA approved drug delivery platform-Abraxane 32

1.6.3 Albumin nanoparticle synthesis 32

1.7 Dissertation Overview....33
CHAPTER 2....36
MULTIFUNCTIONAL ALBUMIN NANOPARTICLES AS....36
COMBINATION DRUG CARRIERS FOR INTRA-TUMORAL CHEMOTHERAPY....36
2.1 Abstract....37
2.2 Introduction....38
2.3 Methods....41
2.3.1. Reagents....41
2.3.2. Cell Culture....41
2.3.3. Albumin Nanoparticle Fabrication....41
2.3.4. Albumin Nanoparticle Purification....42
2.3.5. Physical Characterization of Albumin Nanoparticles....42
2.3.6. Preparation of Collagenase-Coated Nanoparticles....43
2.3.7. Collagenase Activity Assay....43
2.3.8. Cellular uptake of collagenase coated nanoparticles....44
2.3.9. Multicellular Tumor Model Spheroid Formation....44
2.3.10. Nanoparticle Penetration in Tumor Model Spheroids....44
2.3.11. Drug Loading of Albumin Nanoparticles....45
2.3.12. Quantification of Drug Loading....46
2.3.13. Cell Viability Assay....47
2.14. Cell Apoptosis Assay....47
2.3.15. Drug Release....48
2.3.16. In vitro Cellular Uptake of Drug Loaded ANPs....48
2.4. Results....49
2.4.1. Characterization of Nanoparticles....49
2.4.2. Matrix Protease Modified ANPs....49
2.4.3. Penetration of cANPs in a 3-D Multicellular Spheroid Model....51
2.4.4. ANP Drug Loading and Release Kinetics....52
2.4.5. In vitro Cytotoxicity of Curcumin, Riluzole and Combination Treatments....54
2.4.6. Efficacy of Dual Drug Loaded ANPs In vitro....54
2.4.7. Efficacy of Matrix Protease-Modified, Combination Drug ANPs....56
2.5 Discussion....56

2.6. Conclusion 63
2.7 supplemental figures 64
CHAPTER 3 71
RARE EARTH ALBUMIN NANOCOMPOSITES AS SHORT WAVE INFRARED EMITTING *IN VIVO* OPTICAL CONTRAST AGENTS 71
3.1 Abstract 72
3.2 Introduction 72
3.3 Methods 74
3.3.1 Synthesis of rare earth nanoprobes (in collaboration with Riman group) 74
3.3.2 ReANC synthesis and characterization 75
3.3.3 Animal models (in collaboration with Chen group) 75
3.3.4 Imaging prototype 76
3.3.5 Imaging signal processing 77
3.3.6 Qualitative biodistribution imaging 78
3.3.7 Quantitative biodistribution analysis 78
3.4 Results 79
3.4.1 Preparation and characterization of multispectral REs 79
3.4.2 Biomedical application of SWIR-based imaging using REs 81
3.4.3 Tumor imaging using bioactive, albumin-coated REs 81
3.4.4 Evaluation of quantitative biodistribution 86
3.5 Discussion 87
3.6 Conclusion 88
3.7 Supplementary Figures 90
CHAPTER 4 96
CXCR-4 TARGETED, SHORT WAVE INFRARED (SWIR) EMITTING NANOPROBES FOR ENHANCED DEEP TISSUE IMAGING AND MICROMETASTATIC CANCER LESION DETECTION 96
4.1 Abstract 97
4.2 Introduction 97
4.3 Results 100
4.3.1 Synthesis and characterization of nanoparticles 100
4.3.2 Cancer-Targeting Probes: AMD3100 Functionalized ReANCs (fReANCs) 101
4.2.3 Active receptor targeting of fReANCs 104

4.2.4 In vivo SWIR imaging 105
4.2.5 Histopathological analysis of Nanoparticle Biocompatibility 108
4.2.6 Ex vivo SWIR Imaging 109
4.2.6 In vivo detection of tumors in internal organs with SWIR imaging 110
4.3 Discussion 114
4.5. Experimental Methods 118
Reagents: 118
Cell Culture: 118
ReANC Fabrication 118
Preparation of functionalized nanoparticles (fReANCs): 119
Quantification of loading: 119
In Vitro cellular uptake of fReANCs: 120
Cell uptake and confocal imaging 120
Cell viability assay: 120
In Vivo imaging: 121
SWIR-imaging: 121
MRI Imaging: 121
Detection of subcutaneous cancer lesions: 122
Ex vivo analysis of subcutaneous tumors: 122
Detection of lung metastatic lesions: 122
Ex vivo analysis of metastatic tumors: 123
4.6 Supplemental Figures 124
CHAPTER 5 130
EARLY DETECTION AND LONGITUDINAL IMAGING OF CANCER MICROMETASTASES USING BIOFUNCTIONALIZED RARE-EARTH ALBUMIN NANOCOMPOSITES 130
5.1 Abstract 131
5.2 Introduction 132
5.3 Results 134
5.3.1 Detection of Microlesions Using RE Probes 134
5.3.2 Detection of Metastatic Bone Lesions 135
5.3.3 Detection of Multiple Metastatic Sites with Functionalized Probes 139
5.3.4. *Ex Vivo* Evaluation of Tumor Sites 141

5.3.5. Evaluation of the Role of Metastatic Niche on Cell Phenotype 142
5.4 Discussion 145
5.5 Experimental Methods 148
5.5.1 Sample Preparation 148
5.5.2 Microlesion detection 149
5.5.3 SWIR imaging 149
5.5.4 Detection of metastatic lesions in the bones 150
5.5.5 Detection of multiple metastatic sites 151
5.5.6 Generation of organotropic lines (Lines generated by Dr. Vidya Ganapathy in Reiss lab at CINJ) 151
5.5.7 Therapeutic inhibition of metastasis (data not shown) 152
5.6 Conclusions 152
5.7 Supplemental figures 153
CHAPTER 6 154
RESEARCH SUMMARY AND CONCLUSIONS 154
6.1 Summary and Conclusions 155
6.1.1 Modification of albumin carriers for improved payload delivery to solid tumors 155
6.1.2 Development and *in vivo* evaluation of SWIR emitting rare earth albumin nanocomposites 156
6.1.3 Molecular targeting of nanocarriers for improved particle localization and lesion imaging 157
6.1.4 Application of SWIR emitting ReANCs for detection of distant micro-metastatic lesions 157
6.2 Future Directions 159
6.2.1 Theranostic nanoparticles 159
6.2.2. Multispectral imaging 160
6.2.3. Multimodal imaging 162
CHAPTER 7 165
REFERENCES 165

LIST OF FIGURES

Figure 1.1-Progression of Cancer Metastasis. 8
Figure 1.2-Cancer Imaging Modalities 11
Figure 1.3-Wavelength Dependent Tissue Autofluorescence 16
Figure 1.4-Second Window Imaging in Biological Media. 18
Figure 1.5-Mechanism of RE fluorescence 20
Figure 1.6-Multifunctional Nanoparticles for Drug and Contrast Agent Delivery 23
Figure 1.7-Nanoparticle Accumulation at Tumor Sites. 27
Figure 1.8-Crystal Structure of Human Serum Albumin. 31
Figure 2.1. Schematic summarizing the overall design of albumin nanoparticles as advanced healthcare materials for enhanced chemotherapy. 40
Figure 2.2 – SEM and Characterization of Various ANP Formulations. 50
Figure 2.3. – Spheroids penetration of protease modified ANPs 53
Figure 2.4. – Therapeutic effect of Curcumin, Riluzole and Dual Drugs. 55
Figure 2.5. Multimodular ANPs exhibit enhanced tumor cytotoxicity in a size, protease-modification, and dual drug-display dependent manner 59
Supplementary Figure 2.1 – Quantification of Nanoparticle Penetration into Spheroids. 64
Supplementary Figure 2.2 – ANP Auto-fluorescence Spectrum. 65
Supplementary Figure 2.3 – Physical Characterization of Single Drug-Loaded ANPs 66
Supplementary Figure 2.4 – Physical Characterization and Binding Efficiency of Dual Drug-Loaded ANPs. 67
Supplementary Figure 2.5 – ANPs Retard the Release of Various Drug Formulations In Vitro. 68
Supplementary Figure 2.6 – In vitro Cytotoxicity of Curcumin, Riluzole and Dual Drugs. 69
Supplementary Figure 2.7 - The internalization of drugs and ANPs in 2-D C8161+ cell Culture. 70
Figure 3.1 Properties of the Rare-Earth-Doped Nanoprobes 80
Figure 3.2 RE Nanoprobes Enable Real-Time Imaging in vivo 81
Figure 3.3- Biologically Permissive Nanocomposites of REs exhibit SWIR emission 83
Figure 3.4- RE biologic nanocomposites profile disease progression in vivo 86
Supplementary Figure S1 – Organ biodistribution of formulations 90
Supplementary Figure S2 – ICP-MS standard curves correlating yttrium concentration to count rate 91
Supplementary Figure S3 – Absorbance and transmission properties of SWIR and visible light through various tissue samples 92
Supplementary Figure S4 – Physical and optical properties of 300 nm albumin encapsulated rare-earth-doped nanoprobes 93
Supplementary Figure S5 – Size distribution of various formulations 94
Supplementary Figure S6 – In vivo evaluation and clearance of 300 nm albumin encapsulated rare-earth-doped nanoprobes using SWIR imaging 95
Figure 4.1: Design, fabrication, and preclinical efficacy of rare earth nanoprobes. 102
Figure 4.2: Characterization of functionalized Rare Earth Nanoprobes 104

Figure 4.3: Active Cancer Targeting of Rare Earth Nanoprobes 106
Figure 4.4: Functionalized nanoprobes are capable of molecular discrimination of tumors in vivo 107
Figure 4.5: Rare-Earth nanoprobes proved safe for long-term use with no significant impact on animals' weight or damage to organs of accumulation..... 109
Figure 4.6: Targeted fReANCs allow for detection of microscale lung lesions. 112
Figure 4.7: Longitudinal tracking of internal lesions with SWIR imaging. 113
Supplemental Figure 4.1. Size distribution histograms of ReANC and fReANC showing nanoscale, monodisperse populations. 124
Supplemental figure 4.2 125
Supplemental Figure 4.3 126
Supplemental Figure 4.4: 127
Supplemental Figure 4.5: 128
Supplemental Figure 4.6: 129
Figure 5.1: ReANCs retain functionality and allow for resolution of microscale cell clusters 135
Figure 5.2: Detection of bone micrometastasis 136
Figure 5.3: SWIR imaging is capable of identifying metastatic bone lesions prior to their detection with clinically relevant imaging modalities 138
Figure 5.4: Functionalized ReANCs are capable of identifying adrenal metastasis in animals 140
Figure 5.5: Ex vivo SWIR imaging confirms probe accumulation at lesion sites 141
Figure 5.6: Development of organ tropic cell lines. 142
Figure 5.7: The metastatic niche causes alterations in the genetic profile and receptor expression of lesions 144
Supplemental Figure 5.7.1 153
Figure 6.1: *in vitro* imaging of differently doped ReANCs 161
Figure 6.2: Ultrasound imaging of ReANCs through bio mimetic tissue phantoms 164

CHAPTER 1

BACKGROUND AND SIGNIFICANCE

1.1 Breast cancer

1.1.2 Epidemiology

Breast cancer is the second leading cause of cancer death in women, with over 200,000 new cases in the USA annually and nearly 40,000 associated deaths. Affecting approximately 12% of US women over the course of their lifetimes, breast cancer represents a significant area of public health interest. Tumors are classified according to type, grade, and tumor phenotype, with each classification being used to guide therapeutic regimen[1].

Breast cancer type is assessed during biopsy to determine the tumor's characteristics. The majority of breast cancers, called carcinomas, arise from the epithelial cells that line the breast. Carcinomas are further classified as ductal, lobular, or glandular (called adenocarcinoma) depending on where in the breast tissue they originate. Tumor aggressiveness and metastatic potential is described as *in situ* (non-invasive and unlikely to metastasize) or invasive. The most common type of breast cancer is invasive ductal carcinoma, where the malignant cells have spread beyond the walls of the milk ducts and grown into the tissue of the breast. These tumors are likely to metastasize and represent an advanced disease stage. Less than 1 in 10 invasive cancers originates in the milk-producing lobules of the breast-these carcinomas are likely to metastasize and may be more difficult to detect with conventional techniques [1].

Biopsies are also used by pathologists to assign a grade (or stage) to a tumor. Grade is determined by comparing affected tissue to normal breast tissue and determining the rate of cancer cell growth and division, and is critical for determining patient's prognosis. While traditionally grade has been determined based on tissue appearance, recent studies have shown that tumor gene expression can aide in accurate determination of tumor grade and potential

invasiveness, allowing for more efficacious therapeutic intervention and accurate estimation of patient outcome [2]. Lower grade cancers are slow-growing and unlikely to spread, while higher grade cancers are more invasive with a greater propensity for metastasis [1, 2]. Stage I and II malignancies are characterized by primary tumor size with no metastasis. Five year survival for Stage I and II breast cancers is 96%, but this drops to 46% for Stage III cancers with axillary lymph node infiltration. Five year survival rates for Stage IV (distant metastatic) breast cancer drops to 24%, illustrating that patient survival is intrinsically linked to invasiveness [3, 4]. Due to the difficulties with treating stage IV cancer, early detection and treatment of localized or micrometastatic disease are critical to achieve improved patient survival.

Breast carcinomas can be additionally classified by cellular receptor expression. Healthy breast tissue expresses receptors for estrogen and progesterone. Malignant cells can overexpress one, both, or neither of these hormone receptors. Tumors expressing estrogen receptors are referred to as estrogen positive (ER+) tumors, and those expressing progesterone receptors are called progesterone positive (PR+) tumors. In addition to aberrant hormone receptor expression, approximately 1 in 5 breast cancers overexpress the human epidermal growth factor receptor 2 (HER2) and are referred to as HER2 positive cancers [1]. HER2 overexpression has been correlated with a high level of invasiveness and metastatic potential [2]. The 10-17% of malignancies that do not express ER, PR or HER2 receptors are known as ‘triple negative’ cancers. Triple negative cancers are correlated to poor prognosis and limited therapeutic options [5].

1.1.3 Surgical options for breast cancer treatment

Once breast cancer is diagnosed, it is commonly treated with surgical resection of the primary tumor. Surgical procedures can be classified as either breast-conserving (i.e. lumpectomy,

quadrantectomy or partial mastectomy) or breast-removing (i.e. mastectomy). In breast conserving surgery (BCS), only the malignant breast tissue and surrounding margins are removed and the remaining tissue is often re-shaped or replaced to improve breast symmetry (oncoplastic surgery) [6]. Approximately 64% of patients who receive surgery undergo a type of breast conserving procedure [7]. BCS is currently the standard of care for early stage breast cancer, although patients are often treated with adjuvant radiation or chemotherapy for improved outcomes [8].

As opposed to BCS, in which much of the healthy native tissue is conserved, mastectomies are characterized by the complete removal of the affected breast. This may or may not include affected areas of the chest wall muscles. Although mastectomy is the total removal of breast tissue, positive margins may still occur and are associated with poor long-term prognosis. When the margins are clear, mastectomy is not always accompanied by management with additional therapeutics [9]. Multiple studies have demonstrated no difference in survival rates between the two surgical techniques in early stage cancers, although BCS has a higher risk for local disease recurrence [9]. Despite this, the number of women receiving prophylactic and early mastectomies has trended upward, with the mastectomy rate rising from 35.6% of surgical procedures in 2005 to 38.4% in 2008 [10].

During surgical resection of the primary tumor, lymph nodes may be biopsied or removed to determine the presence of regional metastasis. Lymph node surgery consists of either axillary lymph node dissection (ALND) or sentinel lymph node biopsy (SLNB). ALND consists of the surgical removal of a number of axilla lymph nodes, which are then examined for the presence of malignant cells. This technique has, in the past, been critical to patient outcomes as lymph node involvement is a significant factor in cancer staging and prognosis. Although ALND is a vital

tool it has substantial side effects affecting as many as 30% of patients [11, 12]. Therefore, SLNB is often performed as a safe and effective alternative procedure with fewer side effects. SLNB is performed via the injection of a tracer into the tumor space to determine drainage (and probable metastasis) to surrounding lymph nodes. Draining lymph nodes are then surgically resected [13]. Although SLNB presents an attractive method of determining cancer stage and metastasis, it is not without problems. SLNB is known to be a difficult procedure to perform, requiring an especially skilled surgeon. Inexperienced surgeons have been shown to have a false negative rate of 9% when performing SLNB. Additionally, route of tracer injection and injection technique had a very significant impact on the efficacy of SLNB, with false negative rates of up to 12%. SLNB was less effective in detecting metastasis when primary tumors were small, located in the upper outer quadrant of the breast, or when only one SLN was resected [14]. Identification of early micrometastasis is critical for long term survivorship and represents a critical problem in the management of breast cancer.

1.1.4 Chemotherapy for breast cancer treatment

Chemotherapy, in which cancer-killing drugs are administered to a patient, is a common treatment in breast cancer. Chemotherapy is typically administered for one of three reasons: 1. as neoadjuvant therapy prior to surgical resection of the primary tumor, 2. as adjuvant therapy after surgery to prevent recurrence, or 3. to treat metastatic disease. Choice of chemotherapeutic agent is dependent on the patient's specific cancer biology and is often administered in conjunction with biological treatments such as therapeutic monoclonal antibodies. It is critical for clinicians to fully understand the molecular phenotype of a breast malignancy to administer the most efficacious treatment [15]. Although many breast cancers (including metastatic cancers) remain chemosensitive, drug resistance is quickly developed and

response duration is very short. The use of adjuvant chemotherapy is not always correlated with increased overall survival rates[16].

Of the many classes of chemotherapeutic agents prescribed for treatment of breast cancer, taxanes are recognized as critically important in the successful management of disease. However, like all chemotherapeutic agents, taxanes (i.e. paclitaxel) have many toxic off-target side effects that diminish both maximum tolerated dose and patient quality of life. These agents are often hydrophobic and must be administered in detergent-like agents, increasing irritation to the patient and diminishing drug half-life and efficacy[17]. To this end an albumin nanoparticle formulation of paclitaxel (Abraxane) has been synthesized and is FDA approved for treatment of metastatic breast cancer [18]. Compared to free taxanes, Abraxane has improved efficacy with longer overall survival and time to recurrence, and fewer toxic side effects [17]. This drug formulation represents a promising platform for improved drug delivery to difficult-to-treat breast cancers. Despite these improvements, chemotherapeutics remain poorly tolerated by many patients with a high rate of damaging side effects.

1.1.5 Targeted therapies

Variations in cancer cellular receptor expression create the opportunity for more specific receptor-targeted pharmacologic therapeutics. Targeted therapies interact with specific over-expressed on malignant cells, leading to specific, effective patient-specific therapeutics with fewer and less severe off-target side effects than systemic chemotherapy [19]. The most common cellular markers targeted by molecular therapeutics are the estrogen, progesterone and Herceptin receptors. Hormone receptor (estrogen or progesterone) positive breast cancers can often be administered systemic hormone therapy as an adjuvant treatment. The current clinical gold standard for hormonal therapy is tamoxifen, a prodrug whose metabolites have a

very high affinity for the estrogen receptor commonly overexpressed on malignant cells [20]. Tamoxifen's active metabolites act as competitive inhibitors of estrogen and prevent the hormone from binding to its receptor, reducing its downstream effects [21, 22]. Tamoxifen has been shown to be effective against both primary and metastatic tumors, with 5 years of adjuvant tamoxifen reducing breast cancer mortality by 31% [23]. Tamoxifen's success has inspired many therapies that act similarly to reduce a patient's estrogen levels, such as ovarian ablation [20].

Another common therapeutic target in the management of breast cancer is the HER2 receptor. HER2 positive malignancies are frequently treated with therapeutic monoclonal antibodies such as Trastuzumab (Herceptin). Herceptin can be administered as a first line therapy to qualifying patients or in conjunction with traditional chemotherapeutics. Addition of adjuvant trastuzumab to conventional treatment has been associated with improved relapse-free and overall patient survival and has been effective in preventing recurrent metastatic disease[24, 25]. Trastuzumab's success has inspired the development of similar monoclonal antibodies. Pertuzumab, a monoclonal antibody that binds to the HER2 receptor and prevents receptor dimerization, is particularly promising due to its broad clinical applications and low toxicity. Small molecule inhibitors of HER2 such as lapatinib have shown great promise in pre-clinical testing and are currently in phase 1 clinical trials [19].

1.1.6 Breast Cancer Metastasis

While primary and early-stage breast cancers can often be treated with surgery, the management of cancer metastasis is particularly problematic. Breast cancer primarily metastasizes to the bone (44.1%), lung (22.4%), liver and pleura (7.3%) and brain (7.3%), with metastatic populations frequently lying dormant for years before recurring [26]. These

metastatic lesions are often heterogeneous and molecularly distinct from parent tumors, leading to lesions that are resistant to previously administered targeted therapies. For example, a primary lesion that is both ER and PR positive (allowing for hormonal treatment) can give rise to metastatic lesions that are hormone receptor negative, with fewer effective treatment options [27]. While HER2 status is frequently conserved in metastatic populations, approximately 10% of metastatic lesions express different levels of HER2 amplification than parental tumors [28]. These molecular changes often result in triple negative metastatic lesions that are both hormone and chemotherapy resistant, and are associated with limited survival time and poor patient prognosis [27].

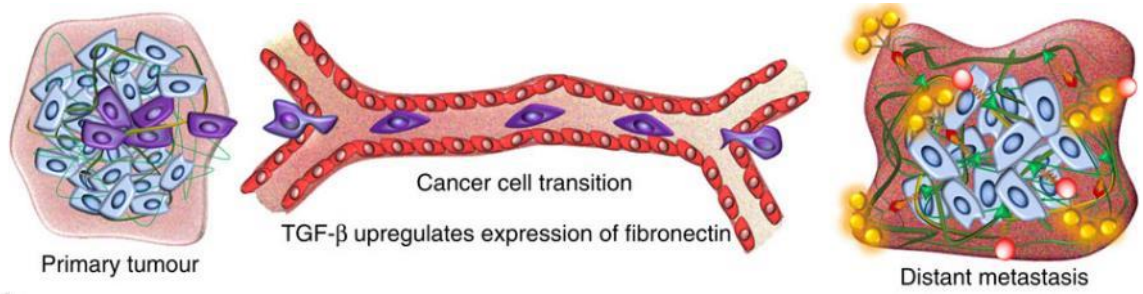

Figure 1.1-Progression of Cancer Metastasis. Cancer cells from the primary tumor site are able to enter the bloodstream through leaky nascent vasculature. Cells migrate to distant organ sites with favorable 'soil'. Once malignant cells ('seed') reach organs with favorable pre-metastatic niche, a metastatic tumor begins to grow. Figure reproduced and adapted with permission from Zhou et. Al. MRI detection of breast cancer micrometastases with a fibronectin-targeting contrast agent. *Nature Communications* 6, 7984 (2015)

Treatment of metastatic disease is further complicated by difficulties in detecting recurrent lesions [5]. As these lesions are often resistant to effective drug therapies, early detection of metastatic populations that are still curable is critical for patient prognosis and survival. Metastatic disease is frequently occult upon recurrence; however, detection in this early stage is associated with a more favorable patient prognosis than detection after the onset of symptoms, once the disease has progressed [29]. Accurate detection and monitoring of metastatic lesions can also help determine drug responsive vs. non-responsive populations to guide therapeutic intervention [30]. Despite its importance, detection of early stage micrometastatic lesions is challenged by limitations of current imaging techniques [26, 31, 32]. This limitation is particularly evident in the case of skeletal metastasis. While bone is the most common site of breast cancer metastasis, current imaging techniques such as MRI are frequently unable to resolve early stage lesions, leading to decreased patient survival time as tumors go undetected until they are too well developed for effective intervention [31]. In light of these challenges and limitations, it is critical to develop new tools capable of the sensitive and specific detection of micrometastatic populations and the molecular determination of tumor responsiveness.

1.2 Cancer Imaging

Biomedical imaging is a key component of cancer diagnosis, care and disease management. Non-invasive imaging techniques are capable of providing a wealth of information on lesion morphology, structure, and metabolism that can be used to guide therapeutic intervention and track response [33]. Many techniques currently used in the oncology clinic are focused primarily on resolving gross anatomical details of the primary tumor, such as location and volume, and do not provide molecular details such as receptor expression on lesions of interest. Anatomical imaging modalities such as magnetic resonance imaging (MRI), X-ray computed tomography

(CT), and ultrasound are capable of deep-tissue imaging and are frequently used in cancer care to provide macroscopic and anatomical data [34, 35]. In spite of their widespread use, these imaging techniques often fall short as a result of their limited sensitivity and inability to provide molecular information on disease states, leading to incomplete tumor evaluation [36]. An emerging challenge for clinicians is to develop clinically relevant approaches that combine anatomical imaging techniques with those that provide information on the molecular makeup of disease on a cellular scale to effectively guide patient-specific treatment [34, 37, 38].

In contrast to anatomical imaging, molecular imaging techniques such as positron emission tomography (PET) provide details on the molecular makeup of a lesion [39]. Molecular imaging allows oncologists to monitor tumor response to interventions and develop personalized treatment plans while providing specific information on the *in situ* behavior of malignancies [37]. However, to date fluorodeoxyglucose (FDG) is the only PET tracer in widespread use with additional tracers in development and testing. With its wide array of possible tracers, molecular imaging can also provide information concerning the propensity for lesions to respond to molecular therapies without a biopsy or surgical intervention, allowing for safer, more effective determination of optimal treatment regimen [40]. Despite their potential advantages, currently available clinical molecular imaging techniques, such as PET, are limited in their ability to detect small, early-stage tumors and certain types of bone metastasis [41].

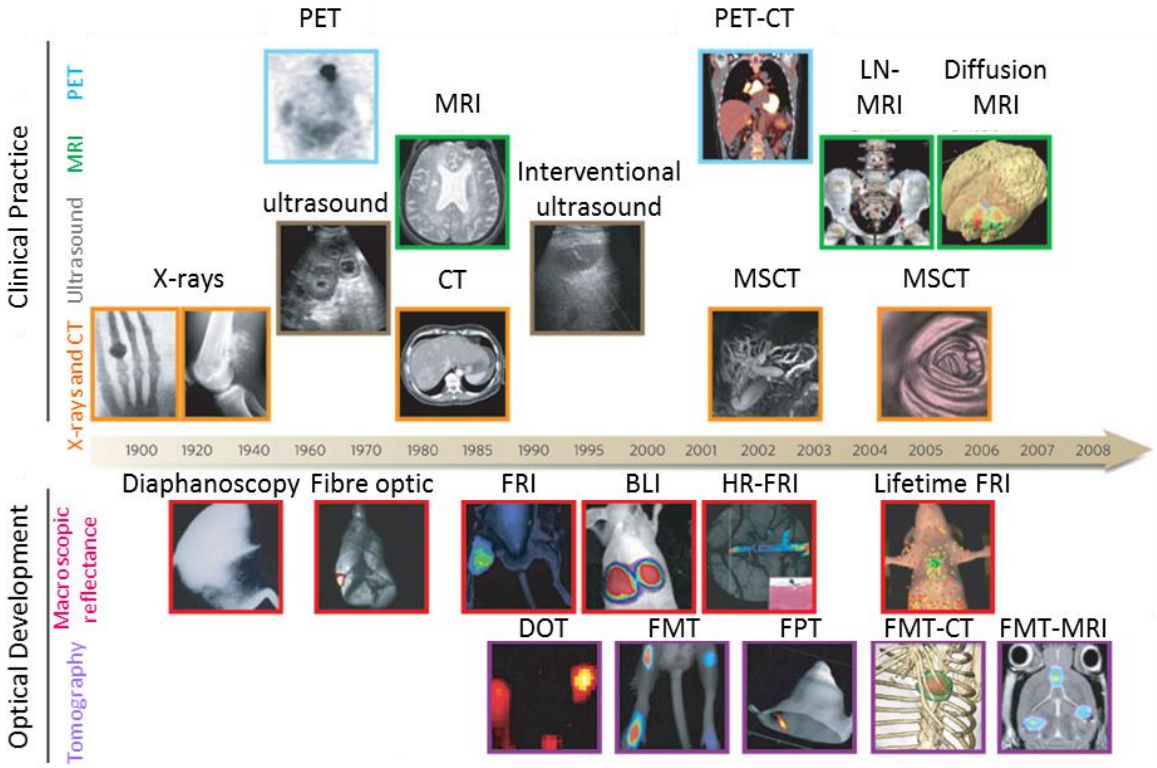

Figure 1.2-Cancer Imaging Modalities. Macroscopic imaging techniques (above the timeline) are used on the oncology clinic to obtain anatomical information on a tumor or lesion. Common anatomical imaging techniques include MRI, X-ray, ultrasound and CT. In contrast, recently developed optical imaging techniques (shown below the timeline) allow resolution of molecular and cellular details. These techniques can be two dimensional or three dimensional and are often used in conjunction with macroscopic imaging to provide a complete picture of a disease state. Figure reproduced and adapted with permission from Weissleder&Pittet, Imaging technologies used in oncology. *Nature* 452(7187), 580-9. (2008)

An ideal imaging system would combine both types of modalities, providing high resolution anatomical information about a lesion while being able to detect cellular changes indicative of disease state. This goal has led to the increasing use of multi-modal techniques that combine molecular and anatomical imaging for comprehensive disease description. Multi-modal and multi-scale imaging has recently proven to be a powerful clinical tool capable of improving disease detection and evaluation compared to single modality approaches [42-44]. However, there are still areas where current clinical tools fall short.

1.3 Optical imaging of disease states

Optical imaging is an extremely useful pre-clinical tool that enjoys several advantages over traditional forms of anatomical and molecular imaging. While its applications in the clinic have previously been limited, it is a growing field with numerous technologies in clinical trials [45]. Optical imaging techniques rely on light (non-ionizing radiation) to interrogate the cellular and molecular details of cancer, and as such are safe for repeated use. This light can be scattered, refracted, or reflected to generate an image of the tissue of interest.

Current optical imaging techniques are sensitive, fast, and typically rely on low-cost and user friendly instrumentation, allowing for rapid clinical adoption [45]. Optical imaging (specifically fluorescence imaging) relies on exogenous contrast agents, and development of new techniques is often driven by contrast agent development [46]. Combining optical imaging with existing modalities has the potential to allow for real-time monitoring of both anatomical and molecular features of disease states, guiding therapy and providing insight into the molecular mechanisms of cancer progression [37].

Optical imaging techniques can be described as either planar or tomographic. Planar imaging techniques are the more common of the two and involve the illumination of the sample with a beam of light with a specific excitation wavelength to excite a contrast agent or fluorochrome of interest. Emitted light from the agent of interest is captured by a highly sensitive, wavelength specific camera and correlated to anatomical features. Planar imaging is fast and simple, and includes fluorescence reflectance imaging (FRI) and bioluminescence imaging (BLI), common staples of pre-clinical research [47]. Planar optical imaging will be a major focus of the investigations reported herein.

Optical tomography relies primarily on light scattering through the media of interest. For biomedical applications, transilluminated light is passed through tissue with varying scattering and absorption properties to generate an image [48]. Tomographic imaging is able to penetrate up to 10 cm into biological mediums, unlike planar imaging which typically has much lower tissue penetration [37]. Tomography can be used in conjunction with appropriate contrast agents, allowing for deep-tissue identification of lesion receptor expression [48].

1.3.1 Contrast agents for biomedical optical imaging

While optical techniques have many benefits for biomedical imaging, several factors have limited their translation into the oncology clinic. The most commonly used optical imaging techniques depend on exogenous contrast agents. The advantage of using exogenous contrast agents (as opposed to native variations in light/tissue interactions) is the ability to engineer their physical and spectral properties for a wide range of applications. Contrast agents are typically classified based on their structure, spectral range, and activity, and can be organic dyes, antibodies, peptides or nanoparticles [49].

One commonly used class of contrast agents is non-specific organic fluorophores. These small molecules are used in pre-clinical and *in vitro* imaging to either detect changes in native tissue or introduce distinct fluorescent properties into a tissue of interest. Organic fluorophores such as fluorecscein and indocyanine green (ICG) are often used to visualize changes in cell morphology or to label specific cellular compartments [50]. These reporters have a number of limitations including poor photostability (leading to photobleaching and thus loss of signal) and a poor signal-to-noise ratio in tissue that restrict their clinical utility [50, 51].

In contrast to non-specific fluorescent dyes, molecular specific contrast agents consist of a reporter-conjugated ligand that targets a specific biomarker of interest. These contrast agents are of particular use in imaging carcinogenesis, metastasis, and angiogenesis. Ligand based molecularly targeted contrast agents can be organic (e.g. antibodies and peptides) or non-organic (e.g. nanoparticles and aptamers). These contrast agents are capable of sensitive and specific reporting on disease states on a single cell level, but frequently suffer from the same limitations as their non-specific counterparts [50]. Molecularly targeted contrast agents are currently limited in their utility and clinical translation. Antibody conjugates can cause an immunogenic response, and small molecules such as peptides and antibody fragments have unfavorable pharmacokinetics and are quickly cleared from circulation due to their small size [52, 53]. Additionally, many optically relevant contrast agents are cytotoxic and are poorly soluble in aqueous mediums, limiting their biomedical applications [53, 54].

1.3.2 Wavelengths for biomedical optical imaging

Traditional exogenous contrast agents and fluorophores are excited in the ultraviolet (UV) or visible ranges of light and emit further in the visible range. These wavelengths, while appropriate for *in vitro* and microscopy techniques, have limited relevance in biological tissues.

UV light is carcinogenic and cytotoxic, damaging surrounding tissue and rendering contrast agents relying on it unsuitable for biomedical applications [55-57]. While safe for biological use, visible light is attenuated rapidly in biological media and has very limited (< 1 cm) depth of penetration [58, 59]. This attenuation results from light being scattered and absorbed by tissue.

Absorption in tissue is caused by photons interacting with biological agents, resulting in dissipation and loss of signal as light propagates. The strongest absorbing molecules present in tissue include water, hemoglobin, and melanin, each with unique absorption spectra dependent on the agent's local concentration [51]. There are numerous examples of absorbent molecules in tissue, ranging from UV absorbers such as nucleotides and aliphatic amino acids, to water, which acts as an infrared absorber around 1100-1300 nm [37]. The prevalence of these absorbing agents greatly limits light penetration through tissue and relegates optical imaging to only the shallowest applications.

Tissue absorption can result in fluorescent light being emitted, termed 'tissue autofluorescence'. This autofluorescence decreases signal-to-noise ratio and further confounds optical imaging in tissue, limiting its utility. Tissue autofluorescence is wavelength dependent, with high levels of 'green' fluorescence seen with UV/blue light exposure and site-specific red fluorescence detectable with green light excitation. Wavelengths of light in the near infrared (NIR, 700-1000 nm) and the short wave infrared (SWIR, 1000-1600 nm) ranges experience little to no tissue autofluorescence [51].

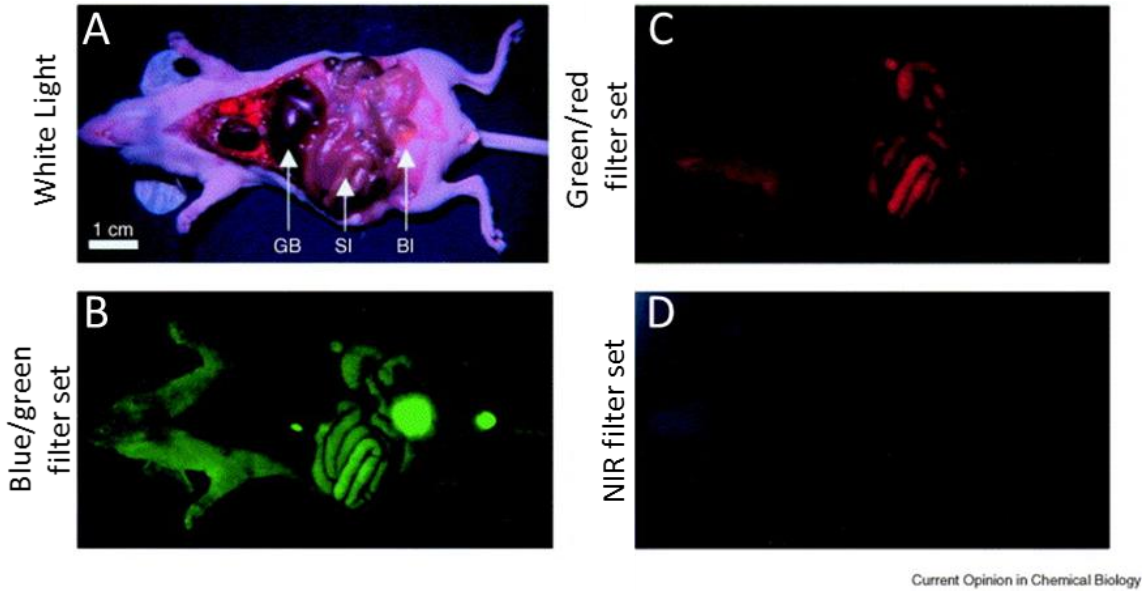

Figure 1.3-Wavelength Dependent Tissue Autofluorescence. An athymic nude mouse (a) with viscera and organs exposed is imaged with (b) a blue/green excitation filter set and (c) a green/red filter set, showing high levels of tissue fluorescence that would decrease signal to noise ratio. In contrast, imaging with a NIR filter set (d) results in less tissue autofluorescence. Figure reproduced with permission from Frangioni, *In vivo* near-infrared fluorescence imaging. *Current Opinion in Chemical Biology* 7(5) 626-634 (2003)

Scattering of light in tissue occurs when photons deviate from their existing path due to interactions with biological elements such as cell membranes and water, leading to de-focusing and loss of signal [51]. In some tissues, light scattering is a greater cause of signal loss through biological media than tissue absorption [60]. Two types of scattering dominate in biological applications: Rayleigh and Mie scattering. Rayleigh scattering dominates when photons interact with particles much smaller than the wavelength of light; in heterogeneous tissue this includes cellular components such as nuclei and mitochondria. Mie scattering refers to scattering

elements that are the same size as the wavelength of light being transmitted [60]. While both Rayleigh and Mie scattering are wavelength dependent, wavelength is much more influential in Rayleigh scattering, with scattering being proportional to λ^{-4}. This results in greater Rayleigh scattering of shorter wavelengths (such as UV and blue light) than longer wavelengths of light (such as red and infrared light). Therefore, longer infrared wavelengths of light experience less attenuation through biological media than traditionally used visible or UV light and are better suited for biological applications [51, 60, 61].

1.3.3 Benefits of SWIR wavelengths for optical imaging

One of the greatest limitations to the clinical translation of optical imaging techniques is the difficulties resolving traditional fluorophores in living tissues [37]. This is partially due to reliance on visible light, which is quickly attenuated through biological media [62]. As opposed to visible light, however, near infrared radiation (NIR, 700-1000 nm) is capable of penetrating deeper into tissue with less scattering, absorption, and autofluorescence from the surrounding biological medium. The NIR region overlapping the region where absorption from tissues is minimized is referred to as the “first optical window” from 650-950 nm and represents an alternative to visible light detection of disease states [63, 64]. Despite the benefits of NIR based imaging, this range is not optimal for clinical applications of optical imaging due to its still limited tissue penetration and high background caused by tissue autofluorescence [63].

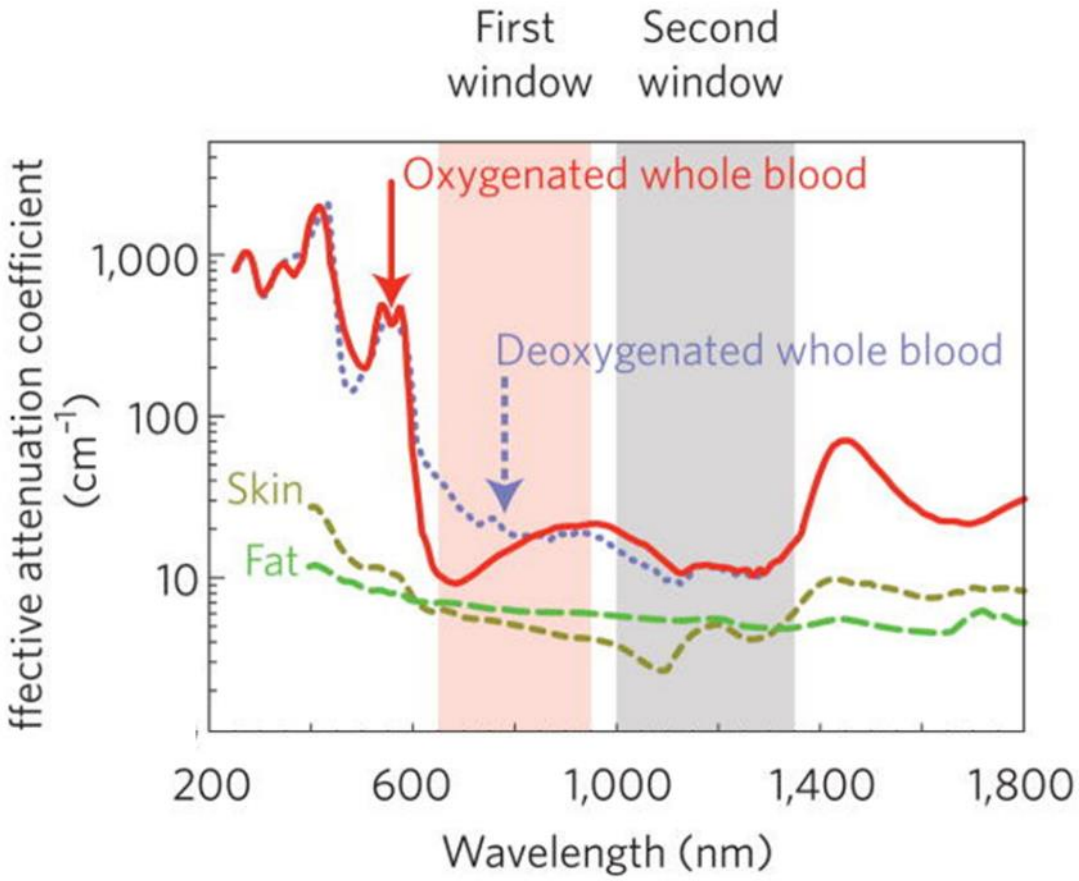

Figure 1.4-Second Window Imaging in Biological Media. Common biological molecules such as hemoglobin, melanin and water limit the transmission of visible light through tissue. These photons are quickly attenuated through scattering and absorption. However, photons in the near infrared range experience less scattering and subsequent attenuation, leading to less signal loss. Figure reproduced and adapted with permission from Smith et. Al. Second Window for *In Vivo* Imaging. *Nature Nanotechnology* 4(11): 710-711 (2009)

Scattering, absorption, and subsequent loss of signal resolution can be further minimized in the SWIR region of light. In this range, photons experience less tissue autofluorescence and absorption from biological molecules [51]. As scattering through tissue is dominated by Rayleigh

diffraction, longer wavelength photons experience improved penetration in biological media as compared to visible or NIR photons [61]. In spite of the obvious benefits of this 'second window' imaging, its adoption has been limited by a lack of sensitive and low-cost cameras capable of SWIR resolution and a paucity of safe, biocompatible probes [63]. The improvement and use of specialized equipment such as SWIR sensitive InGaAs cameras (able to detect λ=900-1700 nm) has enabled inexpensive and high resolution SWIR based *in vivo* imaging [63, 65]. Simultaneously, the development of improved IR emitting contrast agents has made second window optical imaging a reality for many researchers.

1.4 Rare earth nanoparticles as optical imaging contrast agents

Effective SWIR-based imaging requires fluorophores that are bright, stable, tunable and biocompatible. Many inorganic nanoparticles have been shown to have the potential for *in vivo* SWIR imaging such as quantum dots [66], carbon nanotubes [64], and gold nanoparticles [67]. These nanoparticles have numerous advantages over their organic counterparts, such as their stability and stable fluorescence that is not subject to photobleaching. However, they also offer safety and toxicity concerns based on their composition and organ distribution and have suboptimal spectral properties [67]. An alternative is rare-earth doped nanoparticles (REs), ceramic nanoparticles that are doped with lanthanide element ions. These nanoparticles are ideal for *in vivo* imaging as they are excited with NIR light and emit in the SWIR range, allowing for greater penetration of both excitation and emission photons[68]. Additionally, REs exhibit stable upconversion fluorescence by which the low-energy, longer wavelength NIR excitation induces visible emissions that can be detected via conventional confocal microscopy or flow cytometry [69, 70]. This upconversion, while not clinically relevant for *in vivo* detection, provides a benefit for *in vitro* validation and detection. SWIR downconversion from $NaYF_4$ REs is produced

through the transfer of energy from a sensitizer (such as Yb) present in the lattice to an activator (such as Er, Tm, or Ho) resulting in stable emissions whose wavelength range can be tuned by altering the activator [71, 72]. The unique upconversion fluorescence of RE particles occurs when the excitation energies of the sensitizer and activator are nearly equal. Sequential absorption of NIR photons results in energy being transferred from the sensitizer to the activator, exciting the activator before the sensitizer emits photons, yielding a higher energy excitation [71].

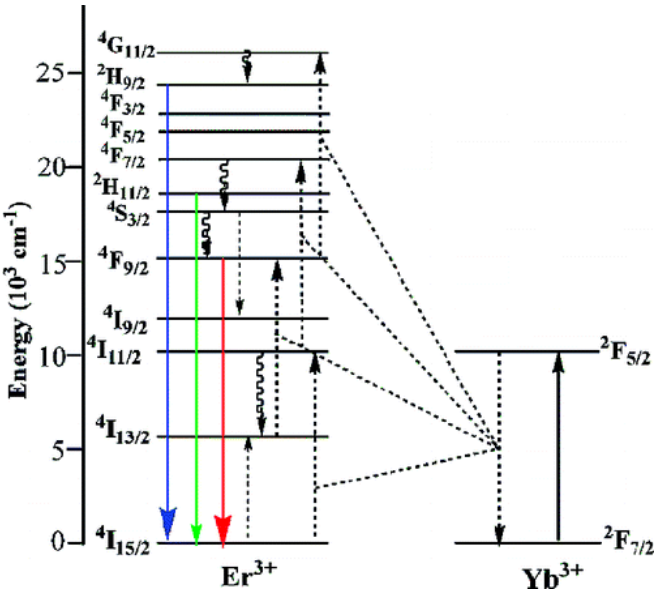

Figure 1.5-Mechanism of RE fluorescence. $NaYF_4$ Yb:Er nanoparticles, when exposed to 980 nm excitation, emit both downconversion and upconversion fluorescence. The 980 photons excite the Yb sensitizer present in the lattice, which transfers energy to the Er dopant in the particle core. Er^{3+} can then relax, resulting in SWIR downconversion fluorescence, or can be excited again by the Yb^{3+} sensitizer resulting in higher energy visible emissions. Figure reproduced with permission from Lin et. Al. Highly Luminescent NIR-to-Visible Upconversion Thin Films and Monoliths Requiring No High-Temperature Treatment. *Chem. Mater.,* 21(14) 3406-3413 (2009)

1.4.1 Synthesis of RE nanoparticles

Rare earth nanoparticles are typically synthesized through solvothermal decomposition. Briefly, lanthanide trifluoroacetate salts dissolved in a solvent such as oleylamine is heated under an inert atmosphere. The reaction proceeds through four crystal growth stages, including burst nucleation caused by Ostwald-ripening, particle growth by monomer supply, particle shrinkage by dissolution, and aggregation. This method has been proven to produce monodisperse nanoparticles, with physical characteristics controlled by tuning reaction parameters [73]. The optical properties of the RE probes used in this work were further enhanced through the use of a core-shell structure. The nanoparticle core consists of a $NaYF_4$ lattice doped with a lanthanide sensitizer and activator, while the shell is a homogenous layer of undoped host material. This core-shell structure serves to enhance upconversion luminescence and limit surface quenching [74]. This work primarily focuses on $NaYF_4$ particles doped with Erbium and Ytterbium to generate bright, stable emissions at both 525 nm and 1530 nm [54].

1.5 Nanoparticles for cancer drug delivery and imaging

1.5.1 Nanoparticle based delivery systems

Many current cancer treatments (e.g. taxanes used to treat breast cancer) are hydrophobic compounds that rely on systemic delivery to reach tumor sites[17]. These non-specific methods involve maximum dose-limiting toxicity and off-target effects that are dangerous and diminish patient quality of life [75]. Likewise, many imaging contrast agents (e.g. quantum dots and carbon nanotubes), while having advantageous and attractive optical properties, are cytotoxic, hydrophobic, and poorly bioavailable [54]. Nanoparticle encapsulation is commonly used to improve the solubility, biodistribution and biocompatability of therapeutic and imaging agents

alike, and particles are frequently used as carriers for improved delivery of agents to solid tumor cancers. Nanoparticle formulations of medicinal drugs benefit from improved efficacy, lower toxic dose, and diminished off-target side effects when compared to traditional drug administration [76]. An attractive characteristic of nanoparticle-based delivery systems is their ability to carry multiple payloads. Particles can be engineered to carry simultaneous therapeutic and imaging agents, allowing for the theranostic detection and treatment of a disease state [77, 78]. In addition to therapeutic and imaging payloads, particles can be molecularly targeted to specific cells, limiting off-target effects and increasing concentration at the site of interest [79]. Nanoparticles can be customized for specific purposes with highly tunable physical properties of varying size, surface charge, and host materials. Careful consideration of design characteristics is critical for improved delivery [78].

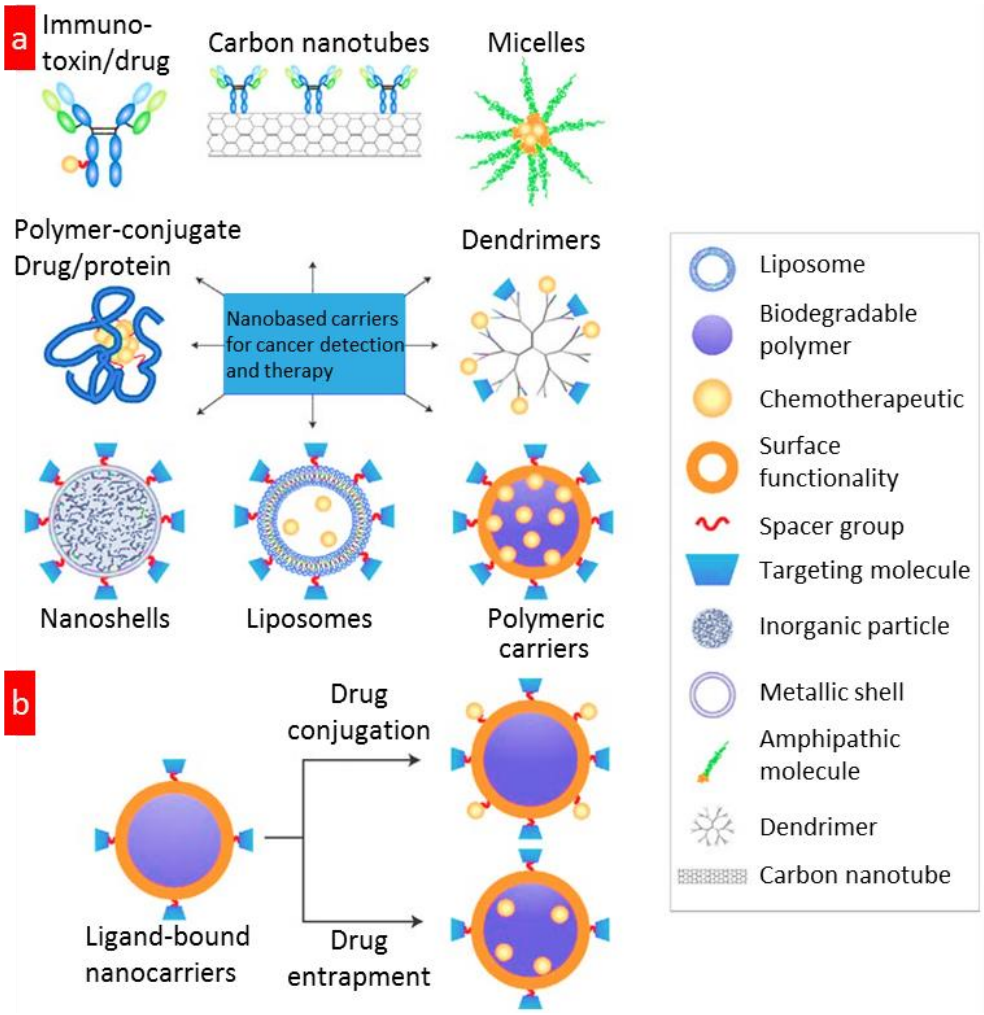

Figure 1.6-Multifunctional Nanoparticles for Drug and Contrast Agent Delivery. Nanoparticle based delivery systems (a) have tunable physical characteristics and can be synthesized from numerous host materials for application specific payload delivery. Particles can carry multiple payloads conjugated to the outer surface or encapsulated in the particle core (b). Figure reproduced with permission from Peer et. Al. Nanocarriers as an Emerging Platform for Cancer Therapy *Nature Nanotechnology* 2, 751-760 (2007)

1.5.2 Nanoparticle design considerations

Effective anti-cancer nanoparticle-based delivery systems must represent an improvement over conventional systemic administration of drugs or contrast agents. Nanoparticle circulation time and tumor accumulation can be influenced by tunable physical characteristics such as particle diameter. Particle size determines *in vivo* fate and method of clearance, toxicity, and targeting ability. Size (and surface area) can also influence factors such as drug loading and release [80]. Smaller nanoparticles (<1,000 nm in diameter), when compared to larger nanoparticles or microparticles (>1,000 nm in diameter) have a high rate of cell uptake and are able to better penetrate submucosal layers in rat models [81, 82]. While larger particles have the potential to inhibit blood flow and embolize in small blood vessels, nanoparticles can remain in circulation with few harmful effects. In addition to cell association and behavior in blood vessels, nanoparticle size often dictates organ accumulation and mechanism of clearance. Particles with a hydrodynamic diameter < 5 nm are quickly cleared through diffusion into the lymphatic system resulting in decreased circulation time, while particles 5-10 nm in diameter are subject to rapid renal clearance [83]. Slightly larger particles benefit from prolonged circulation and slower clearance: particles on the order of 100 nm can passively accumulate in tumors through the enhanced permeation and retention (EPR) effect, by which large molecules leak from blood to accumulate in the tumor interstitial space [84, 85]. The general consensus in literature is that nanoparticles 10-100 nm in diameter are most effective for *in vivo* detection and treatment of solid tumor cancers as they enjoy long circulation time, improved biodistribution, and passive accumulation in the tumor interstitium [86].

A challenge in nanoparticle-based drug delivery is penetration across cell and tissue barriers. Delivery to solid tumor cancers is further inhibited by the dense extracellular matrix generated

by malignant lesions, limiting penetration into the tumor core. Cancer therapies are most effective when the medication is able to permeate the tumor mass, increasing cellular exposure and affecting as many malignant cells as possible. Therefore this poor tumor penetration limits therapeutic efficacy [87]. This barrier to effective treatment can be remedied by modifying a nanoparticle's shell for improved tumor penetration. Recent studies have shown that decorating particles with proteases designed to degrade the extracellular matrix and break through to the interior of a tumor leads to improved therapeutic efficacy as more cells are exposed to drugs[87, 88]. Size represents another critical barrier to tumor penetration. Nanoparticles ~100 nm in diameter are able to localize to a tumor due to the EPR effect, but are often too large to effectively diffuse into the tumor interstitium. Recent studies involving nanoparticles that "shrink" by breaking up into smaller drug loaded components in the tumor interstitium have improved tumor penetration and therapeutic efficacy[89]. These recent studies highlight the fact that reaching a tumor is not necessarily sufficient for therapeutic benefit-the nanoparticles must be able to sufficiently perfuse the mass.

Nanoparticle surface properties likewise influence biodistribution. In circulation, proteins called opsonins bind to the surface of non-stealth and hydrophobic molecules [80]. Opsonization results in blood proteins binding to particle's surface, inducing aggregation, causes circulating macrophages to quickly identify and remove these hydrophobic components before they are able to reach their region of interest. Accumulated proteins also alter the biodistribution of any nanoparticles that escape macrophage recognition. This rapid clearance of molecules (including many therapeutic agents) leads to poor biodistribution, limited efficacy, and off-target effects, representing a critical barrier to effective payload delivery [90]. Particle surface characteristics and hydrophobicity is a key determinant of nanoparticle fate. To improve distribution and limit rapid clearance and off-target effects, many nanoparticles are engineered with hydrophilic

components or coatings to prevent protein binding and prolong circulation time. Particles can be given “stealth” coatings such as hydrophilic poly (ethylene glycol) (PEG), or can be synthesized from hydrophilic polymers [80]. Surface charge, as measured by zeta potential, is another key tunable characteristic of nanoparticle based delivery systems. Zeta potential reflects the electrical potential of a nanoparticle’s surface and can be tuned by controlling particle composition and medium. Nanoparticles with positive zeta potential experience protein adsorption that limits their circulation time and cellular uptake, while samples with negative zeta potential are typically serum stable and can be internalized by cells [91]. Successful nanoparticle based delivery systems tend to have hydrophilic surfaces or coatings and neutral or negative zeta potential to prolong circulation and limit clearance.

To further improve nanoparticle biodistribution and accumulation at sites of interest, delivery systems can be targeted to a specific region. Targeting can be ‘active’, in which a nanocarrier is conjugated to a tissue-specific ligand, or ‘passive’, where other nanoparticle characteristics are altered to encourage accumulation in the tumor interstitium or associated vasculature [76, 92]. While passive targeting is beneficial for nanoparticle localization, it is not sufficient for improved cellular association and uptake and is therefore often used in conjunction with active targeting techniques [92]. Active targeting is accomplished through the use ligands such as antibodies or antibody fragments, aptamers, peptides, or small molecules. Active targeting exploits the highly specific interaction between a ligand and its cognate receptor to promote nanoparticle association with receptor positive tissues. Binding affinity can depend on ligand specificity or multivalent effects [93]. There are many recent examples of actively targeted nanoparticles in literature. Recent studies have shown that aptamer conjugated polymeric nanoparticles showed improved anti-cancer activity compared to non-target controls both *in vitro* and *in vivo* [94]. Small molecules have also been used as inexpensive, multivalent targeting ligands. A study in

2010 by Tassa et. al. demonstrated that even weak, small-molecule targeting ligands increase particle-ligand affinity by up to 4 orders of magnitude through multivalent interactions [95]. Ligands can be covalently bound to a particle surface, passively adsorbed though electrostatic conjugation, or incorporated into the particle structure depending on the host material.

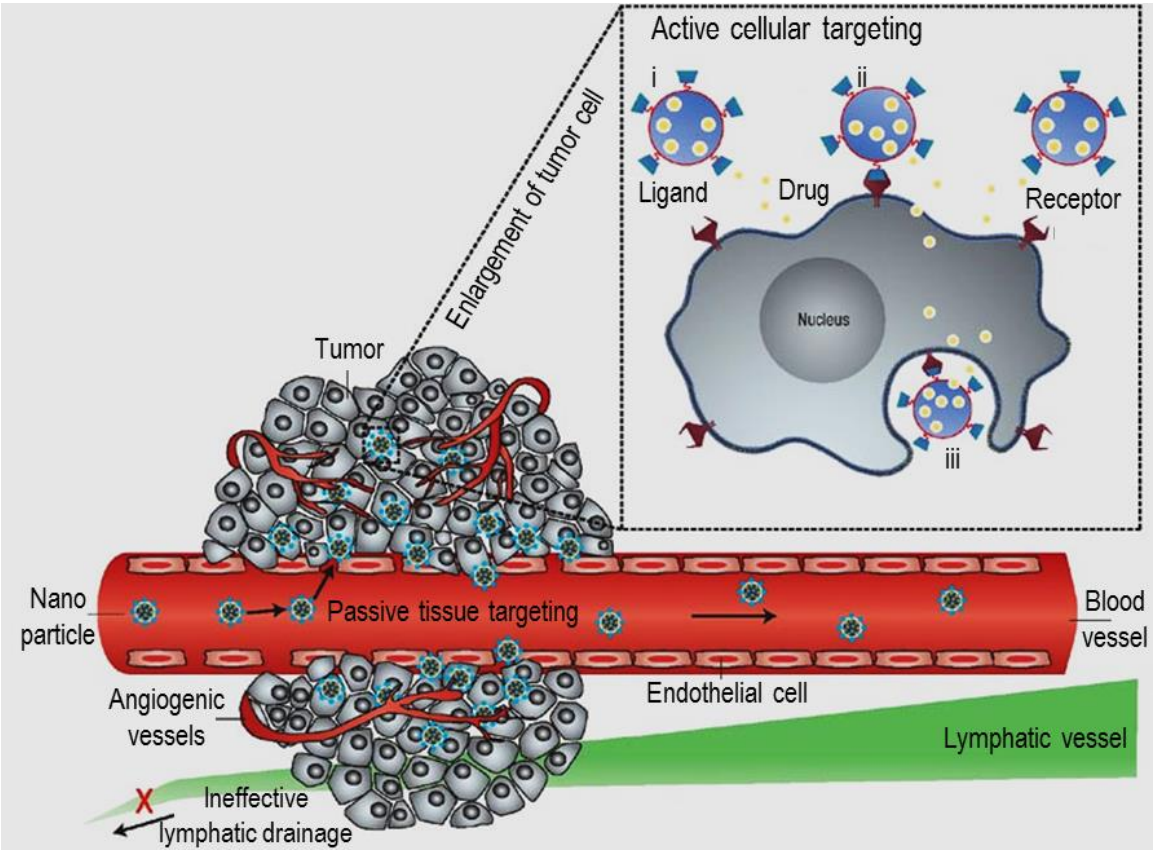

Figure 1.7-Nanoparticle Accumulation at Tumor Sites. Nanoparticles preferentially accumulate in tumor interstitium through the EPR effect due to leaky tumor vasculature and poor lymphatic drainage. Improved cellular association can be achieved through active targeting (inset), through decoration of the particle surface with cell-specific ligands. Figure reproduced with permission from Peer et. Al. Nanocarriers as an Emerging Platform for Cancer Therapy *Nature Nanotechnology* 2, 751-760 (2007)

1.5.3 Nanoparticle materials

Several nanotechnologies have been used for nanoparticle based drug delivery and imaging systems. These nanocarriers must be biocompatible, nontoxic, and non-immunogenic to allow for repeated administration. The first materials to be used as a nanoparticle based drug delivery system were liposomes. Liposomes are spherical vesicles generated through the spontaneous assembly of phospholipids, surfactants, and steroids dispersed in an aqueous solution. Liposomes have tunable size (typically 80-300 nm in diameter) and membrane properties depending on their lipid composition and synthesis method. Payloads are typically encapsulated by the nanovesicle during synthesis and carried in the aqueous core [96]. Drug release is dependent on liposomal composition and environment. Another attractive feature of liposomes is their interaction with cells. Liposomes are capable of fusing with a cell's lipid bilayer, releasing the payload into the cytoplasm or facilitating endosomal escape [86, 97]. Liposomal formulations have been used for many payloads including anticancer drugs, anti-inflammatory drugs, and NMR contrast agents [86, 98, 99]. Studies have shown that liposomal encapsulation increases the circulation of therapeutics and decreases off-target side effects such as nephrotoxicity [98]. PEGylated liposomal doxorubicin (Doxil) is an FDA-approved chemotherapy drug used to treat ovarian cancer with greatly improved pharmacokinetic properties and more favorable biodistribution. As compared to free doxorubicin administered in solution, treatment with Doxil leads to a greater accumulation of drug in the tissue interstitium, resulting in greater drug efficacy with a higher toxic dose and fewer off-target effects [100]. Despite their many attractive properties, liposomes accumulate in cells in the spleen and liver (liver macrophages) leading to cell death and organ specific toxicity [100, 101].

Polymeric nanoparticles are another growing drug delivery system due to their tunable composition and the potential for multifunctional “intelligent” stimulus responsive, controlled release drug delivery[102]. Composed of synthetic polymers (such as polylactic acid (PLA) and polyglycolic acid (PGA)) or naturally occurring polymers such as polysaccharides and proteins, polymeric nanoparticles are further characterized as linear or dendritic (branching) and by their *in vivo* fate as either biodegradable or non-biodegradable [86, 103]. Payloads can be immobilized on particle surface after formation or encapsulated in the nanoparticle’s core during synthesis. Release can occur through desorption, diffusion, or nanoparticle degradation, and is highly controllable by varying particle characteristics [86]. The composition of polymeric nanoparticles can be engineered for ‘controlled drug release’, where a payload is released from the nanoparticle in a predetermined manner or when exposed to specific physiological conditions [104]. Of the many polymers that have been investigated for drug delivery systems, some of the most promising include HPMA (*N*-(2-hydroxypropyl)methacrylamide), PLGA, and PEG (polyethylene glycol), as they are safe for biological use and degrade into nontoxic components [93]. Polymeric encapsulation of anticancer drugs such as docetaxel and doxorubicin has been shown to limit toxic side effects with no change in drug therapeutic efficacy [104, 105].

Metal based nanoparticle systems have also been investigated as drug delivery systems due to their tunable and theranostic characteristics. While metals such as nickel, silver, iron oxide, and titanium dioxide have been used for therapeutic delivery, gold is of particular interest [106]. Gold nanoshells are a multifunctional drug delivery system capable of carrying high doses of therapeutic and imaging agents, and can be functionalized with targeting ligands or PEG for improved pharmacokinetics and distribution *in vivo*. Gold nanoparticles are particularly attractive for their novel physical and optical resonance properties. Gold nanoshells treated with

NIR light generate heat, which can be used for thermal ablation. Once the particles have reached the site of interest or tumor, NIR exposure causes localized hyperthermia leading to cell disruption and necrosis with little damage to surrounding healthy tissue [107]. Heat generation and particle localization can be influenced by particle shape; for example, gold nanorods capable of eradicating ablated xenograft tumors *in vivo* were reported recently [108]. Gold nanoparticles can serve as contrast agents and can be detected and tracked spectroscopically through surface-enhanced Raman scattering, making the carriers themselves theranostic without the addition of a therapeutic payload. Though metallic nanoparticles have many benefits as a drug delivery system the probes can be retained in the body after administration and cause toxicity, raising concerns about their clinical application [109].

1.6 Albumin as a nanoparticle agent

1.6.1 Benefits of albumin nanocarriers

Albumin, the most abundant plasma protein in humans, is extremely robust with a molecular weight of 66.5 kDa and is stable at a wide range of pH and temperatures. One of its key biological functions is to bind to numerous agents in circulation; albumin binds to and transports or sequesters many drugs such as penicillin, sulfonamides, and benzodiazepines, as well as metallic compounds like copper, nickel, and zinc [110]. Albumin's primary structure includes functional groups for facile attachment of therapeutic molecules, and the abundance of charged amino acids allows for the electrostatic adsorption of both positively and negatively charged moieties [111]. Albumin also binds compounds with two native drug binding pockets termed Sudlow's sites I and II, which bind to aromatic molecules, fatty acids, and heterocyclic anions with high affinity [112]. In addition to its drug binding capabilities albumin has been shown to

passively accumulate in solid tumors via a combination of leaky vasculature and the lack of adequate lymphatic drainage in tumor interstitium [110]. Albumin's accumulation at tumor sites is enhanced by the presence of soluble proteins such as SPARC (secreted protein acidic and rich in cysteine) produced by many solid tumor cancers. SPARC, which has been correlated with highly invasive and metastatic malignancies, preferentially binds to albumin and sequesters it at the lesion site [113]. Albumin's drug binding capabilities, biodegradation, and passive accumulation at tumor sites make it an ideal material for nanoparticle drug delivery.

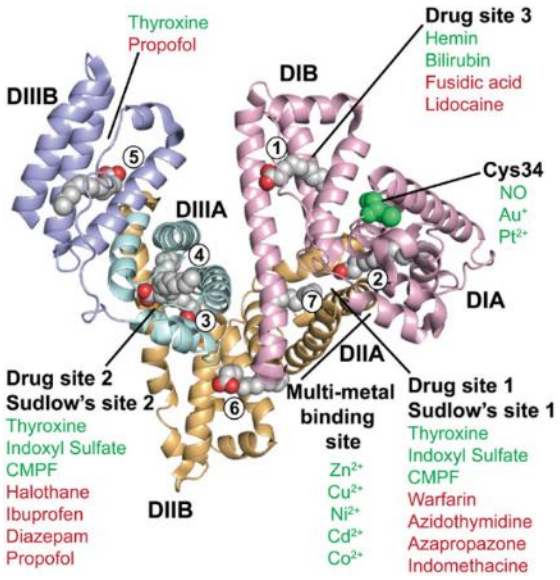

Figure 1.8-Crystal Structure of Human Serum Albumin. Albumin, the body's native drug binding molecule, has multiple binding sites. Two generic drug binding pockets (called Sudlow's site 1 and 2) preferentially bind to large aromatic molecules and heterocyclic anions with high affinity. Figure reproduced with permission from Sand et. al. Unraveling the Interaction Between FcRn and Albumin: Opportunities for Design of Albumin-Based Therapeutics. *Frontiers in Immunology* 26 (2015)

1.6.2 FDA approved drug delivery platform-Abraxane

Albumin nanoparticles have an important precedent in the treatment of breast cancer. A human serum albumin nanoparticle formulation of paclitaxel (Abraxane, Abracix BioScience) was FDA approved for treatment of metastatic breast cancer in 2008. Abraxane is particularly efficacious against cancers that have developed resistance to or are unresponsive to other types of chemotherapy [114]. Nanoparticle albumin-bound paclitaxel (*nab*-paclitaxel), the first commercial protein-based nanoparticle formulation, is synthesized via high-pressure homogenization and results in non-covalently bound nanoparticles approximately 130 nm in diameter [115]. *Nab*-paclitaxel has been shown to be associated with longer overall survival and time to recurrence with fewer toxic side effects than free paclitaxel [17]. This pre-existing platform supports the position that albumin nanoparticles have great potential as delivery agents to breast cancers.

1.6.3 Albumin nanoparticle synthesis

While Abraxane is synthesized through high-pressure homogenization, there are other facile methods for synthesizing albumin nanoparticles including controlled coacervation, thermal denaturation and emulsification [75, 110, 116]. While each of these synthesis methods has benefits, the direction proposed in this thesis focuses on controlled coacervation. Controlled coacervation is simple and reproducible, yielding uniform nanoparticles with tunable sizes. Briefly, albumin is dissolved in a sodium chloride solution and the pH titrated to 8.5. Desolvation is initiated via the dropwise addition of a solvent such as ethanol into the albumin solution under constant stirring at room temperature. The ethanol preferentially binds to water molecules in the aqueous solution through hydrogen bonding. The decrease in protein

hydration drives previously occluded hydrophobic groups in the albumin monomers to become exposed, resulting in aggregation. As the solvent is added the solution's dielectric constant decreases, resulting in enhanced electrostatic interactions among the charged amino acids present in the partially denatured albumin monomers, which may further promote aggregation [117, 118]. The protein aggregates are then stabilized via chemical crosslinking with glutaraldehyde, resulting in stable nanoparticles that can be re-suspended in aqueous mediums without the risk of dissolution. Crosslinked particles can then be washed and purified through centrifugation [119]. Nanoparticle physical characteristics can be controlled by varying parameters during synthesis. Salt concentration of the aqueous phase, the nature and concentration of the coacervating solvent, and the local pH all influence particle diameter, polydispersity, and surface properties [116]. Hydrophobic agents dissolved in the coacervating solvent can be encapsulated in albumin nanocarriers. Previous work has demonstrated that rare earth ceramic particles can be successfully encapsulated in albumin shells during particle synthesis, yielding SWIR-emitting optical imaging probes with improved biological characteristics and little corresponding loss of signal [69].

1.7 Dissertation Overview

The goal of this project is to combine the spectral properties of RE probes with a biocompatible albumin shell to generate a multifunctional nanocomposite optical imaging probe capable of imaging, profiling, and treating malignant tumors. Specifically, this work endeavors to exploit the physical and chemical properties of these nanocomposites to overcome barriers to solid tumor drug delivery, enable optical detection of internal cancerous lesions, and target and molecularly profile micrometastatic tumors. We hypothesize that ReANCs be conjugated to a variety of moieties (both therapeutic payloads and targeting ligands) and can be detected *in vivo*

through non-invasive SWIR optical imaging, allowing for tumor surveillance. We further hypothesize that ReANC probes can be engineered for improved biocompatibility and *in vivo* pharmacokinetics. Finally, we hypothesize that ReANCs imbued with distinct surface modification features can track disease progression and inform on lesion phenotype, providing information that may be ultimately relevant to develop pharmacogenomics strategies for heterogeneous lesion profiles.

This composition of this dissertation is as follows. Chapter 2 details the engineering of albumin nanoprobes for improved delivery of multiple therapeutic payloads to solid tumors. The key message of this chapter is the versatility of albumin nanoshells that can be functionalized with multiple moieties and no loss of efficacy. Chapter 3 focuses on the development of ReANCs as the basis of a SWIR based *in vivo* optical imaging system. Critical outcomes include the ability to influence the pharmacokinetic profile of ReANCs via their size and demonstration of their potential as tumor detection agents in a transgenic murine model of melanoma. Chapter 4 elaborates on the design of cancer-targeted ReANCs for improved specificity and biodistribution, enabling more sensitive detection of deep tissue lesions in a xenograft murine model of metastatic cancer. Chapter 4 also details the targeted probe's ability to provide molecular information on a tumor's phenotype in a non-invasive 'optical biopsy.' Chapter 5 expands on the potential of cancer-targeted nanoprobes to resolve distant site micrometastatic tumors prior to their detection with conventional imaging modalities.

The overall thesis aims are as follows: Aim 1: To engineer multifunctional albumin nanoprobes for improved therapeutic delivery to solid tumors. Aim 2: To evaluate the potential of ReANCs for non-invasive SWIR-based tumor detection in a transgenic murine model of metastatic melanoma. Aim 3: To generate molecularly targeted RE-nanoprobes for sensitive and specific identification of deep tissue lesions in a murine xenograft model of metastatic breast cancer.

Aim 4: To investigate ability of cancer-targeted RE-nanoprobes to identify micro-metastatic lesions prior to their detection with clinically relevant imaging modalities in an *in vivo* mouse model of breast cancer.

CHAPTER 2

MULTIFUNCTIONAL ALBUMIN NANOPARTICLES AS COMBINATION DRUG CARRIERS FOR INTRA-TUMORAL CHEMOTHERAPY

Note: This chapter has been reproduced in its entirety with permission from the following publication:

Cui, M., Naczynski, D.J., Zevon, M.A., Griffith, .K., Sheihet, L., Poventud-Fuentes, I., Chen, S., Roth, C.M., Moghe, P.V. Multifunctional Albumin Nanoparticles As Combination Drug Carriers for Intra-Tumoral Chemotherapy. Advanced Healthcare Materials, 2013. 2(9), p. 1236-1245.[88]

Co-first author

2.1 Abstract

Current cancer therapies are challenged by weakly soluble drugs and by drug combinations that exhibit non-uniform biodistribution and poor bioavailability. In this study we have presented a new platform of advanced healthcare materials based on albumin nanoparticles (ANPs) engineered as tumor penetrating, delivery vehicles of combinatorially applied factors to solid tumors. These materials were designed to overcome three sequential key barriers: tissue level transport across solid tumor matrix; uptake kinetics into individual cancer cells; therapeutic resistance to single chemotherapeutic drugs. The ANPs were designed to penetrate deeper into solid tumor matrices using collagenase decoration and evaluated using a three-dimensional multicellular melanoma tumor spheroid model. Collagenase modified ANPs exhibited 1-2 orders of magnitude greater tumor penetration than unmodified ANPs into the spheroid mass after 96 hours, and showed preferential uptake into individual cancer cells for smaller sized ANPs (<100 nm). For enhanced efficacy, collagenase coated ANPs were modified with two therapeutic agents, curcumin and riluzole, with complementary mechanisms of action for combined cell cycle arrest and apoptosis in melanoma. The collagenase coated, drug loaded nanoparticles induced significantly more cell death within 3-D tumor models than the unmodified, dual drug loaded ANP particles and the kinetics of cytotoxicity was further influenced by the ANP size. Thus, multifunctional nanoparticles can be imbued with complementary size and protease activity features that allow them to penetrate solid tumors and deliver combinatorial therapeutic payload with enhanced cancer cytotoxicity but minimal collateral damage of healthy primary cells.

2.2 Introduction

Dense tumor extracellular matrices (ECM) remain a significant barrier limiting diffusive transport and penetration of drug delivery agents.[120, 121] Limited penetration can lead to heterogeneous drug distribution and concentration gradients within a tumor, further complicating a treatment regimen by promoting drug resistance in cancer cells exposed to low concentrations of therapeutics.[122, 123] In addition, prolonged treatment of tumors with single therapeutic agents has been universally shown to contribute toward drug resistance.[124]

Despite advances in drug discovery, many chemotherapeutic compounds fail to elicit response in solid tumors due to poor solubility,[125, 126] limited tumor penetration,[122, 127] and susceptibility toward drug resistance.[128-131] Drug delivery vehicles have attempted to overcome some these challenges by increasing drug solubility,[132, 133] controlling drug pharmacokinetics and tissue distribution,[134, 135] or prolonging drug stability.[136, 137] Solvent-based delivery approaches are able to improve drug solubility but pose significant risk of toxicity and result in uncontrollable systemic distribution limiting the overall effectiveness of potent drugs.[138-142] The development of nanoscale drug delivery materials, such as nanoparticles, liposomes and micelles, has resulted in greater control over the release and stability of therapeutic cargo, and has led to safer and more effective treatment strategies.[143, 144] However, solid tumor penetration and therapeutic resistance remain significant challenges for chemotherapeutics delivered by nanoscale materials.[122, 145, 146]

Advanced nanomaterials have the multifunctional potential to overcome the varied barriers that hinder drug delivery into solid tumors. [147] Previous work has shown that modifying the permeability of the tumor ECM can facilitate deeper nanoparticle penetration, while combinatorial drug delivery approaches that utilize multiple therapeutic compounds can further reduce the likelihood of drug resistance. Pre-treatment of tumors with protease

enzymes that degrade ECM components, for example, can improve the degree of nanoparticle penetration and distribution within the tumor environment.[148] Combinatorial therapies that capitalize on the synergistic effects of two or more agents acting on separate tumor-promoting pathways have been described using several drug delivery materials.[149, 150] However, drug delivery materials that combine these two capabilities into a single, multifunctional platform have yet to be advanced.

Here, we report on the design of albumin-based nanoparticles that can readily integrate both active tumor penetration and multi-drug delivery within a single structure while enabling size-based tunability of cellular uptake. We hypothesized that the modification of albumin nanoparticles (ANPs) with ECM degrading proteases would increase the degree of nanoparticle penetration into a solid tumor model, which could be further tuned by controlling nanoparticle size (**Figure 1**). As carriers of a novel therapeutic cocktail of two complementary drugs, riluzole (an inhibitory regulator of glutamate receptors) and curcumin (an herbal derivative with chemotherapeutic and anti-inflammatory effects based on the surpression of the nuclear factor-κβ Activation Pathway), the protease modified ANPs markedly enhanced drug functionality in terms of specific cancer cell killing within solid melanoma tumor models *in vitro*.

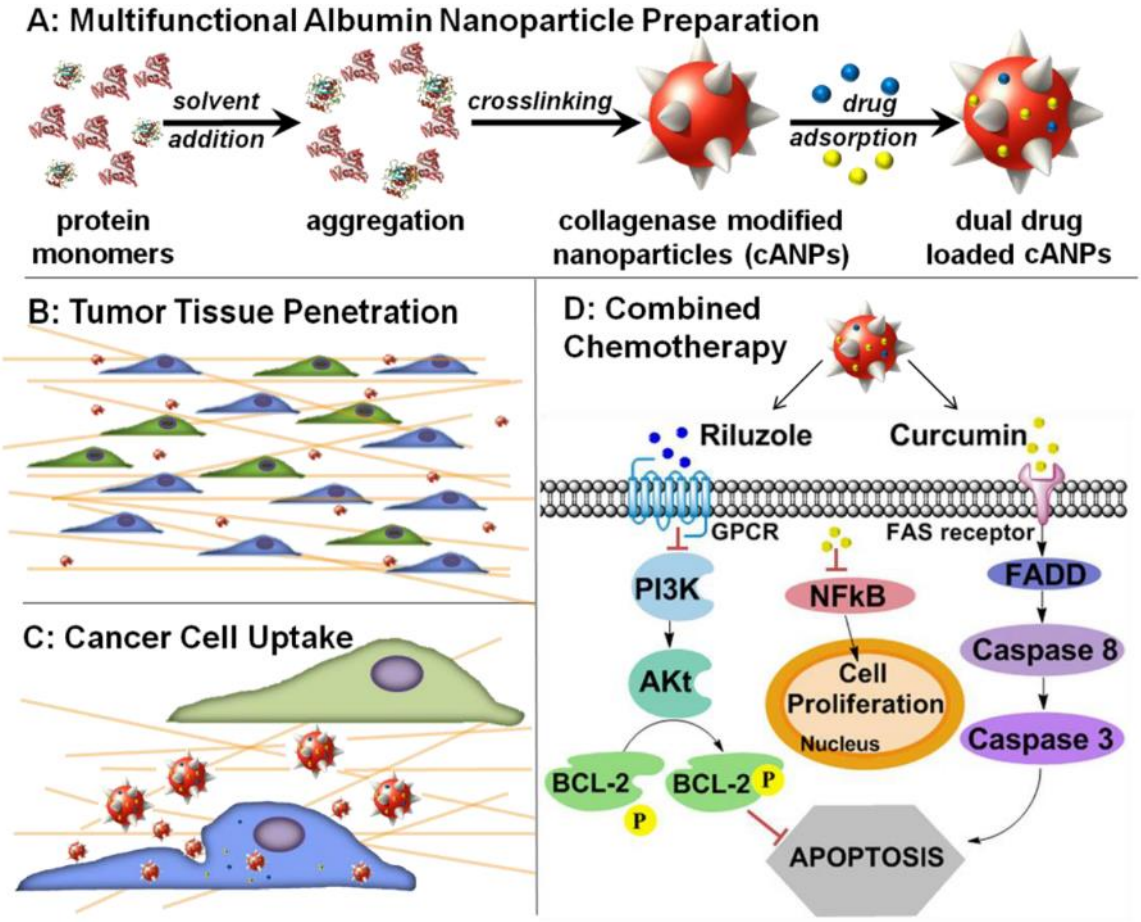

Figure 2.1. Schematic summarizing the overall design of albumin nanoparticles as advanced healthcare materials for enhanced chemotherapy. ANPs synthesized by controlled coacervation can be engineered to overcome barriers to treatment on several scales. (A) The synthesis process can be easily altered to cause the ANPs to display a protease coating on their surface. Drugs can be adsorbed onto the surface after fabrication with no change in therapeutic efficacy. (B) On a multi-cellular tumor level, collagenase coating of ANPs allows for rapid penetration through the dense extracellular matrix to allow for more effective therapeutic treatment. (C) cANPs are taken up by cancerous cells in the tumor mass, allowing for intracellular drug release. Smaller ANPs are taken up preferentially over the larger nanoparticles. (D) Intracellularly the

drugs curcumin and riluzole act on separate pathways that promote apoptosis and inhibit cellular proliferation.

2.3 Methods

2.3.1. Reagents

Molecular biology grade ethanol (99.5%), HPLC grade methanol (99.8%), HPLC grade water with 0.1% trifluoroacetic acid (TFA) and HPLC grade acetonitrile (ACN) with 0.1% TFA were purchased from Sigma-Aldrich and used without further purification. Collagenase from *Clostridium histolyticum* was also purchased from Sigma-Aldrich (St. Louis, MO, USA). Curcumin was purchased from Cayman Chemical Company (Ann Arbor, MI, USA). Riluzole hydrochloride was purchased from Tocris Bioscience (Ellisville, MO, USA).

2.3.2. Cell Culture

WM239A human melanoma cells were provided by Dr. Meenhard Herlyn (Wistar Institute, Philadelphia, PA). C8161(+) and C8161(-) human melanoma cells were from Dr. Mary J.C. Hendrix (Children's Memorial Research Center, Chicago, IL). AR7119 immortalized human melanocytes were provided by Dr. Dorothy Bennett (St. George's, University of London, UK).[151] RPMI-1640 media was purchased from American Type Culture Collection (ATCC, Manassas, VA). Fetal bovine serum (FBS), trypsin–EDTA, streptomycin, and penicillin were purchased from Invitrogen (Carlsbad, CA, USA). Cells were routinely maintained in RPMI-1640 media, supplemented with 10% FBS, penicillin (100 μg ml^{-1}) and streptomycin (100 μg ml^{-1}) at 37 °C, in humidified atmosphere of 5% CO_2.

2.3.3. Albumin Nanoparticle Fabrication

Albumin nanoparticles were fabricated as described previously (**Figure 1A**).[69] Albumin derived from human serum (HSA, fraction V, purity 96–99%, 65 kDa) and glutaraldehyde (8% solution) were obtained from Sigma–Aldrich and used without further purification. 2% (w/v) solution of HSA was dissolved in 10 mM NaCl to prepare 200 nm ANPs, and 2 mM NaCl to prepare 100 nm ANPs. The pH of HSA solution was adjusted to 8.50 ± 0.05 with 0.1 M NaOH. Under continuous stirring at 700 rpm at room temperature, 2 mL ethanol was added at 1.5 mL min^{-1} to the HSA solution (500 µL) with a syringe pump (Harvard Apparatus PHD 2000, Holliston, MA). 2.34 µL glutaraldehyde was added to ANPs suspension as a cross-linker following ethanol addition. The particles were left for crosslinking overnight under stirring at 700 rpm at room temperature.

2.3.4. Albumin Nanoparticle Purification

ANPs were purified by three rounds of centrifugation for 8 min at 4 °C (Beckman Coulter, Avanti J-E Centrifuge). 16 100× *g* was set for 200 nm ANPs, while 48 400x g was set for 100 nm ANPs. Resuspension of the pellets to original volume with PBS was done following each round of centrifugation. Resuspension was performed in an ultrasonication bath (Fisher Scientific, FS60).

2.3.5. Physical Characterization of Albumin Nanoparticles

ANPs were characterized using DLS and SEM. Particle size distributions and polydispersity indices were determined using a zetasizer (Zen 3690, Malvern, Worcestershire, UK). Samples were diluted 40 times with deionized water for *z*-average size and polydispersity measurements of three sequential sample scans (3 runs $scan^{-1}$, 60 s $scan^{-1}$) at a 90° scattering angle and 37°C. Three separate batches of particles were measured and averaged. ANP

autofluorescence was measured using a spectrofluorometer (SpexFluoroMax-3, Horiba Jobin Yvon, Edison, NJ, USA).

2.3.6. Preparation of Collagenase-Coated Nanoparticles

2% (w/v) solution of HSA and 0.1% w/v collagenase were dissolved in 10 mM NaCl to prepare 200 nm ANPs, and 2 mM NaCl to prepare 100 nm ANPs. Similar with the methods for preparing ANPs, the pH of HSA collagenase solution was adjusted to 8.50 ± 0.05 with 0.1 M NaOH. Under continuous stirring at 700 rpm at room temperature, 2 mL ethanol was added at 1.5 mL min^{-1} to 500 µL HSA solution with a syringe. 2.34 µL glutaraldehyde was added and the particles were left to cross link overnight under stirring at 700 rpm and room temperature. Using the same methods with ANPs, collagenase–coated nanoparticles were purified and characterized. Following centrifugation, ANPs pellets were resuspended to 1/10 of original volume with PBS for introduction to the tumor spheroid model.

2.3.7. Collagenase Activity Assay

The amount of collagenase conjugated on ANPs was measured by Rapid Collagenase Assay Kit with Type I Collagen Substrate (Chondrex, Redmond WA). Series dilutions of Reference recombinant Human Collagenase MMP-8 were used to build up standard curves. 100 µL of large or small collagenase coated ANPs in PBS were activated by 10 µL 0.1% w/v trypsin solution at 35°C for 15 min. 200 µL 0.05% w/v FITC-collagen was mixed with activated collagenase-ANP samples and reference standards, followed by 120 min incubation at 35°C. The collagenase-degradation products were then extracted and centrifuged at 10,000 rpm for 10 min. Supernatants of samples were transferred into a black 96-well plate and fluorescence intensities measured at $\lambda(em) = 520$ nm and $\lambda(ex) = 490$ nm (Detector Module 168, Beckman Instruments,

San Ramon, CA). The amounts of collagenase on ANPs were quantified by comparing the fluorescence intensities of samples with reference standards.

2.3.8. Cellular uptake of collagenase coated nanoparticles

C8161(+) cells were seeded onto 48-well microtiter plates at a density of 10^5 cells per well, and incubated at 37°c for 24 hours. To quantify amount of nanoparticle uptake, the cells were treated with collagenase coated large and small ANPs for various times up to 24 hours. The cells were then trypsinized, washed, and fixed prior to being analyzed via fluorescent flow cytometry (FACscalibur; BD Biosciences, San Jose, CA) using the autofluorescence of the ANPs to determine uptake. Data was processed and analyzed using FlowJo. Data was collected for 10,000 cells.

2.3.9. Multicellular Tumor Model Spheroid Formation

Melanoma cells (C8161+) and human foreskin-derived fibroblast cells (HFFs) were grown in monolayer cultures prior to spheroid formation. To produce spheroids, both types of cells were trypsinized, centrifuged and mixed in 1:1 ratio in 200 ml complete media (RPMI media with 10% FBS and antibiotics). 20 µL of cell suspensions were aspirated and applied on a plate cover to form small droplets. Cell droplets were kept in an incubator at 37°C for 4 days. Spheroids that expanded to a diameter of 300-400 µm, were transferred to a 24-well agar plate and allowed to incubate for 2 additional days before processing.

2.3.10. Nanoparticle Penetration in Tumor Model Spheroids

The spheroids were aspirated with a pipette and transferred to a new 24-well agar plate. The medium was removed by aspiration, and spheroids were washed with PBS (pH 7.4)

before further processing. The spheroids were treated with base ANPs, dual drug loaded ANPs, base collagenase-coated nanoparticles and dual drug loaded collagenase-coated nanoparticles with varying concentrations of 0% v/v, 5% v/v, 10% v/v and 25% v/v in culture medium for 72 h and 96h.

For the analysis of spheroids penetration by nanoparticles, spheroids were fixed, Hoechst stained and then processed in two ways: 1) cross sectioning, 2) direct confocal imaging. Spheroids were transferred to a cryomold, covered in optimal cutting temperature compound (O.C.T, Tissue-Tek, Torrance, CA), flash frozen, and processed by cutting 25 µm- thick sections using a cryostat (Shandon Cryotome E, Thermo Scientific, Waltham, MA). Fluorescent images of spheroid sections were obtained with a confocal laser microscope (*Leica* Microsystems Inc., Bannockburn, IL) and analyzed by a series of Matlab algorithms (**Supplementary Figure 1**). Two fluorescence modes were imaged: the green autofluorescence of the albumin shells and the blue nuclear Hoechst stain. The two channels were converted into binary masks, and any holes in the images were filled. The number of pixels per mask was then calculated and used to create a densitometric ratio of albumin fluorescence to cellular fluorescence. This was used as a measure of ANP penetration, as the greater the area of the albumin fluorescence is associated with a greater percentage of nanoparticles within the spheroid**s**.

2.3.11. Drug Loading of Albumin Nanoparticles

Curcumin was dissolved in ethanol to yield a final concentration of 1 mg mL^{-1} and was dissolved at room temperature for 30 min. The curcumin solution was added drop-wise into a suspension of ANPs to yield final concentrations of 10 µM, 20 µM, 30 µM, 40 µM, 50 µM, 80 µM, 100 µM and 140 µM.

Riluzole was dissolved in ethanol to give a final concentration of 10 mM. Riluzole solution was then added into a suspension of ANPs to yield final concentrations of 50 µM (0.135% w/v), 60 µM (0.162% w/v), 70 µM (0.189% w/v), 80 µM (0.216% w/v), 90 µM (0.243% w/v), and 100 µM (0.270% w/v).

For combination drug loading, the curcumin solution was added drop-wise into ANPs suspension to yield final concentrations of 0.1% w/v, while the riluzole solution was added to yield final concentrations of 50 µM (0.135% w/v), 60 µM (0.162% w/v), 70 µM (0.189% w/v), 80 µM (0.216% w/v), 90 µM (0.243% w/v), and 100 µM (0.270% w/v). In all instances, the drug mixtures were adsorbed onto the nanoparticles by agitation for 3 hours at room temperature.

Drug loaded ANPs were purified by one round of centrifugation for 8 minutes at 4 °C (16 100× *g* for 200 nm ANPs, while 48 400x g for 100 nm ANPs). To characterize the drug loaded ANPs, the pellets were resuspended to original volume with PBS following the centrifugation. To test the drug loaded ANPs in physiological conditions, pellets were resuspended to 1/10 of original volume. Resuspension was performed as described before.

2.3.12. Quantification of Drug Loading

The concentration of drugs loaded on ANPs were determined by high-performance liquid chromatography (HPLC, Beckman Coulter Model 166, Brea, CA) equipped with a Luna C18 column (3 µm, 100 x 4.6 mm i.d., Phenomenex, Torrance, CA). The drug loaded ANPs were frozen at -80°C overnight and lyophilized for 48 hours. The powders were resuspended in ethanol to original volume, and subsequently assayed by HPLC to determine curcumin and riluzole concentrations. For chromatographic elution, the flow rate was 0.9 ml min^{-1} over the entire separation. A step gradient was utilized for elution in which the mobile phase consisted initially of 30% ACN and 65% water containing 0.1% TFA for the first 7 min, followed by 75%

ACN and 25% water containing 0.1% TFA for the next 9 min. Curcumin was detected at 420 nm, while riluzole was detected at 255 nm (Detector Module 168, Beckman Instruments, San Ramon, CA). Serial dilutions of curcumin and riluzole standards were used to construct a calibration curve, with the linear portion utilized for measurements.

2.3.13. Cell Viability Assay

The metabolic activity of viable cells was assessed by CellTiter 96 AQueous Non-Radioactive Cell Proliferation Assay (Promega, Madison, WI). Before drug treatment, 2-D melanoma cells were cultured on 96-well polystyrene tissue culture plates at a density of 5000 cells per well for overnight incubation at 37 C, while 3-D spheroids were directly transferred to 96-well culture plate. Wells were treated with different drug regimen (single drugs or single drug loaded nanoparticles or combination free drug or combination drug loaded nanoparticles) of varying concentrations starting from 1 µM to 50 µM. At 0 h, 24 h and 96 h time points, MTS reagent (20 µL) was added to each well of the assay plate containing 10% v/v test samples in culture medium (100 µL). The plates were incubated for 2 h at 37 °C in a 5% CO_2 atmosphere, after which the absorbance was measured at 490 nm using a plate reader. Background absorbance was corrected by preparing a set of control wells without cells containing the same volumes of culture medium, test sample, and MTS reagent. The measurements were carried out in triplicate. Cell viability was quantified by the relative number of live cells compared to a PBS negative control.

2.14. Cell Apoptosis Assay

Melanoma cell lines were cultured on a 48 well microtiter plate at a density of 100,000 cells per well. After an overnight incubation at 37 °C cells were treated with free drugs and incubated for

48 hours. Cells were then trypsinized, washed and fixed in 70% ethanol. DNA was extracted and the cells were stained with propidium iodide (Invitrogen, Carlsbad, CA, USA) prior to being analyzed via flow cytometry (FACscalibur; BD Biosciences, San Jose, CA). Data was processed and analyzed using FlowJo. Data was collected for 10,000 cells.

2.3.15. Drug Release

The release of drugs from ANPs was monitored using dialysis. The dialysis tubes (100 kDa, Spectrum Labs) were immersed in 15% ethanol for 30 min prior to use and then rinsed with phosphate buffered saline (PBS) solution. 1 mL of base ANPs, drug loaded ANPs and the native drug solutions were dialyzed against 200 mL of PBS (pH 7.4) with 10% ethanol. At each time point, 50 µL of ANPs suspension was withdrawn from the tubes, and the PBS was replaced with fresh solution. The samples withdrawn at each time points were lyophilized and re-suspended with ethanol. The levels of curcumin and riluzole in each sample were measured using HPLC as described above.

2.3.16. In vitro Cellular Uptake of Drug Loaded ANPs

C8161(+) cells were seeded onto 8-well Lab-Tek slides (Thermo Scientific, Waltham, MA) at a density of 10^5 cells/well, and incubated at 37°C for 24 h. To quantify the relative degree of drug uptake, C8161(+) cells were treated with free drugs, base ANPs and drug loaded ANPs for 6 h. The cells were fixed, washed, and stained with Hoechst prior to imaging. Auto-fluorescence from albumin and curcumin in the ANPs was captured along with the Hoechst fluorescence by a confocal laser microscope (*Leica* Microsystems Inc., Bannockburn, IL). Images were processed and quantified using ImageJ.

2.4. Results

2.4.1. Characterization of Nanoparticles

Albumin nanoparticles (ANPs) were formed through the solvent-induced controlled coacervation of albumin. By varying the amount of sodium chloride in the HSA solution prior to coacervation, the size of the final nanoparticles could be controlled. Two sets of ANPs were generated with hydrodynamic diameter ~100 nm (small) and ~200 nm (large), as confirmed using dynamic light scattering (DLS). Scanning electron microscopy (SEM) of the ANPs revealed spherical, monodispersed populations of discrete nanoparticles (**Figure 2A and 2B**), corroborating the results seen with DLS. Both sets of ANPs exhibited low polydispersity and negative zeta potentials in phosphate-buffered saline (PBS, pH 7.4) (**Figure 2G**). The yields of human serum albumin (HSA) in producing small and large ANPs were approximately 65% and 50% respectively.

2.4.2. Matrix Protease Modified ANPs

Tumor penetrating ANPs were formulated by decorating the surface of the particles with the matrix protease, collagenase. Small collagenase-embedded ANPs (cANPs) were approximately 10 nm larger in size than unmodified small ANPs and with only slightly larger polydispersity (**Figure 2G**). Large cANPs were similar in both size and polydispersity to unmodified large ANPs. SEM images revealed greater surface texture on both sets of cANP (**Figure 2C and 2D**). Large cANPs presented two fold higher levels of collagenase compared to the smaller cANPs (**Figure 2H**). Small and large cANPs were subsequently loaded with both curcumin and riluzole as before (**Figure 2E and 2F)**. Loading of the drugs led to increase in size and polydispersity for both small and large cANPs (**Figure 2G**).

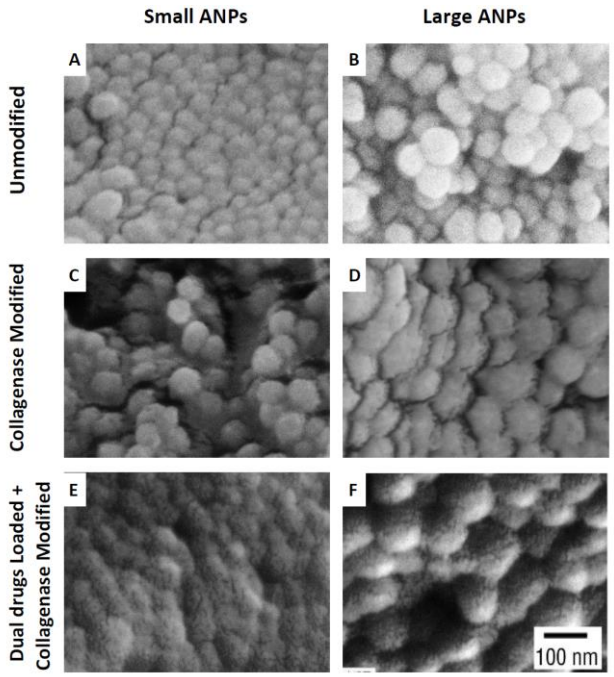

G

ANP Formulation	Collagenase Presence	Riluzole Loaded (μM)	Curcumin Loaded (μM)	Hydrodynamix Diameter (nm)	Polydispersity	Riluzole Loading Efficiency (%)	Curcumin Loading Efficiency (%)
Small	-	---	---	96 ± 1	0.03 ± 0.01	---	---
Small	+	---	---	107 ± 1	0.06 ± 0.02	---	---
Small	+	10	40	113 ± 3	0.14 ± 0.03	24 ± 4	48 ± 4
Large	-	---	---	182 ± 2	0.08 ± 0.02	---	---
Large	+	---	---	194 ± 1	0.09 ± 0.03	---	---
Large	+	10	40	207 ± 2	0.16 ± 0.08	25 ± 5	50 ± 5

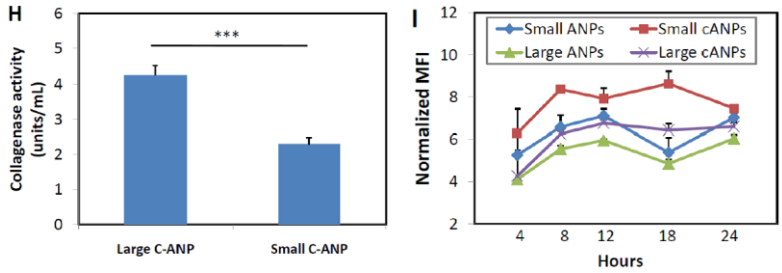

Figure 2.2 – SEM and Characterization of Various ANP Formulations. Scanning electron microscopy (SEM) images of small (A) and large (B) ANPs reveal monodisperse, spherical nanoparticles. Collagenase modification altered the morphology of the small (C) and large (D) ANPs. This change in morphology was more evident after both drugs were loaded on the small (E) and large (F) collagenase ANPs. ANPs were synthesized and characterized at two different sizes by modifying the concentration of NaCl used during synthesis (G). Both sizes exhibit narrow size distributions and negative zeta potentials in PBS. Hydrodynamic diameter,

polydispersity and loading efficiency of ANP formulations with and without collagenase incorporation were characterized. Large Collagenase ANPs carried 2 folds the collagenase compared with smaller C-ANPs (H, one unit of collagenolytic activity is defined as the cleavage of 1 mg of collagen substrate per minute). Cellular uptakes of collagenase conjugated and unmodified ANPs in C8161+ cell line were analyzed by flow cytometry for up to 24 h. The decrease in size and collagenase conjugation quickens the uptake of nanoparticles (I). ± Values: standard deviation (n=3); Error bars represent standard deviation (SD) for n=3. *** $p<0.005$ (*t* test).

Unmodified and collagenase modified ANPs were evaluated in a 2-D cell culture to determine the effect of the ANP size and collagenase coating on uptake and association at the single cancer cell level. Notably, the small ANPs showed greater cellular uptake than the large ANPs, supporting the design of differentially sized ANPs to tune the uptake kinetics. The cANPs showed a higher cellular uptake than the uncoated ANPs as measured by flow cytometry **(Figure 2I)** Confocal microscopy showed internalization of both the nanoparticles and free drugs in solution after 6 hours **(Supplementary Figures 7A-7F)**.

2.4.3. Penetration of cANPs in a 3-D Multicellular Spheroid Model

The collagenase-modified ANPs were further evaluated in a 3-D cell multicellular spheroid model consisting of C8161+ melanoma cells co-cultured with human foreskin-derived fibroblasts for tumor penetration. The penetration of cANPs into the spheroids was visualized using the cANP autofluorescence (**Supplementary Figure 2**).

Spheroids were exposed to small and large ANPs with and without collagenase for 96 hours. The imaging studies revealed that both in presence and absence of collagenase treatment, the size of the nanoparticles influenced their penetration significantly. After 96 hours, a majority of the undecorated particles remained on the periphery of the tumor (**Figure 3A and 3B**). Collagenase decoration improved tumor penetration for both the small and large particles (**Figure 3C and 3D**). The large cANPs showed greater regional accumulation around the periphery of the spheroid (**Figure 3C**), while small cANPs achieved penetration into the center of the spheroid (**Figure 3D**).

Images of cANP penetration were quantified and compared to those of ANPs (**Figure 3E**). Based on total area of the spheroid imaged, small cANPs penetrated approximately 6% of the spheroid compared to 0.6% for small ANPs 96 h. Large cANPs penetrated 27% of the spheroid compared to 0.1% for large ANPs in 96 h. The greatest penetration was exhibited by large cANPs, consistent with their greater collagenase activity.

2.4.4. ANP Drug Loading and Release Kinetics

Curcumin and riluzole were first adsorbed separately at various concentrations onto the surface of fully formed ANPs of both sizes. The particles were then characterized with DLS to determine the effect of drug loading on particle size and polydispersity (**Supplementary Figure 3**). For both small and large ANPs, the concentration of curcumin added to the formulations was fixed at 80 µM and the amount of riluzole varied. Across the concentrations tested, there was no change in the binding efficiency of riluzole or curcumin as quantified using HPLC, and curcumin adsorption had little effect on the binding efficacy to Riluzole (**Supplementary Figure 4A, 4B and 4C**). Riluzole and curcumin bound with efficiencies of ~25% and ~60%, respectively, for both the large and small ANPs(**Supplementary Figure 4C**), which is similar to the loading

efficiencies for each drug individually (data not shown). Both drugs could be released over a time scale of approximately a day from the ANPs (**Supplementary Figure 5**).

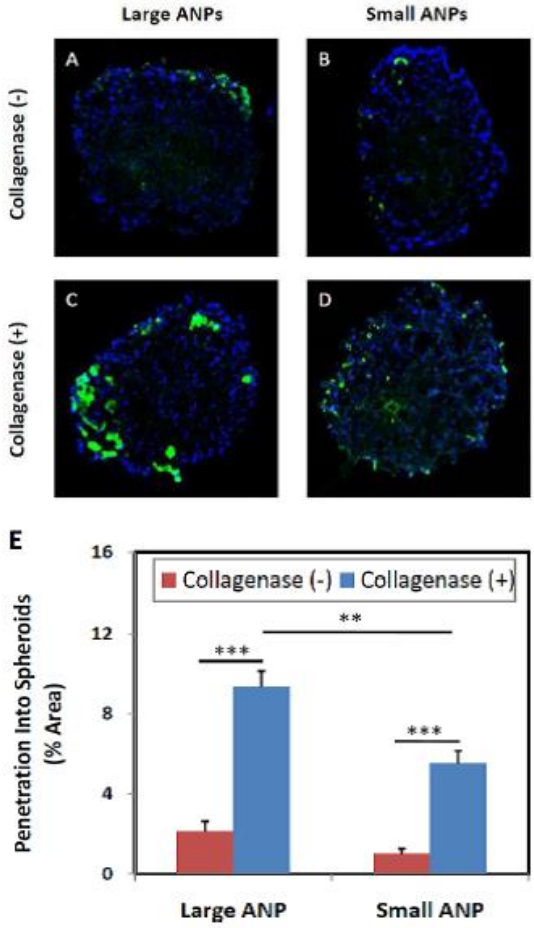

Figure 2.3. – Spheroids penetration of protease modified ANPs. Confocal microscopy images of multicellular spheroids stained with Hoechst (blue) treated with various nanoparticles (green) for 96 hours (A-D): larger ANPs (A), small ANPs (B), large collagenase conjugated ANPs (C), and small collagenase conjugated ANPs (D). Images were taken to show that there is better penetration of both collagenase modified ANPs compared to ANPs. Large C-ANPs penetrate more into the spheroids than the small ones (E) while the smaller C-ANPs displayed deeper penetrations by 96 hours. Error bars represent standard deviation for n=5. ** $p<0.02$; *** $p<0.005$ (*t* test).

2.4.5. In vitro Cytotoxicity of Curcumin, Riluzole and Combination Treatments

The therapeutic effects of curcumin and riluzole were evaluated on malignant versus healthy cells using C8161+ human melanoma cells and AR7119 immortalized human melanocytes, respectively. Both cell lines were exposed to curcumin (**Supplementary Figure 6C and 6D**), riluzole **(Supplementary Figure 6A and 6B),** or cocktails of both compounds for 96 h (**Supplementary Figure 6E and 6F**). C8161+ cells were more sensitive towards curcumin at concentrations above 10 µM than AR7119 cells. Riluzole treatment showed greater dose-dependent cytotoxicity in the C8161+ cells than AR7119 cells. Cell viability assays revealed that while 40 µM riluzole inhibited the proliferation of melanoma cells, cytotoxicity was also induced in healthy melanocytes (~30% reduction of proliferation). To test the effect of combining two therapeutics, the concentration of riluzole was fixed at 10 µM and curcumin concentration was varied. From these studies, the combination of both drugs in solution was chosen as 10 µM riluzole and 40 µM curcumin. This combination of riluzole and curcumin in solution had high cytotoxicity effects against the C8161+ melanoma cells with minimal adverse effect on the viability of the AR7119 melanocytes (**Figure 4A and 4B**). These concentrations were used to determine the apoptotic effect of the drugs in solution. After staining with propidium iodide, apoptotic, G1/G0, and G2 cell populations could be detected based on characteristic fluorescence patterns[152]. After 48 hours, the dual drug treatment resulted in more apoptotic and G2 phase cells than either individual therapy (**Figure 4C**).

2.4.6. Efficacy of Dual Drug Loaded ANPs In vitro

The efficacy of the dual drug-loaded nanoparticles was compared against the free drugs in solution using a 2-D monolayer of cultured cells. For equivalent levels of dual drug loading

concentrations (10 µM riluzole and 40 µM curcumin), both large and small nanoparticles exhibited similar effectiveness by 96 hours against C8161+ melanoma cells (**Supplementary Figure 7G**). Comparative trends were similar for AR7119 melanocytes between free and ANP-bound formulations, though the drug treatment has a less pronounced effect on the melanocytes (**Supplementary Figure 7H**).

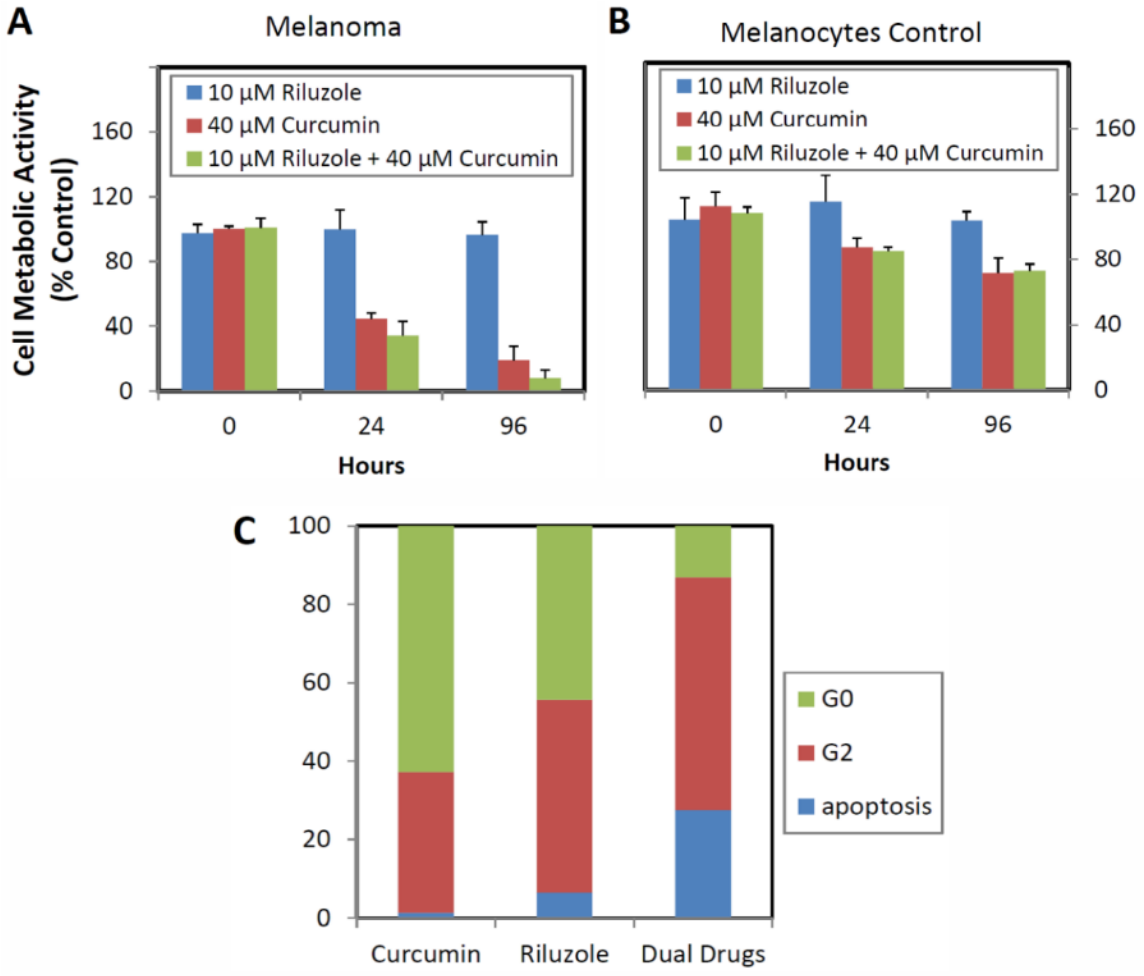

Figure 2.4. – Therapeutic effect of Curcumin, Riluzole and Dual Drugs. In vitro cytotoxicity of riluzole, curcumin, and dual drugs on (A) C8161+ melanoma cells and (B) AR7119 melanocytes. Apoptotic effects of 40 µM curcumin, 10 µM riluzole, and dual drugs (10 µM riluzole + 40 µM curcumin) on C8161+ melanoma cells after 48 hours of incubation were obtained by flow

cytometry. The dual drug treatment resulted in more apoptotic and dividing (G2) cells than either single drug therapy. Error bars represent standard deviation for n=3.

2.4.7. Efficacy of Matrix Protease-Modified, Combination Drug ANPs

Dual drug-loaded cANPs were evaluated in a 2-D cell culture model to determine whether the incorporation of collagenase altered the therapeutic efficacy of the riluzole and curcumin combination. Unloaded cANPs had little effect on cell proliferation for either the C8161+ (**Figure 5A**) or AR7119 cells (**Figure 5B**). Drug-loaded cANPs induced a similar degree of cytotoxicity when compared to both free drug and drug-loaded ANPs in C8161+ cells. This was also seen in AR7119 cells though cytotoxicity was significantly less than with the C8161+ cells.

The therapeutic efficacy of cANPs loaded with both curcumin and riluzole was next tested in a 3-D spheroid model. Spheroids were exposed to drug loaded ANPs with and without collagenase modification. After 24 h, drug-loaded small cANPs induced a significantly greater degree of cytotoxicity in the spheroids than unmodified drug-loaded ANPs (**Figure 5C**). By 96 hours, both the large and small drug-loaded cANPs had induced greater cytotoxicity in the spheroids as compared to ANPs unmodified with collagenase.

2.5 Discussion

The goal of this work was to develop an advanced health care material designed to integratively overcome three successive barriers for chemotherapy of cancerous tissues: intracellular chemo-resistance (through dual drug delivery); cancer cell uptake (through nanoparticle size and albumin chemistry); and multicellular tumor penetration (through enzymatic presentation) (**Figure 1**). We demonstrate that the modification of differentially sized albumin-derived nanoparticles (ANPs) with an ECM protease,[153, 154] permits greater

nanoparticle penetration into a solid tumor model and more effective delivery of a bound-therapeutic cocktail.

Clinically-used ANPs (*nab*-paclitaxel, Abraxane ®, Abraxis BioScience Inc.)[155, 156] have already been shown to sequester large amounts of therapeutic cargo,[110, 112] improve the pharmacokinetics and circulation half-life of antitumor agents,[157] reduce in vivo toxicity associated with solvent delivery systems[139] and possibly enhance tumor uptake of therapeutics via albumin binding interactions.[158-160] However, ANPs exhibit limited penetration into tumors and have not yet been reported to deliver a combination of synergistic chemotherapeutics simultaneously. Multicellular tumor spheroid models exhibit many characteristics of tumors, such as extracellular matrix generation and oxygen and nutrient gradients.[161] Previously, work has shown that drug delivery to solid tumor masses is frequently challenging for nanoparticle-based systems, greatly limiting successful treatment.[127] Here, we developed and characterized a novel multi-protein nanoparticle, consisting of human serum albumin doped with collagenase, and evaluated its ability to penetrate into a multicellular spheroid model of co-cultured human melanoma and fibroblast cells. Collagenase treated nanoparticles have shown increased penetration into tumor spheroid models and improved tumor accumulation in spheroid masses vs. unfunctionalized particles.[153]

Two sizes of collagenase-modified ANPs (cANPs) were synthesized and loaded with both therapeutic compounds. The cANPs did not alter the binding of the drugs to ANPs or their release. Furthermore, cANPs retained the cytotoxic effects of curcumin and riluzole on the cancerous cells; their effect on the C8161+ melanoma cells was nearly identical to that of the ANPs loaded with drugs alone. As expected, [153] confocal imaging of cANP penetration into multicellular spheroids revealed strong size dependence for penetration and confirmed

collagenase activity. While the distribution of smaller cANPs is more diffuse, suggesting cellular internalization, the larger cANPs exhibit pockets of density that appear localized between cells in the spheroid. Smaller sized cANPs, within the size limits of endocytosis,[162] were more rapidly internalized by tumor cells after initially penetrating into the tumor. Large cANPs, decorated with higher levels of collagenase, were able to slowly degrade the collagen fibers and penetrate further into the tumor over time.

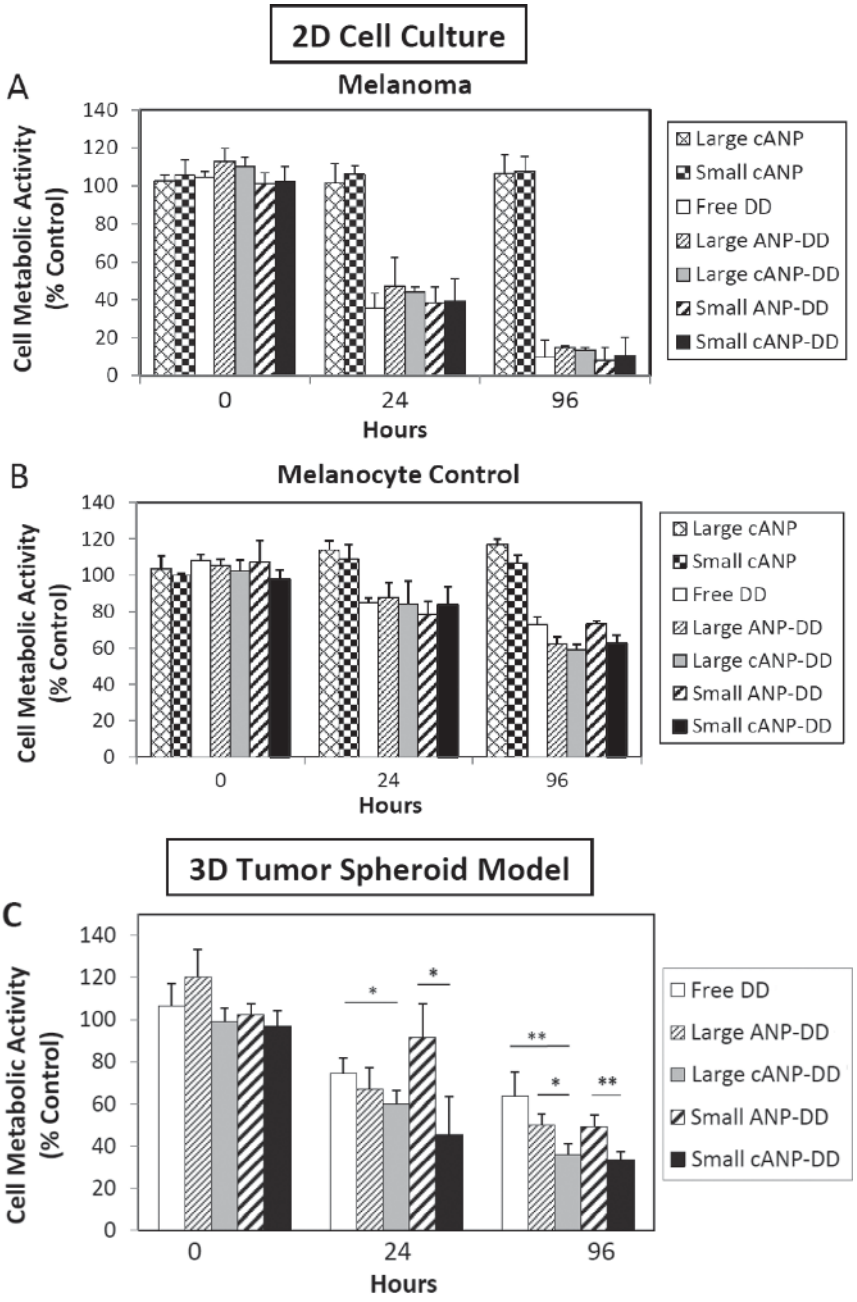

Figure 2.5. Multimodular ANPs exhibit enhanced tumor cytotoxicity in a size, protease-modification, and dual drug-display dependent manner. A dual drug (DD) combination of 10 μ M riluzole and 40 μ M curcumin bound ANPs nanoformulations were tested within 2-D monolayer cultures and showed enhanced cytotoxicity of (A) C8161 + human melanoma cells compared to (B) AR7119 healthy human melanocytes. The cANPs showed no inherent cytotoxicity in either cell line. (C) The multimodular ANPs showed unique effects in the 3-D

multicellular tumor spheroid model as a function of time and ANP size, collagenase modification, and dual drug treatment. ANP-based dual drug delivery showed enhanced efficacy over free drugs. The collagenase modification enhanced efficacy for both large and smaller ANPs but particularly for smaller ANPs. The smaller cANPs showed the most pronounced time dependent therapeutic effect. Overall, the ANPs can be designed as versatile chemotherapy tools to modulate matrix transport rates as well as intracellular uptake rates and effect short-term and longer-term tumor killing. Error bars represent standard deviation for $n = 3$. $* p < 0.05$; $** p < 0.02$ (*t* test).

In contrast with systemic administration of collagenase, which may promote tumor metastasis [163, 164] our system confines the presentation of collagenase on the surface of the nanoparticles enabling strict control of ECM degradation. Passive tumor targeting of nanoparticles through the enhanced retention and permeation effect (EPR) combined with active targeting approaches, such as the conjugation of cyclic RGD or other tumor-targeting moieties,[69, 165] can further lead to controlled ECM degradation at tumor sites.

As drug delivery vehicles, ANPs have been shown to exhibit strong but reversible drug-binding properties.[110] Albumin can simultaneously bind multiple, structurally dissimilar compounds at sites distributed across its surface.[112, 166] We exploited this feature of albumin for the purpose of co-delivering two major therapeutic moieties, curcumin and riluzole, as proof-of-concept agents to cancer cells using ANPs. Curcumin, a poorly bioavailable herbal derivative,[167] is known to have anti-cancer and anti-inflammatory properties.[168-170] Furthermore, curcumin can act as a potent chemosensitizer, improving tumor cell sensitivity towards chemotherapy via downregulation of NF-κB and NF-κB-regulated gene products.[168, 171] Riluzole is a noncompetitive glutamate release inhibitor that is currently approved for use

in patients with amyotrophic lateral sclerosis (Lou Gehrig's disease). Recent work has indicated that neuronal glutamate receptor expression in melanocytes is highly oncogenic and present in human melanoma biopsies,[172, 173] while disruption of this receptor with riluzole can trigger apoptosis in vitro and suppress the metabolic activity of human melanoma.[174, 175] Together, riluzole and curcumin can act on two independent apoptotic pathways: inhibition of P13k/Akt[175] and activation of NF-κB mediated by caspase-8,[176] respectively (**Figure 1D**). In our studies, both drugs were found to bind tightly to ANP substrates. The slower release of curcumin compared to riluzole from the ANPs may be due to its greater hydrophobicity.[167, 177] Although it took 18-21 hours for 50% of the adsorbed drugs to be released from the ANPs in PBS, imaging studies using the inherent fluorescence of ANPs revealed that the nanoparticles were internalized into cells after 6 hours of incubation. Taken together with the evidence that both riluzole and curcumin maintained therapeutic efficacy against melanoma cells when formulated with ANPs in 2D cytotoxicity assays, nanoparticles likely facilitate cellular uptake of both drugs which is followed by release over a time scale appropriate for pharmacological activity. Similarly, other combinations of therapeutics could be delivered via this versatile nanoparticle platform material.

The multimodular nature of the albumin nanoparticles allowed us to explore the individual and combined roles of nanoparticle size, protease modification and dual drug presentation in the context of a tumor-equivalent, multicellular melanoma model using three-dimensional spheroids in vitro. Several interesting trends emerged from this study. First, the larger ANPs showed rapid penetration into tumor spheroids in a size-dependent manner, thus showing early increase in tumor cytotoxicity. Collagenase modification of these large ANPs did not further enhance the efficacy by 24 hours, suggesting that the size-governed transport rate of large ANPs was sufficient to elicit cytotoxicity early on. Because large ANPs also displayed

higher levels of collagenase, these trends could not be easily decoupled. In contrast, the smaller ANPs showed a latent phase of cytotoxicity effects by 24 hours, which we attribute to increased cellular uptake at the spheroid margins, thus depleting the core of spheroids of ANPs. One of the intriguing trends observed was that at longer time points (96 h), these smaller ANPs effect higher levels of cytotoxicity, likely resulting from intracellular release of the dual drugs. When the intracellular activity of smaller ANPs was combined with the collagenase modification, the highest levels of cytotoxicity by 96 h were observed. We attribute this to cooperative effects of increased ANP intracellular uptake and enhanced matrix transport, thus promoting both localized cytotoxicity due to dual drugs and spatially dispersed “reach” of the ANP carriers within the tumors. Thus, the ANP materials could be used as a versatile chemotherapy tool to modulate both the spatial and temporal aspects of cancer cell cytotoxicity within heterogeneous tumor matrix microenvironments.

2.6. Conclusion

A novel formulation of nanoparticles for targeted penetration of tumor tissues was advanced, based on human albumin-derived carriers of two complementary chemotherapeutic agents (curcumin, riluzole), and examined for enhanced cancer cell killing in a 3D melanoma tumor spheroid model. Collagenase decoration of ANPs improved both the ANPs penetration into a multicellular spheroid model and therapeutic outcomes. The proposed albumin nanoparticles thus integrate several functionalities: (1) multi-drug delivery, (2) active tumor penetration and (3) size-dependent single cell uptake. The synthesized nanoparticles could be a useful tool for further investigation of mechanisms of dual drug delivery into the core of a dense tumor mass, improving the efficacy of the associated therapeutic payload.

2.7 supplemental figures

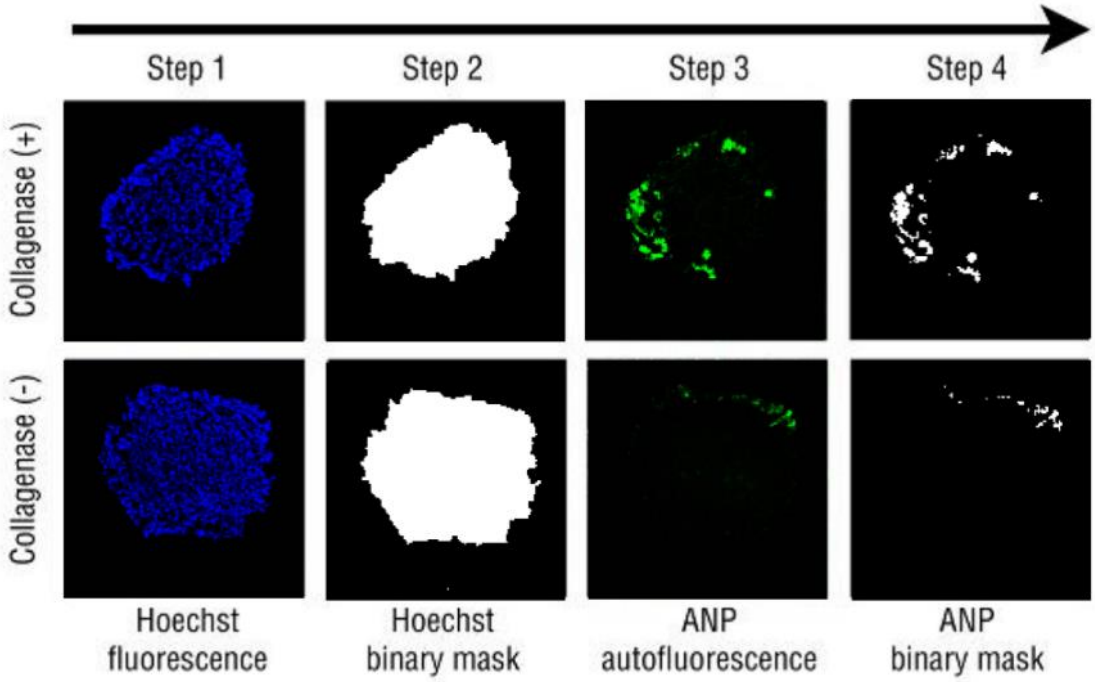

Supplementary Figure 2.1 – Quantification of Nanoparticle Penetration into Spheroids. Flow chart of the processing methodology used to quantify the degree of nanoparticle penetration into spheroids. First, binary masks are created of the spheroid area using Hoechst nuclear stain images (Step 1 to Step 2) and the number of pixels in the mask is determined. Next, background tissue autofluorescence and noise are removed from ANP fluorescence images (Step 3) and the background-corrected ANP images are binarized (Step 4). The number of pixels per area is calculated and the ratio of the two masks is used to quantify nanoparticle association within the spheroid.

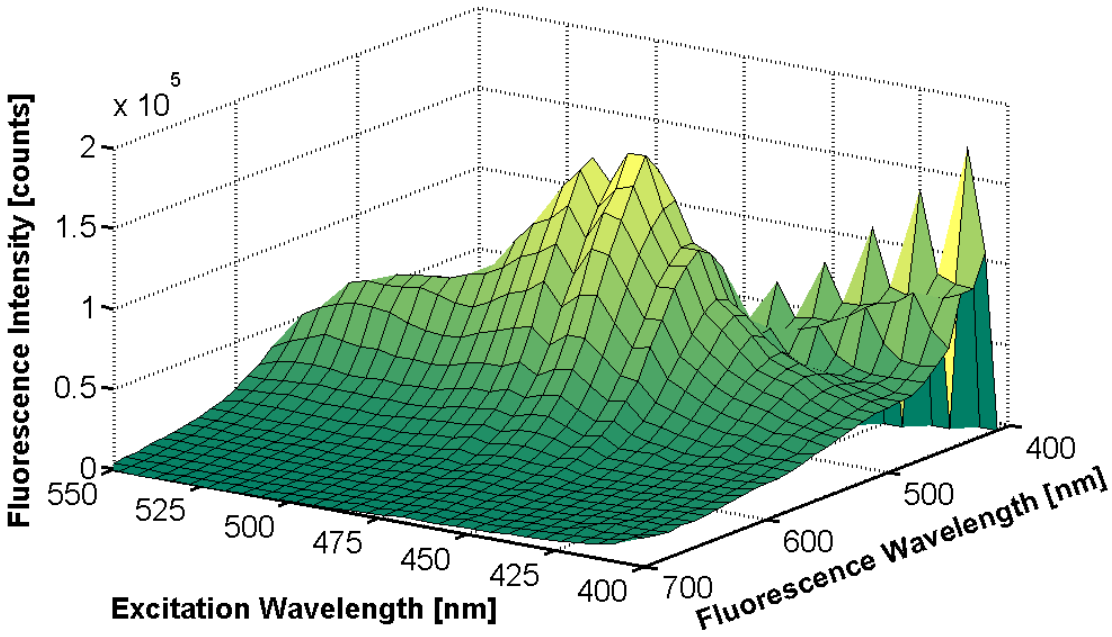

Supplementary Figure 2.2 – ANP Auto-fluorescence Spectrum. Autofluorescence of ANPs due to glutaraldehyde crosslinks as a function of fluorescence intensity. Maximum excitation at λ=480, broad emission ranging up to λ=550.

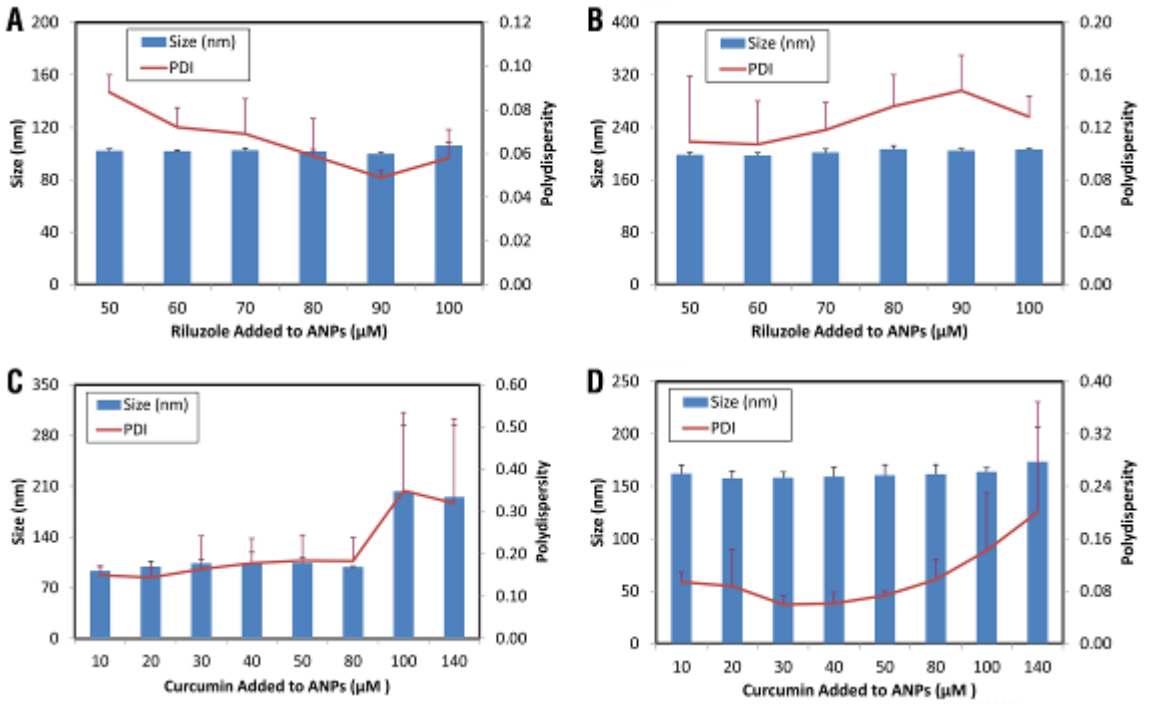

Supplementary Figure 2.3 – Physical Characterization of Single Drug-Loaded ANPs. Size and polydispersity of ANP formulations based on amounts of drug loaded: riluzole loaded small ANPs (A), riluzole loaded large ANPs (B), curcumin loaded small ANPs (C), and curcumin loaded large ANPs (D). Nanoparticle size distribution remains uniform until loading with 120 µM of curcumin. Error bars represent standard deviation for n=3.

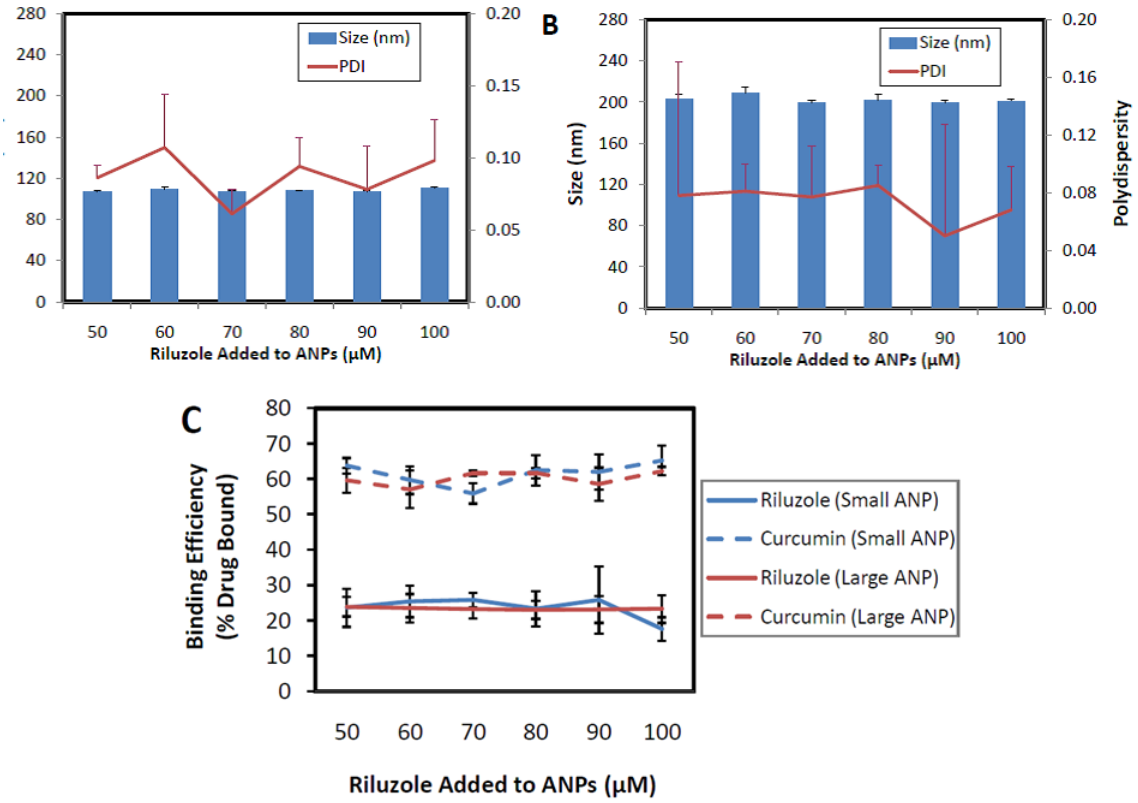

Supplementary Figure 2.4 – Physical Characterization and Binding Efficiency of Dual Drug-Loaded ANPs. Size and polydispersity of dual drug loaded ANPs (80 μM curcumin) as a function of riluzole concentration for small ANPs (A) and large ANPs (B). Binding efficiency for riluzole and curcumin for small and large ANP formulations (C). Error bars represent standard deviation for n=3.

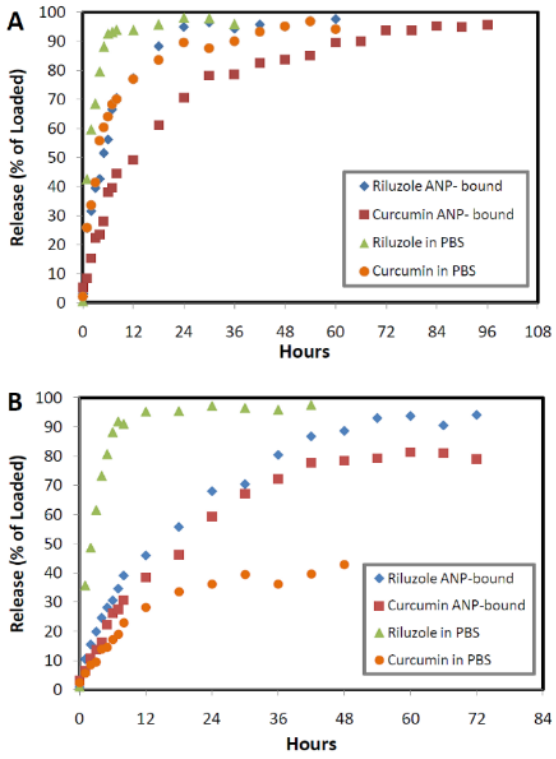

Supplementary Figure 2.5 – ANPs Retard the Release of Various Drug Formulations In Vitro. Time dependent release of curcumin and riluzole from ANPs and PBS solutions (10 µM riluzole or 40 µM curcumin). Solutions were dialyzed against (A) 10% ethanol in PBS, and (B) PBS solution at 37°C. Briefly, free drugs in PBS were released more than three times faster than those sequestered by ANPs. Specifically, when dialyzed against the 10% ethanol solution, ANP associated riluzole and curcumin displayed slower release kinetics from the dialysis cassette than the free drugs, with 50% of riluzole and curcumin release by 1 h and 3 h, respectively. In contrast, 50% of ANP-bound riluzole and curcumin were released by 6 h and 12 h, respectively. When dialyzed against PBS alone, 50% of free riluzole were released by 4 h while 50% of ANP-bound riluzole were released by 18 h. 50% of ANP-bound curcumin were released by 21 h. Due to the poor solubility of curcumin in PBS, the release of free curcumin was substantially slower.

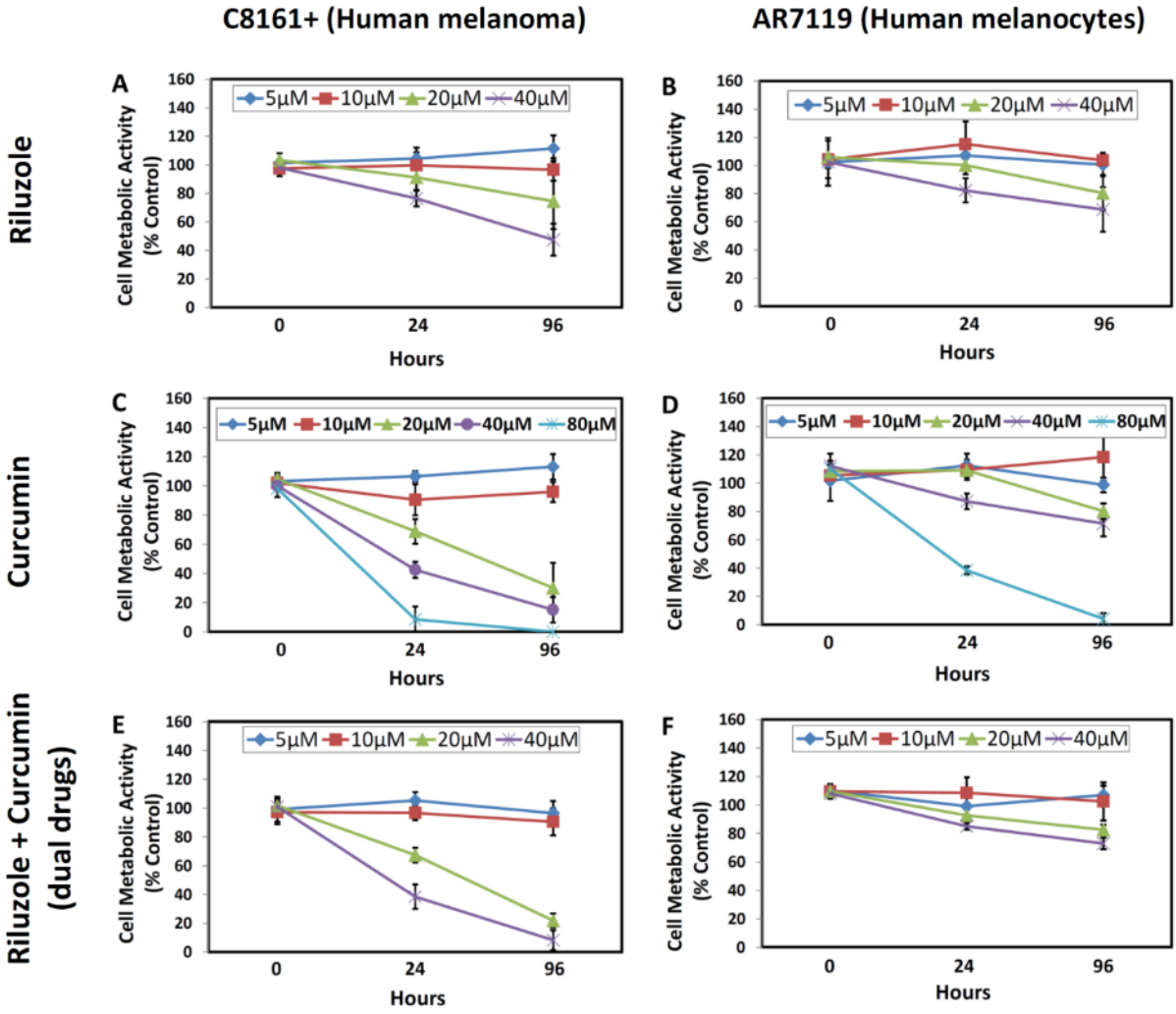

Supplementary Figure 2.6 – In vitro Cytotoxicity of Curcumin, Riluzole and Dual Drugs. Therapeutic effect of riluzole (A-B), curcumin (C-D), and 10 μM riluzole + curcumin (E-F) on C8161+ melanoma cells (A,C,E) and healthy AR7119 melanocytes (B,D,F). Error bars represent standard deviation for n=3.

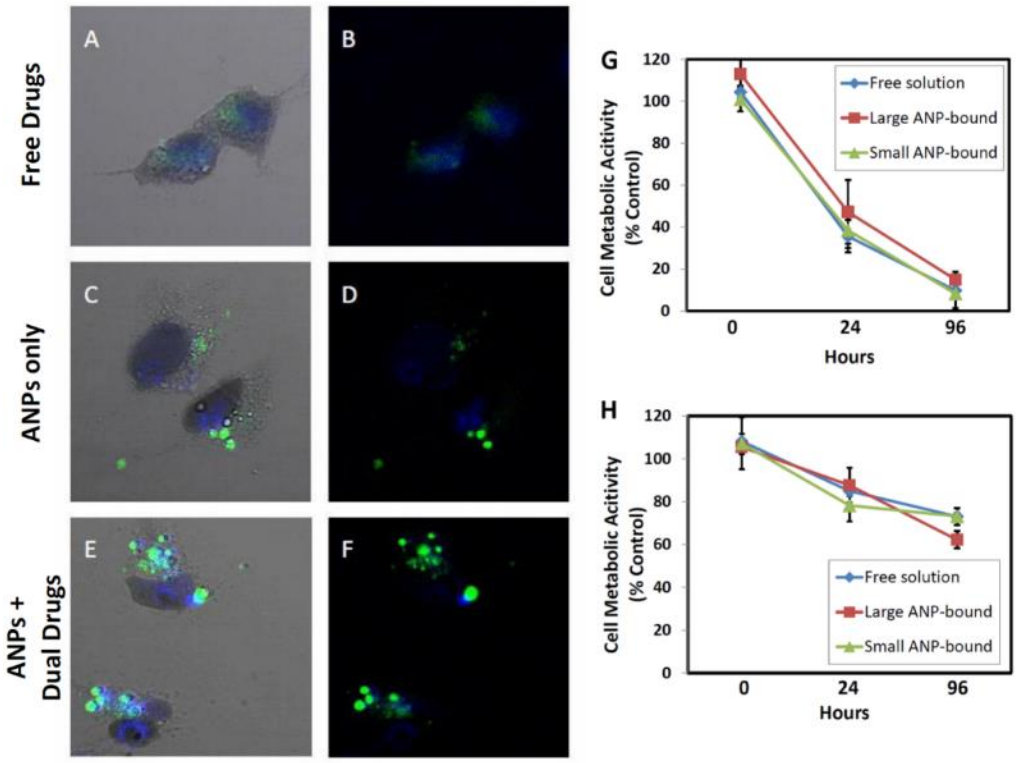

Supplementary Figure 2.7 - The internalization of drugs and ANPs in 2-D C8161+ cell Culture. Confocal microscopy images of 2D monolayer cultures of C8161+ human melanoma cells immersed in Trypan Blue, stained with Hoechst (blue) and treated with drugs loaded ANP formulations (green) after 6 hours incubation at 37°C (A-F): free drugs (A, B), large ANPs only (C, D), large dual loaded ANPs (E, F). Both albumin nanoparticles and curcumin drug emitted green fluorescence while excitation. Free drugs and nanoparticles were internalized within 6 hours of incubation. The internalization of ANPs facilitated the cell uptake of drugs. In vitro cytotoxicity of 10 µM riluzole and 40 µM curcumin formulations on 2D monolayer cultures of (G) C8161+ human melanoma cells and (H) AR7119 healthy human melanocytes. All tested drug conditions showed similar cytotoxicity against the cancerous cell line compared with free drug solutions. Curcumin and riluzole showed no loss of activity after binding to the ANPs. Error bars represent standard deviation for n=3

CHAPTER 3

RARE EARTH ALBUMIN NANOCOMPOSITES AS SHORT WAVE INFRARED EMITTING *IN VIVO* OPTICAL CONTRAST AGENTS

Note: Sections of this chapter have been reproduced with permission from the following publication:

D.J. Naczynski, M.C. Tan, M. Zevon, B. Wall, J. Kohl, A. Kulesa, S. Chen, C.M. Roth, R.E. Riman, P.V. Moghe. Rare-earth-doped biological composites as in vivo shortwave infrared reporters. Nature Communications, 2013. 4(2199).[54]

The work and writing described in this chapter was done in close collaboration with the first two authors, Dr. Dominik Naczynski and Dr. MC Tan. This author's primary contributions were collaboration on obtaining qualitative *in vivo* imaging studies and quantification of particle bio distribution, clearance, and pharmacokinetic profile.

3.1 Abstract

Optical imaging techniques have the potential for non-invasive disease surveillance, but its clinical translation has been limited by reliance on exogenous contrast agents. These agents typically rely on visible or near infrared (NIR) excitation-however, photons in this range have poor penetration through biological media. Effective optical imaging requires brightly emitting probes that can be resolved through living tissue. Recent work has indicated that the short wave infrared (SWIR) region of light represents an alternative to conventionally used visible and NIR wavelengths, with improved penetration leading to increased *in vivo* imaging sensitivity. This chapter is focused on the evaluation of ReANCs of an *in vivo* optical imaging platform. SWIR emitting ReANCs were formulated and evaluated in a biomimetic *in vivo* murine model of melanoma. The thickness of the albumin shell was found to greatly influence nanoparticle pharmacokinetics and biodistribution, with 100 nm albumin coating resulting in increased particle accumulation at the tumor site, allowing for SWIR visualization. Our findings lay the groundwork for a new generation of versatile, biomedical nanomaterials that can advance disease monitoring based on a pioneering infrared imaging technique.

3.2 Introduction

Real-time, non-invasive optical imaging of cancer is limited by a paucity of stable, bright optical probes capable of being detected in biological tissue while highlighting clinically relevant features [37]. Resolution of contrast agents is influenced by factors such as emission brightness and path length through tissue, which are dependent on the properties of the biological media the photons are propagating through [178]. In tissue, molecules such as water, hemoglobin, and melanin absorb light, while tissue composition and morphology serves to scatter incident photons [51, 179, 180]. These factors together greatly attenuate most wavelengths of light,

limiting their penetration through tissue and their clinical utility. In contrast to visible wavelengths, near infrared light (NIR, 700-1000 nm) experiences less absorbance and scattering by tissue components. This results in improved penetration and therefore deeper imaging capabilities in this first “tissue transparent window” [62, 181]. Recent evidence suggests the existence of a second “tissue transparent window” in the short wave infrared (SWIR, 1000-2300 nm) range, with similarly diminished tissue interference but with up to 1000-fold greater reduction in scattering, leading to improvements in imaging depth [178]. Despite its advantages, adoption of SWIR based optical imaging has traditionally been limited by a paucity of available biocompatible contrast agents [182].

Materials currently used for SWIR based optical imaging are frequently not appropriate for biomedical applications, suffering from cytotoxicity and poor optical properties. SWIR-emitting quantum dots (QDs) are typically made from harmful elements such as lead, mercury, and arsenic, limiting their clinical translatability [183, 184]. Likewise, infrared emitting single-walled carbon nanotubes (SWNTs) face many limitations for biological applications, especially for disease-targeted imaging [64, 185, 186]. SWNTs can be hundreds of nanometers long, which poses challenges for effectively reaching the area of interest and penetrating into a tumor [187]. In addition to their undesirable physical characteristics, SWNTs exhibit broad, low-intensity emission peaks spanning over 300 nm, preventing multispectral imaging [64, 186]. A successful SWIR based contrast agent must account for factors such as quantum yield, biodistribution, pharmacokinetics, and *in vivo* toxicity [51]. Recent studies have illustrated that rare-earth nanoparticles (REs) are also capable of generating SWIR emissions following excitation with low power NIR phtons in the first “tissue transparent window”[188]. This as-yet unexplored property of rare earth materials is an attractive alternative to conventional SWIR emitting probes and could be used as to visualize biological features *in vivo*.

In this study we evaluate rare earth nanorpobes as *in vivo* SWIR emitting contrast agents and provide the first description of disease detection with a SWIR imaging platform. These findings show that SWIR photons effectively transmit through biological tissue and that REs are excellent *in vivo* contrast agents. We further investigate the effect of the addition of an albumin coat on RE pharmacokinetics and *in vivo* biodistribution. We illustrate here that by controlling the albumin thickness we can influence particle distribution and clearance, and increase the accumulation of probes in tumor tissue by >10 fold. Thus, rare earth probes combine depth of penetration, detection sensitivity, and improved biological localization, highlighting their excellent potential for *in vivo* biomedical imaging.

3.3 Methods

3.3.1 Synthesis of rare earth nanoprobes (in collaboration with Riman group)

$NaYF_4$:Yb-Er nanoprobe powders were prepared through solvothermal decomposition of rare earth trifluoroacetate precursors in oleylamine as described previously[69]. Briefly, the core precursor solution was prepared by dissolving stoichiometric amounts of 99.9% erbium trifluoroacetate, 99.9% yttrium trifluoroacetate, 99.9% ytterbium trifluoroacetate (GFS Chemicals, Columbus, OH) and 98% sodium trifluoroacetate (Sigma Aldrich, St. Louis, Missouri) were dissolved in oleylamine. The shell precursor solution was prepared by dissolving stoichiometric amounts of the sodium and yttrium trifluoroacetates in oleylamine. The core solution was then heated to 340°C under vigorous stirring in inert argon atmosphere to allow the formation of the core particles. The shell precursor was added and after cooling, the synthesized nanoparticles were washed three times in ethanol by centrifuging at 15 000×g (Beckman Coulter Inc., Avanti J-26 XP, Fullerton, CA) and freeze-dried at -40°C (SP Industries Inc.,

VirTis AdVantage Plus Warminster, PA). Particles were subsequently characterized using transmission electron microscopy (TEM), energy dispersive x-ray spectroscopy (EDS) and optical spectroscopy.

3.3.2 ReANC synthesis and characterization

ReANCs were prepared through a controlled coacervation technique as described previously [69]. Briefly, a 2% (w/v) solution of HSA in NaCl at pH 8.50 +/- 0.05 was prepared and adjusted with 0.1 M NaOH. The concentration of NaCl was varied between 2 and 12 mM to change the thickness of the albumin nanocomposite coating. Under continuous stirring at 700 rpm and room temperature, ethanol (2 mL) sonicated with RE nanoprobes (0.2 mg mL-1) was added with a syringe pump (Harvard Apparatus PHD 2000, Holliston, MA) at 1.5 mL min-1 to the HSA solution (500 mL). Immediately following ethanol addition, glutaraldehyde solution (0.24 µL mg-1 HSA) was added to stabilize and crosslink the nanoparticle suspension. The particles were left to crosslink overnight under magnetic stirring at room temperature. Resulting nanoparticles were concentrated 10-fold through centrifugation (Beckman Coulter, Avanti J-E Centrifuge) and redispersed through ultrasonication (Fisher Scientific, FS60).

ReANCs size, polydispersity, and surface charge were measured from 4 separate particle batches and averaged using a Malvern Zetasizer Nano (Zen 3690, Malvern, Worcestershire, UK). ReANCs were visualized with the SEM (Carl Zeiss Σigma) operated at 5.0 kV with working distance of 10 mm using the secondary electron detector. Approximately 100 ReANCs (measured from SEM images) were used to determine average particle size. The number of REs in the ReANCs was determined by the viscosity-light scattering method [189].

3.3.3 Animal models (in collaboration with Chen group)

Biodistribution and tumor accumulation studies were performed using transgenic mice developed by the Chen group that are predisposed to develop multiple melanomas (TG-3). As described previously [172], these transgenic mice develop spontaneous melanin-containing dermal lesions in the absence of any external stimuli as recently as 12 days after birth. Hairless TG-3 mice, also referred to as TGS, were utilized for these studies due to the ease of tumor identification. Mice were inspected and tumor development was evaluated twice a week. Animals were utilized for these studies once lesions present on the ears reached 1 mm in thickness. All animal studies were approved by the Institutional Review Board for the Animal Care and Facilities Committee of Rutgers University and performed in accordance with institutional guidelines on animal handling.

3.3.4 Imaging prototype

To investigate the use of rare earth nanocomposites for noninvasive SWIR based optical imaging, a prototype small animal imaging system was developed in house. The SWIR-imaging prototype consists of fiber-coupled NIR laser photodiode which operates at 980 nm and 1.4-1.5 W, and an InGaAs camera (Goodrich, Princeton, NJ) positioned at fixed height of approximately 12 in above the object. A collimator with a numerical aperture (NA) of 0.25 and focal length (f) of 37 mm (Thor Labs, Newton, NJ) was attached to the excitation fiber to enable a uniform and constant excitation beam radius which is independent of the distance between source and animal subject. The animal was irradiated with approximately 1.4 W cm^2 of 980 nm light. During the imaging, the excitation fiber was held within 12 in above the animal and slowly scanned across the animal's body. Any SWIR emissions are then captured in real-time at 19-22 frames per second by the SWIR camera positioned above the animal. Optical filters were fitted to eliminate detection of the NIR excitation source and confidently determine that only the SWIR

emissions were captured. Acquired SWIR video files were processed using MATLAB to generate a background-corrected heat map of fluorescence distribution in the animal.

3.3.5 Imaging signal processing

Acquired SWIR video files were processed using a series of MATLAB (Mathworks, Natick, MA) codes to generate a background-corrected heatmap of fluorescence distribution in the animal. In order to correct for any background fluorescence, videos of the irradiated animals were taken before nanoparticle injection and analyzed using a custom designed MATLAB script which reduces the captured video file into individual frames then analyzes each frame recording pixels with the highest intensity values at a given position. The final image is a merge of the highest intensity pixels onto a single composite image. Using ImagePro (Media Cybernetics, Silver Spring, MD), a low radius Gaussian blur filter is then applied to the composite image to eliminate noise. Any background fluorescence is detected using a Sobel edge detection algorithm. The average intensity of all contiguous regions of background fluorescence on the animal body is recorded. Specific regions are identified (head, ears, upper body, lower body, anus, tail) and pixel values within these regions are averaged yielding regional averages that can be used for background subtraction in that particular animal following nanoparticle injection.

Videos of the mice post nanoparticle injection are similarly collected and analyzed in MATLAB. MATLAB is then used to perform a background subtraction using the regional averages recorded previously. Using a contrast enhanced, backlit infrared image, rectangular regions are designated in MATLAB that envelop the head, ears, upper body, lower body, anus, and tail. The background algorithm then subtracts the regional averages from these regions. To create a heat map, each grey level in the image is assigned an RGB value on a gradient. In Adobe Photoshop,

the black pixels were removed and any remaining color pixels are overlaid on the contrast enhanced backlit infrared image to yield the final image. In order to quantify fluorescence, ImagePro was used to select areas of fluorescence and report the average intensity of all selected pixels. For each image, the average intensities of fluorescent regions of interest (ROI) are measured, and the average intensity of the non-fluorescent background is subtracted from each value.

3.3.6 Qualitative biodistribution imaging

TGS mice were fully anesthetized with an intraperitoneal injection (IP) of Avertin (240 mg kg^{-1}) (Sigma-Aldrich, Milwaukee, WI) prior to imaging. Mice were scanned with the collimated 980 nm laser prior to nanocomposite injection (background image). Mice were then injected via IP with either 10 mg kg^{-1} of uncoated REs, ReANCs or 300 nm ReANCs resuspended in PBS and normalized to RE content for all formulations. Mice were irradiated under anesthesia with the collimated 980 nm laser in various positions at different post-injection time points.

3.3.7 Quantitative biodistribution analysis

Mice exhibiting vascularized melanoma tumors were injected via IP with either 2 mg kg^{-1} of uncoated REs, ReANCs or 300 nm ReANCs resuspended in PBS and normalized to RE content for all formulations. At 24 h the mice were euthanized and their organs were collected, rinsed with PBS and weighed. Mice were housed in metabolic chambers for the collection of feces. To quantify REs in circulation, blood was intermittently sampled through the tail vein. Samples were stored at −80 °C before acid digestion. The yttrium content of digested organs was quantified using a Thermo X series II ICP-MS (Thermo Scientific, Waltham, MA) to determine particle concentration after injection.

3.4 Results

3.4.1 Preparation and characterization of multispectral REs

Core-shell rare earth nanoparticles were synthesized with an Yb and Er doped $NaYF_4$ core completely encaspulated by an undoped $NaYF_4$ shell. **(fig. 3.1a)**. RE particles were uniformly spherical, with size confirmed to be 10-12 nm by TEM micrographs (**Fig. 3.1 b)**. Differently emitting probes were generated by changing the lanthanide dopant present in the particle's core. By changing the erbium (Er) dopant to one such as thulium (Tm), holmium (Ho), or praseodymium (Pr), the emission properties of the particles can be altered **(fig. 3.1 c)**. Fluorescence occurs following the NIR excitation of a sensitizer (Yb) present in the particle's lattice. Energy is transferred to the activator dopant, which then relaxes to generate the SWIR emission unique to that specific lanthanide dopant (**Fig. 3.1d)** [71, 190]. The particles used in this work were hexagonal-phase $NaYF_4$ Yb:Er nanoparticles **(Fig. 3.1 e)**, as they were the brightest emitting phosphor nanoprobes **(Fig. 3.1 f)** and therefore were used to demonstrate the benefits and potential of SWIR-based optical imaging techniques and evaluate the system's potential or biomedical applications [191].

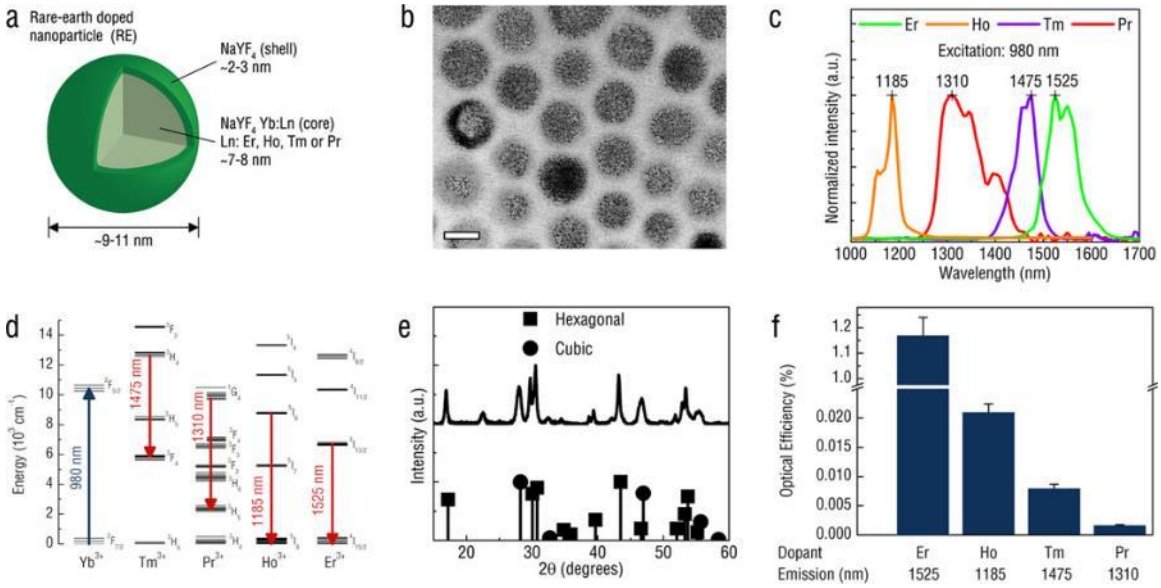

Figure 3.1 Properties of the Rare-Earth-Doped Nanoprobes. (a) ReNPs have a NaYF4 Yb:Ln doped core (Ln: Er, Ho, Tm or Pr) surrounded by undoped $NaYF_4$. TEM images of the rare earth phosphors **(b)** reveal that particles are uniform spheres 10 nm in diameter (scale bar = 10 nm). ReNP probe emissions can be tailored **(c)** by changing the lanthanide dopant present in the particle core. NaYF4 probes doped with ytterbium (Yb) and one or more lanthanide elements selected from holmium (Ho), praseodymium (Pr), thulium (Tm) and erbium (Er) enable emissions at 1185, 1310, 1475 and 1525 nm, respectively. The 1185, 1310, 1475 and 1525 nm emissions of Ho-, Pr-, Tm- and Er-doped samples are attributed to the $^5I_6 \rightarrow {}^5I_8$, $^1G_4 \rightarrow {}^3H_5$, $^3H_4 \rightarrow {}^3F_4$, and $^4I_{13/2} \rightarrow {}^4I_{15/2}$ transitions, respectively **(d)**. Particle crystal phase was confirmed with X-ray crystallography (XRD) **(e),** which confirmed that ReNPs have a predominately hexagonal phase structure. The ranking for the optical efficiencies **(f)** of the differently doped systems is: Er- > Ho- > Tm- > Pr-, where the relative ratios are 688:12:5:1, respectively. Bar graph data are expressed as mean values ± standard deviation (s.d.); n=3. This figure was provided by Dr. Dominik Naczynski and Dr. MC Tan with approval

3.4.2 Biomedical application of SWIR-based imaging using REs

SWIR-based optical imaging is limited not only by a paucity of appropriate contrast agents, but by a lack of existing high-resolution systems available for preclinical imaging and clinical translation. To this end we have designed a portable, inexpensive *in vivo* imaging system utilizing NIR light excitation below the laser exposure limit for skin (defined as 0.73 W/cm^2 for 980 nm)[192] that is able to capture high resolution SWIR images and videos (**Fig. 3.2 a-b**). We evaluated the capabilities of this system to imaging challenges such as real-time SWIR fluorescence detection, high-resolution macroscopic anatomical imaging, and multispectral SWIR imaging.

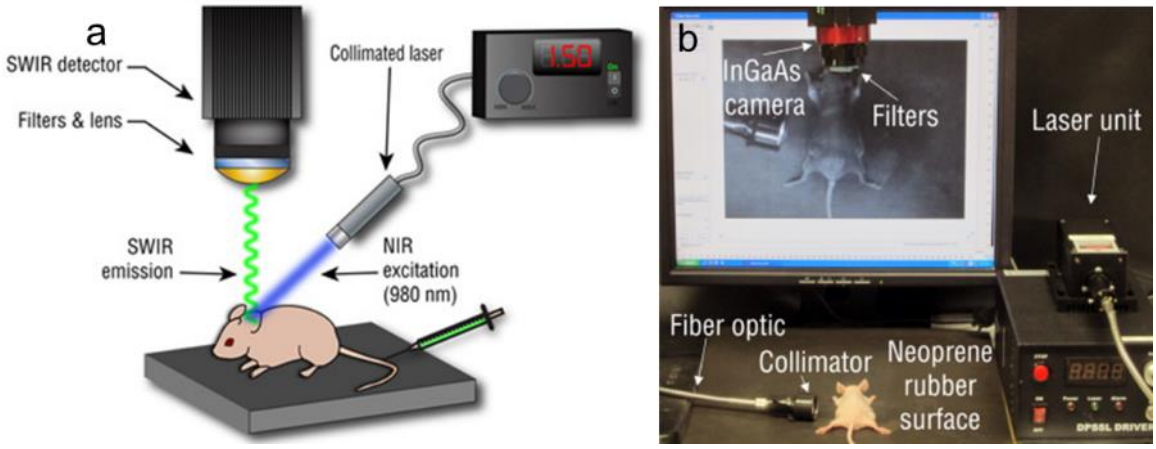

Figure 3.2 RE Nanoprobes Enable Real-Time Imaging in vivo. Schematic (a) and photograph (b) of our portable SWIR-imaging prototype. The prototype consists of a SWIR sensitive InGaAs camera with customizable filters, a collimated NIR laser capable of outputting at a power density of 1.7 W cm^{-1}, and a black rubber imaging surface to minimize reflections.

3.4.3 Tumor imaging using bioactive, albumin-coated REs

The application of SWIR-based optical imaging to tumor detection requires safe and effective probes with favorable biological properties capable of directed tissue distribution. Ceramic rare earth particles are not optimal for *in vivo* use as synthesized. To this end, ReNPs were encapsulated in FDA-approved human serum albumin to form rare-earth albumin nanocomposites (ReANCs) through controlled coacervation **(Fig. 3.3. a,b)**. Our lab's previous work has shown that ReANCs have improved aqueous solubility and diminished cytotoxic effects compared to un-encapsulated RE particles [69]. The addition of the albumin shell did not inhibit RE emissions **(Fig. 3.3 c),** indicating that ReANCs are appropriate for *in vivo* detection [193]. ReANCs were synthesized at 100 nm in diameter with narrow size distributions and slightly negative zetapotential in PBS (**Fig. 3.3 d**). The number of REs encapsulated per ReANC was calculated to be approximately 30 REs per ReANC using the viscosity/light scattering method [189].

d

Formulation	Lyophilized diameter (nm)	Hydrodynamic diameter (nm)	Polydispersity index	Zeta potential (mv)	RE content (μg ml⁻¹)	RE content (# per particle)	Protein content (μg ml⁻¹)
(RE)ANC	46 ± 6	100 ± 5	0.12 ± 0.05	-13 ± 0.6	485 ± 65	30 ± 4	3200 ± 50

Figure 3.3- Biologically Permissive Nanocomposites of REs exhibit SWIR emission. Rare-earth albumin nanocomposites (ReANCs) **(a)** have NaYF4 ReNP cores surrounded by human serum albumin, forming nanocomposites with tunable physical characteristics. SEM images **(b)** of ReANCs show that particles are spherical and uniform (scale bar = 200 nm). Encapsulated ReNPs retain their SWIR emissions while encapsulated in albumin shells **(c)**, with peak emission between 1550–1600 nm upon 980 nm excitation. Dynamic light scattering **(d)** confirm monodisperse particle popultions with slightly negative zetapotential in PBS. ReANCs contain approximately 30 ReNP cores per particle. Data in **(d)** are expressed as mean values ± s.d.; n=5. This figure done in collaboration with Dr. Dominik Naczynski

The potential cytotoxicity of ReNPs and ReANCs was evaluated using healthy human melanocytes (NHEM). All concentrations of ReANCs tested proved safe for biological use, and had no effect on cell viability. In contrast, uncoated REs reduced cell viability, indicating that the albumin coating is sufficient to shield the cellular environment from any cytotoxic effects. These data support previously reported toxicity data [194, 195] . The FDA has previously approved yttrium microparticles for the treatment of liver cancer, indicating the long-term safety and translational potential of ReNP component materials [196].

Tumor targeting and *in vivo* imaging capabilities was assessed using 10 nm REs, 100 nm ReANCs, and 300 nm ReANCs (**Fig. 3.3 d**). Particles were injected into the peritoneal cavity (IP) of TGS mice, an orthotopic melanoma model that spontaneously develops pigmented lesions [172]. Mice were imaged over 72 hours with the previously described custom SWIR imaging prototype to determine the effect of the albumin coating on probe distribution. ReANC-associated SWIR emissions at the peritoneal cavity diminished over 72 hours, while the signal from the uncoated REs remained localized at the site of injection **(Fig. 3.4 a)**. This phenomenon is most likely due to the previously reported propensity of ReNPs to aggregate in aqueous conditions [69]. Despite the aggregation of ReNPs at the injection site, all particle formulations seemed to undergo clearance through the reticuloendothelial organs such as the liver and spleen **(Supplementary Fig. S1),** which is characteristic of similar nanomaterials including SWNTs [197]. Particle accumulation was determined by the presence of yttrium in organ samples. Yttrium was detected through the use of inductively coupled plasma–mass spectrometry (ICP-MS) and was correlated to nanoprobe concentration **(Supplementary Fig. S2)**. Pharmacokinetic studies showed that ReANCs enter circulation approximately 5 minutes after IP administration, while ReNPs remained at the injection site for up to 6 hours after injection **(Fig. 3.4 b).**

ReANC SWIR-associated fluorescence was detected at tumors surrounding the animal's ears between 12-48 hours post injection (**Fig. 3.4 c**), with maximum emission intensity being seen 24 hours after particle administration **(Fig 3.4 d)**, in agreement with similar studies investigating nanoparticle biodistribution after IP injection[198, 199]. Tumors at this region were consistent, large, and well-vascularized. In contrast, uncoated REs were not detected at tumor sites. The REs did not distribute far from the injection site, where they were still observable 144 hours post injection (data not shown). This illustrates the potential of ReANCs as brightly emitting *in vivo* contrast agents capable of identifying tumor tissue. Our results present the first

evidence of SWIR imaging capable of passive identification of malignant lesions in an animal model. Particle emission benefited from improved signal-to-noise ratio in the SWIR range, improving imaging sensitivity, confirming the low absorbance we observed biocompatible SWIR-emitting ReANCs *ex vivo* (**Supplementary Fig. S3**).

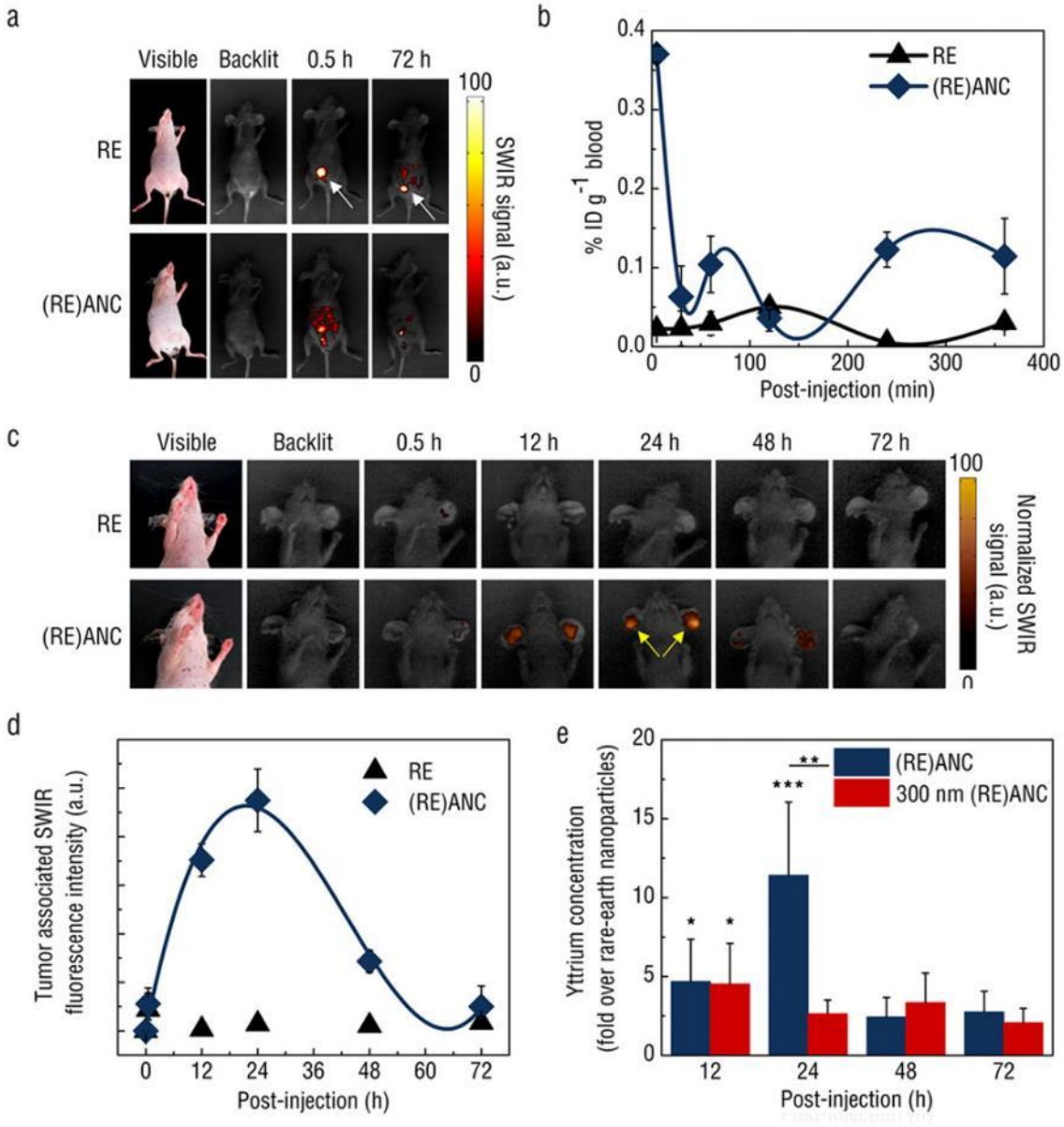

Figure 3.4- RE biologic nanocomposites profile disease progression in vivo. SWIR imaging of ReNPs and ReANCs subsequent to IP administration **(a)** into a transgenic orthotopic murine melanoma model ("TGS") over 72 h. SWIR emission of ReNPs was observed at the site of injection in the animal's abdomen up to 72 hours post administration (white arrows). Blood concentration (% ID g^{-1}) of yttrium **(b)** after ReNP and ReANC IP injection showing ReANCs rapid entrance into circulation, while REs remain sequestered in the abdomen. Data in **(b)** are expressed as mean values ± s.e.m.; n = 3. ReNPs and ReANCs accumulated over 72 hours **(c)** in tumors around the animal's ears. SWIR signal from ReANCs around tumors indicated by yellow arrows. Representative images (n=3) viewed from the ventral aspect are shown in all instances. The accumulation and clearance of SWIR fluorescence **(d)** in the tumors was described by a third-order polynomial fit for ReANCs (R^2 =0.99) but could not be detected for REs. Data in **(d)** are expressed as mean values ± s.d.; n = 3. ICP-MS was performed **(e)** to detect the presence of yttrium in the tumors and quantify the imaging results observed in **(c)**, and revealed a significant increase in nanoparticle accumulation at tumor sites with the addition of an albumin coating. Bar graph data are expressed as mean values ± s.e.m.; n=10 for 12 h and 24 h, n=5 for 48 h and 72 h. *P < 0.10; **P < 0.05; ***P < 0.02, determined by one-way ANOVA, Tukey post-hoc. Data in **(e)** are presented as a fold increase compared to REs.

3.4.4 Evaluation of quantitative biodistribution

Imaging results and particle biodistribution were quantified through non-optical techniques. Yttrium concentration in tissue samples was used to quantify particle organ association using ICP-MS. Through this technique we confirmed that ReANCs show a 10-fold increase in tumor

accumulation compared to un-encapsulated REs by 24 hours **(Fig. 3.4 e)**. This increase in accumulation is likely due to albumin-mediated transport into the tumor space [200], and to the enhanced permeation and retention (EPR) effect. The EPR effect allows particles approximately 100 nm in diameter to accumulate in the tumor interstitial space through leaky vasculature [84, 85]. To determine the effect of albumin coating thickness particle biodistribution, ReANCs with a larger HSA coating (~300 nm) **(Supplementary Fig. S4)** were developed and injected into TGS mice. The particle biodistribution was similarly tracked over 72 hours. Compared to the 100 nm ReANCs **(Supplementary Fig. S5)**, the larger particles had less accumulation at lesion sites around the animal's ears and increased clearance through the liver (**Fig. 3.4 e, Supplementary Fig. S1 and S6**). These results indicate that the presence of an albumin coating improves particle biodistribution and pharmacokinetic properties, while highlighting the importance of both size and surface characteristics for influencing probe accumulation.

3.5 Discussion

While SWIR based optical imaging has many advantages compared to traditional optical imaging modalities utilizing light in the visible and NIR regions, its clinical utility has been limited by a lack of effective materials. When compared to anatomical imaging modalities, optical imaging has the potential for safe, sensitive, and specific real-time imaging of biological features. Currently used SWIR emitting contrast agents have not leveraged these advantages to fully realize the potential for in vivo imaging applications. To address this need we have here developed non-toxic, brightly emitting rare earth nanoprobes with tailored SWIR emissions and evaluated their performance for *in vivo* imaging applications.

Here we have demonstrated real-time SWIR-based *in vivo* imaging. ReANCs proved capable of resolving anatomical structures including organs, tumors, and blood vessels millimeters into tissue using optical imaging. ReANCs have been shown to be capable of molecular-level imaging [69] and our current work describes the application of REs for real time imaging of anatomical features by exploiting the tissue transmission benefits of SWIR photons.

Critically, this work represents the first demonstration of *in vivo* SWIR imaging of malignant tumors using REs modified to target melanoma. By encapsulating these ceramic nanoparticles with FDA-approved human serum albumin, we were able to improve the bioactive properties of the probes, leading to improved pharmacokinetics and particle passive localization to tumors. Albumin encapsulation leads to nanocomposites with tunable size, and this technique can be used to improve the bioavailability of other inorganic contrast agents such as QDs for improved pharmacokinetics and tumor localization. Furthermore, albumin offers multiple available functional groups that can be conjugated to biomarker-specific targeting agents[69] as well as multiple drug binding site that can carry therapeutic compounds[88]. Thus, this work as generated a library of tunable, biocompatible SWIR emitting contrast agents and a novel imaging technology capable of being adapted to a variety of applications including deep tissue imaging and tumor detection.

3.6 Conclusion

SWIR emitting rare earth probes exhibit strong and tunable optical emissions. These rare earth particles can be encapsulated in human serum albumin to generate biocompatible, non-toxic probes that retain their optical emissions. The presence and size of the albumin coating has a great impact on particle *in vivo* pharmacokinetics and biodistribution, with 100 nm albumin

coating greatly increasing particle localization to well vascularized tumor sites, allowing for more sensitive detection of lesions. We hypothesize that the albumin coating can also be exploited in the future for targeted imaging or delivery of therapeutic payloads to generate theranostic particles capable of providing molecular level information on a tumor or lesion.

3.7 Supplementary Figures

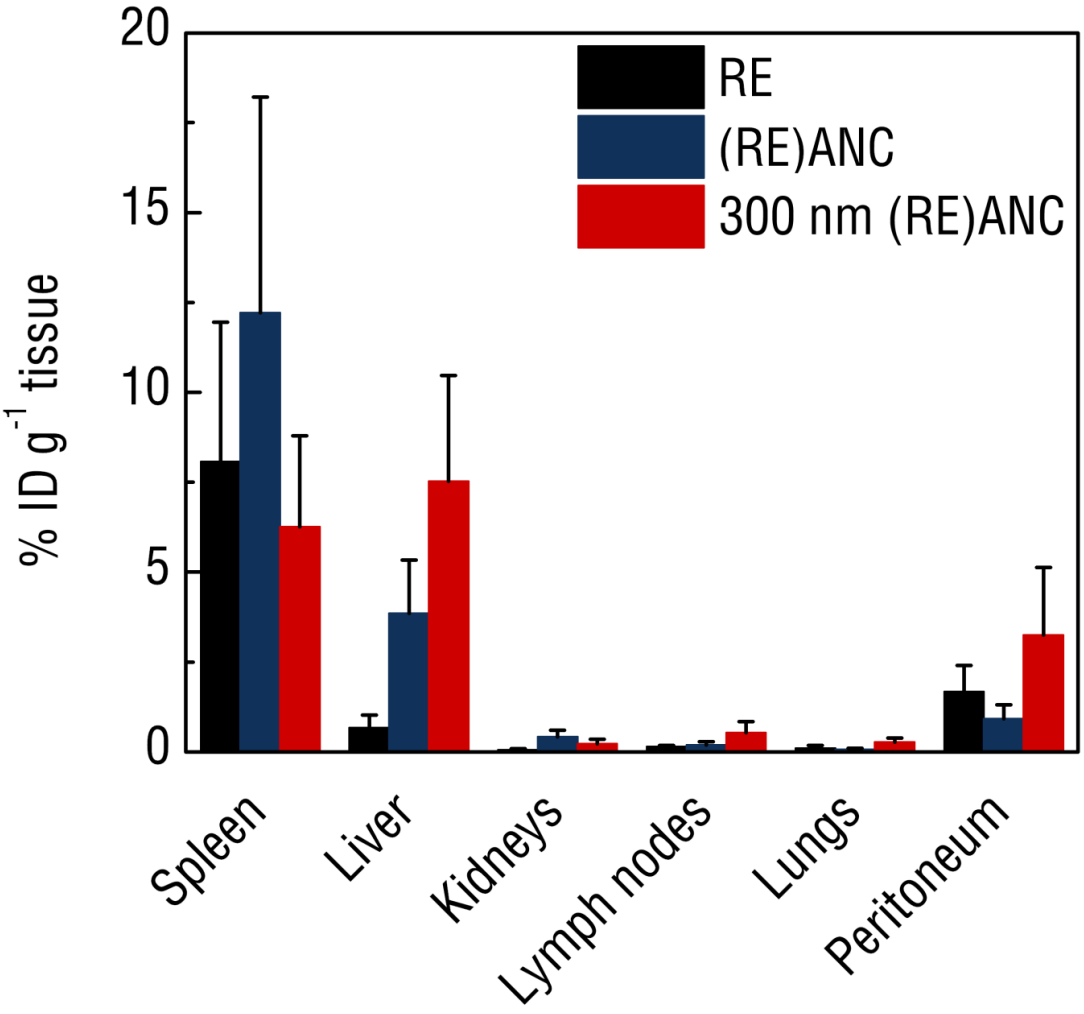

Supplementary Figure S1 – Organ biodistribution of formulations – REs and both formulations of ReANCs were injected IP into TGS mice. Animals were sacrificed and organs analyzed at 24 h post-injection by ICP-MS to reveal predominate accumulation in the spleen, liver and feces (*data not shown*). Blood, brain and heart displayed negligible yttrium presence (<0.1% ID g_{-1} tissue). Data shown in graphs are expressed as mean values ± s.e.m.; n = 5.

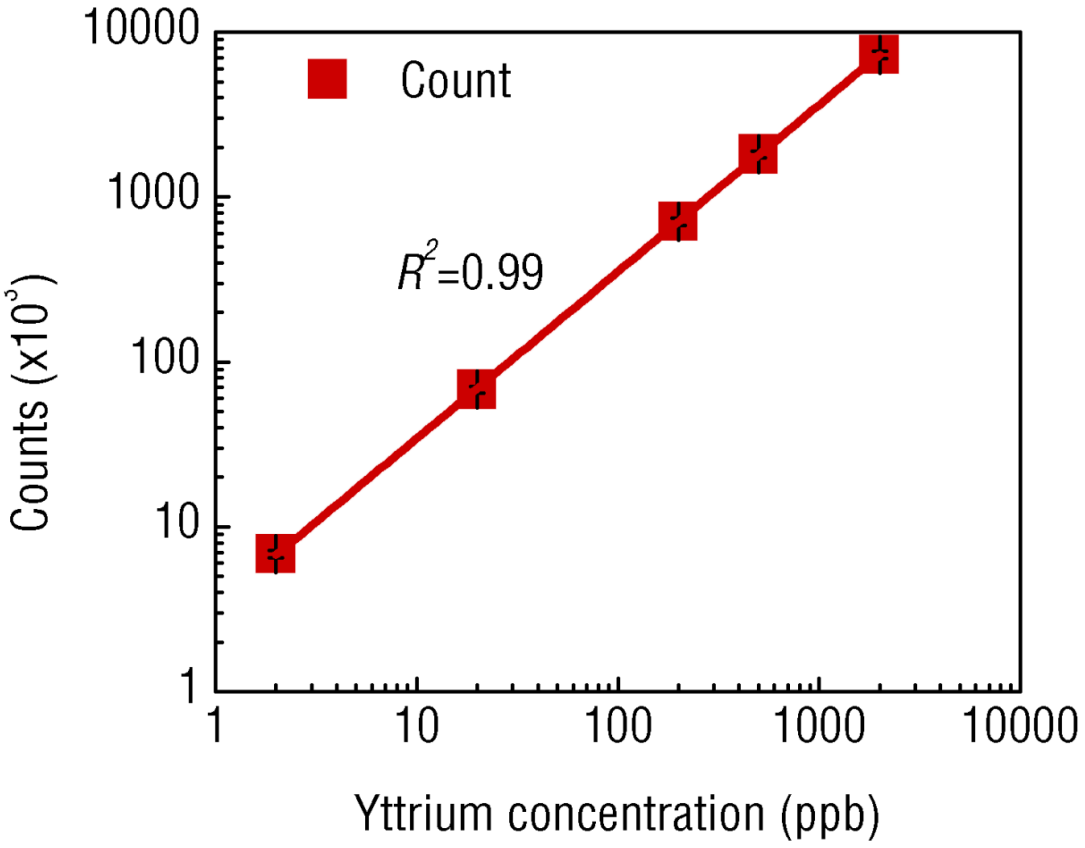

Supplementary Figure S2 – ICP-MS standard curves correlating yttrium concentration to count rate – A typical yttrium standard curve generated prior to tissue analyses shows linear correlation between yttrium concentration (ppb) and ICP-MS count rate. These standard curves were used to determine the yttrium concentration in the nanoparticle stock solutions and subsequent nanoparticle concentration in biological tissue.

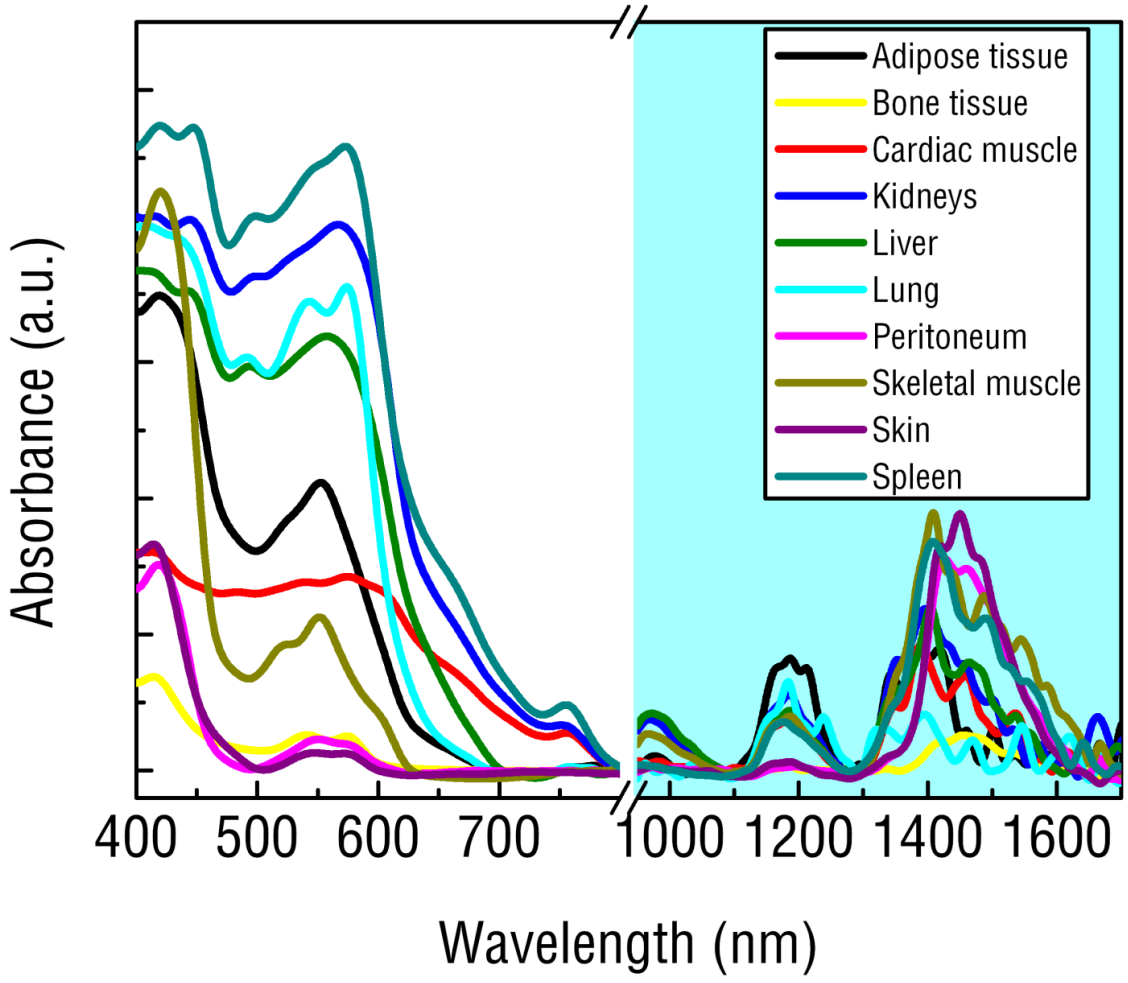

Supplementary Figure S3 – Absorbance and transmission properties of SWIR and visible light through various tissue samples – Absorbance spectra of various tissue components spanning from 400 to 1700 nm reveals a distinct region between 900-1300 and 1500-1700 nm exhibiting very low tissue absorbance. Note the break in the spectra from 800 to 900 nm is due to the spectrometer detector change.

a

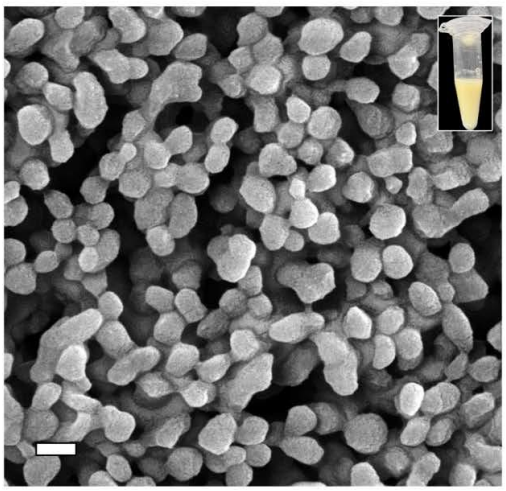

b

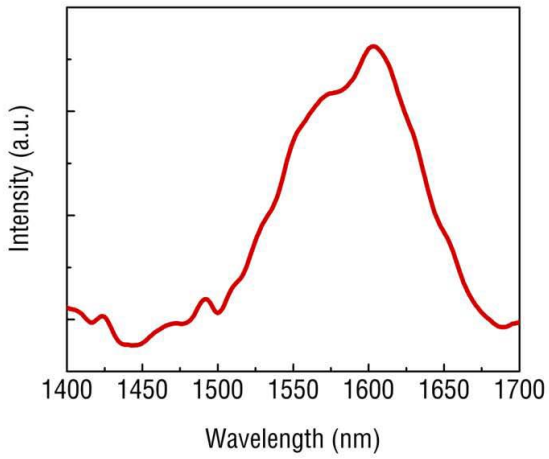

c

(RE)ANC Type	Lyophilized diameter (nm)	Hydrodynamic diameter (nm)	Polydispersity index	Zeta potential (mv)	RE content (μg ml^{-1})	Protein content (μg ml^{-1})
300 nm	100 ± 15	280 ± 9	0.12 ± 0.03	-13 ± 1.0	510 ± 40	3590 ± 90

Supplementary Figure S4 – Physical and optical properties of 300 nm albumin encapsulated rare-earth-doped nanoprobes – SEM images **(a)** of 300 nm ReANCs (scale bar = 200 nm). The 300 nm ReANCs retain the SWIR emission of the encapsulated REs **(b)**, exhibiting peak emission between 1550-1600 nm following 980 nm excitation. As with the smaller formulation of ReANCs, 300 nm ReANCs swell when hydrated, exhibit low polydispersity and negative zeta potential in PBS (pH 7.4) **(c)**. Data in **(c)** is expressed as mean values ± s.d.; n=5. Data for this figure was provided by Dr. Dominik Naczynski

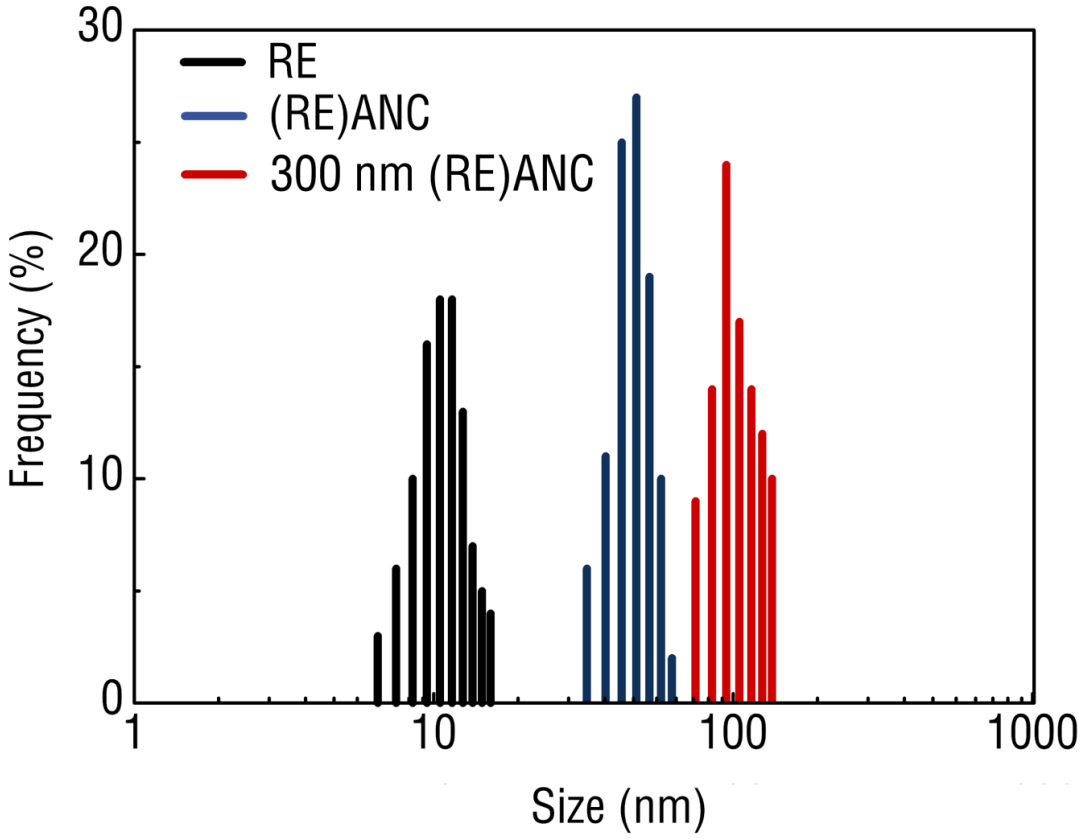

Supplementary Figure S5 – Size distribution of various formulations – Size distributions of the various formulations tested in TGS mice determined by SEM and TEM reveal three distinct size populations. The sizes of 100 nanoparticles was analyzed from electron microscopy images for each formulation. Data for this figure was provided by Dr. Dominik Naczynski

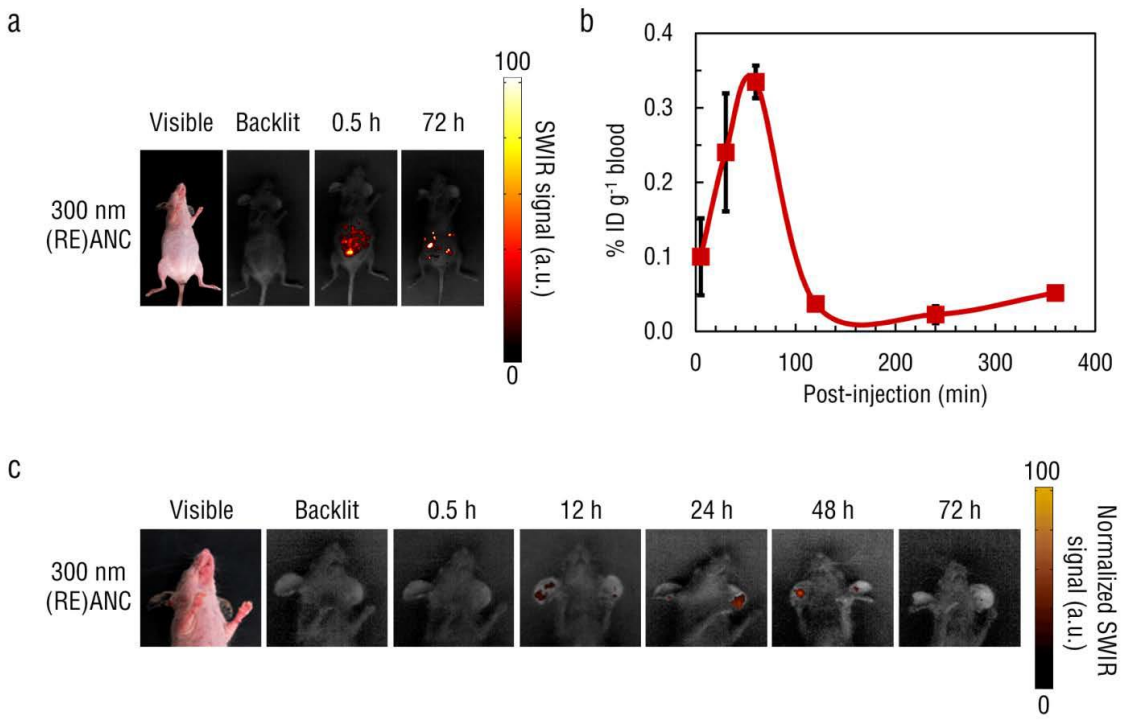

Supplementary Figure S6 – In vivo evaluation and clearance of 300 nm albumin encapsulated rare-earth-doped nanoprobes using SWIR imaging – SWIR imaging of 300 nm ReANCs after IP injection into TG3 mice **(a)** shows widespread fluorescence in the abdominal cavity which diminishes after 72 h. After IP injection of the 300 nm ReANCs, the concentration of yttrium reaches a maximum at 60 min in sampled blood **(b)**. Data in **(b)** are expressed as mean values ± s.e.m.; n = 3. The 300 nm ReANCs show some accumulation at tumor sites near the TG3 mice ears between 12-48 h post-injection **(c)** which could be detected with SWIR. Representative images (n = 3) viewed from the ventral aspect are shown in all instances.

CHAPTER 4

CXCR-4 TARGETED, SHORT WAVE INFRARED (SWIR) EMITTING NANOPROBES FOR ENHANCED DEEP TISSUE IMAGING AND MICROMETASTATIC CANCER LESION DETECTION

Note: This chapter have been reproduced with permission from the following publication:

Margot Zevon, Vidya Ganapathy, Harini Kantamneni, Marco Mingozzi, Paul Kim, Derek Adler, Yang Sheng, Mei Chee Tan, Mark Pierce, Richard E. Riman, Charles M. Roth, Prabhas V. Moghe. Cxcr-4 Targeted Swir Emitting Nanoprobes for Enhanced Deep Tissue Imaging and Micrometastatic Lesion Detection. *Small* 11: 6347–6357 (2015)[201]

4.1 Abstract

Realizing the promise of precision medicine in cancer therapy depends on identifying and tracking of cancerous growths in order to maximize treatment options and improve patient outcomes. However, this goal of early detection remains unfulfilled by current clinical imaging techniques that fail to detect diseased lesions, due to their small size and sub-organ localization. With proper probes, optical imaging techniques can overcome this limitation by identifying the molecular phenotype of tumors at both macroscopic and microscopic scales. In this study, we propose the first use of nanophotonic short wave infrared technology to molecularly phenotype small sub-surface lesions for more sensitive detection and improved patient outcomes. To this end, we designed human serum albumin encapsulated rare-earth (RE) nanoparticles (ReANCs) [69, 202] with ligands for targeted lesion imaging. AMD3100, an antagonist to CXCR4 (a chemokine receptor involved in cell motility and a classic marker of cancer metastasis) was adsorbed onto ReANCs to form functionalized ReANCs (fReANCs). Functionalized nanoparticles were able to discriminate and preferentially accumulate in receptor positive lesions when injected intraperitoneally in a subcutaneous tumor model. Additionally, fReANCs, administered intravenously, were able to target sub-tissue tumor micro-lesions, at a maximum depth of 10.5 mm, in a lung metastatic model of breast cancer. Internal lesions identified with fReANCs were 2.25 times smaller than those detected with unfunctionalized ReANCs ($p < .01$) with the smallest tumor being 18.9 mm^3. Thus, we present an integrated nanoprobe detection platform that allows target-specific identification of sub-tissue cancerous lesions.

4.2 Introduction

Breast cancer, the most common form of cancer among women, is a heterogeneous disease with substantial inter-individual variability in the molecular phenotypic expression.[203.]

Despite recent advances in treatment, 40% of breast cancer patients die as a result of distant site metastasis, commonly disseminated from the breast tissue to the patient's lungs, bones or liver.[204] Early detection of small metastatic populations in these organs is critical to reducing the burden of metastatic disease. Development of sensitive and specific methods for non-invasively identifying these cancerous lesions can aid in determining optimal treatment regimens and improving patient outcomes. Unfortunately, current diagnostic methods lack the sensitivity and specificity to provide actionable biological readouts during cancer therapy.[205, 206] Techniques such as MRI, ultrasound and PET/SPECT, though capable of anatomical imaging and detection of breast tumors, are limited by their high cost, lack of targeted contrast agents (MRI) and use of radionuclides (PET/SPECT). Hence, these techniques are unable to provide molecular information about lesions in a low cost, high-resolution platform, which is pivotal to determining treatment regimen and patient response to therapy.

Optical imaging is a promising technique for high resolution detection that can facilitate molecular classification of disease lesions and avoid the hazard of radionuclides used in PET/SPECT imaging. Novel optical imaging tools have the potential to aid clinicians in detecting small metastatic tumors and tracking pharmacological agents, facilitating selection of appropriate therapeutic agents for nascent lesions and monitoring of molecular responses to therapy. However, current optical imaging modalities are faced with several limitations. One important limitation is the small number of clinically approved contrast agents. An additional limitation of widely used fluorescent organic dyes is their poor photostability and low quantum efficiency, [207-209] and their excitation and emission in visible light wavelengths. These wavelengths are absorbed and scattered by tissues and thus are limited in their ability to penetrate biological materials. Signal from these fluorophores is further attenuated by tissue absorption and autofluorescence in this visible wavelength range, limiting the utility and

translational potential of the fluorophores. While the visible and near infrared wavelengths of light often used in biomedical optical imaging suffer from endogenous tissue autofluorescence, the short wave infrared range (1500-1700 nm) has less associated interference. This allows for improved detection of fluorescent moieties, greater sensitivity and improved penetration through biological tissue,.[210] Additionally, contrast agents with emissions in this range are frequently excited using NIR photons. Therefore, their excitation wavelength reduces associated tissue autofluorescence and scattering (as compared to UV and visible excitation wavelengths) leading to improved imaging.[211] Stable near-infrared emitting agents such as quantum dots and carbon nanotubes have shown promise for in vivo imaging, but do not achieve appreciable tissue penetration in vivo at biologically safe doses, limiting their clinical applicability.

To address limitations of existing technologies, in our previous work we have engineered optical nanoprobes as a new approach for detection of small sub-tissue cancerous lesions. These probes are based on ceramic nanoparticles doped with rare-earth (RE) cations that absorb near infrared (NIR) radiation to luminesce in the shortwave infrared (SWIR) spectrum (1000-3000 nm),[212, 213] emitting in the overlooked second “tissue transparent short-wave infrared window” of biological imaging.[182] Rare-Earth Albumin Nanocomposites (ReANCs), fabricated by encapsulating the RE nanoparticles within a human recombinant albumin shell, can be functionalized with ligands that complement cancer receptor markers. This functionalization results in imaging probes with selectivity to specific tumor molecular receptors.[69] Additionally, because of the hydrophobic nature of several binding pockets within the albumin shell, these probes exhibit high adsorptive capacity for small molecules pharmacologic drugs, and can be used for lesion-targeted delivery of antagonist molecules to cancers.[214]

In this study we investigated whether such functionalized nanoprobes could detect small cancerous lesions based on the combination of three key design features: the relative tissue transparency afforded by SWIR emitting nanoprobes, deeper tissue illumination potential of SWIR probes, and molecular targeting to cancerous lesion markers. Cancer targeting nanoprobes were generated by passive adsorption on albumin shells of AMD3100[215, 216] a hydrophobic small molecule inhibitor of the chemokine receptor CXCR4.[217-219] CXCR4 is strongly expressed on highly motile cancer cells, and has been previously used to target a PET imaging agent that localizes to metastatic lesions in the lungs.[220] CXCR4-targeted, AMD3100 functionalized nanoprobes preferentially accumulate withing receptor positive cells and tumors allowing for more sensitive detection of small-scale lung lesions in an in vivo metastatic breast cancer model (**Figure 1)**. This is of particular clinical relevance as CXCR4 has previously been indicated in the site specific invasion and metastasis of breast cancer cells to the lungs, and is correlated to decreased survival time and poor prognosis.[218] Strikingly, the cancer targeted probes enabled imaging of microlesions (~25 mm^3) in the lungs at a depth of approximately 1 cm while allowing for simultaneous molecular identification of the tumor population phenotype.

4.3 Results

4.3.1 Synthesis and characterization of nanoparticles

Rare earth nanoparticles were synthesized via burst nucleation as previously described. Nanoparticle structure consisted of a $NaYF_4$ core doped with ytterbium (Yb) and erbium (Er) coated in an undoped shell. Dopants were found to comprise 30% of the total nanoparticle atomic weight. Lifetime emissions scans revealed that the calculated delay time for the particles 1530 emissions was found to be 3.55 ms (**Supplementary Figure 1**). Rare earths were

incorporated into albumin nanocomposites (ReANCs) by solvent induced controlled coacervation of albumin.[69, 202] Hydrodynamic diameters of ReANCs were determined using dynamic light scattering (DLS) (**Figure 2A**), which revealed monodisperse particle populations. The yield of ReANCs was found to be approximately 70% by BCA protein assay.

4.3.2 Cancer-Targeting Probes: AMD3100 Functionalized ReANCs (fReANCs)

Functionalized ReANCs (fReANCs), namely, ReANCs targeting the CXCR4 receptor over-expressed on motile cancer cells, were generated by adsorbing AMD3100, a small molecule antagonist of CXCR4, onto the ReANC surface (**Figure 1A**) by exploiting the native drug binding pockets on human serum albumin.[221] The particles were characterized to determine the effect of functionalization on the physical properties of the probes. fReANCs were somewhat larger than unmodified ReANCs (5-35 nm increase in diameter depending on loading concentration), with marginally but not statistically significant greater polydispersity (**Figure 2A**). Emission spectra for albumin coated ReANCs have been previously reported, showing that albumin encapsulated rare earth particles exhibit detectable SWIR emissions.[69] The adsorption of AMD3100 onto the albumin surface had a slight dampening effect on SWIR emissions; nonetheless, fluorescence was strong enough to be resolved via the current imaging prototype **(supplemental figure 1).**

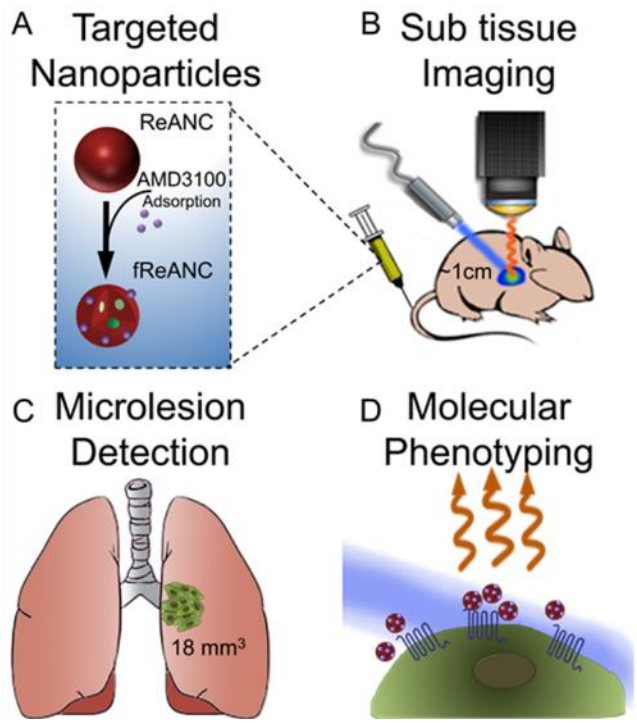

Figure 4.1: Design, fabrication, and preclinical efficacy of rare earth nanoprobes.

ReANCs were synthesized by controlled coacervation of albumin monomers in solution and REs dissolved in a solvent. (A) AMD3100 was adsorbed onto the surface of fully formed ReANCs to generate AMD3100 functionalized ReANCs, or fReANCs. (B) Athymic nude mice were inoculated with human breast cancer cells through the tail vein. Animals were treated with either ReANCs or fReANCs and SWIR imaging performed to determine nanoprobe-tumor localization. fReANCS were imaged in tumors up to 1 cm into the animal (B). Microlesions as small as 18 mm^3 were detected with targeted probes (C). Probe localization to receptor positive tumors enabled optical molecular phenotyping (D).

Scanning electron microscopy (SEM) of ReANCs and fReANCs revealed spherical populations indicating successful adsorption, as evidenced by a change in surface texture with varying concentrations of AMD3100 (**Figure 2B-E; Supplementary Figure 1)**. Loading efficiency was validated by HPLC and was determined to be dependent on the amount of AMD3100 introduced, ranging up to 70% **(Figure 2A**). Scatchard analysis of the loading data revealed a binding affinity of K_d=1.8x10^{-7} M. This value is comparable with binding of drug moieties such as paclitaxel to albumin indicating that drug binding activity is retained by albumin in a nanoshell form.[222] Additionally, AMD3100 loading of ReANCs had no significant effect on the viability of MDA-MB-231 breast cancer cells **(Figure 2F).**

A

NP Formulation	AMD3100 Loaded (μM)	Hydrodynamic Diameter (nm)	Polydispersity	Loading Efficiency (%)
ReANC	--	99.6 ± 4.5	0.14 ± .04	--
fReANC 1	12.5	135.6 ± 1.5	0.18 ± .05	30.0
fReANC 2	1.25	121.6 ± 1.2	0.20 ± .04	57.5
* fReANC 3	0.125	117.6 ± 1.9	0.17 ± .04	69.3
fReANC 4	0.037	106.2 ± 3.2	0.21 ±.05	--

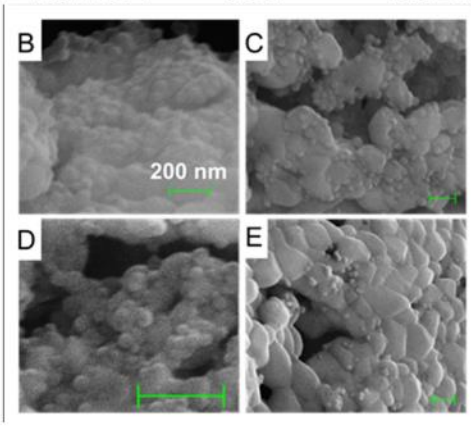

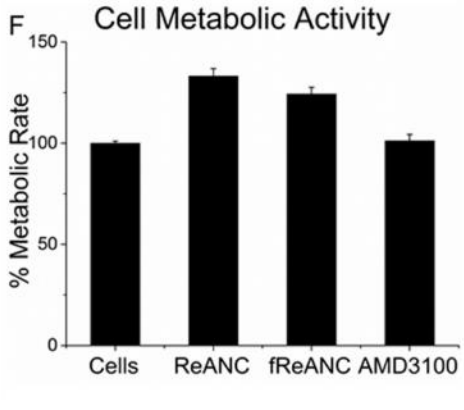

Figure 4.2: Characterization of functionalized Rare Earth Nanoprobes. (A) fReANCs were synthesized by adsorbing AMD3100 onto fully formed ReANCs. Both populations had narrow size distributions and low polydispersity index. The formulation used for in vivo studies is as indicated with asterisk. (B) Scanning election microscopy (SEM) of fReANCs revealed spherical particles. The addition of AMD3100 at concentrations of 12.5 µM (B), 1.25 µM (C), 125 nM (D) and 37.5 nM (E) yielded an increase in granulated surface texture directly proportional to the loading concentration. Drug loading efficiency (last column) was determined using HPLC as described in methods section. Cellular treatment with REANCs, fReANCs or free drug did not have an effect on cell metabolic activity (F), suggesting that the nanoprobes are non-cytotoxic. (F) Error bars denote standard deviation (n = 3), $p < .05$

4.2.3 Active receptor targeting of fReANCs

Effective targeting of fReANCs was determined by cellular association of AMD3100 functionalized probes using three breast cancer cell lines with varying levels of CXCR4 expression: 1) 4175-TR (a highly aggressive, lung-tropic subpopulation of the MDA-MB-231 cancer cell line[223]) with low CXCR4 expression, 2) MDA-MB-231, with moderate levels of CXCR4 expression, and 3) MCF-7, with relatively high levels of CXCR4 expression,[224] We observed a 3-fold increase in cellular association of fReANCs when compared to ReANCs by both receptor positive cell lines as determined by flow cytometry, with no significant change in association with receptor negative 4175-TR cells **(Supplementary Figure 2 and Figure 3A, 3B, and 3E)**. Based on cell surface binding and cytotoxicity studies, the optimal concentration for loading REANCs was determined to be 125 nM. Confocal microscopy showed that nanoprobe internalization of both ReANCs and fReANCs occurred within 24 hours, with nanoprobes distributed in a punctate pattern throughout the cell cytoplasm and the increased intracellular

fluorescence signal leading to overall increased signal in each individual cell. **(Figure 3C and 3D; Supplementary Figure 3).**

4.2.4 In vivo SWIR imaging

Tumor-Specificity of Targeted Nanoprobes:

The ability of the functionalized probes to discriminate between receptor-positive (MDA-MB-231) and receptor-negative (4175-TR) lesions in vivo was assessed using nude mice bearing palpable bilateral subcutaneous tumors. Animals were treated with a bolus dose of 200 µL (10 mg kg^{-1}) of either unfunctionalized ReANCs or fReANCs into the intraperitoneal cavity (i.p. administration). Immediately following injection of the particles, SWIR emissions were visualized in the abdominal cavity around the site of injection. The fReANCs cleared much more rapidly from the site of injection than the ReANCs, which were retained in the peritoneal cavity up to 48 hours post administration (data not shown).

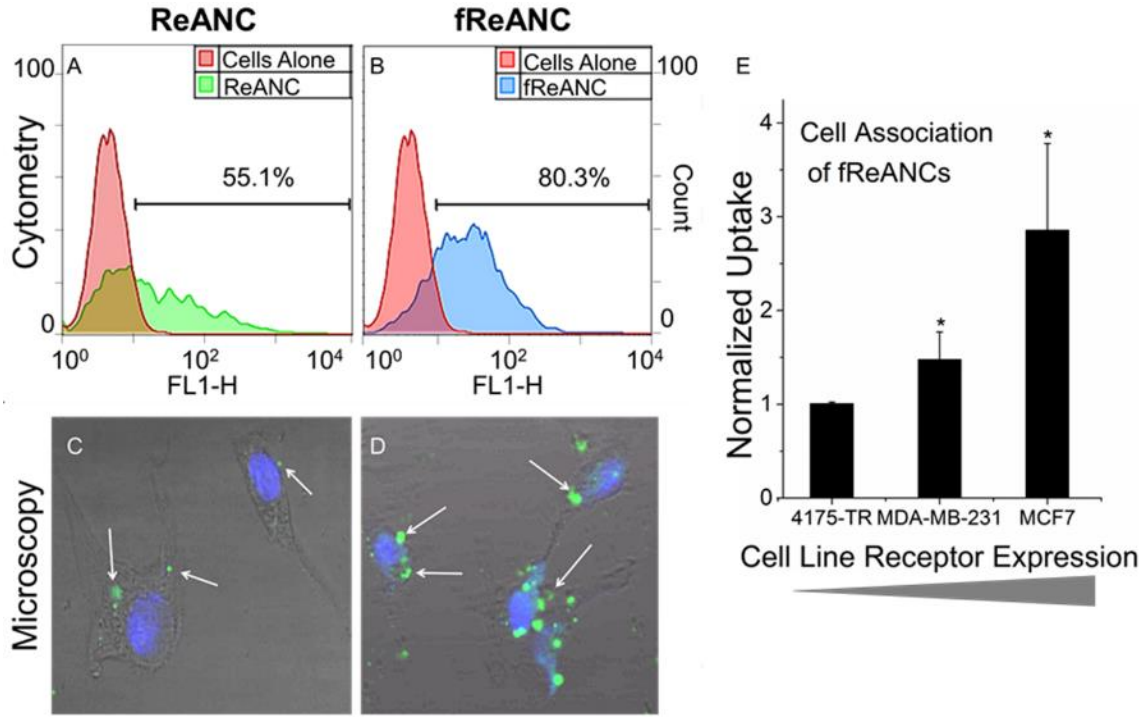

Figure 4.3: Active Cancer Targeting of Rare Earth Nanoprobes. Cellular uptake and association between ReANCs (A) and fReANCs (B) by MDA-MB-231 breast cancer cells was analyzed by flow cytometry for up to 24 hours. Functionalization increased particle uptake as determined by FACS. This was confirmed with confocal imaging of receptor positive cells treated with ReANCs (C) or fReANCs (D) for 24 hours. White arrows indicate nanoparticle fluorescence. While ReANCs showed some cellular association, the degree of nanoprobe association was greater with the functionalized constructs. Quantitative flow cytometry analysis revealed that nanoprobe association increased with greater expression of the targeted CXCR4 receptor (E). Error bars denote standard deviation for $n = 3$. * $p < .05$ (t test, comparing between ReANC and fReANCs groups)

SWIR fluorescence was detected 24 h after fReANCs administration at the receptor-positive, left dorsal tumor (**Figure 4B and C**). This was in contrast to little or no SWIR signal seen with ReANC administration (**Figure 4A**). Additionally, little SWIR signal was observed with fREANC administration from the receptor-negative (4175-TR derived) right dorsal tumor **(Figure 4B and C)**. Ex-vivo SWIR imaging also revealed irregular fluorescence patterns surrounding the receptor positive tumor validating tumor-specificity of our nanoprobes in vivo, indicated by white arrows **(Figure 4E).** There was no fluorescence associated with the receptor negative tumors excised from the animals' right flank **(Figure 4F and 4G)** or the receptor positive tumors treated with ReANCs **(Figure 4D).**

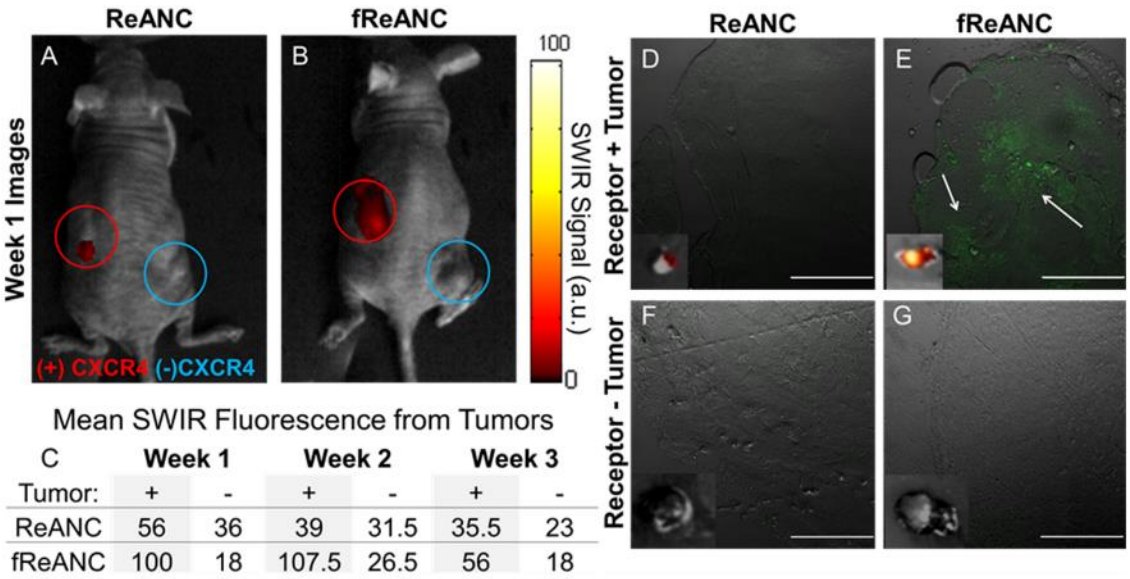

Mean SWIR Fluorescence from Tumors

C	Week 1		Week 2		Week 3	
Tumor:	+	-	+	-	+	-
ReANC	56	36	39	31.5	35.5	23
fReANC	100	18	107.5	26.5	56	18

Figure 4.4: Functionalized nanoprobes are capable of molecular discrimination of tumors in vivo. The ability of targeted constructs to molecularly target in vivo lesions was evaluated using nude mice bearing bilateral, subcutaneous, dorsal tumors derived from human breast cancer cells. Receptor positive MDA-MB-231 cells (Red open circle) were injected into the left dorsal flank, while receptor negative 4175-TR cells (Blue Open circle) were injected on the right. Unfunctionalized ReANCs (A) showed little associated red SWIR fluorescence at either lesion sites, while fReANCs (B) had red SWIR fluorescence associated with only the receptor positive tumor. The maximum SWIR values for each region of interest (C) show that fReANCs accumulated preferentially to the receptor positive left tumor. *n* = 2. (D-G insets) *Ex vivo* SWIR imaging revealed SWIR fluorescence associated with the receptor positive tumor treated with fReANCs. Excised tumors treated with (D, F) ReANC and (E, G) fReANC were sectioned and imaged to determine nanoprobe localization (green fluorescence) within the tumor mass. Scale bars represent 500 µm. Representative images from week 1.

Strikingly, the receptor-positive tumors were 4x smaller than the receptor-negative tumors **(Figure 4D-G insets).** This indicated that fReANCs possess the ability to detect and target small, poorly vascularized tumor microlesions. The maximum SWIR signal elicited with fReANCs was observed at 1-2 weeks of tumor growth and then declined, which may correlate with a decrease in CXCR4 expression as the metastasis develops into a mature tumor. These results validated the ability of targeted fReANCs to molecularly phenotype tumors in vivo.

Additionally, there was no overt toxicity from injection of the particles, and the particles were cleared 72-96 h post injection to non-detectable levels in the mouse (data not shown). Repeated injections of REANCs and fReANCs over time did not lead to toxicity as evidenced by uniform body weight over the course of the 11 week study **(Figure 5A)** and by lack of distress signals exhibited by the animals, as determined by the IACUC monitoring.

4.2.5 Histopathological analysis of Nanoparticle Biocompatibility

At experimental endpoints, animals were sacrificed and organs of clearance (liver and spleen) were analyzed for toxicity due to the administered ReANCs. Analysis of H&E sections revealed no alterations suggestive of toxicity when compared to untreated controls **(Figure 5B and C)**. Lung sections, obtained from lesions from the lung tumor model described in later sections, revealed a high degree of tumor burden **(Figure 5E)**. Notably, administration of ReANCs to control animals did not show overt toxicity or changes in lung architecture on H&E staining (**Figure 5D**). Taken together these results support the biocompatibility of the targeted-nanoprobes and their utility to detect microlesions and enable real-time imaging of tumors.

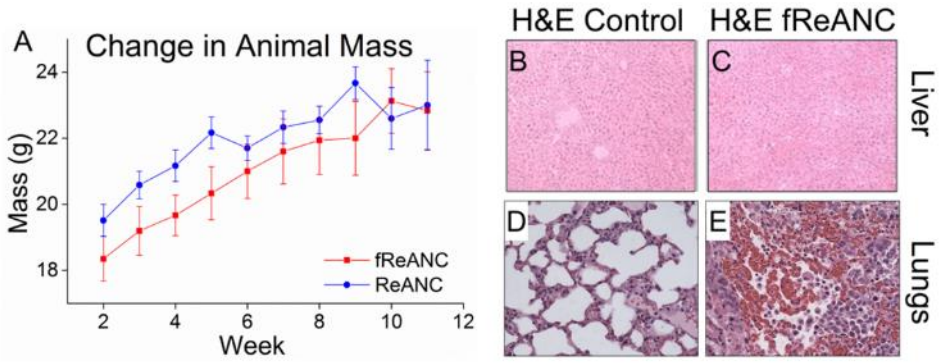

Figure 4.5: Rare-Earth nanoprobes proved safe for long-term use with no significant impact on animals' weight or damage to organs of accumulation. Animal's body weight was recorded weekly over the course of the experiment (A) and animals were closely monitored for any signs of distress. Repeated injections were well tolerated by animals. Animals' livers were excised and examined to determine changes in the organ's structure with no (B) and fReANC (C) treatment. Analysis showed no change in the liver's integrity with dosing. Lung sections, from fREANC treated animals showed tumor infiltration in tumor bearing animals (E) and no morphological change in the control healthy animals (D) confirming the safety of the nanoprobes. *n* = 6.

4.2.6 Ex vivo SWIR Imaging

Following necropsy, *ex vivo* SWIR imaging of tumors and organs revealed SWIR fluorescence associated with the livers of animals given i.v. injections of both ReANCs and fReANCs. E*x vivo* analysis of animals that received intra-peritoneal injections of the particles showed SWIR fluorescence in the major organs of clearance (spleen and liver) for both ReANC and fReANC treatment groups (**Supplementary Figure 4**).

Excised tumors were sectioned and imaged with confocal fluorescence microscopy to determine the localization of the nanoprobes within the tumor interstitium. Analysis of receptor positive tumors treated with fReANCs revealed a punctate pattern of nanoparticles distributed throughout the tumor mass (**Figure 4E and Supplementary Figure 5).** *Ex vivo* results thus far confirmed that the targeted fReANCs are able to molecularly phenotype lesions in vivo.

4.2.6 In vivo detection of tumors in internal organs with SWIR imaging

We assessed the ability of the SWIR nanoprobe imaging approach to locate tumors in sub-tissue organs using female athymic nude mice bearing lung tumors in an established model of metastatic breast cancer.[225-227] One of the most significant observations was that the nanoprobe-related SWIR signal was detectable up to 10.5 mm into the animal. Animals were treated with 200 µL of unfunctionalized ReANCs or fReANCs (10 mg kg^{-1}) via i.v. administration and imaged up to 24h post-injection and yet no toxicity was associated with repeated use of probes. SWIR fluorescence was distinguishable in animal's livers immediately after injection. Notably, we obtained discernible SWIR signal using fReANCs in the lungs as early as three weeks following the inoculation of tumor cells (**Figure 6D**), compared to unfunctionalized ReANCs (**Figure 6B and 6C)** where signal was observed approximately 7 weeks post-inoculation. Preferential accumulation of fReANCs in tumors within lungs is indicated by the combination of enhanced lung-related and depressed liver-related signal in fReANC treated animals as compared to unfunctionalized, ReANC treated animals (**Figure 6D and 6E**). In particular, as shown in **Figure 6D**, fReANC accumulation in lungs increased significantly from week 2 after inoculation to week 4 after inoculation, which was in correlation with the increase in tumor volume.

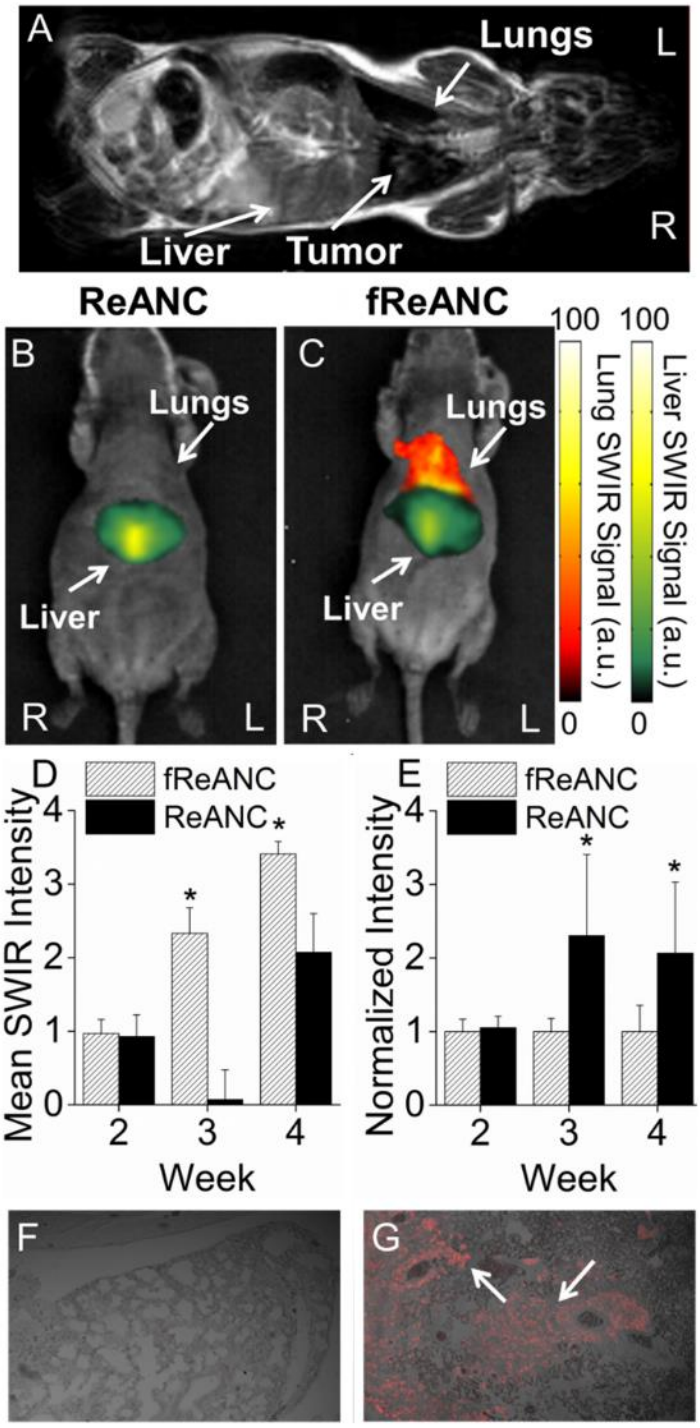
A
Lungs
L
Liver
Tumor
R
ReANC
fReANC
B
Lungs
Liver
R
L
C
Lungs
Liver
R
L
100
100
Lung SWIR Signal (a.u.)
Liver SWIR Signal (a.u.)
0
0
D
fReANC
ReANC
Mean SWIR Intensity
Week
E
fReANC
ReANC
Normalized Intensity
Week
F
G

Figure 4.6: Targeted fReANCs allow for detection of microscale lung lesions. Nude mice were inoculated i.v. with CXCR4 expressing MBA-MB-231 cells. Cells colonized in the lungs and were monitored using MRI (A). Xenograft mice were administered either ReANCs (B) or fReANCs (C) at early stages (< 6 weeks) after inoculation. SWIR signal from the lung region was quantified at 24 h (D) post-injection. The fReANC associated SWIR signal was greater than the ReANC signal for early time-points, correlating to the presence of microlesions quantified by volumetric reconstruction of the MRIs. The SWIR signal from the liver was quantified for 0 h post injection (E) and showed a 2 fold increase in ReANC accumulation in the organs of clearance. Representative images (n=6) shown in all instances from week 3 of the study. The presence of tumors in the lungs was confirmed with vimentin staining of healthy (F) and tumor bearing (G) lungs, with the red fluorescence marked by arrows indicating tumor cells. (D) Error bars indicate SEM for $n = 6$. * indicates $p < .01$ (Wilcoxson Rank-Sum test) (E) * = $p < .05$ (Wilcoxson Rank-Sum test)

Tumor burden and depth of lesions relative to the surface of the animal were determined by bi-weekly MRI from time of inoculation of tumor cells **(Figure 6A; Representative MRI)**. An especially significant outcome was that the tumors detected using fReANCs were found to be 27.8 mm^3 in volume on average with the lowest tumor volume detectable being 18.9 mm^3 **(Figure 7B and C**). In contrast, tumors detected with ReANCs were an average of 62.6 mm^3 (2.25 times larger than those resolved with the functionalized particles) with a tumor minimum volume of 55.6 mm^3 **(Figure 7A and C)**. Tumors were located 7-10 mm from the surface of the animal. SWIR fluorescence and MRI images were overlaid (data not shown) to determine particle accumulation at lesion sites, confirming that the SWIR signal was associated with the lesions. The volumetric analysis reveals that fReANCs, in addition to detecting tumor lesions in

sub-tissue earlier than ReANCs, are also able to resolve micro-lesions approximately 2.25 times smaller than those detected by ReANCs **(Figure 7).** *Ex vivo* analysis of excised organs revealed SWIR signal from multiple lesions in the lungs and chest wall **(Supplementary Figure 4)**, thus establishing the tumor-specific targeting ability of fReANCs in the lung model

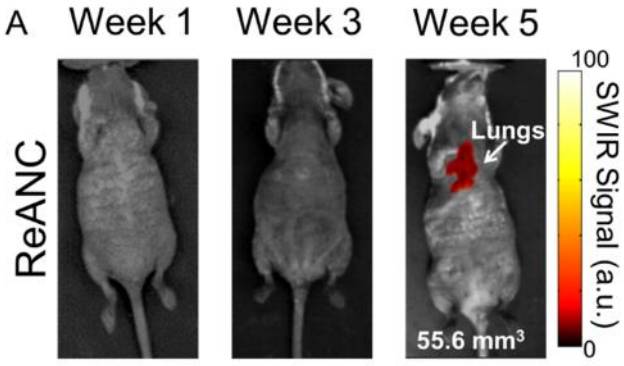

C	Mean Tumor Volume(mm^3)	Lowest Tumor Volume(mm^3)
ReANC	62.6 ± 8.1	55.6
fReANC	27.8 ± 8.5	18.9

Figure 4.7: Longitudinal tracking of internal lesions with SWIR imaging. SWIR fluorescence images were taken each week for animals treated with both ReANC (A) and fReANC (B). Tumor burden was determined each week through MRI and compared to SWIR signal. Mean and minimum volume (C) of tumors detectable via SWIR imaging was calculated to determine the smallest tumors capable of resolution using the InGaAs camera. Treatment with fReANCs enabled detection of tumors on average 2.25 times smaller than those detected using ReANCs. (n=6)

Ex vivo tumors were analyzed for presence of infiltrating tumor cells by immunohistochemical staining for vimentin, a tumor-cell specific marker **(Figure 6F and 6G)**. Taken together, these results confirm the ability of fReANCs to detect small (< 30 mm^3) tumors up to 1 cm into biological tissue.

4.3 Discussion

Breast cancer, one of the most common causes of cancer death among women, is difficult to treat due to the frequency of micrometastatic populations that are phenotypically distinct from the parent tumor. It is therefore of critical importance to develop technologies capable of safe and sensitive detection and characterization of small sub-tissue tumors, based on their distinct molecular phenotype, with accurately defined margins. This study provides the first proof of concept model for optical-probe based molecular detection of sub-tissue micro-lesions. Here we demonstrate cancer-targeted SWIR emitting fREANCs target CXCR4-positive tumors in a bilateral tumor model of receptor-positive and negative tumors. Specifically, fREANCs are also shown to molecularly target CXCR4-positive tumors that are 4X smaller than receptor-negative tumors. The most significant observation from this study was the ability of cancer-targeted nanoprobes to detect sub-tissue lesions at a depth of approximately 1 cm and also to resolve micro-scale lesions. fREANCs were able to resolve tumors as small as 18.8 mm^3 compared to lesions that were 62.6 mm^3 detected by control REANCs.

SWIR emitting rare-earth albumin nanocomposites have previously been shown to be effective in vivo contrast agents that passively accumulate at the site of malignant lesions, possibly due to the enhanced permeability and retention (EPR) effect, allowing for imaging in vivo.[202] However, imaging of metastatic micro-lesions present additional challenges as the malignancy has not yet established its own vasculature to enable passive targeting. Prior work

has shown that active targeting of nanoparticle based contrast agents to a specific disease marker can greatly improve their localization to targets of interest.[228, 229] Active targeting of contrast agents has been shown to improve particle biodistribution, improve signal-to-noise ratio, provide molecular information about a region of interest, and increase the optical signal allowing for more sensitive imaging.[165, 230-235] Here, we have designed and characterized a novel targeted imaging probe consisting of rare-earth doped phosphors and human serum albumin onto which is adsorbed AMD3100 as the targeting ligand.

The approach to targeting of the ReANCs was designed based on the native drug binding properties of human serum albumin.[221, 236] HSA has been shown to simultaneously bind multiple distinct moieties at various 'drug binding pockets' across its surface.[221] Albumin nanocarriers retain the ability to strongly bind multiple therapeutic agents with little loss of efficacy.[214, 236] We utilized this property to adsorb AMD3100 as a targeting ligand onto the surface of the particles for tumor cell targeting with a high (up to 70%) efficiency of loading and affinity (K_d=1.8x10^{-7} M) owing to the several albumin drug binding sites within a nanoshell. The loading efficiency and binding affinity were found to be similar to reported values for albumin loading with other small molecule therapeutics such as paclitaxel and doxorubicin.[222] The resulting nanoprobe localization, combined with the sensitivity of an in-house SWIR imaging system, enables detection of small internal tumors with high specificity.

The fReANCs were synthesized and loaded with varying concentrations of the small molecule antagonist, AMD3100. fReANCs not only showed improved association with receptor positive MDA-MB-231 and MCF7 cells in vitro but also exhibited a lack of association with receptor negative MDA-4175 cells, with no appreciable effect on cell viability. This effect was largely independent of bound AMD3100 concentration on fReANCs (**Supplementary Figure 2**),

suggesting that the particles with modest net loading and a maximum loading efficiency (approximately 70% by HPLC) could provide efficient targeting selectivity. Confocal fluorescence microscopy of fReANCs' association with malignant cells confirmed visually the increased association of fReANCs when compared to unfunctionalized ReANCs.

Proof of concept studies in a mouse xenograft breast cancer model showed tumor-specific binding of fReANCs to receptor-positive tumors and successful targeting of tumors that were 4x smaller than the corresponding receptor negative tumors. This clearly highlights the ability of fReANCs to accurately detect and molecularly phenotype early tumor lesions. Future longitudinal studies will address the ability of molecularly targeted ReANCs in tumor-dynamic tracking. It is important to note that fReANCs were able to accumulate in tumors enabling detection in contrast to unfunctionalized ReANCs that post-injection cleared immediately to the liver.

Thus far, one of the hurdles faced by optical imaging agents has been their inability to be resolved deeper for detection of lesions in internal organs.[237-239] Notably, targeted fReANCs were able to resolve lesions as small as 18.9 mm^3 in the lungs of tumor bearing animals, with a depth of penetration of 10.5 mm through the tissue. Furthermore, the preferential accumulation in lung lesions was seen up to 24 h post-injection with little loss in SWIR signal. Future studies using large animal models will need to address improvement in depth of penetration using these probes to clinically acceptable depths. A limitation of near infrared excitation is localized photothermal effects.[240] Due to strong absorption of 980nm photons by water molecules, prolonged exposure of tissue to NIR wavelengths can induce non-localized temperature fluctuations.[241, 242] This effect can be mitigated by limiting the exposure of near infrared light to the skin. Thermal heating effects are typically generated after

minutes of exposure at a high laser power (from 3-6 W cm^{-2}).[243, 244] In contrast, the system presented here requires an intensity of only 1.7 W cm^{-2} with seconds of exposure. By limiting laser power and duration it is possible to circumvent detrimental effects on biological tissues post exposure.

Of significance is the fact that we were able to perform real-time imaging with no observed toxicity for a period of 11 weeks, as shown by consistent body weight and the lack of pathological evidence of toxicity in major organs of clearance such as the liver and spleen. Both nanoparticle formulations cleared completely from the animal's body within 7 days. There was no apparent difference in organ accumulation between the functionalized and unfunctionalized particles (**Supplementary figure 4**). Since athymic nude mice used in this study lack a robust immune system, studies to validate lack of immunogenicity and toxicity to establish safety profile of the probes will be done in immunocompetent mice.

Emergent patient therapy towards metastatic disease is currently centered on a molecularly targeted therapeutic strategy.[245] Several recent preclinical studies have provided proof of concept that early targeting of metastasis-specific signaling pathways can result in enhanced therapeutic responses. [143, 165, 225, 226, 246] Implicit in the precision medicine approach is the need for cost-effective, safe and easy to use molecular diagnostic agents. Targeted nanoprobes from this study exhibit translational potential to monitor tumor progression, molecularly phenotype tumors and provide physicians with a diagnostic tool to make improved choices for tailored therapy and monitor in real-time response to therapy.

4.4 Conclusion

The albumin nanoshells utilized in this work show a high affinity and capacity for ligands and upon functionalization are capable of cellular discrimination based on receptor phenotype in vitro. Functionalized nanoprobes are able to preferentially localize to receptor positive tumors in mice, allowing for detection of positive tumors 4x smaller than receptor negative tumors. The most significant observation of clinical importance from this study was the ability of functionalized nanoprobes a) to detect sub-tissue microlesions approximately 1 cm from the imaging surface and b) to resolve microlesions as small as 18.9 mm^3 when compared to 2.25 times larger lesions detected by ReANCs. The safety profile of both fReANCs and ReANCs, as indicated by no overt toxicity during the course of the study, is an added benefit for plausible clinical applicability of these agents.

4.5. Experimental Methods

Reagents: AMD3100 was purchased from EMD Millipore (Billerica, MA, USA) and used without further modification.

Cell Culture: MDA-MB-231, MCF7 (ATCC, Manassas, VA) and MDA-MB-231 derived 4175-TR cells (kind gift from Dr. Yibin Kang, Princeton University, USA) were cultured in DMEM (ATTC, Manassas, VA) supplemented with 10% FBS and 1% penicillin-streptomycin (Invitrogen, Carlsbad, CA, USA) at 37°C in an atmosphere of 5% CO_2.

ReANC Fabrication*:* ReANCs were synthesized as previously described.[69, 202] Briefly, 2% (w/v) solution of human serum albumin (Sigma-Aldrich, St. Louis, Mo) was dissolved in NaCl (2 mM) and the pH was adjusted to 8.50 ± 0.05 with NaOH (.1 M). Under continuous stirring at 700 rpm at room temperature, ethanol (2 mL) sonicated with rare-earth nanoprobes (0.2 mg mL^{-1}) was added at 1.5 mL min^{-1} to the HSA solution (500 µL) with a syringe pump

(Harvard Apparatus PHD 2000, Holliston, MA). Subsequently glutaraldehyde (2.34 µL) (Sigma-Aldrich, St Louis, Mo) was added to the suspension as a cross-linker following ethanol addition and particles were allowed to crosslink overnight. Particles were then purified by 3 cycles of centrifugation at 48,400 g. Particles were characterized by BCA assay (Pierce Biotechnology, Rockford, Il) to determine % yield. DLS was performed to determine particle size and polydispersity.

Preparation of functionalized nanoparticles (fReANCs): AMD3100 (EMD Millipore, Darmstadt, Germany) was dissolved in sterile water (1 mg ml^{-1}) and was added into a suspension of ReANCs in PBS+1 mM EDTA to yield final concentrations ranging from 0.0125-12.5 µM. AMD3100 adsorption was achieved by constant agitation of samples at room temperature for 3h followed by purification through centrifugation. AMD3100 functionalized ReANCs (fReANCs) were characterized as described above.

Quantification of loading: The concentration of AMD3100 loaded on ReANCs was determined via high-performance liquid chromatography (HPLC, Beckman Coulter Model 166, Brea, CA) used with a Luna C18 column (3 µm, 100 x 4.6 mm i.d., Phenomenex, Torrance, CA). Briefly, the functionalized fReANCs were flash frozen and lyophilized for 48 hours. The powders were re-suspended in water and assayed on HPLC to determine AMD3100 concentrations. For chromatographic elution the flow rate was 1 mL $minute^{-1}$. The mobile phase consisted of 0.1% TFA in de-ionized water and acetonitrile. AMD3100 was detected at 212 nm. Binding affinity between albumin nanoparticles and AMD3100 was determined via scatchard analysis: The ratio of bound/free ligand was determined for various concentrations of ligand from the HPLC data and plotted against the amount of ligand loaded onto the particles. Slope of the resulting best fit line was used to determine the particle dissociation constant.

In Vitro cellular uptake of fReANCs: MDA-MB-231, MCF-7, and 4175-TR cells expressing different relative amounts of CXCR4 were seeded onto 96-well microtiter plates at a density of $5x10^5$ cells/well and incubated for 24 hours at 37 °C. To quantify the amount of nanoparticle uptake, cells were treated with 10% w/v of either ReANCs or differently functionalized fReANCs for up to 48 hours. Cells were subsequently trypsinized, washed and fixed in 1% PFA prior to being analyzed with fluorescent flow cytometry (FACscalibur, BD Biosciences, San Jose, CA) using the autofluorescence of the albumin shell to determine uptake as described previously. Data was collected for 10,000 cells.

Cell uptake and confocal imaging*:* To further visualize and confirm active targeting of receptor + cells, MDA-MB-231 and MCF7 cells (with elevated expression of CXCR4) and 4175-TR cells (with low expression of the receptor) were seeded on borosilicate Lab-Tek chambers (Nuc, Rochester, NY) and incubated overnight at 37 °C. Cells were then treated with either unfunctionalized ReANCs or AMD3100 loaded fReANCs for 24 hours. Cells were then washed, fixed, and stained with DAPI. NIR imaging was performed using a titanium:sapphire laser on a Leica TCS SP2 fluorescence microscope (Leica Microsystems, Exton, PA) to confirm cellular uptake.

Cell viability assay: The metabolic activity of cells treated with ARAs was assessed using the CellTiter96 Aqueous One Solution Reagent (3-(4,5-dimethylthiazol-2-yl)-5-(3-carboxymethoxyphenyl)-2-(4-sulfophenyl)-2H-tetrazolium, MTS) (Promega, Madison, WI). MDA-MB-231 and 4175-TR cells were cultured on 96 well microtiter plates at a density of 5000 cells/well and treated with 10% w/v ReANCs or fReANCs suspended in PBS for 24 hours. After 24 hours culture media was changed and MTS reagent was added to each well, and the plate was allowed to incubate for an additional 4 hours at 37°C. Absorbance was measured at 450 nm

using a microplate reader (Bio-Rad Model 680, Hercules, CA). Cell viability was calculated relative to the absorbance of the untreated cell population.

In Vivo imaging: Imaging studies were conducted using female homozygous nude mice (Taconic, Hudson, NY). For subcutaneous tumor imaging studies, MDA-MB-231 and 4175-TR human breast cancer cells were injected into the dorsal area at 10^7 cells per site. Animals were used for imaging studies once tumors became palpable. For imaging of internal organs at a sub-tissue level, MDA-MB-231 cells were injected via the tail vein at $3x10^5$ cells per animal. All animal studies were approved by the Institutional Review Board for the Animal Care and Facilities Committee of Rutgers University and performed in accordance with institutional guidelines on animal handling.

SWIR-imaging: Animals were imaged using a previously described in-house small animal SWIR imaging prototype for real time non-invasive optical imaging. Mice were fully anesthetized using 2% isoflurane (Butler-Schein, Dublin, OH) and were continuously scanned with a 1.7 W collimated 980 nm laser in various positions to excite nanoparticles. SWIR fluorescence was detected with an IR sensitive InGaAs camera (Sensors Unlimited, Princeton, NJ) equipped with long-pass 1000 nm and band-pass 1550 nm filters (Semrock, Rochester, NY) and a 25 mm SWIR lens (StingRay Optics, Keene, NH. This system is capable of real-time live animal imaging with an exposure time of ~50 ms $frame^{-1}$.[202] Images were acquired as .bin video files and were processed using custom Matlab scripts (**Supplementary Figure 6**).

MRI Imaging: MR images are acquired using 1 tesla M2-High Performance MRI System (Aspect Magnet Technologies Ltd, Netanya, Israel). All imaging procedures were performed under inhalation anesthesia with isoflurane at a concentration of 4% for induction of anesthesia

and 1–2% for maintenance. MRI images were analyzed using VivoQuant software (Aspect Magnet Technologies Ltd, Netanya, Israel).

Detection of subcutaneous cancer lesions: MDA-MB-231 (CXCR4+) and 4175-TR (CXCR4 -) cells were cultured in DMEM supplemented with 10% FBS (Invitrogen, Carlsbad, CA) and 1% penicillin-streptomycin. Female athymic nude mice were purchased from Taconic laboratories at 3-4 weeks of age and inoculated with bilateral dorsal injections of MDA-MB-231 and 4175-TR cells at 10^7 cells per site and allowed to grow until palpable. Animals were treated with weekly i.p. injections of ReANCs or fReANCs at a dose of 10 mg kg^{-1} and imaged with SWIR imaging at 24 h post injection to determine particle accumulation in the tumor space. Animals were sacrificed once tumor volume reached 500 mm^3 and organs were excised and imaged *ex vivo* to determine particle distribution.

Ex vivo analysis of subcutaneous tumors: At experimental endpoints animals were euthanized and subcutaneous tumors were excised and flash frozen. Tumors were cut to 25 µM sections with a cryotome (Thermo Fisher, Waltham, MA) and counterstained with Hoechst to detect cell nuclei. Sections were imaged using confocal microscopy to determine particle accumulation in the tumor mass.

Detection of lung metastatic lesions: Female homozygous athymic nude mice were obtained from Taconic Laboratories (Hudson, NY) at 3-4 weeks of age and were injected through the tail vein with MDA-MB-231 cells in an established model of lung metastasis. Tumor burden and location was evaluated using twice-monthly MRI (Aspect Imaging, Shoam, Israel) as described above. Animals were treated with weekly i.v. injections of either ReANCs or fReANCs at a dose of 10mg kg^{-1} body weight and imaged at 24h post treatment to determine the ability of functionalized nanoprobes to resolve changes in the tumor burden over time. SWIR signal was

correlated to tumor size and location as determined by MRI. Animals were sacrificed upon weight loss and organs were excised and imaged with SWIR imaging *ex vivo* to determine particle biodistribution and localization to lesion sites.

Ex vivo analysis of metastatic tumors: At experimental endpoints, animals were euthanized and tumors were excised, and fixed in formalin. Paraffin-embedded sections were imaged using confocal microscopy to determine particle accumulation in the tumor microenvironment. Slides were stained with Haemotoxylin and Eosin (Sigma-Aldrich, St. Louis, MO) to determine changes in microlesion architecture and photographed using (Nikon, Chiyoda, Japan). For staining with Vimentin, paraffin-embedded sections were warmed at 40^0C for 1h and deparaffination procedure performed. Antigen retrieval using citrate buffer at pH 6.0 was performed by microwave heating method. Following staining with anti-human Alexa647 conjugated Vimentin antibody (Santacruz Biotechnology, St.Louis,MO, USA) sections were counterstained with Hoechst 3342 to stain nuclei. Vimentin staining was visualized by fluorescence microscopy. Isotype matched control antibody staining was performed for non-specific binding.

4.6 Supplemental Figures

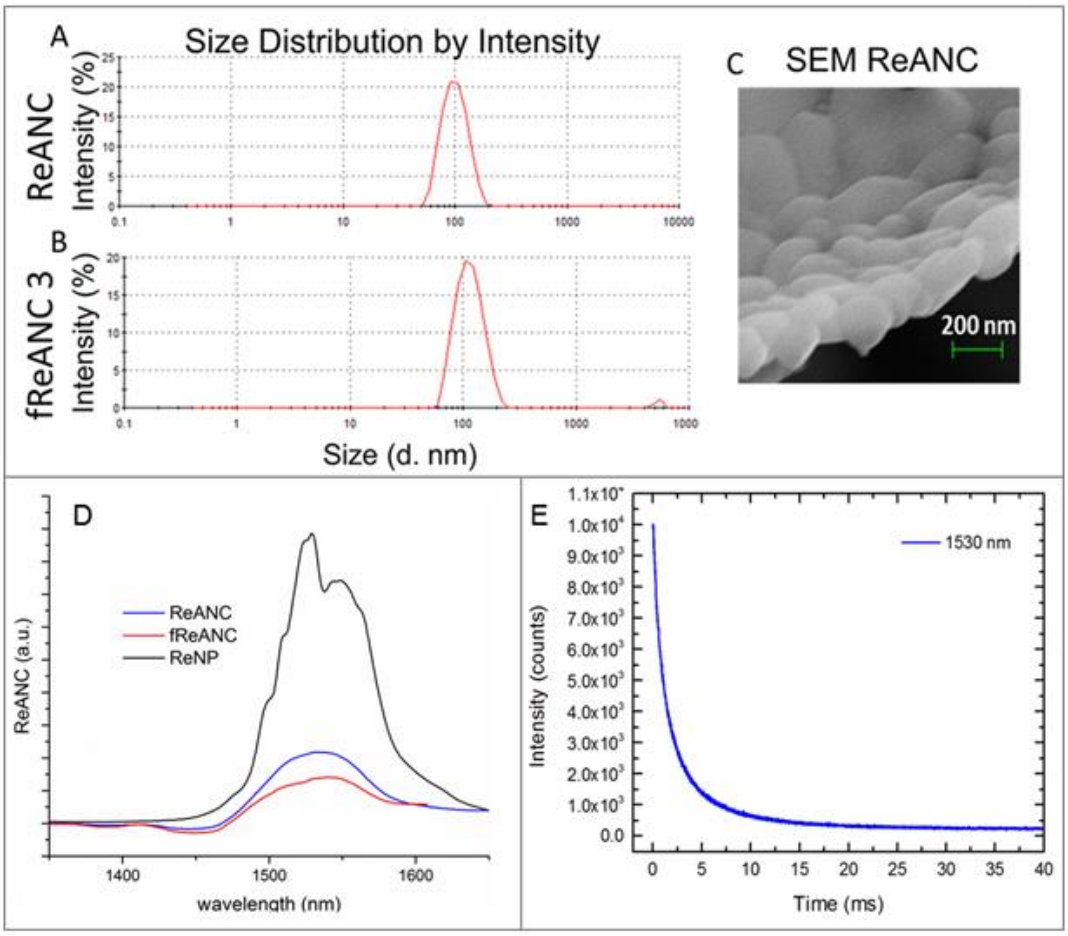

Supplemental Figure 4.1**. Size distribution histograms of ReANC and fReANC showing nanoscale, monodisperse populations.** ReANC (A) and fReANC (B) formulations were physically characterized using a zetasizer. Sizing histograms (shown here for unfunctionalized ReANCs and fReANCs functionalized with 125 nm AMD3100) revealed populations centered around 100 nm. SEM of ReANCs (C) revealed spherical particles with a smooth surface texture. Infrared emission spectra (D) showed that functionalization slightly decreased SWIR emission strength. Temporal emission intensity (E) at 1530 nm for $NaYF_4$: Er, Yb rare earth nanoparticles was measured under 980 nm laser excitation. The calculated decay time was found to be approximately 3.55 ms.

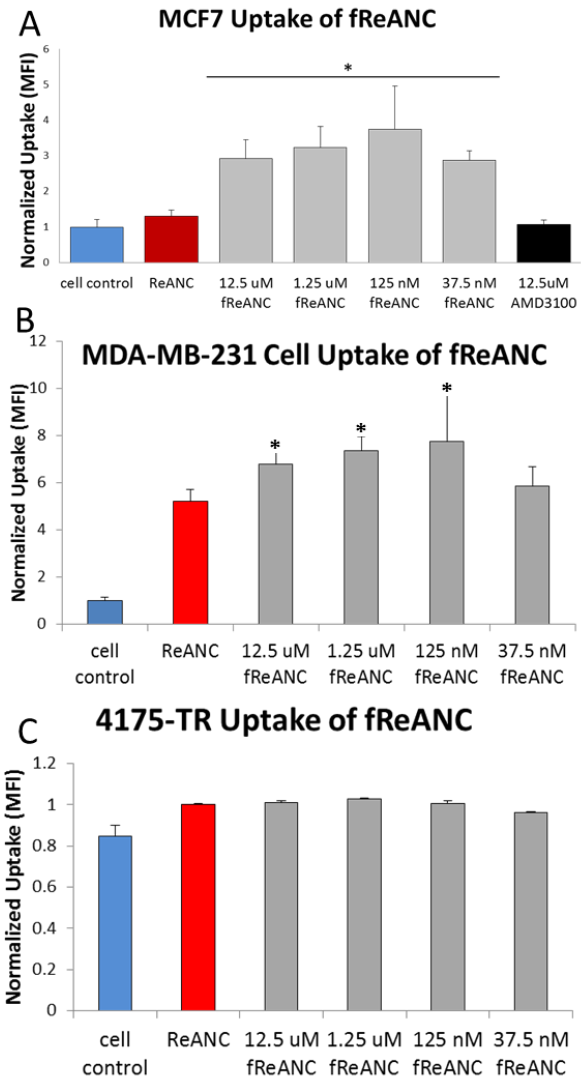

Supplemental figure 4.2: Effect of various concentrations of AMD3100 on cellular uptake of fReANC, showing that uptake is largely independent of loading concentration. Optimal loading was determined to be 125 nM AMD3100 based on results. Constructs were tested on cells lines with varying receptor expression. Uptake was determined via flow cytometry for (A) receptor positive MCF7 cells, (B) receptor positive MDA-MB-231 cells, and (C) receptor negative 4175-TR cells. Cellular uptake for all cell lines tested was largely independent of degree of functionalization. Error bars denote standard deviation for n=3. * p<.05 (t test, comparing between ReANC and fReANCs groups)

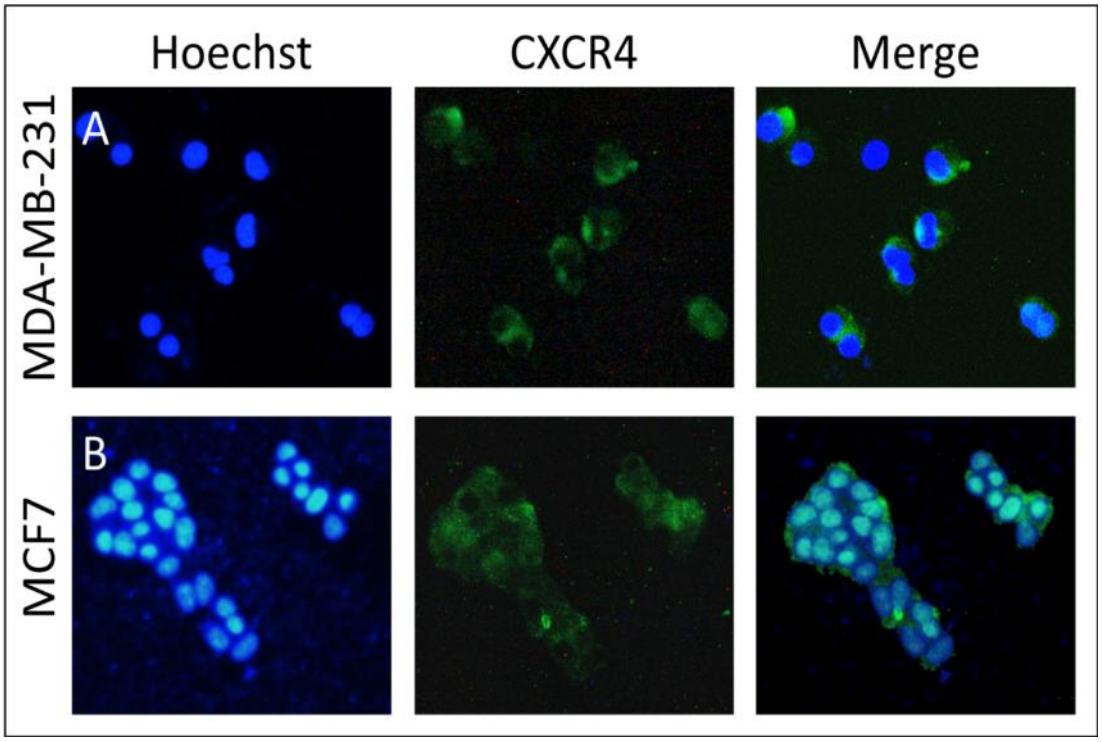

Supplemental Figure 4.3: Quantification of receptor expression of relevant cell lines showing co-localization of Hoechst (identified by blue nuclei) and anti-CXCR4 (green fluorescence). MDA-MB-231 (A) and MCF7 (B) cell lines were plated on glass slides prior to being fixed and treated with a CXCR4 antibody to confirm the presence of the receptor on the cell membrane. Cells were counter stained with Hoechst to detect nuclei. Results indicate that both cell lines express the receptor of interest.

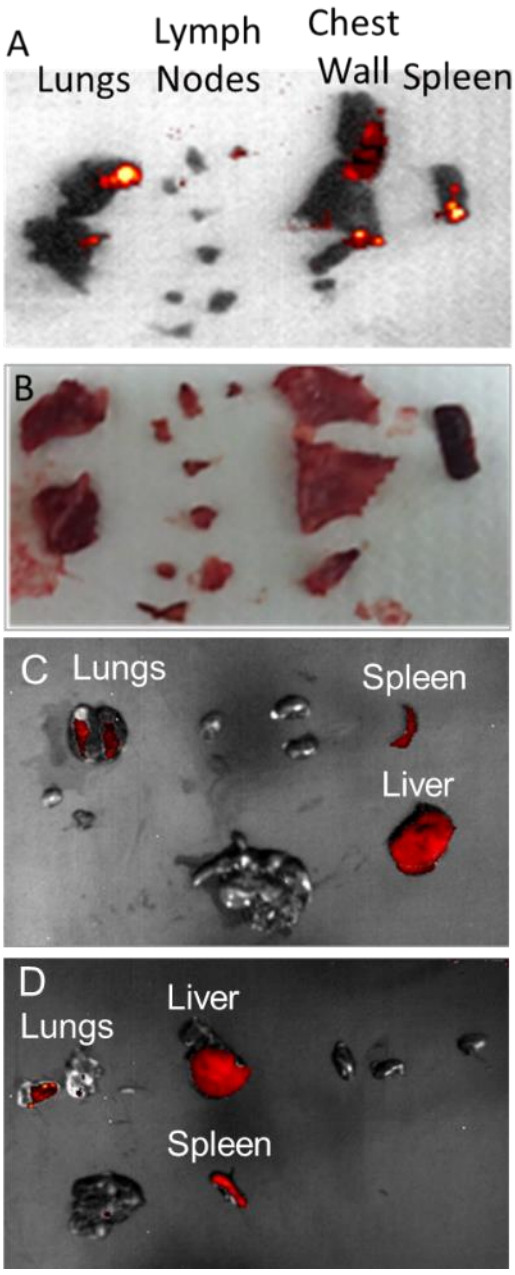

Supplemental Figure 4.4: *Ex vivo* analysis of organs showing punctate pattern of fluorescence associated with visible metastatic tumors. (A) SWIR signal from excised organs was punctate and confined to the lungs, areas with tumors on the animal chest wall, and organs of clearance. The areas of SWIR fluorescence in the lungs correspond to tumors visible in the white light image (B). Animals treated with ReANCs (C) and fReANCs (D) were sacrificed at experimental endpoints and organs were excised and imaged to determine particle accumulation. Analysis showed SWIR fluorescence in the liver and spleen as well as the lungs, at the site of the tumors. There was no apparent difference in organ accumulation between the functionalized and unfunctionalized particle formulations. Both formulations cleared from the body within 7 days.

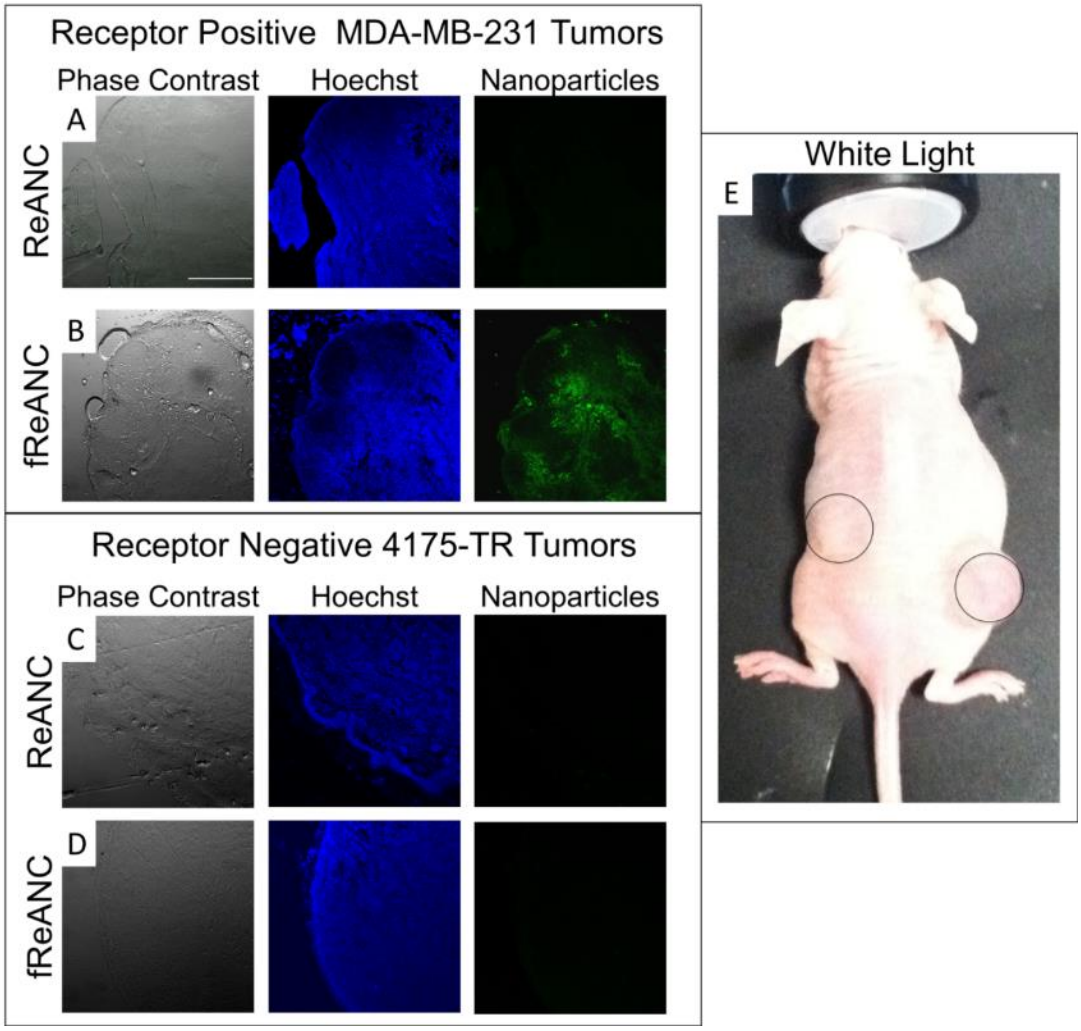

Supplemental Figure 4.5: *Ex vivo* analysis of excised subcutaneous tumors. Receptor positive MDA-MB-231 (A,B) tumors and receptor negative 4175-TR (C,D) tumors showing selective nanoparticle accumulation. Significant particle fluorescence was only observed in receptor positive tumors treated with fReANCs. Particle distribution was determined for receptor positive tumors treated with ReANCs (A) and fReANCs (B); receptor negative tumors treated with ReANCs (C) and fReANCs (D) by analysis of phase contrast, Hoechst, and nanoparticle fluorescence imaging. The subcutaneous tumors were allowed to develop in nude mice until they were palpable (E) and were distinguishable on the animal's flanks.

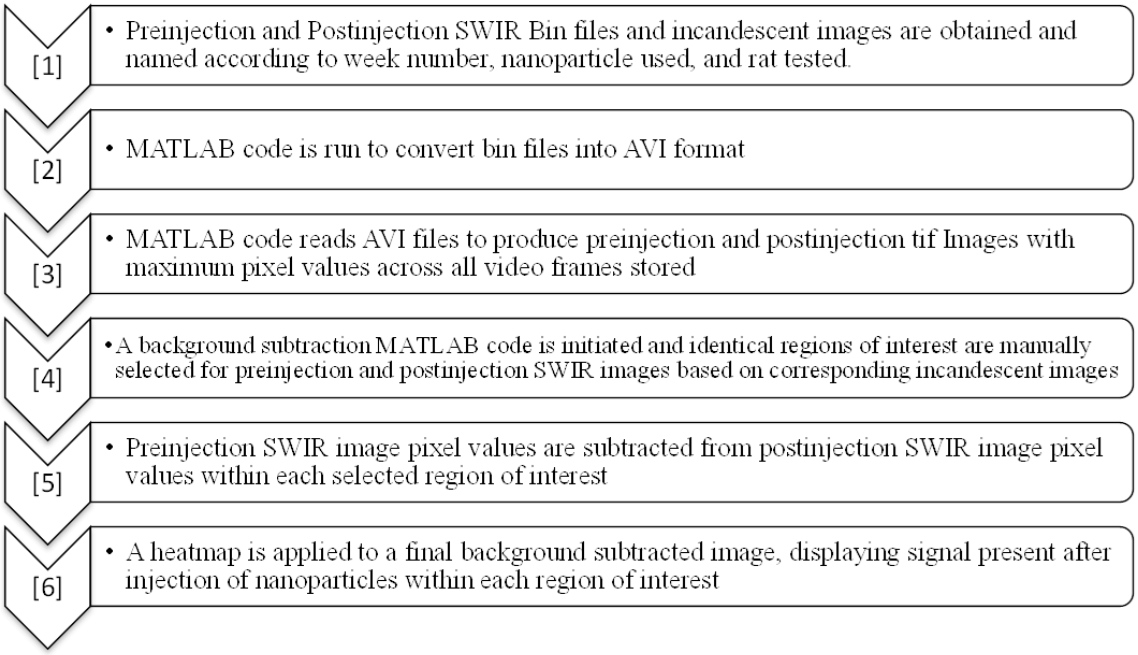

Supplemental Figure 4.6: flow chart detailing the matlab scripts used to process videos. The SWIR video files were obtained from the imaging prototype in .bin format. For each animal, pre-inject and post-inject images were taken and named according to the conditions of each animal. The matlab scripts converted each .bin file into an .avi file and background values determined from pre-inject images were subtracted from individually set regions of interest. A uniform heatmap was applied to the final image to indicate the relative intensity of the SWIR signal in the region of interest, and the image was overlaid onto single frame images of the mice captured with ambient light.

CHAPTER 5

EARLY DETECTION AND LONGITUDINAL IMAGING OF CANCER MICROMETASTASES USING BIOFUNCTIONALIZED RARE-EARTH ALBUMIN NANOCOMPOSITES

Sections of this chapter have been submitted to be published with the following citation:

Zevon, M., Katamneni, Ganapathy, V., H., Higgins, L., Mingozzi, M., Adler, D., Tan, M.C., Pierce, M., Riman, R., Roth, C.M., Moghe, P.V. Early detection and longitudinal imaging of cancer micrometastases using biofunctionalized rare-earth albumin nanocomposites. *Proc. SPIE Laser Sensors and Systems; and Next-Generation Sensors and Systems Includes volumes*, 2016. Accepted for Publication

-Sections of this chapter are being prepared for publication elsewhere entitled: "Early detection and longitudinal imaging of cancer micrometastases using biofunctionalized rare-earth albumin nanocomposites" **Zevon, M., Katamneni, Ganapathy, V., H., Tan, M.C., Pierce, M., Riman, R., Roth, C.M., Moghe, P.V.**

5.1 Abstract

Metastatic disease accounts for almost 90% of cancer-related deaths, but the mechanisms that initiate and drive this process remain poorly understood and difficult to control[247, 248]. The fate and evolution of distant site metastasis can significantly alter the efficacy of a treatment regimen [249-251]. Current clinical imaging techniques such as MRI are often unable to identify early metastatic populations, leading to recurrent disease and limited patient survival [26, 252]. In this study, we have advanced an optical surveillance nanotechnology that can enable detection and profiling of distal metastatic tumors. The approach is based on short wave infrared (SWIR) emitting rare earth albumin nanocomposites (ReANCs) targeted to molecular markers of metastatic disease. These ReANCs form the basis of a safe, non-toxic optical imaging platform with improved spectral properties when compared to similar near infrared (NIR) emitting agents like quantum dots and carbon nanotubes[70]. Previous work in our lab has illustrated that the constructs rapidly accumulate in and highlight lung lesions in murine models of distant site metastatic breast cancer[201]. In the present work, we further challenged our imaging system to detect micrometastatic lesions in an *in vivo* model of bone metastasis, as the early detection of bone lesions by clinical imaging modalities is limited [253, 254]. Significantly, ReANCs were able to discern lytic bone lesions even prior to their identification via MRI. Athymic nude mice bearing multiple metastatic sites were used to determine the effect of probe functionalization on tumor identification. Through the design of selectively functionalized probes, lesion molecular profile could be determined through a non-invasive 'optical biopsy', identifying multiple, phenotypically distinct, metastatic populations in a single animal with varying CXCR4 (a receptor correlated to cancer metastasis) expression. This information on lesion composition is especially critical for guiding timely therapeutic intervention in the treatment of recurring disease. The molecular differences among these lesions were elucidated,

revealing that pathways associated with tumor invasiveness were overexpressed in adrenal tumors, while bone lesions expressed markers associated with bone reabsorption, leading to the formation of lytic lesions. This analysis further revealed a number of attractive molecules for future targeted imaging or therapy. This technology can be applied to track the molecular profiles of metastatic and chemoresistant cancers, thus mitigating the chance for future disease relapse.

5.2 Introduction

Metastatic disease is the primary cause of breast cancer deaths in America [247, 248]. Early detection of metastatic lesions has a significant impact on patient prognosis and can guide therapeutic intervention [249-251]. Identification of metastatic sites is limited by a paucity of available diagnostic tests that are able to resolve small, early-stage lesions. Clinical imaging modalities such as radiometric scans, MRI, and PET/CT have resolution limits and expose patients to ionizing radiation. These tools have difficulty accurately identifying bone metastasis in particular, which is the most common site of distant metastasis [255-257]. There exists a critical need to develop diagnostic agents and modalities that can accurately detect and track the progression and development of metastatic tumors.

Optical imaging has the potential to identify and profile micrometastatic lesions and possess many advantages over traditional imaging techniques. Optical imaging allows for high sensitivity, multi-spectral anatomical imaging without the use of dangerous ionizing radiation [258]. Its translation into the clinic has not been exploited due to reliance on exogenous contrast agents with poor quantum efficiency and stability that typically excite and emit in the visible region of light, leading to poor penetration and scattering through tissue[259]. Near infrared radiation (NIR, 700-1000 nm) is capable of improved penetration though biological

media with less scattering, absorption, and tissue autofluorescence, making it ideal for biological applications [64, 182].

An ideal optical imaging contrast agent for biomedical use is ceramic rare earth (RE) nanoparticles that absorb NIR radiation and emit in both the short wave infrared (SWIR, 1000-3000 nm) and the visible ranges. These wavelengths allow for greater depth of detection than visible or NIR emitting contrast agents such as quantum dots and carbon nanotubes[54]. These probes are stable, optically efficient, and do not photobleach like organic phosphors. REs can be doped with various rare earth elements (like thulium, erbium, and holmium) to generate multispectral particles with distinct SWIR and visible emissions without changing the nanoparticle's physical characteristics [54, 68]. In this work, erbium doped RE probes emitting at 1525 nm were encapsulated in human serum albumin to generate stable, non-cytotoxic Rare Earth Albumin NanoComposites (ReANCs) capable of carrying a wide variety of ligands and payloads [54, 201].

A current challenge in cancer imaging is the sensitive and specific detection of micro-metastatic bone lesions [254]. Bone is the most common site of distant metastasis, and early detection has a significant impact on prognosis and choice of treatment [260]. The paucity of imaging modalities capable of resolving early stage bone tumors is a significant problem in disease management. Our findings demonstrate that ReANCs are able to detect tumor lesions in the leg bones of mice prior to their detection with conventional imaging techniques such as MRI and CT. *Ex vivo* analysis of tumor bearing bones shows that repeated nanoparticle injections are safe and have no negative effects on off-target organs or animal well-being.

Cancer treatment and detection is also often confounded by the presence of multiple phenotypically distinct metastatic sites. Patients with multiple distant lesions have a poorer

prognosis and decreased survival time compared to those with only one metastatic population. Identifying these lesions and determining the optimal treatment regimen is critical for long-term patient survival. Here we exploit the ligand binding properties of albumin to generate functionalized fReANCs targeted to CXCR4, a common marker of cancer metastasis overexpressed on a range of solid tumor cancers [201, 215]. CXCR4 expression is correlated in patients with poor prognosis, decreased survival time and diminished quality of life, and has previously been used to target PET imaging agents[218, 220]. In this work, athymic nude mice with metastatic breast cancer lesions in their adrenal glands and long bones were generated to evaluate the potential of biofunctionalized ReANCs (fReANCs) to distinguish between these two populations. Our results indicate that fReANCs functionalized to a marker of cancer metastasis preferentially accumulated in the fast-growing adrenal lesions, allowing for their detection prior to other metastatic sites. We further elucidated the changes in protein expression between these metastatic populations through the generation of organ-tropic cell lines to investigate differential nanoparticle localization and identify future potential cellular targets.

5.3 Results

5.3.1 Detection of Microlesions Using RE Probes

We first validated the ability of our SWIR imaging prototype to resolve microlesions. MDA-MB-231 human metastatic breast cancer cells were incubated with ReANC constructs for 24 hours prior to being pelleted to form tumor analogs of volumes up to 45 mm^3 (**Figure 5.1A)**. These pellets were imaged using a custom SWIR imaging prototype, which successfully resolved labeled cell clusters down to volumes of 0.85 mm^3, corresponding to a cluster of approximately 10^4 cells (**Figure 5.1B and C**). These clusters correlate to early-stage cancerous lesions, at a stage

where they are relatively emenable to therapeutic intervention [70, 201]. To calibrate the prototype's *in vivo* resolution, athymic nude mice were inoculated with the pre-incubated cells into their dorsal flanks and imaged over four weeks. Imaging at 2 weeks post inoculation identified lesions as small as 39.1 mm^3, indicating that the SWIR whole body imaging can support high resolution and sensitive detection in living systems (F**igure 5.1D and E**). These results demonstrate the capacity of ReANCs to identify very small lesions *in vivo* and the systems' potential for clinical translation and detection of microtumors.

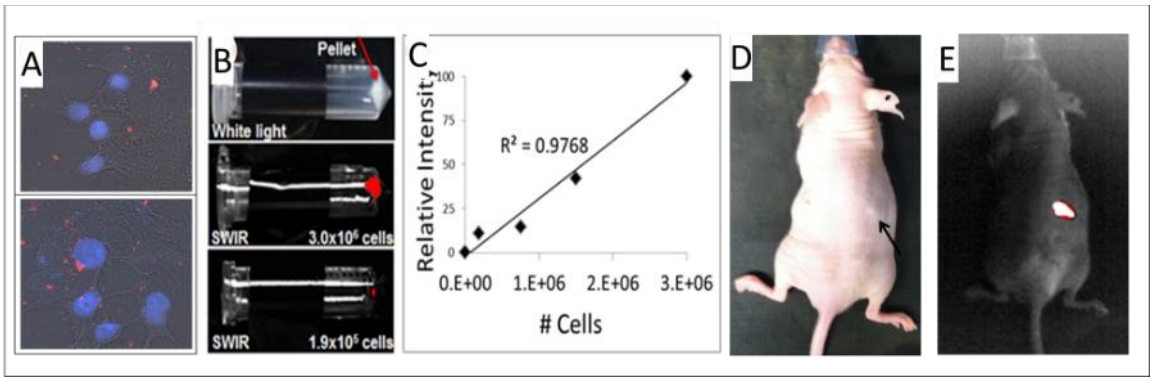

Figure 5.1: ReANCs retain functionality and allow for resolution of microscale cell clusters. Tumor cells incubated with ReANCs (A) remain associated with the particles. Cells were then pelleted to generate tumor analogs (B) that could be imaged with a custom SWIR imaging prototype. SWIR signal was proportional to pellet size, with pellets as small as 10,000 cells able to be identified (C). Tumors grown from pre-incubated cells inoculated into athymic nude mice (D) were able to be identified with SWIR fluorescence (pseudo colored red) as small as 39 mm^3 (E).

5.3.2 Detection of Metastatic Bone Lesions

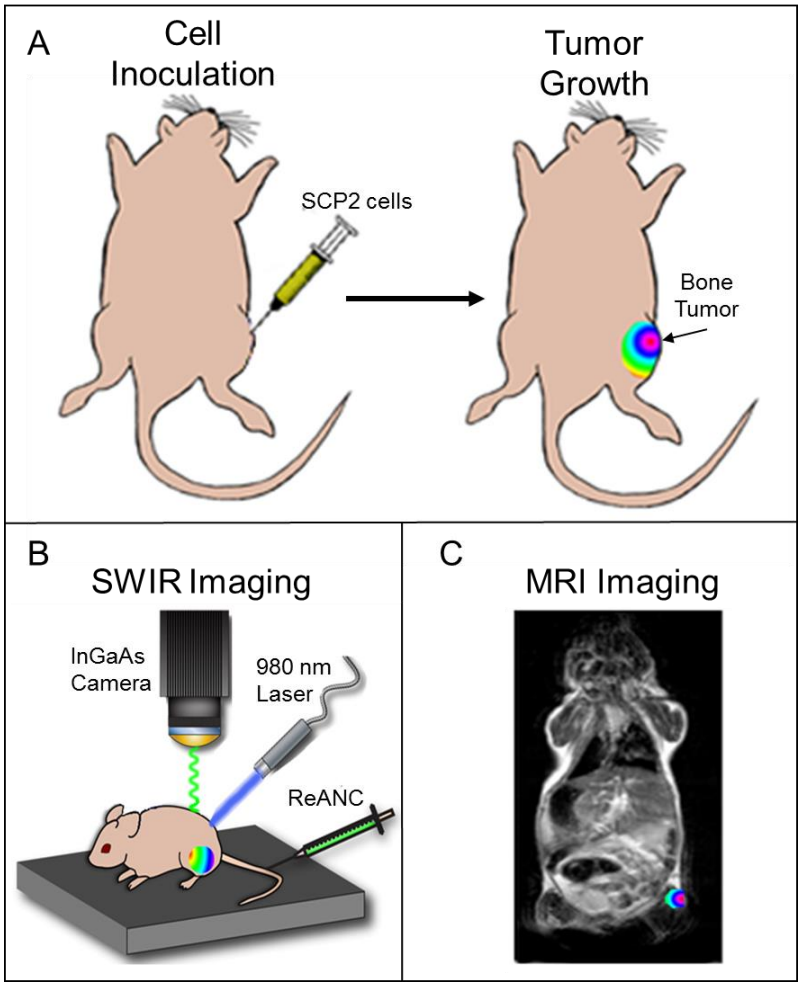

Figure 5.2: Detection of bone micrometastasis. Athymic nude mice were inoculated with SCP2 cells (a bone tropic subclone of human MDA-MB-231 human metastatic breast cancer cells). Tumor growth and development in the bone space was monitored through whole body BLI (A). Tumor bearing mice were administered weekly injections of ReANCs and imaged to determine particle localization (B). Time until tumor detection was compared to MRI (C) to determine early detection potential of SWIR optical imaging.

We next sought to evaluate our system's ability to detect clinically relevant metastatic lesions in long bones. Athymic nude mice were inoculated into the intratibial space with SCP2 cells, a bone tropic subclone of the MDA-MB-231 human breast cancer cell line (**Figure 5.2 A**) [261]. Tumor growth and lesion formation were monitored by whole body luminescence imaging (BLI) and MRI in a clinically relevant model of tumor assessment (**Figure 5.2 B and C**). At 5 weeks post inoculation there was a significant 2-fold increase in SWIR fluorescence from the tumor bearing legs indicating successful identification of lytic tumors (**Figure 5.3 A and B**) with tumors being tracked with whole body BLI for validation (**Figure 5.3 D**). In contrast, MRI could not resolve these lesions at this time (**Figure 5.3 E**), highlighting the ability of phosphor-nanoparticle contrast agents to accumulate in and associate with bone lesions prior to their resolution with clinically relevant imaging modalities **(Figure 5.3 F**). The presence of lytic tumors was supported by the loss in bone volume and density in tumor bearing legs as quantified through micro CT (**Figure 5.3 F**). *Ex vivo* analysis of tumor bearing bones corroborated visible hypocellularization and a paucity of normal hematapoetic cell types. (**Figure 5.3 G**) By contrast, long bones of healthy animals that received equivalent doses of nanoparticle injections showed no changes to bone marrow, and maintained robust cellularization and diversity of cell types.

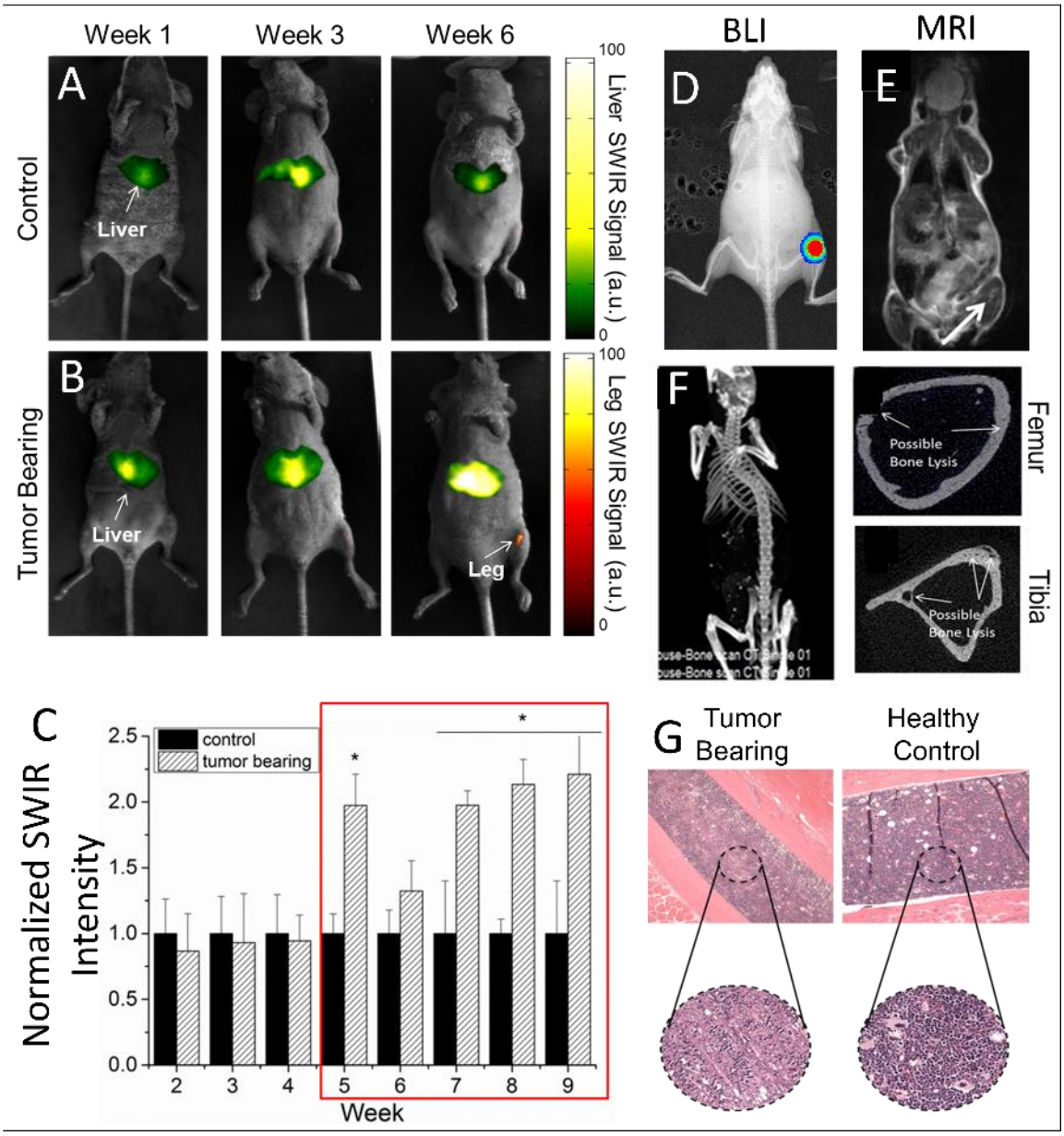

Figure 5.3: SWIR imaging is capable of identifying metastatic bone lesions prior to their detection with clinically relevant imaging modalities. Athymic nude mice were inoculated with human metastatic breast cancer cells directly into their tibia. ReANC nanoprobes administered to control (A) and tumor bearing mice (B) are able to identify lesions in tumor bearing legs 5 weeks post inoculation. SWIR fluorescence (C) from tumor bearing leg increased 2 fold compared to non-tumor bearing legs at 5 weeks. SWIR signal remained significantly elevated

allowing for tumor identification for up to 10 weeks (*$p < 0.1$, n=6, t-test). Tumor location was confirmed with whole body BLI (D) at 6 weeks. At 5 weeks (the time lesions were able to be resolved with SWIR imaging) tumors were unable to be detected with MRI (E) or CT (F). MicroCT (F) confirmed a loss of bone density associated with the presence of metastatic lesions. *Ex vivo* histopathology (G) showed hypocellularization and a lack of normal cellular diversity in tumor bearing legs compared to healthy control legs, indicating both the presence of lesions and that repeated ReANC injections are not damaging to hematopoietic tissue.

5.3.3 Detection of Multiple Metastatic Sites with Functionalized Probes

We further evaluated the effect of functionalized ReANCs on probe localization to multiple metastatic sites *in vivo*. Athymic nude mice received intracardiac injections of MCF-7 human metastatic breast cancer cells into their left ventricle. Animals were administered weekly injections of either CXCR4-targeted fReANCs or ReANCs and imaged over 24 hours to determine particle localization and tumor accumulation. Particle associated SWIR fluorescence was first observed in the animal's dorsal region 3 weeks post-inoculation. Longitudinal imaging showed an increase in fReANC associated SWIR fluorescence in the animal's dorsal region (**Figure 5.4 A)**, while ReANC signal from the same area remained low **(Figure 5.4 B**), indicating that the biofunctionalized probes are capable of tracking the growth and development of adrenal tumors over time. At week 5, fReANCs were able to identify tumors approximately 10 mm^3 in volume (**Figure 5.4 C**) as determined through bi-monthly MRI (**Figure 5.4 D**). In contrast, unfunctionalized ReANCs did not accumulate around adrenal tumors (approximately 14 mm^3). Tumor burden and metastatic sites were confirmed through whole-body bioluminescence imaging (**Figure 5.4 E**), showing primary metastatic sites in the animal's adrenal glands. The rapid growth of adrenal tumors likely prevented the development and detection of other

metastatic sites, as previous data (**Figure 5.3 C**) indicated that bone lesions were not detected until 6 weeks post-inoculation [262].

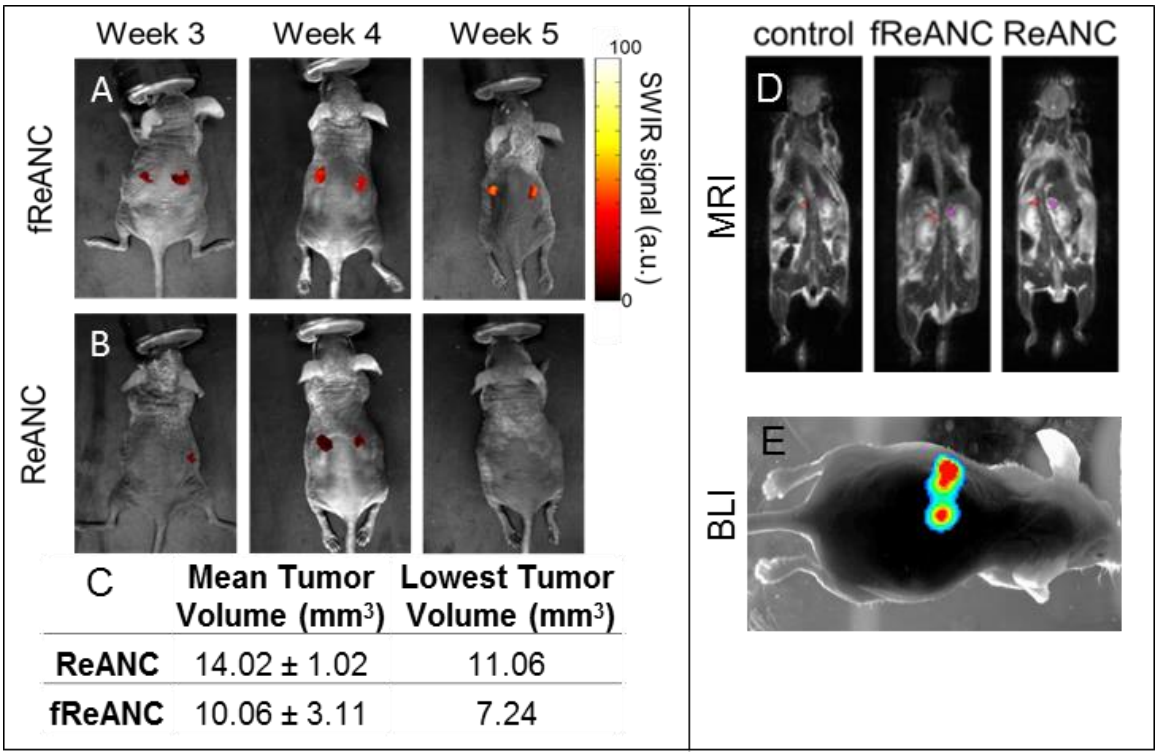

C

	Mean Tumor Volume (mm^3)	Lowest Tumor Volume (mm^3)
ReANC	14.02 ± 1.02	11.06
fReANC	10.06 ± 3.11	7.24

Figure 5.4: Functionalized ReANCs are capable of identifying adrenal metastasis in animals. Athymic nude mice were inoculated with human breast cancer cells through intracardiac injection and allowed to seed at multiple metastatic sites. Longitudinal imaging of mice administered fReANCs (A) showed SWIR fluorescence from the animal's dorsal region corresponding to tumors developing in the adrenal glands. In contrast, ReANC (B) treatment did not result in significant SWIR fluorescence. At week 5, tumors identified with fReANCs were found to be 10 mm^3 (C) while adrenal tumors in animals receiving ReANC injections were slightly larger, measuring 14 mm^3 in volume as determined through bi-monthly MRI (D). Metastatic populations were identified through whole-body bioluminescence imaging (E), which identified adrenal lesions as the primary metastatic population.

5.3.4. *Ex Vivo* Evaluation of Tumor Sites

At experimental endpoints, animals were sacrificed and necropsied. *Ex vivo* SWIR imaging of organs and previously identified tumor sites revealed SWIR associated fluorescence at the adrenal tumors of mice given injections of fReANCs (**Figure 5.5 A**). In contrast, the adrenal tumors of mice administered non-functionalized ReANCs showed comparatively little SWIR fluorescence **(Figure 5.5 B**). Analysis of pixel intensity showed that fReANC treatment led to a 7-fold increase in SWIR fluorescence at lesion sites when compared to non-tumor bearing animals (**Figure 5.5 C**).

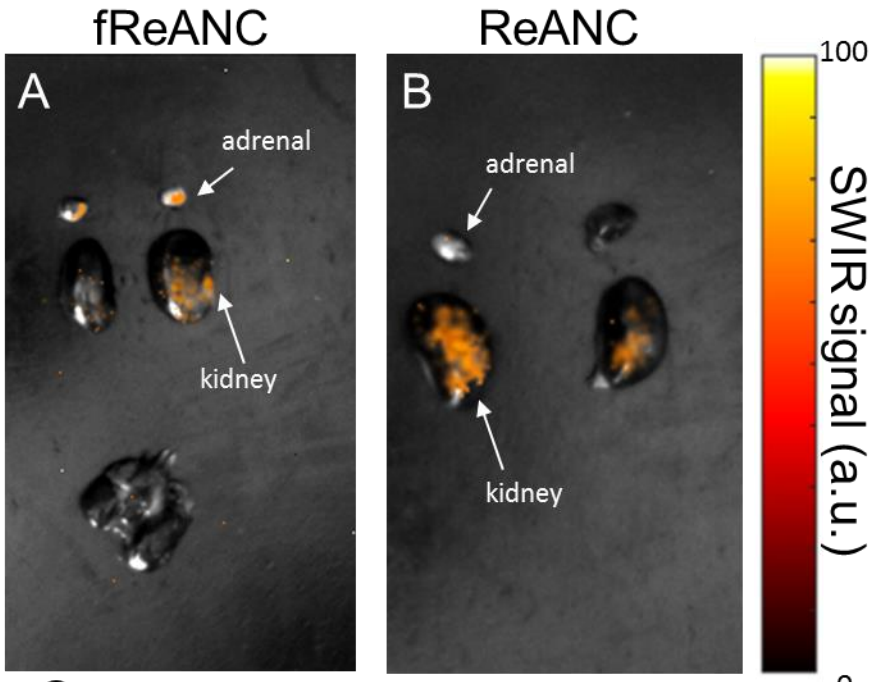

C

	ReANC	fReANC*	Control
Fold Increase in SWIR Signal	5.58 ±2.84	7.31±2.89	1±.12

Figure 5.5: Ex vivo SWIR imaging confirms probe accumulation at lesion sites. Athymic nude mice inoculated with breast cancer cells as described in Figures 5.2-5.3 were administered either fReANCs (A) or ReANCs (B) and sacrificed by week 5 to determine probe accumulation.

Enhanced levels of probe-associated SWIR fluorescence was observed from the adrenal glands of mice administered functionalized fReANCs (A) after removal, whereas less SWIR signal could be resolved from the tumors of animals administered ReANCs (B). Treatment with fReANCs led to a 7.3 fold increase in SWIR signal from adrenal lesions when compared to healthy controls (C) *p<0.15, n=6, t-test. The increase in SWIR signal from ReANC treated adrenal glands was not significant when compared to healthy controls. Necropsy performed 5 weeks post inoculation.

5.3.5. Evaluation of the Role of Metastatic Niche on Cell Phenotype

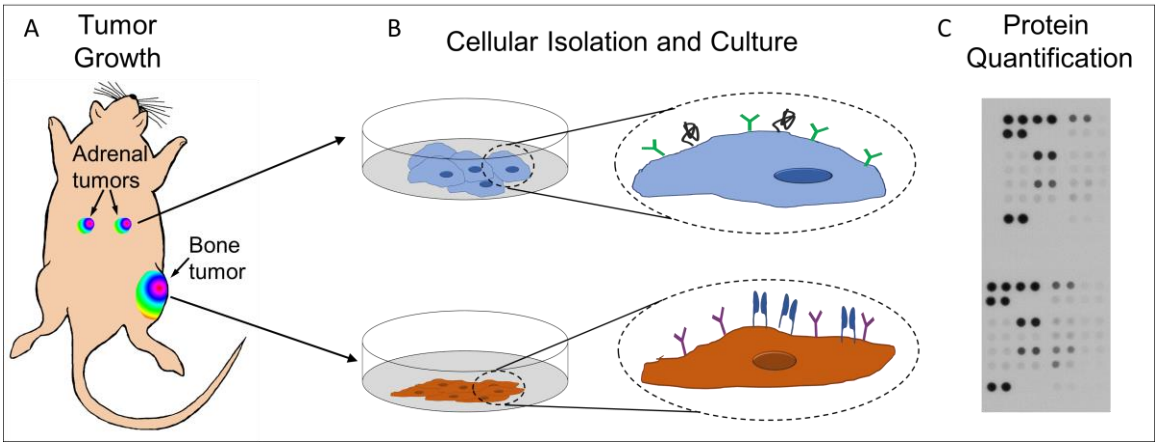

Figure 5.6: Development of organ tropic cell lines. Athymic nude mice receiving supplemental estrogen were administered intracardiac injections of MCF7 cells. Distant metastatic sites were allowed to grow and were monitored through whole body BLI (A). Animals were then sacrificed and tumor bearing organs were flushed with resulting cells collected and cultured *in vitro* (B). Resulting changes in cellular protein expression dependent on metastatic niche were quantified through protein array (C).

The molecular differences between cell populations at different metastatic sites were determined to identify potential targets for improved imaging. MCF7-derived parental cells were introduced into athymic nude mice via intraventricular injection and allowed to seed in distant organs. Tumor development was monitored with whole body BLI (**Figure 5.6 A**). Upon sacrifice, metastatic cells from varying sites were harvested and allowed to propagate, generating organ-tropic cell lines (**Figure 5.6 B**). Cells harvested from the bones (MCF7-5624a) and adrenal glands (MCF7-6124A) were analyzed for differences in protein expression in order to elucidate potential molecular targets for therapy and phenotyping based on metastatic organ sites and were characterized using an antibody array (**Figure 5.6 C**). Analysis of array pixel density (**Figure 5.7 A and B**) revealed upregulation of N-Cadherin, ADAM17, and JAM-A in adrenal-tropic cells (**Figure 5.7 C and D**). In contrast, bone-tropic cells upregulated markers including Notch-1, amphiregulin, and EGF-R **(Figure 5.7 C and D**). These differences in protein expression represent attractive future targets for probe targeting and functionalization.

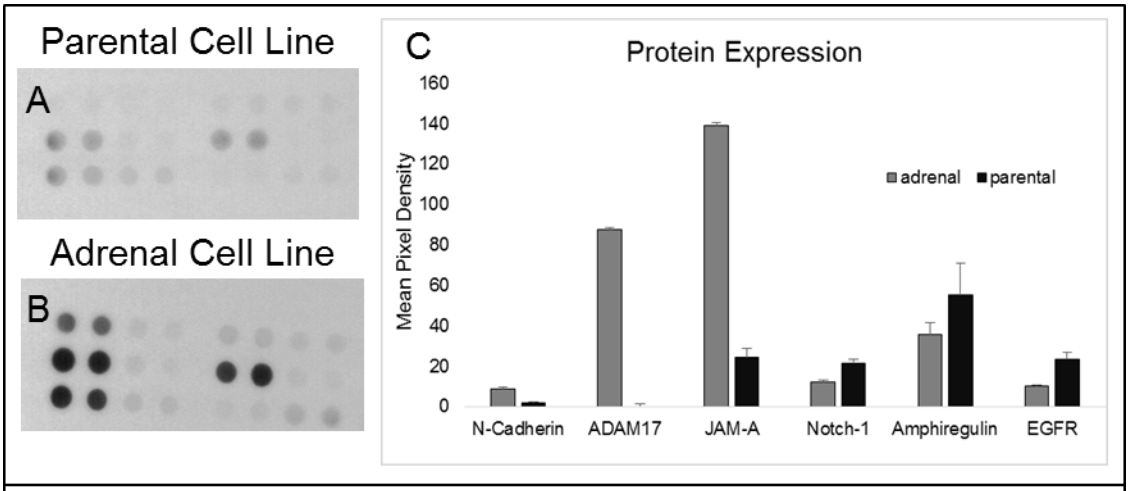

D

PROTEINS UPREGULATED IN ADRENAL-TROPIC MCF7-6124A CELLS

Protein	Fold Change	Pathway activated	Clinical relevance
N-Cadherin	4.75	Sustains activation of ERK and activates MMP-9 production	Promotes invasive activity and increases tumor metastasis
ADAM17	6.5	Activates EGFR-MEK-ERK pathway and upregulates MMP-2 and MMP-9, stimulates the release of TGFα	Increases cellular invasion and proliferation
JAM-A	4.5	activates Rap1 GTPase and upregulates β1-integrin	Increases cell motility Indicates poor patient prognosis
PROTEINS UPREGULATED IN BONE-TROPIC MCF7-5624A CELLS			
Notch-1	2	Activated by downstream products of TGFβ-SMAD pathway to promote osteoclast differentiation in bone	Promotes bone reabsorption and osteolytic lesions
Amphiregulin	2	Stimulates and increases EGFR signalling	Important for bone colonization
EGFR	2.27	Activation with MMP-1 leads to reduced production of osteoprotegrin, increasing RANKL activation of osteoclasts	Impacts recruitment of osteoblasts, limiting bone mineralization

Figure 5.7: The metastatic niche causes alterations in the genetic profile and receptor expression of lesions. Cellular protein expression was determined through antibody array analysis of parental bone tropic (A) and adrenal tropic (B) cell lines. Differences in protein expression were quantified based on antibody array pixel density (C). Fold changes in protein expression were calculated using differences in pixel density (D). Cellular markers upregulated in adrenal-tropic lines (D) were typically associated with increased tumor growth and invasion, while those upregulated in bone-tropic lines (D) acted in the metastatic niche to promote bone resorption.

5.4 Discussion

Early detection of micrometastatic tumors is critical to long term patient prognosis, but identification of emerging lesions is limited by current imaging modalities[251]. In this study, we utilized short wave infrared (SWIR) emitting rare earth albumin nanocomposites (ReANCs) as an optical surveillance approach to characterize and profile metastatic pathways. We generated the first proof of concept of optical probe-based identification of distant site metastasis prior to detection with MRI, a clinically relevant imaging modality. Nanoprobes were designed to utilize both active and passive targeting mechanisms, enabling multi-organ lesion identification. Unfunctionalized ReANCs were capable of identifying small bone lesions through passive targeting, while cancer targeted nanoprobes accumulated in rapidly growing lesions in the animal's adrenal glands. We further elucidated molecular differences in metastatic lesions based on niche, providing information that will guide future intervention.

SWIR emitting albumin nanocomposites have previously been utilized as safe and effective *in vivo* contrast agents, capable of being molecularly targeted to disease states [201]. However, the detection of metastasis is often confounded in tissues such as bone, where clinical imaging techniques such as MRI have difficulty accurately resolving early stage microlesions [26, 254]. As bone is a common metastatic site for malignancies such as breast cancer, the lack of imaging technologies capable of sensitive identification of bone lesions represents a critical barrier to the successful treatment of recurring disease. Bone lesions are frequently undetected until they are symptomatic, which leads to a poor prognosis and decreased patient survival time [253].

In vivo studies in a mouse xenograft metastatic breast cancer model showed passive accumulation of ReANCs in bone lesions at 5 weeks post inoculation, at levels allowing for lesion identification through SWIR imaging (**Figure 5.3**). In contrast, at this time lesions were not able

to be resolved with MRI or CT, two imaging techniques commonly used in the oncology clinic to identify metastatic populations. This indicates that nanoprobe-targeted SWIR imaging is more sensitive and able to resolve metastatic microlesions earlier than these established clinical modalities in this animal model [31]. These results highlight the ability of ReANCs to sensitively detect metastatic bone lesions prior to their detection with 'gold standard' imaging technologies through passive targeting alone. Future studies will focus on active targeting within the bone space using molecularly targeted ReANCs for improved sensitivity. Of significance was the observation that repeated nanoparticle injections had no effect on the development of healthy bone marrow, indicating that ReANCs are non-damaging to the hematopoietic niche.

A significant barrier to treatment of recurrent disease is the presence of multiple, often phenotypically distinct, metastatic populations in a single patient. Patients with multiple metastatic sites frequently have a lower quality of life and poorer prognosis than those with a single distant lesion [253]. Therefore, it is imperative for an effective imaging agent to be able to identify multiple lesions to improve detection and limit disease recurrence. We have previously shown that differentially functionalized ReANCs are capable of detecting both bone and lung metastatic populations in separate models; here, we sought to evaluate the potential for probes to target multiple metastatic sites in a single animal.

The effect of nanoprobe targeting on localization to multiple metastatic sites in a single animal was evaluated in a biomimetic model of cancer. *In vivo* studies in a xenograft murine model of metastatic disease showed that cancer-targeted fReANCs accumulated in fast-growing, receptor positive adrenal tumors. fReANCs allowed for identification of metastatic lesions as small as 7.26 mm^3 within 3 weeks post inoculation (**Figure 5.4**), illustrating the ability of targeted probes to accurately detect and phenotype early stage lesions. While literature suggests the eventual

presence of metastatic populations in the animal's long bones, the rapid development of adrenal tumors did not allow for the growth and development of less invasive lesions [262]. Future studies will focus on the detection of multiple metastatic sites with more similar growth and development rates to accurately assess the ability of differently functionalized ReANCs to target multiple populations.

During the course of this work we observed differences in lesion size and growth between treatment groups. At 5 weeks post inoculation, adrenal tumors in animals receiving CXCR4 targeted fReANCs were smaller than those receiving non-functionalized ReANCs, with less tumor infiltration into the gland (**Figures 5.4C**). Although not of statistical significance, these unexpected findings indicate that fReANC exposure could potentially have an inhibitory effect on tumor development, limiting infiltration and growth. Previous literature has shown that inhibition of CXCR4 decreases cellular metastasis and invasive potential [263, 264]. Further *in vitro* investigation indicated that fReANCs inhibited cell migration *in vitro*, indicating that AMD3100 functionalized fReANCs could act to stabilize and limit tumor invasiveness (**data not shown**).

Recent studies have illustrated the role of organ site on the frequency and receptor expression of metastatic lesions, leading to metastatic populations that are phenotypically distinct from parent cells [27, 28]. The identification of these differing factors can present potential therapeutic targets for the management of metastatic disease as well as elucidate the role of pre-metastatic niche on cancer progression [227]. To further explore the role of metastatic niche on tumor receptor expression, organotropic lines were developed by Dr. Vidya Ganapathy and her co-investigators by harvesting metastatic cells from the bones (MCF7-5624a) and adrenal glands (MCF7-6124a) of athymic nude mice inoculated with MCF7 derived cells via

intracardiac injection. The main observation was that proteins upregulated in adrenal-tropic cells correlate to a high degree with malignant cell motility and tumor invasiveness [265-268]. Proteins upregulated in bone-tropic cells interacted with pathways that increased bone reabsorption, leading to the generation of osteolytic lesions [223, 269-271].

Of particular note was the difference in the expression of Notch-1 and N-cadherin. Bone tropic 5624a cells expressed a 2-fold increase in Notch-1 compared to the adrenal tropic cells. Notch-1 upregulation has previously been correlated to bone metastatic disease and the presence of lytic lesions [272]. Since we are able to show ReANC accumulation in bone lesions, Notch-1 presents an attractive potential target to improve particle localization while simultaneously conferring a therapeutic benefit[273]. N-cadherin is associated with tumor invasiveness, growth, and metastasis [274]. Adrenal tropic cells had a 4.75 fold increase in N-cadherin expression compared with bone tropic cells, indicating a more aggressive phenotype, providing a possible explanation for the increased infiltration of adrenal glands [275]. These results could be used to drive future studies by presenting potential proteins for molecular targeting, guiding further probe development and design.

5.5 Experimental Methods

5.5.1 Sample Preparation

Rare earth nanoprobes were synthesized as previously described via burst nucleation reaction[276]. ReANCs were synthesized through solvent-induced controlled coacervation of albumin. Briefly, lyophilized human serum albumin (Sigma-Aldrich, St. Louis, MO) was prepared by dissolution in a sodium chloride solution and pH was titrated to 8.5. Rare earth nanoparticles dissolved in ethanol were added dropwise into the albumin stock to induce particle

coacervation surrounding the inorganic cores. These aggregates were chemically crosslinked with glutaraldehyde (Sigma-Aldrich, St. Louis, MO) for 10-18 hours to form stable, monodisperse nanocomposites[54, 69]. Functionalized probes were generated through passive absorption of AMD3100 (EMD Millipore, Darmstadt, Germany) onto the surface of fully formed ReANCs. A range of AMD3100 concentrations from 12.5 µM-12.5 nM were generated for *in vitro* testing to determine optimal loading. A loading concentration of 1.25 µM AMD3100 was used for *in vivo* experiments. Probe diameter and polydispersity was determined through dynamic light scattering (DLS), and probe yield was found to be approximately 70% by BCA protein assay [201].

5.5.2 Microlesion detection

The ability of REANC probes to detect microlesions *in vitro* was evaluated using cellular microclusters. MDA-MB-231 human metastatic breast cancer cells were cultured in DMEM (ATTC, Manassas, VA) supplemented with 10% FBS and 1% pen-strep (Invitrogen, Carlsbad, CA, USA). Cells were plated and incubated with ReANCs for 24 hours to allow for particle internalization. Cells were then washed, trypsinized, diluted to specific cell quantities, and pelleted to generate tumor analogs of various sizes. The minimum threshold for detection of micro-clusters was evaluated using a custom SWIR imaging prototype previously described. For subcutaneous tumor imaging studies, MDA-MB-231 human breast cancer cells pre-labeled with REANCs were injected into the dorsal area of an athymic nude mouse at 10^7 cells per site. Tumors were allowed to develop and were imaged to determine system resolution of lesions *in vivo*.

5.5.3 SWIR imaging

SWIR imaging was done using a previously described in-house small animal SWIR imaging prototype for real time non-invasive optical imaging. Samples were continuously scanned with a 1.7W collimated 980 nm laser to excite nanoprobes. SWIR fluorescence was detected with an IR sensitive InGaAs camera (Sensors Unlimited, Princeton, NJ) equipped with long-pass 1000 nm and band-pass 1550 nm filters (Semrock, Rochester, NY) and a 25 mm SWIR lens (StingRay Optics, Keene, NH) capable of resolving nanoparticle emissions. Images were acquired as .bin video files and were processed using custom Matlab scripts to subtract background and quantify pixel intensity based on region of interest. This system is capable of real-time live animal imaging with an exposure time of ~50 ms/frame[2]. Mice were fully anesthetized using 2% isoflurane (Butler-Schein, Dublin, OH) prior to handling and were imaged in various positions. Imaging studies were conducted using female homozygous nude mice (Taconic, Hudson, NY). Animals were sacrificed upon weight loss and organs were excised and imaged with SWIR imaging ex vivo to determine particle biodistribution and localization to lesion sites.

5.5.4 Detection of metastatic lesions in the bones

Female athymic nude mice (Taconic, Hudson, NY) were injected directly into the tibia of the left leg with SCP2 cells, a bone tropic subclone of the MDA-MB-231 cell line. Tumor development was monitored through whole body bioluminescence imaging (BLI) and compared to weekly MRI scans. Mice received weekly injections of ReANCs at 10 mg/kg body weight and were imaged up to 24 hours post administration. SWIR signal from the tumor bearing leg bones was quantified and compared to clinically relevant modalities to determine lowest detectable tumor burden. Animals were sacrificed upon weight loss and organs were excised and imaged via *ex vivo* SWIR imaging to determine probe biodistribution. Tumor bearing and healthy bones were

compared *ex vivo* to determine the effect of repeated injections on bone marrow and hematopoietic tissue.

5.5.5 Detection of multiple metastatic sites

Female athymic nude mice (Taconic, Hudson, NY) supplemented with low-dose estrogen pellets (.18 mg) were injected directly into the left ventricle with MCF-7 human breast cancer cells. Tumor development and size was monitored through whole body bioluminescence imaging (BLI) and MRI. Mice received weekly injections of ReANCs or fReANCs functionalized with 12.5 µM AMD3100 at 10 mg/kg body weight and were imaged up to 24 hours post administration. SWIR signal from the leg bones and dorsal area corresponding to adrenal location was detected and processed. Animals were sacrificed upon weight loss and organs were excised. Adrenal tumors were stained with Hematoxylin and eosin (Sigma-Aldrich, St Louis, MO) to determine changes to organ architecture. Tumor infiltration into tissue was confirmed with immunostaining of human Er receptor expressed on MCF-7 cells **(Supplementary Figure 1).**

5.5.6 Generation of organotropic lines (Lines generated by Dr. Vidya Ganapathy in Reiss lab at CINJ)

Athymic nude mice (Taconic, Hudson, NY) supplemented with low-dose estrogen pellets (.18 mg) were injected directly into the left ventricle with MCF-7 human breast cancer cells. Tumors were allowed to grow and develop for 6 weeks. Animals were then sacrificed and organs bearing metastatic tumors were processed, with resulting cells collected and cultured. Cell line protein expression was evaluated using with the Human Soluble Receptor Array Kit Non-Hematopoietic Panel (R&D systems, Minneapolis, MN) according to manufacture instructions. Array results were analyzed as a function of pixel density.

5.5.7 Therapeutic inhibition of metastasis (data not shown)

fReANCs were functionalized with 12.5 µM AMD3100 were generated as described above. ReANCs and fReANCs were tested for inhibition of metastasis using CXCR4 expressing MCF7 cells for the scratch healing assay and MDA-MB-231 human breast cancer cells for migration through a membrane. In the scratch assay, confluent wells of MCF7 cells were scored using a pipette tip and treated with 10% v/v either ReANCs, fReANCs, or free AMD3100 in solution. Wells were imaged up to 12 hours post inoculation and cellular migration into the wound was determined with imagej analysis. To evaluate the effect of functionalized constructs on cell migration, MDA-MB-231 cells were plated on a 0.8 µM transwell insert and treated with 10% v/v either ReANCs, fReANCs, or free AMD3100 in solution. After 24 hours cells on the top of the membrane were removed and remaining cells were stained with crystal violet (Sigma-Aldrich, St Louis, MO) to quantify cellular migration through the membrane.

5.6 Conclusions

Taken together, our results describe an innovative optical imaging platform capable of detecting multiple micrometastatic sites in distal organs where resolution is traditionally limited. Customizable optical nanoprobes with SWIR emissions are capable of the sensitive and specific early detection and longitudinal tracking of metastatic lesions, allowing for molecular discrimination of the dominant lesion phenotype. This non-invasive ‘optical biopsy’ can help determine optimal therapeutic intervention and real-time information on tumor growth and development. Molecular characterization of adrenal tumors revealed overexpression of markers relating to tumor aggressiveness and invasion, while bone lesions overexpressed markers that interact with the bone microenvironment to promote resorption. These receptors represent potential future therapeutic and imaging targets.

5.7 Supplemental figures

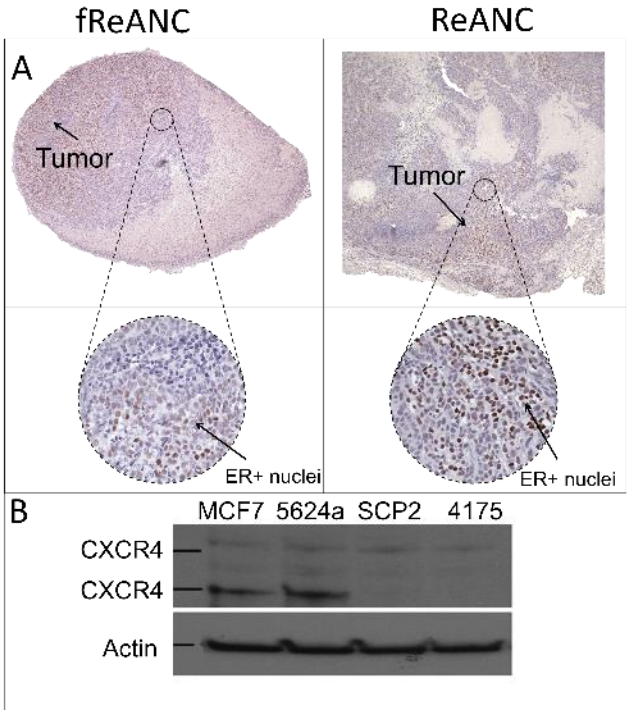

Supplemental Figure 5.7.1. Tumor bearing adrenal glands were stained for the ER receptor expressed by MCF-7 cells to confirm presence of tumor and organ infiltration (A). Brown nuclei indicate ER^+ cells while blue nuclei indicate healthy tissue. Adrenals harvested from mice administered ReANCs showed a greater degree of tumor infiltration (A). Tropic cell lines were analyzed to determine their levels of CXCR4 expression through western blotting (B).

CHAPTER 6

RESEARCH SUMMARY AND CONCLUSIONS

6.1 Summary and Conclusions

The goal of this dissertation is to engineer multifunctional albumin nanoparticles capable of improved payload delivery to solid tumors, enabling drug delivery, *in vivo* lesion surveillance, and molecular phenotyping of difficult-to-detect tumors. These objectives address a number of significant limitations in cancer treatment today: 1. Improved penetration into solid tumors for improved therapeutic efficacy 2. Limited *in vivo* translation of optical imaging techniques 3. Rapid, non-invasive determination of a lesion's dominant molecular phenotype to improve imaging and inform on treatment decisions, and 4. Identification of problematic metastatic lesions at early stages ideal for intervention and prior to their detection with clinically relevant imaging modalities.

6.1.1 Modification of albumin carriers for improved payload delivery to solid tumors

This dissertation focuses on the modification of albumin nanocarriers to overcome these barriers. Chapter 2 is predicated on the theory that nanoparticle-based drug delivery to solid tumors is impeded by the dense extracellular matrix generated by malignant lesions. This limited penetration leads to reduced therapeutic efficacy and multi-drug resistance. Here it has been demonstrated that albumin particles can be modified with proteases for improved penetration into tumor masses and that this results in improved therapeutic and imaging efficacy. Collagenase decoration caused improved association with single cancer cells, with small collagenase coated albumin nanoparticles (cANPs) being taken up by cells more than large cANPs. Our results show that particle size and protein composition can be varied to improve tumor penetration, overcoming one of the key barriers to solid tumor delivery.

The effect of improved tumor penetration on drug and contrast agent delivery was further evaluated via drug loaded particles. Particles were loaded with curcumin and riluzole via passive absorption. The drug loaded particles retained therapeutic efficacy against malignant cells with and without the collagenase coating and did not impede cellular uptake. From this work, it is evident that ANPs can be modified to carry a variety of payloads to generate multifunctional particles capable of simultaneous payload delivery, overcoming multiple barriers to particle-based drug delivery.

6.1.2 Development and *in vivo* evaluation of SWIR emitting rare earth albumin nanocomposites

Next, we further developed albumin nanocomposites encapsulating SWIR emitting rare earth nanoprobes and evaluated their potential as the basis of an optical *in vivo* imaging system. We hypothesized that ReANCs could act as safe and effective *in vivo* contrast agents capable of accumulating in tumors and allowing for non-invasive optical imaging of disease. These probes could allow for a novel paradigm in infrared imaging techniques, with improved penetration through tissue when compared to traditional optical imaging. SWIR emitting rare earth particles encapsulated in albumin nanoshells proved to be safe and non-toxic while retaining their optical emissions. SWIR fluorescence was able to be resolved in mice using a custom imaging prototype. The albumin coating led to more favorable biodistribution and passive accumulation of ReANCs in well vascularized cutaneous lesions, allowing for their non-invasive identification. Coat thickness can be tuned for variable biodistribution and was optimized for tumor detection. This work established ReANCs as safe and effective SWIR emitting contrast agents, capable of being resolved by our lab's custom SWIR imaging platform for improved optical imaging in biological systems.

6.1.3 Molecular targeting of nanocarriers for improved particle localization and lesion imaging

Chapter 4 focuses on the application of SWIR emitting ReANCs for early detection and molecular phenotyping of metastatic tumors to generate a multifunctional screening tool capable of non-invasive tumor identification and surveillance. Molecularly functionalized probes were capable of discriminating between cellular phenotypes both *in vitro* and *in vivo*, allowing for non-invasive determination of lesion composition. This targeting led to an increase in particle association with receptor positive cells, causing an increase in SWIR emission intensity from positive lesions treated with functionalized nanoprobes. This increased association led to the early detection of metastatic lung lesions as small as 18.9 mm^3 in volume and over a centimeter from the animal's surface. This improved tumor resolution represents a significant improvement over currently used optical imaging techniques that rely on visible and NIR wavelengths of light.

6.1.4 Application of SWIR emitting ReANCs for detection of distant micro-metastatic lesions

We then sought to evaluate the potential for SWIR emitting ReANCs to fill a critical unmet need in cancer management and care. Metastasis is the cause of 90% of cancer deaths, with distant lesions being associated with poor prognosis and diminished patient survival time. We evaluated the ability of ReANCs to detect metastatic bone lesions prior to their detection with MRI in an *in vivo* model of metastatic breast cancer. ReANCs were capable of accumulating in and identifying bone lesions weeks after their inoculation and prior to their resolution with MRI and CT. Additionally, repeated ReANC injections were well tolerated by animals and had no effect on hematopoietic tissue. Findings from this study support the promise of an imaging platform using

high-resolution RE nanoprobes that has immediate clinical translatability in microlesion detection. These results are of great clinical significance as the presence of microlesions in the bone marrow is an accurate indicator of poor prognosis in breast cancer patients [26]. Early detection of these lesions is a challenge due to the lack of sensitive imaging modalities. Enhanced resolution of lesions by SWIR emitting ReANCs renders them as potential novel optical imaging agents to detect micrometastasis to bone, and highlights an innovated paradigm in optical imaging.

Next, we further evaluated the ability of ReANCs and CXCR4-targeted fReANCs to seek out multiple distant metastatic sites in an experimental metastatic model of luminal breast cancer that closely mimics the progression of human disease. We found that when compared to ReANCs, fReANCs preferentially accumulated in adrenal tumors as small as 10 mm^3 allowing for their identification as early as 3 weeks post inoculation. Metastastic lesions in other locations (such as the animal's long bones) were slower growing and were not well established at experimental endpoints. Bone and adrenal tropic cell lines were generated from parental breast cancer cells, and evaluation revealed upregulation of metastatic and invasive markers in the adrenal lines, revealing a number of future potential cellular targets. This innovation is highly clinically relevant, as patients with multiple metastatic lesions have poorer outcomes than those with only one distant metastatic site.

6.2 Future Directions

6.2.1 Theranostic nanoparticles

Multifunctional nanoparticles are attractive delivery vehicles due to their ability to carry multiple payloads. Recent interest has centered on the development of 'theranostic' materials that are capable of simultaneously treating and monitoring disease. Theranostic nanoparticles have to potential to combine passive and active tumor targeting, molecular imaging, and drug release into a single highly efficient particle and could play a significant role in personalized medicine in the future [78, 277]. The key to an effective theranostic platform is sensitive diagnosis and effective treatment of early stage cancerous lesions [278].

The albumin nanocomposites described in this dissertation provide an ideal material to form the basis of a theranostic nanoparticle system. Chapter 2 describes the modification of the albumin shell with multiple therapeutic agents, while subsequent chapters describe effective incorporation of an imaging agent. The success of these endeavors indicates that both imaging and therapeutic agents could be incorporated into one particle with little associated loss of emission intensity or therapeutic efficacy.

To evaluate albumin nanocarriers as a theranostic probes, therapeutic agents can be easily adsorbed onto the surface of fully formed ReANCs in a manner similar to that described above in chapter 2. Potential therapeutics include doxorubicin and curcumin, both therapeutic compounds that have previously been shown to benefit from nanoparticle formulations [235, 279]. In addition to their efficacy against metastatic breast cancer, both doxorubicin and curcumin have unique fluorescent properties that allows for non-invasive imaging of drug

localization [123, 280, 281]. Once synthesized, theranostic constructs can be evaluated to confirm no loss of therapeutic efficacy or SWIR emission strength.

Further studies could focus on the *in vivo* evaluation of optimized theranostic nanoparticles. Success in this endeavor will further advance the possibility of using multifunctional ReANCs for real-time disease surveillance to monitor therapeutic efficacy and changes in tumor phenotype. For example, our previous work has described that molecularly targeted fReANCs are capable of reporting on a lesion's composition *in vivo*. This is particularly critical in the treatment of breast cancer, where therapy is often dictated by cellular receptor phenotype. The use of functionalized nanoprobes may elucidate not only changes in tumor size in response to therapy but also the receptor expression of remaining cells, informing their responsiveness to therapy and metastatic potential.

6.2.2. Multispectral imaging

One of the attractive design features of rare earth doped nanoprobes is their tunable emission spectra. The excitation and emission characteristics can be tailored by controlling the dopant and host chemistries without altering the nanoparticle's physical characteristics. In this way, a library of differently emitting probes can be generated with a single excitation wavelength but distinct visible and SWIR emissions [71, 72]. This property provides exciting potential for multispectral imaging of disease states. Traditional optical imaging is based on single marker targeting, providing only limited information on a lesion composition or disease state. This model fails to properly inform on tumor heterogeneity and disease progression, particularly in response to therapeutic intervention. A library of differently emitting RE probes capable of unique, distinct SWIR emissions could be targeted to multiple prognostic and signaling markers, enabling simultaneous imaging of multiple clinically relevant features [54].

Previous work has shown that multispectral particles can be generated and resolved *in vivo* by the current custom SWIR imaging system described above [54]. Thulium doped rare earth particles ($NaYF_4$: Tm, Yb) have been generated and successfully encapsulated in human serum albumin, with the albumin coating being sufficient to completely shield the biological environment from the cytotoxic effects of the ceramic core particles. We have also shown that cells treated with Er-doped 100 nm ReANCs and Tm-doped 300 nm ReANCs remain viable for 24 hours post-treatment. The differently doped particles could be distinguished through fluorescent microscopy, with the smaller, Er doped particles accumulating in the cell's cytoplasm and the larger, Tm-doped ReANCs localizing to the cell's nucleus [282]. These results indicate that the differently doped ReNPs can be distinguished both *in vitro* and *in vivo*, thus offering unique abilities to probe multiple relevant cellular markers.

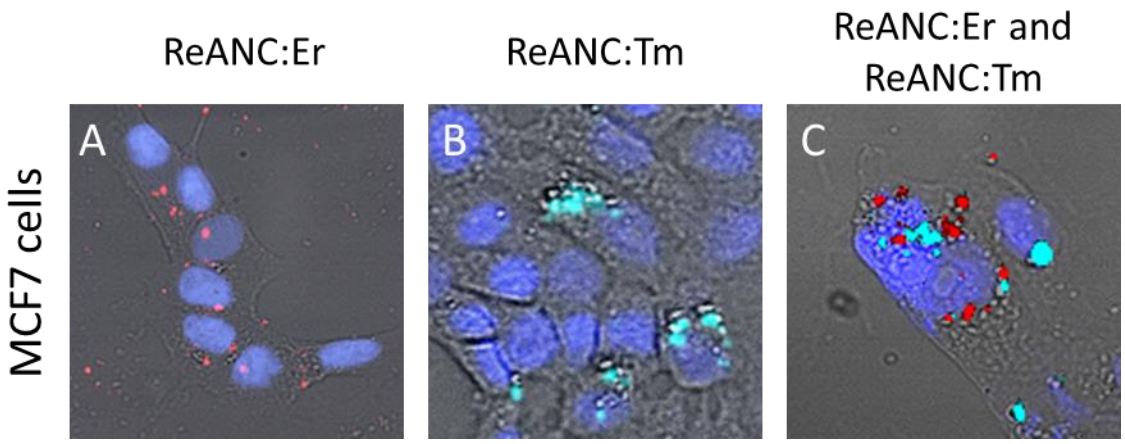

Figure 6.1: *in vitro* imaging of differently doped ReANCs. Human metastatic breast cancer MCF7 cells treated with (A) 100 nm Er-doped ReANCs and (B) 300 nm Tm-doped ReANCs show differential cellular localization after 24 hour incubation, with the 100 nm particles accumulating in the cytoplasm and the larger 300 nm ReANCs circling the nucleus. Simultaneous treatment with both particle formulations (C) showed similar patterns.

Future studies could focus on exploiting this differential intracellular accumulation to provide real time information on lesion heterogeneity. For example, by using both size and dopant chemistry, ReANCs could be design to discern between lesion heterogeneity and the nature of cancer markers. One specific embodiment of a binary probe system could be 100 nm Er-doped ReANCs functionalized to metastatic markers such as CXCR4, co-administered with 300 nm Tm-doped ReANCs functionalized to nuclear markers such as estrogen. Such functionalized probes could be used to differentiate *in vivo* lesion composition and monitor changes in receptor expression in response to hormonal therapy. If successful, this approach would enable simultaneous imaging of multiple cancer features, such as location and progression of tumor burden, details on tumor architecture regarding vascular density and degree of angiogenesis as well as detection and quantification of metastasis.

Success in this endeavor will further advance the possibility of using multifunctional ReANCs for real-time disease surveillance to monitor therapeutic efficacy and changes in tumor phenotype. For example, our previous work has described that molecularly targeted fReANCs are capable of reporting on a lesion's composition *in vivo*. This is particularly critical in the treatment of breast cancer, where therapy is often dictated by cellular receptor phenotype. The use of functionalized nanoprobes may elucidate not only changes in tumor size in response to therapy but also the receptor expression of remaining cells, informing on their responsiveness to therapy and metastatic potential. This could be instrumental in determining optimal treatment regimen.

6.2.3. Multimodal imaging

Current diagnostic imaging methods such as MRI, PET, and ultrasound typically lack the sensitivity and specificity to provide real-time biological readouts during cancer therapy [207].

While optical imaging has many advantages and provides routes to molecular imaging of tumors, it is typically limited by poor tissue penetration and spatial resolution [56]. Simultaneous use of multiple imaging modalities can overcome many of these limitations, allowing for improved disease detection, surveillance, and monitoring in response to therapy [207]. An ideal multimodal imaging platform would combine the anatomical imaging capabilities of MRI or ultrasound with the molecular resolution provided by optical imaging techniques.

Multimodal contrast agents capable of being resolved with both anatomical and optical imaging modalities have been previously reported. Rare earth nanoprobes have been triple doped with Yb, Er, and gadolinium (Gd) to provide both SWIR emissions and MRI contrast, allowing for multimodal detection of a single nanoparticle construct [283, 284]. Future animal studies could focus on exploiting the whole-body anatomical imaging capabilities and the molecular phenotyping of functionalized SWIR emitting ReANCs for improved detection and surveillance of internal *in vivo* metastatic lesions.

Another potentially exciting multimodal application of Re probes is to exploit their unique acoustic signature and refractive properties in tissue, providing ultrasound and optical coherence tomography (OCT) contrast. These modalities allow for 3-d localization of particle distribution with no additional changes to the particle's composition or structure. Of particular interest is ultrasound imaging, which relies on the diffraction of sound waves to generate an image and has been used in conjunction with albumin microbubbles to provide enhanced optical contrast [285]. This indicates that our ReANC particles could be utilized with little modification for contrast enhanced ultrasound imaging, allowing for more specific anatomical resolution of probe biodistribution. Previous work has indicated that ReANCs have a brightening effect when

imaged using ultrasound through tissue mimetic phantoms, indicating that they may function as multimodal contrast agents.

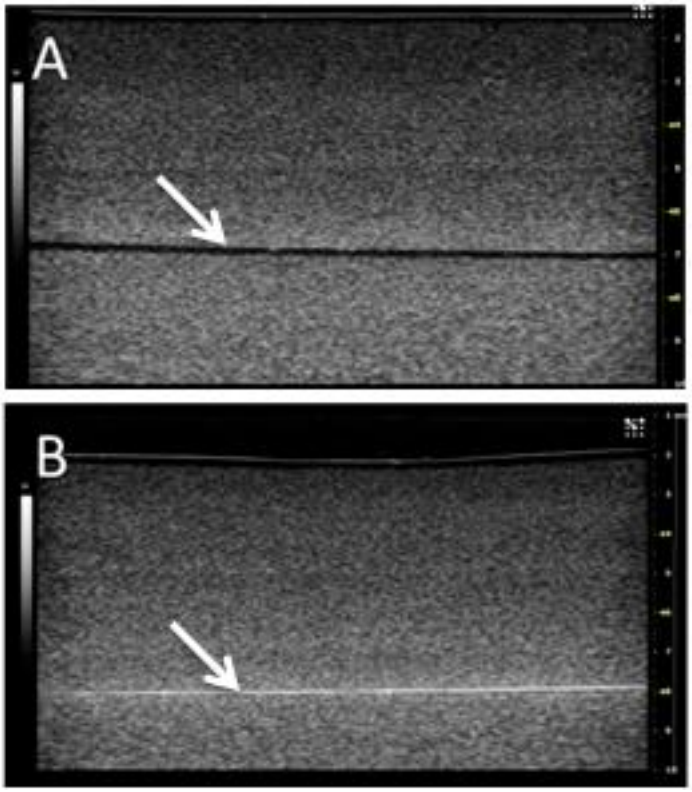

Figure 6.2: Ultrasound imaging of ReANCs through bio mimetic tissue phantoms. Ultrasound imaging of phantoms without (A) and with (B) ReANCs at the interface between two 0.5 cm sections (arrow) shows that the addition of nanoprobes causes a bright contrast, enhancing visualization.

CHAPTER 7

REFERENCES

1. Breast Cancer. http://www.cancer.org/cancer/breastcancer (accessed 3).
2. Sotiriou, C.; Neo, S. Y.; McShane, L. M.; Korn, E. L.; Long, P. M.; Jazaeri, A.; Martiat, P.; Fox, S. B.; Harris, A. L.; Liu, E. T., *Proceedings of the National Academy of Sciences of the United States of America* **2003,** *100* (18), 10393-8. DOI 10.1073/pnas.1732912100.
3. Nemoto, T.; Vana, J.; Bedwani, R. N.; Baker, H. W.; McGregor, F. H.; Murphy, G. P., *Cancer* **1980,** *45* (12), 2917-24.
4. stages of breast cancer. http://www.cancer.gov/cancertopics/pdq/treatment/breast/patient/ (accessed 3).
5. Haffty, B. G.; Yang, Q.; Reiss, M.; Kearney, T.; Higgins, S. A.; Weidhaas, J.; Harris, L.; Hait, W.; Toppmeyer, D., *Journal of clinical oncology : official journal of the American Society of Clinical Oncology* **2006,** *24* (36), 5652-7. DOI 10.1200/JCO.2006.06.5664.
6. Tenofsky, P. L.; Dowell, P.; Topalovski, T.; Helmer, S. D., *American journal of surgery* **2014,** *207* (3), 398-402. DOI 10.1016/j.amjsurg.2013.09.017.
7. Takada, M.; Ishiguro, H.; Nagai, S.; Ohtani, S.; Kawabata, H.; Yanagita, Y.; Hozumi, Y.; Shimizu, C.; Takao, S.; Sato, N.; Kosaka, Y.; Sagara, Y.; Iwata, H.; Ohno, S.; Kuroi, K.; Masuda, N.; Yamashiro, H.; Sugimoto, M.; Kondo, M.; Naito, Y.; Sasano, H.; Inamoto, T.; Morita, S.; Toi, M., *Breast cancer research and treatment* **2014**. DOI 10.1007/s10549-014-2907-9.
8. Medina-Franco, H.; Rojas-Garcia, P.; Suarez-Bobadilla, Y. L.; Sanchez-Ramon, A., *Revista de investigacion clinica; organo del Hospital de Enfermedades de la Nutricion* **2013,** *65* (5), 379-83.
9. Yu, J.; Al Mushawah, F.; Taylor, M. E.; Cyr, A. E.; Gillanders, W. E.; Aft, R. L.; Eberlein, T. J.; Gao, F.; Margenthaler, J. A., *The Journal of surgical research* **2012,** *177* (1), 102-8. DOI 10.1016/j.jss.2012.03.046.
10. Mahmood, U.; Hanlon, A. L.; Koshy, M.; Buras, R.; Chumsri, S.; Tkaczuk, K. H.; Cheston, S. B.; Regine, W. F.; Feigenberg, S. J., *Annals of surgical oncology* **2013,** *20* (5), 1436-43. DOI 10.1245/s10434-012-2732-5.
11. Krag, D. N.; Anderson, S. J.; Julian, T. B.; Brown, A. M.; Harlow, S. P.; Ashikaga, T.; Weaver, D. L.; Miller, B. J.; Jalovec, L. M.; Frazier, T. G.; Noyes, R. D.; Robidoux, A.; Scarth, H. M.; Mammolito, D. M.; McCready, D. R.; Mamounas, E. P.; Costantino, J. P.; Wolmark, N., *The lancet oncology* **2007,** *8* (10), 881-8. DOI 10.1016/S1470-2045(07)70278-4.
12. Melvin Silverstein, E. G., James R. Aaisman, Gergory M. Senofsky, William J. Colburn, Parvais Gamagami, *Cancer* **1994,** *73* (3), 664-667.
13. Zengel, B.; Yararbas, U.; Sirinocak, A.; Ozkok, G.; Denecli, A. G.; Postaci, H.; Uslu, A., *Tumori* **2013,** *99* (2), 149-153.
14. McMasters, K. M.; Wong, S. L.; Chao, C.; Woo, C.; Tuttle, T. M.; Noyes, R. D.; Carlson, D. J.; Laidley, A. L.; McGlothin, T. Q.; Ley, P. B.; Brown, C. M.; Glaser, R. L.; Pennington, R. E.; Turk, P. S.; Simpson, D.; Edwards, M. J.; Stu, U. L. B. C., *Ann Surg* **2001,** *234* (3), 292-299. DOI Doi 10.1097/00000658-200109000-00003.
15. Hassan, M. S.; Ansari, J.; Spooner, D.; Hussain, S. A., *Oncology reports* **2010,** *24* (5), 1121-31.
16. Rizack, T.; Abu-Khalaf, M. M.; Legare, R. D.; Strenger, R.; Fenton, M. A.; Sakr, B. J.; Kennedy, T. A.; Harris, L.; Sikov, W. M.; Univ, B., *Journal of Clinical Oncology* **2010,** *28* (15).
17. Lluch, A.; Alvarez, I.; Munoz, M.; Segui, M. A.; Tusquets, I.; Garcia-Estevez, L., *Critical reviews in oncology/hematology* **2014,** *89* (1), 62-72. DOI 10.1016/j.critrevonc.2013.08.001.
18. Brady, M. L.; Diaz, M. R.; Iuso, A.; Everett, J. C.; Valenzuela, C. F.; Caldwell, K. K., *The Journal of neuroscience : the official journal of the Society for Neuroscience* **2013,** *33* (3), 1062-7. DOI 10.1523/JNEUROSCI.1217-12.2013.

19. Rojo, F.; Albanell, J.; Rovira, A.; Corominas, J. M.; Manzarbeitia, F., *Seminars in diagnostic pathology* **2008,** *25* (4), 245-61.
20. Jones, K. L.; Buzdar, A. U., *Endocrine-related cancer* **2004,** *11* (3), 391-406.
21. Shiau, A. K.; Barstad, D.; Loria, P. M.; Cheng, L.; Kushner, P. J.; Agard, D. A.; Greene, G. L., *Cell* **1998,** *95* (7), 927-937. DOI Doi 10.1016/S0092-8674(00)81717-1.
22. Sawka, C. A.; Pritchard, K. I.; Paterson, A. H. G.; Sutherland, D. J. A.; Thomson, D. B.; Shelley, W. E.; Myers, R. E.; Mobbs, B. G.; Malkin, A.; Meakin, J. W., *Cancer Res* **1986,** *46* (6), 3152-3156.
23. Abe, O.; Abe, R.; Enomoto, K.; Kikuchi, K.; Koyama, H.; Masuda, H.; Nomura, Y.; Sakai, K.; Sugimachi, K.; Tominaga, T.; Uchino, J.; Yoshida, M.; Haybittle, J. L.; Davies, C.; Harvey, V. J.; Holdaway, T. M.; Kay, R. G.; Mason, B. H.; Forbes, J. F.; Wilcken, N.; Gnant, M.; Jakesz, R.; Ploner, M.; Yosef, H. M. A.; Focan, C.; Lobelle, J. P.; Peek, U.; Oates, G. D.; Powell, J.; Durand, M.; Mauriac, L.; Di Leo, A.; Dolci, S.; Piccart, M. J.; Masood, M. B.; Parker, D.; Price, J. J.; Hupperets, P. S. G. J.; Jackson, S.; Ragaz, J.; Berry, D.; Broadwater, G.; Cirrincione, C.; Muss, H.; Norton, L.; Weiss, R. B.; Abu-Zahra, H. T.; Portnoj, S. M.; Baum, M.; Cuzick, J.; Houghton, J.; Riley, D.; Gordon, N. H.; Davis, H. L.; Beatrice, A.; Mihura, J.; Naja, A.; Lehingue, Y.; Romestaing, P.; Dubois, J. B.; Delozier, T.; Mace-Lesec'h, J.; Rambert, P.; Andrysek, O.; Barkmanova, J.; Owen, J. R.; Meier, P.; Howell, A.; Ribeiro, G. C.; Swindell, R.; Alison, R.; Boreham, J.; Clarke, M.; Collins, R.; Darby, S.; Davies, C.; Elphinstone, P.; Evans, V.; Godwin, J.; Gray, R.; Harwood, C.; Hicks, C.; James, S.; MacKinnon, E.; McGale, P.; McHugh, T.; Mead, G.; Peto, R.; Wang, Y.; Albano, J.; de Oliveira, C. F.; Gervasio, H.; Gordilho, J.; Johansen, H.; Mouridsen, H. T.; Gelman, R. S.; Harris, J. R.; Henderson, I. C.; Shapiro, C. L.; Andersen, K. W.; Axelsson, C. K.; Blichert-Toft, M.; Moller, S.; Mouridsen, H. T.; Overgaard, J.; Overgaard, M.; Rose, C.; Cartensen, B.; Palshof, T.; Trampisch, H. J.; Dalesio, O.; de Vries, E. G. E.; Rodenhuis, S.; van Tinteren, H.; Comis, R. L.; Davidson, N. E.; Gray, R.; Robert, N.; Sledge, G.; Tormey, D. C.; Wood, W.; Cameron, D.; Chetty, U.; Forrest, P.; Jack, W.; Rossbach, J.; Klijn, J. G. M.; Treurniet-Donker, A. D.; van Putten, W. L. J.; Costa, A.; Veronesi, U.; Bartelink, H.; Duchateau, L.; Legrand, C.; Sylvester, R.; van der Hage, J. A.; van de Velde, C. J. H.; Cunningham, M. P.; Catalano, R.; Creech, R. H.; Bonneterre, J.; Fargeot, P.; Fumoleau, P.; Kerbrat, P.; Namer, M.; Jonat, W.; Kaufmann, M.; Schumacher, M.; von Minckwitz, G.; Bastert, G.; Rauschecker, H.; Sauer, R.; Sauerbrei, W.; Schauer, A.; Schumacher, M.; de Schryver, A.; Vakaet, L.; Belfiglio, M.; Nicolucci, A.; Pellegrini, F.; Sacco, M.; Valentini, M.; McArdle, C. S.; Smith, D. C.; Galligioni, E.; Boccardo, F.; Rubagotti, A.; Dent, D. M.; Gudgeon, C. A.; Hacking, A.; Erazo, A.; Medina, J. Y.; Izuo, M.; Morishita, Y.; Takei, H.; Fentiman, I. S.; Hayward, J. L.; Rubens, R. D.; Skilton, D.; Graeff, H.; Janicke, F.; Meisner, C.; Scheurlen, H.; Kaufmann, M.; von Fournier, D.; Dafni, U.; Fountzilas, G.; Klefstrom, P.; Blomqvist, C.; Saarto, T.; Margreiter, R.; Asselain, B.; Salmon, R. J.; Vilcoq, J. R.; Arriagada, R.; Hill, C.; Laplanche, A.; Le, M. G.; Spielmann, M.; Bruzzi, P.; Montanaro, E.; Rosso, R.; Sertoli, M. R.; Venturini, M.; Amadori, D.; Benraadt, J.; Kooi, M.; van de Velde, A. O.; van Dongen, J. A.; Vermorken, J. B.; Castiglione, M.; Cavalli, F.; Coates, A.; Collins, J.; Forbes, J.; Gelber, R. D.; Goldhirsch, A.; Lindtner, J.; Price, K. N.; Rudenstam, C. M.; Senn, H. J.; Bliss, J. M.; Chilvers, C. E. D.; Coombes, R. C.; Hall, E.; Marty, M.; Borovik, R.; Brufman, G.; Hayat, H.; Robinson, E.; Wigler, N.; Bonadonna, G.; Camerini, T.; De Palo, G.; Del Vecchio, M.; Formelli, F.; Valagussa, P.; Martoni, A.; Pannuti, F.; Cocconi, G.; Colozza, A.; Camisa, R.; Aogi, K.; Takashima, S.; Abe, O.; Ikeda, T.; Inokuchi, K.; Kikuchi, K.; Sawa, K.; Sonoo, H.; Korzeniowski, S.; Skolyszewski, J.; Ogawa, M.; Yamashita, J.; Bonte, J.; Christiaens, R.; Paridaens, R.; Van den Boegart, W.; Martin, P.; Romain, S.; Hakes, T.; Hudis, C. A.; Norton, L.; Wittes, R.; Giokas, G.; Kondylis, D.; Lissaios, B.; de la Huerta, R.; Sainz, M. G.; Altemus, R.; Cowan, K.; Danforth, D.; Lichter, A.; Lippman, M.; O'Shaughnessy, J.; Pierce, L. J.; Steinberg, S.; Venzon, D.; Zujewski, J.; Paradiso, A.; De Lena, M.; Schittulli, F.; Myles, J. D.; Pater, J. L.; Pritchard, K. I.;

Nomura, Y.; Anderson, S.; Bass, G.; Brown, A.; Bryant, J.; Costantino, J.; Dignam, J.; Fisher, B.; Redmond, C.; Wieand, S.; Wolmark, N.; Baum, M.; Jackson, I. M.; Palmer, M. K.; Ingle, J. N.; Suman, V. J.; Bengtsson, N. O.; Jonsson, H.; Larsson, L. G.; Lythgoe, J. P.; Swindell, R.; Kissin, M.; Erikstein, B.; Hannisdal, E.; Jacobsen, A. B.; Varhaug, J. E.; Erikstein, B.; Gundersen, S.; Hauer-Jensen, M.; Host, H.; Jacobsen, A. B.; Nissen-Meyer, R.; Blamey, R. W.; Mitchell, A. K.; Morgan, D. A. L.; Robertson, J. F. R.; Di Palma, M.; Mathe, G.; Misset, J. L.; Clark, R. M.; Levine, M.; Morimoto, K.; Sawa, K.; Takatsuka, Y.; Crossley, E.; Harris, A.; Talbot, D.; Taylor, M.; Cocconi, G.; di Blasio, B.; Ivanov, V.; Semiglazov, V.; Brockschmidt, J.; Cooper, M. R.; Ueo, H.; Falkson, C. I.; A'Hern, R.; Ashley, S.; Powles, T. J.; Smith, I. E.; Yarnold, J. R.; Gazet, J. C.; Cocoran, N.; Deshpande, N.; di Martino, L.; Douglas, P.; Hacking, A.; Host, H.; Lindtner, A.; Notter, G.; Bryant, A. J. S.; Ewing, G. H.; Firth, L. A.; Krushen-Kosloski, J. L.; Nissen-Meyer, R.; Foster, L.; George, W. D.; Stewart, H. J.; Stroner, P.; Malmstrom, P.; Moller, T. R.; Ryden, S.; Tengrup, I.; Tennvall-Nittby, L.; Carstenssen, J.; Dufmats, M.; Hatschek, T.; Nordenskjold, B.; Soderberg, M.; Carpenter, J. T.; Albain, K.; Crowley, J.; Green, S.; Martino, S.; Osborne, C. K.; Ravdin, P. M.; Glas, U.; Johansson, U.; Rutqvist, L. E.; Singnomklao, T.; Wallgren, A.; Castiglione, M.; Goldhirsch, A.; Maibach, R.; Senn, H. J.; Thurlimann, B.; Brenner, H.; Hercbergs, A.; Yoshimoto, M.; DeBoer, G.; Paterson, A. H. G.; Pritchard, K. I.; Meakin, J. W.; Panzarella, T.; Pritchard, K. I.; Shan, Y.; Shao, Y. F.; Wang, X.; Zhao, D. B.; Boreham, J.; Chen, Z. M.; Pan, H. C.; Peto, R.; Bahi, J.; Reid, M.; Spittle, M.; Deutsch, G. P.; Senanayake, F.; Kwong, D. L. W.; Bianco, A. R.; Carlomagno, C.; De Laurentiis, M.; De Placido, S.; Buzdar, A. U.; Smith, T.; Bergh, J.; Holmberg, L.; Liljegren, G.; Nilsson, J.; Seifert, M.; Sevelda, P.; Zielinsky, C. C.; Buchanan, R. B.; Cross, M.; Royle, G. T.; Dunn, J. A.; Hills, R. K.; Lee, M.; Morrison, J. M.; Spooner, D.; Litton, A.; Chlebowski, R. T.; Caffier, H.; Ebctcg, *Lancet* **2005,** *365* (9472), 1687-1717.

24. Vici, P.; Pizzuti, L.; Natoli, C.; Moscetti, L.; Mentuccia, L.; Vaccaro, A.; Sergi, D.; Di Lauro, L.; Trenta, P.; Seminara, P.; Santini, D.; Iezzi, L.; Tinari, N.; Bertolini, I.; Sini, V.; Mottolese, M.; Giannarelli, D.; Giotta, F.; Maugeri-Sacca, M.; Barba, M.; Marchetti, P.; Michelotti, A.; Sperduti, I.; Gamucci, T., *Breast cancer research and treatment* **2014,** *147* (3), 599-607. DOI 10.1007/s10549-014-3133-1.

25. Murthy, R. K.; Varma, A.; Mishra, P.; Hess, K. R.; Young, E.; Murray, J. L.; Koenig, K. H.; Moulder, S. L.; Melhem-Bertrandt, A.; Giordano, S. H.; Booser, D.; Valero, V.; Hortobagyi, G. N.; Esteva, F. J., *Cancer* **2014,** *120* (13), 1932-8. DOI 10.1002/cncr.28689.

26. Berman, A. T.; Thukral, A. D.; Hwang, W. T.; Solin, L. J.; Vapiwala, N., *Clin Breast Cancer* **2013,** *13* (2), 88-94. DOI 10.1016/j.clbc.2012.11.001.

27. Ogba, N.; Manning, N. G.; Bliesner, B. S.; Ambler, S. K.; Haughian, J. M.; Pinto, M. P.; Jedlicka, P.; Joensuu, K.; Heikkila, P.; Horwitz, K. B., *Breast Cancer Res* **2014,** *16* (6). DOI Artn 489

10.1186/S13058-014-0489-4.

28. Gancberg, D.; Di Leo, A.; Cardoso, F.; Rouas, G.; Pedrocchi, M.; Paesmans, M.; Verhest, A.; Bernard-Marty, C.; Piccart, M. J.; Larsimont, D., *Ann Oncol* **2002,** *13* (7), 1036-1043. DOI 10.1093/annonc/mdf252.

29. Schneble, E. J.; Graham, L. J.; Shupe, M. P.; Flynt, F. L.; Banks, K. P.; Kirkpatrick, A. D.; Nissan, A.; Henry, L.; Stojadinovic, A.; Shumway, N. M.; Peoples, G. E.; Setlik, R. F., *J Cancer* **2014,** *5* (4), 281-290. DOI 10.7150/jca.8016.

30. Graham, L. J.; Shupe, M. P.; Schneble, E. J.; Flynt, F. L.; Clemenshaw, M. N.; Kirkpatrick, A. D.; Gallagher, C.; Nissan, A.; Henry, L.; Stojadinovic, A.; Peoples, G. E.; Shumway, N. M., *J Cancer* **2014,** *5* (1), 58-68. DOI 10.7150/jca.7047.

31. Glendenning, J.; Cook, G., *Semin Nucl Med* **2013,** *43* (4), 317-323. DOI 10.1053/j.semnuclmed.2013.02.002.

32. Pantel, K.; Cote, R. J.; Fodstad, O., *J Natl Cancer I* **1999,** *91* (13), 1113-1124. DOI DOI 10.1093/jnci/91.13.1113.
33. Fass, L., *Molecular oncology* **2008,** *2* (2), 115-52. DOI 10.1016/j.molonc.2008.04.001.
34. Willmann, J. K.; van Bruggen, N.; Dinkelborg, L. M.; Gambhir, S. S., *Nature reviews. Drug discovery* **2008,** *7* (7), 591-607. DOI 10.1038/nrd2290.
35. Weissleder, R., *Science* **2006,** *312* (5777), 1168-1171. DOI 10.1126/science.1125949.
36. Wang, X.; Yang, L. L.; Chen, Z.; Shin, D. M., *Ca-Cancer J Clin* **2008,** *58* (2), 97-110. DOI 10.3322/Ca.2007.0003.
37. Weissleder, R.; Pittet, M. J., *Nature* **2008,** *452* (7187), 580-589. DOI 10.1038/nature06917.
38. Kaijzel, E. L.; van der Pluijm, G.; Lowik, C. W., *Clinical cancer research : an official journal of the American Association for Cancer Research* **2007,** *13* (12), 3490-7. DOI 10.1158/1078-0432.CCR-07-0402.
39. Brindle, K., *Nature reviews. Cancer* **2008,** *8* (2), 94-107. DOI 10.1038/nrc2289.
40. Li, C., *Nature materials* **2014,** *13* (2), 110-5. DOI 10.1038/nmat3877.
41. Yang, S. K.; Cho, N.; Moon, W. K., *Korean journal of radiology* **2007,** *8* (5), 429-37. DOI 10.3348/kjr.2007.8.5.429.
42. Weber, W. A.; Figlin, R., *J Nucl Med* **2007,** *48*, 36s-44s.
43. Czernin, J.; Allen-Auerbach, M.; Schelbert, H. R., *J Nucl Med* **2007,** *48*, 78s-88s.
44. Antoch, G.; Vogt, F. M.; Freudenberg, L. S.; Nazaradeh, F.; Goehde, S. C.; Barkhausen, J.; Dahmen, G.; Bockisch, A.; Debatin, J. F.; Ruehm, S. G., *Jama-J Am Med Assoc* **2003,** *290* (24), 3199-3206. DOI DOI 10.1001/jama.290.24.3199.
45. Hadjipanayis, C. G.; Jiang, H.; Roberts, D. W.; Yang, L., *Seminars in oncology* **2011,** *38* (1), 109-18. DOI 10.1053/j.seminoncol.2010.11.008.
46. Luker, G. D.; Luker, K. E., *J Nucl Med* **2008,** *49* (1), 1-4. DOI 10.2967/jnumed.107.045799.
47. Ntziachristos, V.; Ripoll, J.; Wang, L. V.; Weissleder, R., *Nature biotechnology* **2005,** *23* (3), 313-20. DOI 10.1038/nbt1074.
48. Arridge, S. R., *Inverse Problems* **1999,** *15*, 41-93.
49. Solomon, M.; Liu, Y.; Berezin, M. Y.; Achilefu, S., *Medical principles and practice : international journal of the Kuwait University, Health Science Centre* **2011,** *20* (5), 397-415. DOI 10.1159/000327655.
50. Pierce, M. C.; Javier, D. J.; Richards-Kortum, R., *International journal of cancer* **2008,** *123* (9), 1979-90. DOI 10.1002/ijc.23858.
51. Frangioni, J. V., *Current opinion in chemical biology* **2003,** *7* (5), 626-34.
52. Frangioni, J. V., *Journal of clinical oncology : official journal of the American Society of Clinical Oncology* **2008,** *26* (24), 4012-21. DOI 10.1200/JCO.2007.14.3065.
53. Park, K.; Lee, S.; Kang, E.; Kim, K.; Choi, K.; Kwon, I. C., *Adv Funct Mater* **2009,** *19* (10), 1553-1566. DOI 10.1002/adfm.200801655.
54. Naczynski, D. J.; Tan, M. C.; Zevon, M.; Wall, B.; Kohl, J.; Kulesa, A.; Chen, S.; Roth, C. M.; Riman, R. E.; Moghe, P. V., *Nat Commun* **2013,** *4*. DOI Artn 2199

10.1038/Ncomms3199.
55. Chatteriee, D. K.; Rufalhah, A. J.; Zhang, Y., *Biomaterials* **2008,** *29* (7), 937-943. DOI 10.1016/j.biomaterials.2007.10.051.
56. de Chermont, Q. L.; Chaneac, C.; Seguin, J.; Pelle, F.; Maitrejean, S.; Jolivet, J. P.; Gourier, D.; Bessodes, M.; Scherman, D., *Proceedings of the National Academy of Sciences of the United States of America* **2007,** *104* (22), 9266-9271. DOI 10.1073/pnas.0702427104.
57. Haase, M.; Schaefer, H., *Angewandte Chemie* **2011,** *50*, 2-24.

58. Luedtke, M. A.; Papazoglou, E.; Neidrauer, M.; Kollias, N., *Skin Research and Technology* **2009,** *15* (4), 482-488. DOI DOI 10.1111/j.1600-0846.2009.00394.x.
59. Meinhardt, M.; Krebs, R.; Anders, A.; Heinrich, U.; Tronnier, H., *Journal of Biomedical Optics* **2008,** *13* (4), -. DOI Artn 044030

Doi 10.1117/1.2957970.
60. Jacques, S. L., *Phys Med Biol* **2013,** *58* (14), 5007-5008. DOI 10.1088/0031-9155/58/14/5007.
61. Saidi, I. S.; Jacques, S. L.; Tittel, F. K., *Appl Optics* **1995,** *34* (31), 7410-7418.
62. Hilderbrand, S. A.; Weissleder, R., *Current opinion in chemical biology* **2010,** *14* (1), 71-9. DOI 10.1016/j.cbpa.2009.09.029.
63. Smith, A. M.; Mancini, M. C.; Nie, S. M., *Nature Nanotechnology* **2009,** *4* (11), 710-711. DOI DOI 10.1038/nnano.2009.326.
64. Welsher, K.; Liu, Z.; Sherlock, S. P.; Robinson, J. T.; Chen, Z.; Daranciang, D.; Dai, H., *Nat Nanotechnol* **2009,** *4* (11), 773-80. DOI nnano.2009.294 [pii]

10.1038/nnano.2009.294.
65. Sordillo, L. A.; Pu, Y.; Pratavieira, S.; Budansky, Y.; Alfano, R. R., *Journal of Biomedical Optics* **2014,** *19* (5). DOI Artn 056004

10.1117/1.Jbo.19.5.056004.
66. Gao, J. H.; Chen, X. Y.; Cheng, Z., *Curr Top Med Chem* **2010,** *10* (12), 1147-1157.
67. Altinoglu, E. I.; Adair, J. H., *Wiley interdisciplinary reviews. Nanomedicine and nanobiotechnology* **2010,** *2* (5), 461-77. DOI 10.1002/wnan.77.
68. Meiser, F.; Cortez, C.; Caruso, F., *Angew Chem Int Ed Engl* **2004,** *43* (44), 5954-7. DOI 10.1002/anie.200460856.
69. Naczynski, D. J.; Andelman, T.; Pal, D.; Chen, S.; Riman, R. E.; Roth, C. M.; Moghe, P. V., *Small* **2010,** *6* (15), 1631-40. DOI 10.1002/smll.200902403.
70. Naczynski, D. J.; Tan, M. C.; Zevon, M.; Wall, B.; Kohl, J.; Kulesa, A.; Chen, S.; Roth, C. M.; Riman, R. E.; Moghe, P. V., *Nature communications* **2013,** *4*, 2199. DOI 10.1038/ncomms3199.
71. Chen, J.; Zhao, J. X., *Sensors-Basel* **2012,** *12* (3), 2414-2435. DOI 10.3390/s120302414.
72. Auzel, F., *Chem Rev* **2004,** *104* (1), 139-173. DOI 10.1021/cr020357g.
73. Mai, H. X.; Zhang, Y. W.; Sun, L. D.; Yan, C. R., *J Phys Chem C* **2007,** *111* (37), 13730-13739. DOI 10.1021/jp073919e.
74. Wang, Y.; Tu, L. P.; Zhao, J. W.; Sun, Y. J.; Kong, X. G.; Zhang, H., *J Phys Chem C* **2009,** *113* (17), 7164-7169. DOI 10.1021/jp9003399.
75. Hawkins, M. J.; Soon-Shiong, P.; Desai, N., *Adv Drug Deliver Rev* **2008,** *60* (8), 876-885. DOI DOI 10.1016/j.addr.2007.08.044.
76. Acharya, S.; Sahoo, S. K., *Advanced Drug Delivery Reviews* **2011,** *63* (3), 170-183. DOI 10.1016/j.addr.2010.10.008.
77. Ferrari, M., *Nature Reviews Cancer* **2005,** *5* (3), 161-171. DOI 10.1038/nrc1566.
78. Janib, S. M.; Moses, A. S.; MacKay, J. A., *Advanced Drug Delivery Reviews* **2010,** *62* (11), 1052-1063. DOI 10.1016/j.addr.2010.08.004.
79. Wang, A. Z.; Langer, R.; Farokhzad, O. C., *Annu Rev Med* **2012,** *63*, 185-198. DOI DOI 10.1146/annurev-med-040210-162544.
80. Singh, R.; Lillard, J. W., *Exp Mol Pathol* **2009,** *86* (3), 215-223. DOI 10.1016/j.yexmp.2008.12.004.
81. Redhead, H. M.; Davis, S. S.; Illum, L., *J Control Release* **2001,** *70* (3), 353-363. DOI Doi 10.1016/S0168-3659(00)00367-9.

82. Panyam, J.; Labhasetwar, V., *Advanced Drug Delivery Reviews* **2003,** *55* (3), 329-347. DOI 10.1016/S0169-409x(02)00228-4.
83. Longmire, M.; Choyke, P. L.; Kobayashi, H., *Nanomedicine-Uk* **2008,** *3* (5), 703-717. DOI 10.2217/17435889.3.5.703.
84. Davis, M. E.; Chen, Z.; Shin, D. M., *Nature Reviews Drug Discovery* **2008,** *7* (9), 771-782. DOI 10.1038/nrd2614.
85. Cho, K.; Wang, X.; Nie, S.; Chen, Z. G.; Shin, D. M., *Clinical cancer research : an official journal of the American Association for Cancer Research* **2008,** *14* (5), 1310-6. DOI 10.1158/1078-0432.CCR-07-1441.
86. Wilczewska, A. Z.; Niemirowicz, K.; Markiewicz, K. H.; Car, H., *Pharmacological reports : PR* **2012,** *64* (5), 1020-37.
87. Li, H. J.; Du, J. Z.; Du, X. J.; Xu, C. F.; Sun, C. Y.; Wang, H. X.; Cao, Z. T.; Yang, X. Z.; Zhu, Y. H.; Nie, S.; Wang, J., *Proceedings of the National Academy of Sciences of the United States of America* **2016**. DOI 10.1073/pnas.1522080113.
88. Cui, M.; Naczynski, D. J.; Zevon, M.; Griffith, C. K.; Sheihet, L.; Poventud-Fuentes, I.; Chen, S.; Roth, C. M.; Moghe, P. V., *Advanced healthcare materials* **2013,** *2* (9), 1236-45. DOI 10.1002/adhm.201200467.
89. Wong, C.; Stylianopoulos, T.; Cui, J. A.; Martin, J.; Chauhan, V. P.; Jiang, W.; Popovic, Z.; Jain, R. K.; Bawendi, M. G.; Fukumura, D., *Proceedings of the National Academy of Sciences of the United States of America* **2011,** *108* (6), 2426-2431. DOI 10.1073/pnas.1018382108.
90. Owens, D. E., 3rd; Peppas, N. A., *International journal of pharmaceutics* **2006,** *307* (1), 93-102. DOI 10.1016/j.ijpharm.2005.10.010.
91. Patil, S.; Sandberg, A.; Heckert, E.; Self, W.; Seal, S., *Biomaterials* **2007,** *28* (31), 4600-7. DOI 10.1016/j.biomaterials.2007.07.029.
92. Bazak, R.; Houri, M.; Achy, S. E.; Hussein, W.; Refaat, T., *Molecular and clinical oncology* **2014,** *2* (6), 904-908. DOI 10.3892/mco.2014.356.
93. Alexis, F.; Pridgen, E.; Molnar, L. K.; Farokhzad, O. C., *Molecular pharmaceutics* **2008,** *5* (4), 505-15. DOI 10.1021/mp800051m.
94. Farokhzad, O. C.; Cheng, J.; Teply, B. A.; Sherifi, I.; Jon, S.; Kantoff, P. W.; Richie, J. P.; Langer, R., *Proceedings of the National Academy of Sciences of the United States of America* **2006,** *103* (16), 6315-20. DOI 10.1073/pnas.0601755103.
95. Tassa, C.; Duffner, J. L.; Lewis, T. A.; Weissleder, R.; Schreiber, S. L.; Koehler, A. N.; Shaw, S. Y., *Bioconjugate chemistry* **2010,** *21* (1), 14-9. DOI 10.1021/bc900438a.
96. Allen, T. M.; Cullis, P. R., *Adv Drug Deliver Rev* **2013,** *65* (1), 36-48. DOI 10.1016/j.addr.2012.09.037.
97. Varkouhi, A. K.; Scholte, M.; Storm, G.; Haisma, H. J., *J Control Release* **2011,** *151* (3), 220-8. DOI 10.1016/j.jconrel.2010.11.004.
98. Safdar, A.; Ma, J.; Saliba, F.; Dupont, B.; Wingard, J. R.; Hachem, R. Y.; Mattiuzzi, G. N.; Chandrasekar, P. H.; Kontoyiannis, D. P.; Rolston, K. V.; Walsh, T. J.; Champlin, R. E.; Raad, II, *Medicine* **2010,** *89* (4), 236-44. DOI 10.1097/MD.0b013e3181e9441b.
99. Magin, R. L.; Wright, S. M.; Niesman, M. R.; Chan, H. C.; Swartz, H. M., *Magnetic resonance in medicine* **1986,** *3* (3), 440-7.
100. Gabizon, A.; Shmeeda, H.; Barenholz, Y., *Clinical pharmacokinetics* **2003,** *42* (5), 419-36. DOI 10.2165/00003088-200342050-00002.
101. Daemen, T.; Hofstede, G.; Ten Kate, M. T.; Bakker-Woudenberg, I. A.; Scherphof, G. L., *International journal of cancer* **1995,** *61* (5), 716-21.
102. Liechty, W. B.; Kryscio, D. R.; Slaughter, B. V.; Peppas, N. A., *Annu Rev Chem Biomol Eng* **2010,** *1*, 149-73. DOI 10.1146/annurev-chembioeng-073009-100847.

103. Wang, M.; Thanou, M., *Pharmacol Res* **2010,** *62* (2), 90-99. DOI 10.1016/j.phrs.2010.03.005.
104. Alexis, F.; Rhee, J. W.; Richie, J. P.; Radovic-Moreno, A. F.; Langer, R.; Farokhzad, O. C., *Urol Oncol-Semin Ori* **2008,** *26* (1), 74-85. DOI 10.1016/j.urolonc.2007.03.017.
105. Park, J.; Fong, P. M.; Lu, J.; Russell, K. S.; Booth, C. J.; Saltzman, W. M.; Fahmy, T. M., *Nanomed-Nanotechnol* **2009,** *5* (4), 410-418. DOI 10.1016/j.nano.2009.02.002.
106. Doria, G.; Conde, J.; Veigas, B.; Giestas, L.; Almeida, C.; Assuncao, M.; Rosa, J.; Baptista, P. V., *Sensors-Basel* **2012,** *12* (2), 1657-1687. DOI 10.3390/s120201657.
107. Dreaden, E. C.; Austin, L. A.; Mackey, M. A.; El-Sayed, M. A., *Therapeutic delivery* **2012,** *3* (4), 457-78.
108. von Maltzahn, G.; Park, J. H.; Agrawal, A.; Bandaru, N. K.; Das, S. K.; Sailor, M. J.; Bhatia, S. N., *Cancer Res* **2009,** *69* (9), 3892-3900. DOI 10.1158/0008-5472.CAN-08-4242.
109. Diaz, M. R.; Vivas-Mejia, P. E., *Pharmaceuticals (Basel)* **2013,** *6* (11), 1361-80. DOI 10.3390/ph6111361.
110. Kratz, F., *J Control Release* **2008,** *132* (3), 171-183. DOI DOI 10.1016/j.jconrel.2008.05.010.
111. Elzoghby, A. O.; Samy, W. M.; Elgindy, N. A., *J Control Release* **2012,** *157* (2), 168-182. DOI 10.1016/j.jconrel.2011.07.031.
112. Fasano, M.; Curry, S.; Terreno, E.; Galliano, M.; Fanali, G.; Narciso, P.; Notari, S.; Ascenzi, P., *IUBMB life* **2005,** *57* (12), 787-96. DOI 10.1080/15216540500404093.
113. Desai, N.; Trieu, V.; Damascelli, B.; Soon-Shiong, P., *Translational oncology* **2009,** *2* (2), 59-64.
114. Abraxane. http://www.abraxane.com/ (accessed 4).
115. Neesse, A.; Michl, P.; Tuveson, D. A.; Ellenrieder, V., *Zeitschrift fur Gastroenterologie* **2014**. DOI 10.1055/s-0034-1366002.
116. Langer, K.; Balthasar, S.; Vogel, V.; Dinauer, N.; von Briesen, H.; Schubert, D., *International journal of pharmaceutics* **2003,** *257* (1-2), 169-80.
117. Bohidar, H. B.; Mohanty, B., *Physical review. E, Statistical, nonlinear, and soft matter physics* **2004,** *69* (2 Pt 1), 021902.
118. Mohanty, B.; Bohidar, H. B., *Biomacromolecules* **2003,** *4* (4), 1080-6. DOI 10.1021/bm034080l.
119. Weber, C.; Coester, C.; Kreuter, J.; Langer, K., *International journal of pharmaceutics* **2000,** *194* (1), 91-102.
120. Minchinton, A. I.; Tannock, I. F., *Nature Reviews Cancer* **2006,** *6* (8), 583-592. DOI Doi 10.1038/Nrc1893.
121. Jain, R. K.; Stylianopoulos, T., *Nat Rev Clin Oncol* **2010,** *7* (11), 653-664. DOI Doi 10.1038/Nrclinonc.2010.139.
122. Hambley, T. W., *Cancer Res* **2009,** *69* (4), 1259-1261. DOI Doi 10.1158/0008-5472.Can-08-3786.
123. Primeau, A. J.; Rendon, A.; Hedley, D.; Lilge, L.; Tannock, I. F., *Clinical Cancer Research* **2005,** *11* (24), 8782-8788. DOI Doi 10.1158/1078-0432.Ccr-05-1664.
124. Szakacs, G.; Paterson, J. K.; Ludwig, J. A.; Booth-Genthe, C.; Gottesman, M. M., *Nature Reviews Drug Discovery* **2006,** *5* (3), 219-234. DOI Doi 10.1038/Nrd1984.
125. Lipinski, C. A.; Lombardo, F.; Dominy, B. W.; Feeney, P. J., *Advanced Drug Delivery Reviews* **2001,** *46* (1-3), 3-26.
126. Rabinow, B. E., *Nature Reviews Drug Discovery* **2004,** *3* (9), 785-796. DOI Doi 10.1038/Nrd1494.

127. Tannock, I. F.; Lee, C. M.; Tunggal, J. K.; Cowan, D. S. M.; Egorin, M. J., *Clinical Cancer Research* **2002,** *8* (3), 878-884.
128. Gottesman, M. M., *Annual Review of Medicine* **2002,** *53*, 615-627.
129. Morgillo, F.; Lee, H. Y., *Drug Resistance Updates* **2005,** *8* (5), 298-310. DOI DOI 10.1016/j.drup.2005.08.004.
130. Smalley, K. S. M.; Haass, N. K.; Brafford, P. A.; Lioni, M.; Flaherty, K. T.; Herlyn, M., *Molecular Cancer Therapeutics* **2006,** *5* (5), 1136-1144. DOI Doi 10.1158/1535-7163.Mct-06-0084.
131. Flaherty, K. T.; Puzanov, I.; Kim, K. B.; Ribas, A.; McArthur, G. A.; Sosman, J. A.; O'Dwyer, P. J.; Lee, R. J.; Grippo, J. F.; Nolop, K.; Chapman, P. B., *New England Journal of Medicine* **2010,** *363* (9), 809-819.
132. Petros, R. A.; DeSimone, J. M., *Nature Reviews Drug Discovery* **2010,** *9* (8), 615-627. DOI Doi 10.1038/Nrd2591.
133. Merisko-Liversidge, E. M.; Liversidge, G. G., *Toxicol Pathol* **2008,** *36* (1), 43-48. DOI Doi 10.1177/0192623307310946.
134. Kim, T. Y.; Kim, D. W.; Chung, J. Y.; Shin, S. G.; Kim, S. C.; Heo, D. S.; Kim, N. K.; Bang, Y. J., *Clinical Cancer Research* **2004,** *10* (11), 3708-3716.
135. Nyman, D. W.; Campbell, K. J.; Hersh, E.; Long, K.; Richardson, K.; Trieu, V.; Desai, N.; Hawkins, M. J.; Von Hoff, D. D., *Journal of Clinical Oncology* **2005,** *23* (31), 7785-7793. DOI Doi 10.1200/Jco.2004.00.6148.
136. Haag, R.; Kratz, F., *Angew Chem Int Edit* **2006,** *45* (8), 1198-1215. DOI Doi 10.1002/Anie.200502113.
137. Min, K. H.; Park, K.; Kim, Y. S.; Bae, S. M.; Lee, S.; Jo, H. G.; Park, R. W.; Kim, I. S.; Jeong, S. Y.; Kim, K.; Kwon, I. C., *J Control Release* **2008,** *127* (3), 208-218. DOI Doi 10.1016/J.Jconrel.2008.01.013.
138. Gelderblom, H.; Verweij, J.; Nooter, K.; Sparreboom, A., *Eur J Cancer* **2001,** *37* (13), 1590-1598.
139. Hawkins, M. J.; Soon-Shiong, P.; Desai, N., *Advanced Drug Delivery Reviews* **2008,** *60* (8), 876-885. DOI Doi 10.1016/J.Addr.2007.08.044.
140. Kearns, C. M., *Pharmacotherapy* **1997,** *17* (5), S105-S109.
141. Mross, K.; Hollander, N.; Hauns, B.; Schumacher, M.; Maier-Lenz, H., *Cancer Chemoth Pharm* **2000,** *45* (6), 463-470.
142. Cortes, J.; Saura, C., *Ejc Suppl* **2010,** *8* (1), 1-10.
143. Allen, T. M., *Nature Reviews Cancer* **2002,** *2* (10), 750-763. DOI Doi 10.1038/Nrc903.
144. Cho, K. J.; Wang, X.; Nie, S. M.; Chen, Z.; Shin, D. M., *Clinical Cancer Research* **2008,** *14* (5), 1310-1316. DOI Doi 10.1158/1078-0432.Ccr-07-1441.
145. Ruoslahti, E.; Bhatia, S. N.; Sailor, M. J., *J Cell Biol* **2010,** *188* (6), 759-68. DOI jcb.200910104 [pii]

10.1083/jcb.200910104.
146. Heldin, C. H.; Rubin, K.; Pietras, K.; Ostman, A., *Nature reviews. Cancer* **2004,** *4* (10), 806-13. DOI nrc1456 [pii]

10.1038/nrc1456.
147. Ferrari, M., *Nat Rev Cancer* **2005,** *5* (3), 161-71. DOI nrc1566 [pii]

10.1038/nrc1566.
148. Goodman, T. T.; Olive, P. L.; Pun, S. H., *Int J Nanomedicine* **2007,** *2* (2), 265-74.

149. Aryal, S.; Hu, C. M. J.; Zhang, L. F., *Small* **2010,** *6* (13), 1442-1448. DOI Doi 10.1002/Smll.201000631.
150. Sengupta, S.; Eavarone, D.; Capila, I.; Zhao, G. L.; Watson, N.; Kiziltepe, T.; Sasisekharan, R., *Nature* **2005,** *436* (7050), 568-572. DOI Doi 10.1038/Nature03794.
151. Shin, S. S.; Wall, B. A.; Goydos, J. S.; Chen, S. Z., *Pigm Cell Melanoma R* **2010,** *23* (1), 103-111. DOI Doi 10.1111/J.1755-148x.2009.00648.X.
152. Riccardi, C.; Nicoletti, I., *Nature protocols* **2006,** *1* (3), 1458-61. DOI 10.1038/nprot.2006.238.
153. Goodman, T. T.; Olive, P. L.; Pun, S. H., *International Journal of Nanomedicine* **2007,** *2* (2), 265-274.
154. Kuhn, S. J.; Finch, S. K.; Hallahan, D. E.; Giorgio, T. D., *Nano Letters* **2006,** *6* (2), 306-312. DOI Doi 10.1021/Nl052241g.
155. Ibrahim, N. K.; Samuels, B.; Page, R.; Doval, D.; Patel, K. M.; Rao, S. C.; Nair, M. K.; Bhar, P.; Desai, N.; Hortobagyi, G. N., *Journal of Clinical Oncology* **2005,** *23* (25), 6019-6026. DOI Doi 10.1200/Jco.2005.11.013.
156. Harries, M.; Ellis, P.; Harper, P., *Journal of Clinical Oncology* **2005,** *23* (31), 7768-7771. DOI Doi 10.1200/Jco.2005.08.002.
157. Ibrahim, N. K.; Desai, N.; Legha, S.; Soon-Shiong, P.; Theriault, R. L.; Rivera, E.; Esmaeli, B.; Ring, S. E.; Bedikian, A.; Hortobagyi, G. N.; Ellerhorst, J. A., *Clinical cancer research : an official journal of the American Association for Cancer Research* **2002,** *8* (5), 1038-44.
158. Desai, N., *Nanomed-Nanotechnol* **2007,** *3* (4), 339-339. DOI DOI 10.1016/j.nano.2007.10.021.
159. Desai, N.; Trieu, V.; Damascelli, B.; Soon-Shiong, P., *Translational Oncology* **2009,** *2* (2), 59-64. DOI Doi 10.1593/Tlo.09109.
160. Desai, N.; Trieu, V.; Yao, Z., *Clinical Cancer Research* **2006,** *12* (12), 3869-3869.
161. Sutherland, R. M., *Science* **1988,** *240* (4849), 177-84.
162. Petros, R. A.; DeSimone, J. M., *Nat Rev Drug Discov* **2010,** *9* (8), 615-627.
163. Curran, S.; Murray, G. I., *J Pathol* **1999,** *189* (3), 300-8. DOI 10.1002/(SICI)1096-9896(199911)189:3<300::AID-PATH456>3.0.CO;2-C [pii]

10.1002/(SICI)1096-9896(199911)189:3<300::AID-PATH456>3.0.CO;2-C.
164. Eikenes, L.; Bruland, O. S.; Brekken, C.; Davies Cde, L., *Cancer Res* **2004,** *64* (14), 4768-73. DOI 10.1158/0008-5472.CAN-03-1472

64/14/4768 [pii].
165. Anhorn, M. G.; Wagner, S.; Kreuter, J.; Langer, K.; von Briesen, H., *Bioconjugate chemistry* **2008,** *19* (12), 2321-31. DOI 10.1021/bc8002452.
166. Ghuman, J.; Zunszain, P. A.; Petitpas, I.; Bhattacharya, A. A.; Otagiri, M.; Curry, S., *Journal of Molecular Biology* **2005,** *353* (1), 38-52. DOI DOI 10.1016/j.jmb.2005.07.075.
167. Anand, P.; Kunnumakkara, A. B.; Newman, R. A.; Aggarwal, B. B., *Molecular pharmaceutics* **2007,** *4* (6), 807-818. DOI Doi 10.1021/Mp700113r.
168. Aggarwal, B. B.; Sung, B., *Trends in Pharmacological Sciences* **2009,** *30* (2), 85-94. DOI DOI 10.1016/j.tips.2008.11.002.
169. Bush, J. A.; Cheung, K. J., Jr.; Li, G., *Experimental cell research* **2001,** *271* (2), 305-14. DOI 10.1006/excr.2001.5381.
170. Odot, J.; Albert, P.; Carlier, A.; Tarpin, M.; Devy, J.; Madoulet, C., *International journal of cancer* **2004,** *111* (3), 381-7. DOI 10.1002/ijc.20160.

171. Garg, A. K.; Buchholz, T. A.; Aggarwal, B. B., *Antioxidants & Redox Signaling* **2005,** *7* (11-12), 1630-1647.
172. Pollock, P. M.; Cohen-Solal, K.; Sood, R.; Namkoong, J.; Martino, J. J.; Koganti, A.; Zhu, H.; Robbins, C.; Makalowska, I.; Shin, S. S.; Marin, Y.; Roberts, K. G.; Yudt, L. M.; Chen, A.; Cheng, J.; Incao, A.; Pinkett, H. W.; Graham, C. L.; Dunn, K.; Crespo-Carbone, S. M.; Mackason, K. R.; Ryan, K. B.; Sinsimer, D.; Goydos, J.; Reuhl, K. R.; Eckhaus, M.; Meltzer, P. S.; Pavan, W. J.; Trent, J. M.; Chen, S., *Nat Genet* **2003,** *34* (1), 108-12. DOI 10.1038/ng1148

ng1148 [pii].
173. Namkoong, J.; Shin, S. S.; Lee, H. J.; Marin, Y. E.; Wall, B. A.; Goydos, J. S.; Chen, S., *Cancer Res* **2007,** *67* (5), 2298-305. DOI 10.1158/0008-5472.can-06-3665.
174. J. Namkoong, S. S. S., H. J. Lee, Y. E. Marin, B. A. Wall, J. S. Goydos, S. Chen,, *Cancer Res* **2007**, 2298-2305.
175. Yip, D.; Le, M. N.; Chan, J. L.; Lee, J. H.; Mehnert, J. A.; Yudd, A.; Kempf, J.; Shih, W. J.; Chen, S.; Goydos, J. S., *Clinical cancer research : an official journal of the American Association for Cancer Research* **2009,** *15* (11), 3896-902. DOI 10.1158/1078-0432.ccr-08-3303.
176. Bush, J. A.; Cheung, K. J. J.; Li, G., *Experimental cell research* **2001,** *271* (2), 305-314. DOI Doi 10.1006/Excr.2001.5381.
177. Alelyunas, Y. W.; Empfield, J. R.; McCarthy, D.; Spreen, R. C.; Bui, K.; Pelosi-Kilby, L.; Shen, C., *Bioorganic & Medicinal Chemistry Letters* **2010,** *20* (24), 7312-7316. DOI DOI 10.1016/j.bmcl.2010.10.068.
178. Lim, Y. T.; Kim, S.; Nakayama, A.; Stott, N. E.; Bawendi, M. G.; Frangioni, J. V., *Molecular imaging* **2003,** *2* (1), 50-64.
179. Bashkatov, A. N.; Genina, E. A.; Kochubey, V. I.; Tuchin, V. V., *Opt Spectrosc+* **2005,** *99* (5), 836-842. DOI Doi 10.1134/1.2135863.
180. Zonios, G.; Bykowski, J.; Kollias, N., *J Invest Dermatol* **2001,** *117* (6), 1452-1457. DOI DOI 10.1046/j.0022-202x.2001.01577.x.
181. Weissleder, R.; Ntziachristos, V., *Nat Med* **2003,** *9* (1), 123-128. DOI 10.1038/nm0103-123.
182. Smith, A. M.; Mancini, M. C.; Nie, S., *Nat Nanotechnol* **2009,** *4* (11), 710-1. DOI 10.1038/nnano.2009.326.
183. Rogach, A. L.; Eychmuller, A.; Hickey, S. G.; Kershaw, S. V., *Small* **2007,** *3* (4), 536-557. DOI 10.1002/smll.200600625.
184. Hardman, R., *Environ Health Persp* **2006,** *114* (2), 165-172. DOI 10.1289/ehp.8284.
185. Welsher, K.; Sherlock, S. P.; Dai, H., *Proceedings of the National Academy of Sciences of the United States of America* **2011,** *108* (22), 8943-8. DOI 10.1073/pnas.1014501108.
186. Hong, G.; Lee, J. C.; Robinson, J. T.; Raaz, U.; Xie, L.; Huang, N. F.; Cooke, J. P.; Dai, H., *Nat Med* **2012,** *18* (12), 1841-6. DOI 10.1038/nm.2995.
187. Perrault, S. D.; Walkey, C.; Jennings, T.; Fischer, H. C.; Chan, W. C., *Nano Lett* **2009,** *9* (5), 1909-15. DOI 10.1021/nl900031y.
188. Mei Chee Tan, G. A. K., Richard E. Riman, M. G. Brik, E. Brown and U. Hommerich, *Journal of Applied Physics* **2009,** *106* (063118).
189. Reynolds, F.; O'Loughlin, T.; Weissleder, R.; Josephson, L., *Analytical chemistry* **2005,** *77* (3), 814-7. DOI 10.1021/ac049307x.
190. Bryan van Saders, L. A.-B., Mei Chee Tan, and Richard E. Riman *Optical Materials Express* **2013,** *3* (5), 566-573. DOI 10.1364/OME.3.000566.
191. Tan MC, C. J., Riman RE, *The Journal of Physical Chemistry* **2011,** *115* (36), 17952-17957. DOI 10.1021/jp203735n.

192. *Health physics* **2000,** *79* (4), 431-40.
193. Davis, M. E.; Chen, Z. G.; Shin, D. M., *Nature reviews. Drug discovery* **2008,** *7* (9), 771-82. DOI 10.1038/nrd2614.
194. Xiong, L.; Yang, T.; Yang, Y.; Xu, C.; Li, F., *Biomaterials* **2010,** *31* (27), 7078-85. DOI 10.1016/j.biomaterials.2010.05.065.
195. Abdul Jalil, R.; Zhang, Y., *Biomaterials* **2008,** *29* (30), 4122-8. DOI 10.1016/j.biomaterials.2008.07.012.
196. Murthy, R.; Nunez, R.; Szklaruk, J.; Erwin, W.; Madoff, D. C.; Gupta, S.; Ahrar, K.; Wallace, M. J.; Cohen, A.; Coldwell, D. M.; Kennedy, A. S.; Hicks, M. E., *Radiographics : a review publication of the Radiological Society of North America, Inc* **2005,** *25 Suppl 1*, S41-55. DOI 10.1148/rg.25si055515.
197. Liu, Z.; Cai, W.; He, L.; Nakayama, N.; Chen, K.; Sun, X.; Chen, X.; Dai, H., *Nat Nanotechnol* **2007,** *2* (1), 47-52. DOI 10.1038/nnano.2006.170.
198. Harivardhan Reddy, L.; Sharma, R. K.; Chuttani, K.; Mishra, A. K.; Murthy, R. S., *J Control Release* **2005,** *105* (3), 185-98. DOI 10.1016/j.jconrel.2005.02.028.
199. Arvizo, R. R.; Miranda, O. R.; Moyano, D. F.; Walden, C. A.; Giri, K.; Bhattacharya, R.; Robertson, J. D.; Rotello, V. M.; Reid, J. M.; Mukherjee, P., *PloS one* **2011,** *6* (9), e24374. DOI 10.1371/journal.pone.0024374.
200. Desai, N.; Trieu, V.; Yao, Z.; Louie, L.; Ci, S.; Yang, A.; Tao, C.; De, T.; Beals, B.; Dykes, D.; Noker, P.; Yao, R.; Labao, E.; Hawkins, M.; Soon-Shiong, P., *Clinical cancer research : an official journal of the American Association for Cancer Research* **2006,** *12* (4), 1317-24. DOI 10.1158/1078-0432.CCR-05-1634.
201. Zevon, M.; Ganapathy, V.; Kantamneni, H.; Mingozzi, M.; Kim, P.; Adler, D.; Sheng, Y.; Tan, M. C.; Pierce, M.; Riman, R. E.; Roth, C. M.; Moghe, P. V., *Small* **2015,** *11* (47), 6347-57. DOI 10.1002/smll.201502202.
202. Cui, M.; Naczynski, D. J.; Zevon, M.; Griffith, C. K.; Sheihet, L.; Poventud-Fuentes, I.; Chen, S.; Roth, C. M.; Moghe, P. V., *Adv Healthc Mater* **2013,** *2* (9), 1236-45. DOI 10.1002/adhm.201200467.
203. Clemons, M.; Danson, S.; Hamilton, T.; Goss, P., *Cancer treatment reviews* **2001,** *27* (2), 67-82. DOI 10.1053/ctrv.2000.0204.
204. Weigelt, B.; Peterse, J. L.; van 't Veer, L. J., *Nature reviews. Cancer* **2005,** *5* (8), 591-602. DOI 10.1038/nrc1670.
205. Seemann, M. D., *Technology in cancer research & treatment* **2005,** *4* (5), 577-82.
206. Antoch, G.; Bockisch, A., *European journal of nuclear medicine and molecular imaging* **2009,** *36 Suppl 1*, S113-20. DOI 10.1007/s00259-008-0951-6.
207. Hwang, J. Y.; Park, J.; Kang, B. J.; Lubow, D. J.; Chu, D.; Farkas, D. L.; Shung, K. K.; Medina-Kauwe, L. K., *PloS one* **2012,** *7* (4), e34463. DOI 10.1371/journal.pone.0034463.
208. Resch-Genger, U.; Grabolle, M.; Cavaliere-Jaricot, S.; Nitschke, R.; Nann, T., *Nat Methods* **2008,** *5* (9), 763-75. DOI nmeth.1248 [pii]

10.1038/nmeth.1248.
209. He, H.; Xie, C.; Ren, J., *Analytical chemistry* **2008,** *80* (15), 5951-7. DOI 10.1021/ac8005796.
210. Diao, S., Hong, Guosong, Antaris, Alexander, Blackburn, Jeffrey, Cheng, Kai, Cheng, Zhen, Dai, Hongjie, *Nano Research* **2015,** *8* (9), 3027-3034. DOI 10.1007/s12274-015-0808-9.
211. Villa, I.; Vedda, A.; Cantarelli, I. X.; Pedroni, M.; Piccinelli, F.; Bettinelli, M.; Speghini, A.; Quintanilla, M.; Vetrone, F.; Rocha, U.; Jacinto, C.; Carrasco, E.; Rodriguez, F. S.; Juarranz, A.; del

Rosal, B.; Ortgies, D. H.; Gonzalez, P. H.; Sole, J. G.; Garcia, D. J., *Nano Research* **2015,** *8* (2), 649-665. DOI 10.1007/s12274-014-0549-1.

212. Riman, R. E.; Kumar, G. A.; Atakan, V.; Brennan, J. G.; Ballato, J., *Proc. SPIE-Int. Soc. Opt. Eng.* **2007,** *6707* (Copyright (C) 2013 American Chemical Society (ACS). All Rights Reserved.), 670707/1-670707/11. DOI 10.1117/12.740828.

213. Riman, R. E.; Tan, M. C.; Gangadharan, K. A. Near Infrared-Emitting ER and Yb/Er doped CeF3 Nanoparticulates with no visible upconversion. **2012**.

214. Cui, M.; Naczynski, D. J.; Zevon, M.; Griffith, C. K.; Sheihet, L.; Poventud-Fuentes, I.; Chen, S.; Roth, C. M.; Moghe, P. V., *Adv Healthc Mater* **2013**. DOI 10.1002/adhm.201200467.

215. Hendrix, C. W.; Flexner, C.; MacFarland, R. T.; Giandomenico, C.; Fuchs, E. J.; Redpath, E.; Bridger, G.; Henson, G. W., *Antimicrobial agents and chemotherapy* **2000,** *44* (6), 1667-73.

216. Le Bon, B.; Van Craynest, N.; Daoudi, J. M.; Di Giorgio, C.; Domb, A. J.; Vierling, P., *Bioconjugate chemistry* **2004,** *15* (2), 413-23. DOI 10.1021/bc034220o.

217. Hinton, C. V.; Avraham, S.; Avraham, H. K., *Clinical & experimental metastasis* **2010,** *27* (2), 97-105. DOI 10.1007/s10585-008-9210-2.

218. Muller, A.; Homey, B.; Soto, H.; Ge, N.; Catron, D.; Buchanan, M. E.; McClanahan, T.; Murphy, E.; Yuan, W.; Wagner, S. N.; Barrera, J. L.; Mohar, A.; Verastegui, E.; Zlotnik, A., *Nature* **2001,** *410* (6824), 50-6. DOI 10.1038/35065016.

219. Zlotnik, A., *Contributions to microbiology* **2006,** *13*, 191-9. DOI 10.1159/000092973.

220. Nimmagadda, S.; Pullambhatla, M.; Stone, K.; Green, G.; Bhujwalla, Z. M.; Pomper, M. G., *Cancer Res* **2010,** *70* (10), 3935-44. DOI 10.1158/0008-5472.CAN-09-4396.

221. Kratz, F., *J Control Release* **2008,** *132* (3), 171-83. DOI 10.1016/j.jconrel.2008.05.010.

222. Paal, K.; Muller, J.; Hegedus, L., *European journal of biochemistry / FEBS* **2001,** *268* (7), 2187-91.

223. Kang, Y.; Siegel, P. M.; Shu, W.; Drobnjak, M.; Kakonen, S. M.; Cordon-Cardo, C.; Guise, T. A.; Massague, J., *Cancer cell* **2003,** *3* (6), 537-49.

224. Sun, Y.; Mao, X.; Fan, C.; Liu, C.; Guo, A.; Guan, S.; Jin, Q.; Li, B.; Yao, F.; Jin, F., *Tumour biology : the journal of the International Society for Oncodevelopmental Biology and Medicine* **2014,** *35* (8), 7765-73. DOI 10.1007/s13277-014-1816-1.

225. Ganapathy, V.; Ge, R.; Grazioli, A.; Xie, W.; Banach-Petrosky, W.; Kang, Y.; Lonning, S.; McPherson, J.; Yingling, J. M.; Biswas, S.; Mundy, G. R.; Reiss, M., *Molecular cancer* **2010,** *9*, 122. DOI 10.1186/1476-4598-9-122.

226. Minn, A. J.; Gupta, G. P.; Siegel, P. M.; Bos, P. D.; Shu, W.; Giri, D. D.; Viale, A.; Olshen, A. B.; Gerald, W. L.; Massague, J., *Nature* **2005,** *436* (7050), 518-24. DOI 10.1038/nature03799.

227. Minn, A. J.; Kang, Y.; Serganova, I.; Gupta, G. P.; Giri, D. D.; Doubrovin, M.; Ponomarev, V.; Gerald, W. L.; Blasberg, R.; Massague, J., *The Journal of clinical investigation* **2005,** *115* (1), 44-55. DOI 10.1172/JCI22320.

228. Kelly, K. A.; Bardeesy, N.; Anbazhagan, R.; Gurumurthy, S.; Berger, J.; Alencar, H.; DePinho, R. A.; Mahmood, U.; Weissleder, R., *Plos Med* **2008,** *5* (4), 657-668. DOI ARTN e85

DOI 10.1371/journal.pmed.0050085.

229. Xiao, Z. Y.; Levy-Nissenbaum, E.; Alexis, F.; Luptak, A.; Teply, B. A.; Chan, J. M.; Shi, J. J.; Digga, E.; Cheng, J.; Langer, R.; Farokhzad, O. C., *Acs Nano* **2012,** *6* (1), 696-704. DOI Doi 10.1021/Nn204165v.

230. Bartlett, D. W.; Su, H.; Hildebrandt, I. J.; Weber, W. A.; Davis, M. E., *Proceedings of the National Academy of Sciences of the United States of America* **2007,** *104* (39), 15549-54. DOI 10.1073/pnas.0707461104.

231. Kang, M. J.; Park, S. H.; Kang, M. H.; Park, M. J.; Choi, Y. W., *Int J Nanomedicine* **2013,** *8*, 1155-65. DOI 10.2147/IJN.S39491.
232. Low, K.; Wacker, M.; Wagner, S.; Langer, K.; von Briesen, H., *Nanomed-Nanotechnol* **2011,** *7* (4), 454-463. DOI DOI 10.1016/j.nano.2010.12.003.
233. Ming, X.; Carver, K.; Wu, L., *Biomaterials* **2013,** *34* (32), 7939-49. DOI 10.1016/j.biomaterials.2013.06.066.
234. Vlashi, E.; Kelderhouse, L. E.; Sturgis, J. E.; Low, P. S., *Acs Nano* **2013,** *7* (10), 8573-82. DOI 10.1021/nn402644g.
235. Wang, Z.; Yu, Y.; Dai, W.; Lu, J.; Cui, J.; Wu, H.; Yuan, L.; Zhang, H.; Wang, X.; Wang, J.; Zhang, X.; Zhang, Q., *Biomaterials* **2012,** *33* (33), 8451-60. DOI 10.1016/j.biomaterials.2012.08.031.
236. Kratz, F.; Elsadek, B., *J Control Release* **2012,** *161* (2), 429-45. DOI 10.1016/j.jconrel.2011.11.028.
237. Hellebust, A.; Richards-Kortum, R., *Nanomedicine (Lond)* **2012,** *7* (3), 429-45. DOI 10.2217/nnm.12.12.
238. Chinnathambi, S.; Chen, S.; Ganesan, S.; Hanagata, N., *Advanced healthcare materials* **2014,** *3* (1), 10-29. DOI 10.1002/adhm.201300157.
239. Biju, V.; Itoh, T.; Anas, A.; Sujith, A.; Ishikawa, M., *Analytical and bioanalytical chemistry* **2008,** *391* (7), 2469-95. DOI 10.1007/s00216-008-2185-7.
240. Jayakumar, M. K.; Idris, N. M.; Huang, K.; Zhang, Y., *Nanoscale* **2014,** *6* (15), 8441-3. DOI 10.1039/c4nr02422b.
241. Wang, Y. F.; Liu, G. Y.; Sun, L. D.; Xiao, J. W.; Zhou, J. C.; Yan, C. H., *Acs Nano* **2013,** *7* (8), 7200-6. DOI 10.1021/nn402601d.
242. Haro-Gonzalez, P.; Ramsay, W. T.; Martinez Maestro, L.; del Rosal, B.; Santacruz-Gomez, K.; Iglesias-de la Cruz Mdel, C.; Sanz-Rodriguez, F.; Chooi, J. Y.; Rodriguez Sevilla, P.; Bettinelli, M.; Choudhury, D.; Kar, A. K.; Sole, J. G.; Jaque, D.; Paterson, L., *Small* **2013,** *9* (12), 2162-70. DOI 10.1002/smll.201201740.
243. Maestro, L. M.; Haro-Gonzalez, P.; del Rosal, B.; Ramiro, J.; Caamano, A. J.; Carrasco, E.; Juarranz, A.; Sanz-Rodriguez, F.; Sole, J. G.; Jaque, D., *Nanoscale* **2013,** *5* (17), 7882-9. DOI 10.1039/c3nr01398g.
244. Li, X.; Wang, R.; Zhang, F.; Zhou, L.; Shen, D.; Yao, C.; Zhao, D., *Sci Rep* **2013,** *3*, 3536. DOI 10.1038/srep03536.
245. Kummar, S.; Gutierrez, M.; Doroshow, J. H.; Murgo, A. J., *British journal of clinical pharmacology* **2006,** *62* (1), 15-26. DOI 10.1111/j.1365-2125.2006.02713.x.
246. Horm, T. M.; Schroeder, J. A., *Cell adhesion & migration* **2013,** *7* (2), 187-98. DOI 10.4161/cam.23131.
247. Kennecke, H.; Yerushalmi, R.; Woods, R.; Cheang, M. C.; Voduc, D.; Speers, C. H.; Nielsen, T. O.; Gelmon, K., *Journal of clinical oncology : official journal of the American Society of Clinical Oncology* **2010,** *28* (20), 3271-7. DOI 10.1200/JCO.2009.25.9820.
248. Chaffer, C. L.; Weinberg, R. A., *Science* **2011,** *331* (6024), 1559-64. DOI 10.1126/science.1203543.
249. Manders, K.; van de Poll-Franse, L. V.; Creemers, G. J.; Vreugdenhil, G.; van der Sangen, M. J.; Nieuwenhuijzen, G. A.; Roumen, R. M.; Voogd, A. C., *BMC cancer* **2006,** *6*, 179. DOI 10.1186/1471-2407-6-179.
250. Falck, A. K.; Bendahl, P. O.; Ingvar, C.; Isola, J.; Jonsson, P. E.; Lindblom, P.; Lovgren, K.; Rennstam, K.; Ferno, M.; Ryden, L., *BMC cancer* **2012,** *12*, 403. DOI 10.1186/1471-2407-12-403.
251. Janni, W.; Gastroph, S.; Hepp, F.; Kentenich, C.; Rjosk, D.; Schindlbeck, C.; Dimpfl, T.; Sommer, H.; Braun, S., *Cancer* **2000,** *88* (10), 2252-9.

252. Pantel, K.; Cote, R. J.; Fodstad, O., *Journal of the National Cancer Institute* **1999,** *91* (13), 1113-24.
253. Ahn, S. G.; Lee, H. M.; Cho, S. H.; Lee, S. A.; Hwang, S. H.; Jeong, J.; Lee, H. D., *Yonsei medical journal* **2013,** *54* (5), 1168-77. DOI 10.3349/ymj.2013.54.5.1168.
254. Glendenning, J.; Cook, G., *Semin Nucl Med* **2013,** *43* (4), 317-23. DOI 10.1053/j.semnuclmed.2013.02.002.
255. Jeruss, J. S.; Kuerer, H. M., *New England Journal of Medicine* **2005,** *353* (20), 2191-2191.
256. Alix-Panabieres, C.; Muller, V.; Pantel, K., *Curr Opin Oncol* **2007,** *19* (6), 558-563.
257. Houssami, N.; Costelloe, C. M., *Ann Oncol* **2012,** *23* (4), 834-U1. DOI 10.1093/annonc/mdr397.
258. Hillman, E. M. C.; Amoozegar, C. B.; Wang, T.; McCaslin, A. F. H.; Bouchard, M. B.; Mansfield, J.; Levenson, R. M., *Philos T R Soc A* **2011,** *369* (1955), 4620-4643. DOI 10.1098/rsta.2011.0264.
259. Luker, G. D.; Luker, K. E., *Journal of Nuclear Medicine* **2008,** *49* (1), 1-4. DOI 10.2967/jnumed.107.045799.
260. Berman, A. T.; Thukral, A. D.; Hwang, W. T.; Solin, L. J.; Vapiwala, N., *Clin Breast Cancer* **2013,** *13* (2), 88-94. DOI 10.1016/j.clbc.2012.11.001.
261. Lu, X.; Yan, C. H.; Yuan, M.; Wei, Y.; Hu, G.; Kang, Y., *Cancer Res* **2010,** *70* (10), 3905-14. DOI 10.1158/0008-5472.CAN-09-3739.
262. Ganapathy, V.; Banach-Petrosky, W.; Xie, W.; Kareddula, A.; Nienhuis, H.; Miles, G.; Reiss, M., *Clinical & experimental metastasis* **2012,** *29* (5), 493-509. DOI 10.1007/s10585-012-9466-4.
263. Li, J. K.; Yu, L.; Shen, Y.; Zhou, L. S.; Wang, Y. C.; Zhang, J. H., *World journal of gastroenterology* **2008,** *14* (15), 2308-13.
264. Liao, Y. X.; Fu, Z. Z.; Zhou, C. H.; Shan, L. C.; Wang, Z. Y.; Yin, F.; Zheng, L. P.; Hua, Y. Q.; Cai, Z. D., *Oncology reports* **2015,** *34* (1), 33-42. DOI 10.3892/or.2015.3992.
265. Hulit, J.; Suyama, K.; Chung, S.; Keren, R.; Agiostratidou, G.; Shan, W.; Dong, X.; Williams, T. M.; Lisanti, M. P.; Knudsen, K.; Hazan, R. B., *Cancer Res* **2007,** *67* (7), 3106-16. DOI 10.1158/0008-5472.CAN-06-3401.
266. McGowan, P. M.; Ryan, B. M.; Hill, A. D.; McDermott, E.; O'Higgins, N.; Duffy, M. J., *Clinical cancer research : an official journal of the American Association for Cancer Research* **2007,** *13* (8), 2335-43. DOI 10.1158/1078-0432.CCR-06-2092.
267. McSherry, E. A.; Brennan, K.; Hudson, L.; Hill, A. D. K.; Hopkins, A. M., *Breast Cancer Res* **2011,** *13* (2). DOI Artn R31

10.1186/Bcr2853.
268. Zhao, C.; Lu, F. N.; Chen, H. X.; Zhao, X. D.; Sun, J.; Chen, H. L., *Int J Clin Exp Patho* **2014,** *7* (10), 7242-7248.
269. Foley, J.; Nickerson, N. K.; Nam, S.; Allen, K. T.; Gilmore, J. L.; Nephew, K. P.; Riese, D. J., 2nd, *Seminars in cell & developmental biology* **2010,** *21* (9), 951-60. DOI 10.1016/j.semcdb.2010.08.009.
270. Sethi, N.; Dai, X.; Winter, C. G.; Kang, Y., *Cancer cell* **2011,** *19* (2), 192-205. DOI 10.1016/j.ccr.2010.12.022.
271. Lu, X.; Wang, Q.; Hu, G.; Van Poznak, C.; Fleisher, M.; Reiss, M.; Massague, J.; Kang, Y., *Genes & development* **2009,** *23* (16), 1882-94. DOI 10.1101/gad.1824809.
272. Sethi, N.; Kang, Y., *British journal of cancer* **2011,** *105* (12), 1805-10. DOI 10.1038/bjc.2011.497.

273. Al-Hussaini, H.; Subramanyam, D.; Reedijk, M.; Sridhar, S. S., *Molecular Cancer Therapeutics* **2011,** *10* (1), 9-15. DOI 10.1158/1535-7163.MCT-10-0677.
274. Hazan, R. B.; Phillips, G. R.; Qiao, R. F.; Norton, L.; Aaronson, S. A., *The Journal of cell biology* **2000,** *149* (1), 239-239.
275. Hazan, R. B.; Phillips, G. R.; Qiao, R. F.; Norton, L.; Aaronson, S. A., *The Journal of cell biology* **2000,** *148* (4), 779-90.
276. Wang, Q.; Tan, M. C.; Zhuo, R.; Kumar, G. A.; Riman, R. E., *Journal of nanoscience and nanotechnology* **2010,** *10* (3), 1685-92.
277. Xie, J.; Lee, S.; Chen, X., *Adv Drug Deliver Rev* **2010,** *62* (11), 1064-79. DOI 10.1016/j.addr.2010.07.009.
278. Muthu, M. S.; Leong, D. T.; Mei, L.; Feng, S. S., *Theranostics* **2014,** *4* (6), 660-677. DOI 10.7150/thno.8698.
279. Liu, D.; Chen, Z., *J Breast Cancer* **2013,** *16* (2), 133-7. DOI 10.4048/jbc.2013.16.2.133.
280. Zhang, X.; Tian, Y.; Li, Z.; Tian, X.; Sun, H.; Liu, H.; Moore, A.; Ran, C., *J Am Chem Soc* **2013,** *135* (44), 16397-409. DOI 10.1021/ja405239v.
281. Chignell, C. F.; Bilski, P.; Reszka, K. J.; Motten, A. G.; Sik, R. H.; Dahl, T. A., *Photochem Photobiol* **1994,** *59* (3), 295-302.
282. Shang, L.; Nienhaus, K.; Nienhaus, G. U., *J Nanobiotechnology* **2014,** *12*, 5. DOI 10.1186/1477-3155-12-5.
283. Liu, J. N.; Bu, W.; Pan, L. M.; Zhang, S.; Chen, F.; Zhou, L.; Zhao, K. L.; Peng, W.; Shi, J., *Biomaterials* **2012,** *33* (29), 7282-90. DOI 10.1016/j.biomaterials.2012.06.035.
284. Zhou, J.; Sun, Y.; Du, X. X.; Xiong, L. Q.; Hu, H.; Li, F. Y., *Biomaterials* **2010,** *31* (12), 3287-3295. DOI 10.1016/j.biomaterials.2010.01.040.
285. Blomley, M. J.; Cooke, J. C.; Unger, E. C.; Monaghan, M. J.; Cosgrove, D. O., *BMJ* **2001,** *322* (7296), 1222-5.